Synthesis and Characterization of Multichromophoric Iron(II) Complexes as Novel Photosensitizers

---

Philipp Dierks

Universität Paderborn

Fakultät für Naturwissenschaften

Department Chemie – Anorganische Chemie

Arbeitsgruppe Prof. Dr. Matthias Bauer

Synthesis and Characterization of Multichromophoric Iron(II) Complexes as Novel Photosensitizers

Philipp Dierks

Dissertation zur Erlangung des akademischen Grades

doctor rerum naturalium (dr. rer. nat.)

2022

Philipp Dierks

Synthesis and Characterization of Multichromophoric Iron(II) Complexes as Novel Photosensitizers

Gutachter: Prof. Dr. Matthias Bauer

Privatdozent Dr. Hans Egold

Universität Paderborn

Arbeitsgruppe Prof. Dr. Mattias Bauer

Fakultät für Naturwissenschaften

Department Chemie – Anorganische Chemie

Warburgerstraße 100

33098 Paderborn

Für meine Familie.

“Life is tragic if it weren’t funny”

- Stephan Hawking

Abstract

In times of fossil fuel scarcity, the use of solar energy to initiate chemical processes is a promising alternative to reduce the fossil energy consumption. This approach offers the possibility of a sustainable form of energy production and storage in the form of transportable energy carriers. Carrying out such reactions with 3d metals such as iron instead of expensive and environmentally critical precious metals would be a milestone on the road to a sustainable future.

In this dissertation, the application of the multichromophoric approach – a concept successfully used in noble metal complexes – in iron(II) photosensitizers is investigated in detail. In this approach, organic chromophores are integrated in the backbone of the coordinating ligands, which can fundamentally improve the photophysics of these photosensitizers. By introducing an organic chromophore, a reservoir effect can drastically extends the lifetime of catalytically active states. Additionally, an antenna effect – an intramolecular energy transfer – that significantly increases the fraction of occupied catalytically active states is observed for noble metal-based photosensitizers.

To investigate these effects also in iron complexes, five different classes of ligands and complexes have been synthesized, each functionalized with different organic chromophores. A reservoir effect, which was originally targeted, could not be observed but by functionalization three main effects were discovered in these complexes. Firstly, the functionalization leads to a red shift and an increase in the extinction coefficient of the MLCT absorption bands. Secondly, the lifetime of the catalytically active MLCT states also increases. And thirdly, all presented ligands and complexes are emissive due to the additional organic chromophore. This leads to an antenna effect, which results in a larger occupation of MLCT states. All these effects were found for all fully characterized complexes.

Catalytic energy transfer and electron transfer reactions were performed for selected complexes prepared as part of this work. One iron complex shows energy transfer from an excited state to oxygen ($^3O_2$), leading to the formation of reactive oxygen ($^1O_2$). This kind of energy transfer has never been described for iron complexes in the literature before. The reactive oxygen was successfully combined with various organic diene systems. On multichromophoric ruthenium complexes, an improvement of catalytic properties in proton reduction was demonstrated, showing the potential of the multichromophoric approach in electron transfer reactions.

The obtained results of the photophysical studies of the ground and excited states provide a fundamental understanding of the complexes after excitation with light and show a significant improvement in both the absorption properties and the lifetimes of the catalytically active states. The results of the catalytic experiments demonstrate the potential of this class of complexes in both energy transfer and electron transfer reactions.

Kurzfassung

In Zeiten sinkender Vorkommen fossiler Energieträger, muss der Menschheit bewusstwerden, dass die aktuell zur Energiegewinnung genutzten Ressourcen endlich sind. Daher kommen der Entwicklung und Nutzung von erneuerbaren Energieträgern ein hohes gesellschaftliches und ökologisches Interesse zu. Die Entwicklung von Systemen zur effektiven Nutzung von solarer Energie auf molekularer Ebene steht daher aktuell im Fokus der Forschung. Dieser Ansatz bietet die Möglichkeit einer nachhaltigen Form der Energieerzeugung und -speicherung in Form von transportablen Energieträgern. Die Durchführung solcher Reaktionen mit 3d-Metallen wie Eisen anstelle von teuren und umweltkritischen Edelmetallen wäre ein Meilenstein auf dem Weg in eine nachhaltige Zukunft.

Im Rahmen dieser Dissertation wird die Anwendung des multichromophoren Ansatzes in Eisen(II)-Photosensibilisatoren ausführlich untersucht. In diesem Ansatz werden organische Chromophore im Rückgrat der koordinierenden Liganden integriert, was die Photophysik dieser Photosensibilisatoren fundamental verbessern kann. Durch die Einführung eines organischen Chromophors wird für edelmetallbasierte Photosensibilisatoren ein Reservoir-Effekt, der die Lebenszeit katalytisch aktiver Zustände deutlich verlängert, erreicht. Zusätzlich wird ein Antennen-Effekt – ein intramolekularer Energietransfer – beschrieben, wodurch die Häufigkeit, mit der die katalytisch aktiven Zustände besetzt werden, deutlich erhöht wird.

Um diese Effekte auch in Eisenkomplexen zu untersuchen, wurden in dieser Arbeit fünf verschiedene Liganden- und Komplexklassen synthetisiert, die jeweils mit verschiedenen organischen Chromophoren funktionalisiert wurden. Ein Reservoir-Effekt, welche ursprünglich anvisiert wurde, konnte nicht beobachtet werden, aber durch die Funktionalisierung wurden drei wesentliche Effekte in diesen Komplexen entdeckt. Zum ersten führt die Funktionalisierung zu einer Rotverschiebung und einer Erhöhung des Extinktionskoeffizienten der katalytisch aktiven MLCT Zustände. Zum zweiten erhöht sich auch die Lebenszeit der katalytisch aktiven MLCT Zustände. Und zum dritten lumineszieren alle dargestellten Liganden und Komplexe aufgrund des zusätzlichen organischen Chromophors. Dieses führt zu einem Antennen-Effekt, der eine häufigere Besetzung von MLCT Zuständen bewirkt. All diese Effekte wurden für alle vollständig untersuchten Komplexe gefunden.

Für ausgewählte Komplexe wurden katalytische Energietransfer- und Elektronentransfer-Reaktionen durchgeführt. Ein dargestellter Eisenkomplex zeigt einen bisher in der Literatur für Eisenkomplexe nie zuvor beschriebenen Energietransfer von einem photo-angeregten Zustand auf Sauerstoff ($^3O_2$), was zur Bildung von reaktivem Sauerstoff ($^1O_2$) führt. Dieser wurde mit verschiedenen organischen Dien-Systemen umgesetzt. An multichromophoren Rutheniumkomplexen konnte eine Verbesserung der katalytischen Eigenschaften in der Protonenreduktion gezeigt werden, wodurch das Potential des multichromophoren Ansatzes auch in Elektronentransferreaktionen gezeigt wurde.

Die erhaltenen Ergebnisse der photophysikalischen Untersuchungen der Grund- und angeregten Zustände liefern ein grundlegendes Verständnis der Komplexe nach Anregung mit Licht und zeigen eine deutliche Verbesserung sowohl der Absorptionseigenschaften als auch der Lebenszeiten der katalytisch aktiven Zustände. Die Ergebnisse der katalytischen Experimente zeigen das Potential dieser Komplexklasse in sowohl Energietransfer- als auch Elektronentransferreaktionen.

Eidesstattliche Erklärung

Hiermit versichere ich, die vorliegende Arbeit selbständig angefertigt und keine anderen als die von mir angegebenen Hilfsmittel verwendet zu haben. Wörtliche und sinngemäße Zitate wurden als solche gekennzeichnet und die Genehmigungen zur Veröffentlichung der urheberrechtlich geschützten Publikationen wurden eingeholt.

Paderborn, der 02.05.2022 _____

Philipp Dierks

Danksagung

An dieser Stelle möchte ich allen Personen, die mich während meines Studiums und meiner Promotion unterstützt, durch Höhen und Tiefen getragen und zum erfolgreichen Abschluss dieser Zeit beigetragen haben, von ganzem Herzen danken.

Prof. Dr. Matthias Bauer möchte ich für die Betreuer meiner Arbeit in seiner Arbeitsgruppe danken. Dieser Dank gilt für eine spannendes Forschungsthema und damit verbundene Diskussionen, Anregungen und Verwirklichungsmöglichkeiten, viele persönliche und wissenschaftliche Freiheiten, sowie wissenschaftliche und persönliche Ratschläge in – nicht nur in wissenschaftlicher Hinsicht – herausfordernden Zeiten.

Herrn PD Dr. Hans Egold danke ich für die Übernahme des Zweitgutachtens, sowie seiner durchgehenden Hilfsbereitschaft und Unterstützung bei der NMR-Analytik. Mein Dank gilt außerdem den beiden weiteren Prüfern Prof. Dr. Thomas D. Kühne und Prof. Dr. Thomas Werner für die Begutachtung dieser Arbeit.

Des Weiteren möchte ich mich bei allen anderen bedanken, die an der Erstellung dieser Arbeit behilflich waren: Für die Einkristallstrukturanalyse – Dr. Roland Schoch. Für die Massenspektrometrischen Analysen – Dr. Adam Neuba und Christiane Gloger, denen ebenfalls für die spektroelektrochemischen Analysen beziehungsweise den Elementaranalysen zu danken ist. Für zahlreiche NMR-Messungen gilt mein Dank Frau Karin Stolte.

Das Gelingen dieser Arbeit beruht auch auf den hervorragenden Kooperationen mit anderen Arbeitsgruppen. Daher möchte ich der Arbeitsgruppe von Prof. Dr. Stefan Lochbrunner – im besonderen Ayla Kruse und Miguel Andre Argüello Cordero – für die Messung, Auswertung und Diskussion von transienten Absorptions- und Streak-Kamera Messungen, der Arbeitsgruppe von Prof. Dr. Oliver Kühn – im besonderen Olga Bokareva – für quantenmechanische Berechnungen und der Arbeitsgruppe von Prof. Dr. Stefan Hohloch für synthetische Hinweise und Diskussionen danken.

Dem Fond der chemischen Industrie des Verbandes der Chemischen Industrie e.V. möchte ich für eine zweijährige finanzielle Unterstützung dieser Promotion danken.

Während meiner Promotion hatte ich die Ehre viele talentierte und motivierte Studierende betreuen zu dürfen. Ein besonderer Dank gilt den Studierenden, die durch ihre Arbeit aktiv am Gelingen dieser Promotion beteiligt waren. Namentlich möchte ich dabei Lavinia Nimczewski, Ina Kopp, Sebastian Schicktanz und Yuan You nennen.

Allen Kollegen meiner Arbeitsgruppe möchte ich sehr herzlich für die wunderbare Arbeitsatmosphäre danken. Ohne Input, Diskussion, aber auch Pausen mit euch wäre diese Arbeit nicht möglich gewesen. Ganz besonders danken möchte ich an dieser Stelle meinen langjährigen Laborkollegen Marina Huber-Gedert und Lennart Schmitz. Ich danke euch für eine

freundschaftliche Arbeitsatmosphäre, die kaum zu vergleichen und mit Sicherheit schwer wieder zu finden ist.

Neun Jahre an der Universität hinterlassen auch im Freundeskreis Spuren. Daher möchte ich meinen ehemaligen Studienkollegen danken, die bis heute an meiner Seite stehen und diese Arbeit teilweise auch als Kollegen verfolgt und immer unterstützt haben.

Zu guter Letzt gilt mein aller größter Dank meinen Freunden und meiner Familie. Ich danke meinen Eltern, meinem Bruder, meinen Großeltern und meiner Frau, die in jeder nur vorstellbaren Situation ein Rückhalt für mich waren. Euch gilt mein allergrößter Dank dafür, dass ihr mich in schweren Phasen unterstützt und motiviert habt, aber mich auch in den oft schwierigen Phasen dieser Promotion in die Realität zurückgeholt habt.

Content

Abstract vii

Kurzfassung viii

Eidesstattliche Erklärung xi

Danksagung xiii

Content xv

List of general abbreviations xvii

List of chemical abbreviations xix

Introduction 1

1.1 Utilization of solar Energy on a Molecular Scale 1

1.2 Substitution of Platinum Group Metals by Iron 3

1.3 Structure of this work 5

Scientific background 7

2.1 Hydrogen 7

2.1.1 Production of hydrogen 8

2.1.2 Photocatalytic Proton Reduction 10

2.2 Photosensitizers 11

2.2.1 Photophysical properties of d^6-TMCs 11

2.2.2 Strategies to improve the photophysical properties of iron(II) complexes 13

2.2.3 The Multichromophoric Approach 17

Aim of this work 23

3.1 Aim of this work 23

Synthesis 25

4.1 Synthesis of terpyridine-based ligands and complexes 25

4.2 Syntheses of (benz)imidazole-based complexes 26

4.3 Synthesis of triazole and mesoionic-carbene based ligands and complexes 35

4.4 Synthesis of multichromophoric ruthenium complexes 40

Characterization 41

5.1 Photophysics of $[Fe(tpy\text{-}R)_2](PF_6)_2$ complexes 41

5.2 Photophysics of $[Fe(bim\text{-}R)_2](PF_6)_2$ complexes 44

5.3 Photophysics of $[Fe(bbp\text{-}R)_2](PF_6)_2$ complexes 51

5.4 Photophysics of $[Fe(btp\text{-}R)_2](PF_6)_2$ complexes 57

5.5 Photophysics of $[Fe(tri\text{-}R)_2](PF_6)_2$ complexes 60

5.6 Photophysics of $[Ru(bbp\text{-}R)_2](PF_6)_2$ complexes 63

Catalytic Experiments 67
6.1 Photocatalytic Protonreduction 67
6.2 Sensitization of oxygen 69
Summary and Conclusion 73
Perspectives 77
8.1 Short-, medium-, and long-term perspectives 77
Experimental Details 81
9.1 General information on equipment and chemicals 81
9.2 Annotations to the used analytical and spectroscopic techniques 81
9.3 Syntheses 85
References 138
List of figures 146
List of schemes 149
List of tables 150
Scientific publications and presentations 151
List of publications 151
List of oral presentations 152
List of poster presentations 152
Appendix 153

List of general abbreviations

1,4-DB	1,4-dichloro-benzene
BL	bridging ligand
CC	climate change
CCS	carbon capture and storage
CE	global CO2 emission
Chrom	chromophore
CS	criticality score
DAS	decay associated spectrum
DWD	Deutscher Wetterdienst
ED	electron donator
EM	electron mediator
EnT	energy transfer
eq	equation/equivalents
ESA	excited state absorption
ET	electron transfer
et al	et alii
f	femto
FRET	Förster Resonance Energy Transfer
g	gram
GP	global production
GS	ground state
GSB	ground state bleach
HOMO	highest occupied molecular orbital
HT	human toxicity
Hz	Hertz
IC	internal conversion
ISC	intersystem crossing
K	Kelvin
kWh	Kilowatt-hour
LIESST	light-induced excited spin-state trapping
LMCT	ligand to metal charge transfer
LUMO	lowest unoccupied molecular orbital
m	milli
M	mega
MC	metal centered
ME	marine ecotoxicity
MIC	mesoionic carbens
MLCT	ligand to metal charge transfer
MO	molecular orbital
n	nano
NHC	N-heterocyclic carbenes
NMR	nuclear magnetic resonance spectroscopy
p	Piko
PEM	Proton Exchange Membrane
PHMED	photo-hydrogen-evolving molecular devices

PMG	platinum group metals
pos	positive
ppm	parts per million
PS	photosensitizer
RT	room temperature
s	seconds
t	ton
T	terra
TA	transient absorption
TCSPC	time correlated single photon counting
TDDFT	time dependent density functional theory
TE	terrestrial ecotoxicity
TMC	transition metal complex
WRC	water reduction catalyst

List of chemical abbreviations

ant	anthracene
bbp	(pyridine-2,6-diyl)bis(1-methyl-benzimidazol-2-ylidene)
bim	1,1'-(pyridine-2,6-diyl)bis(3-methyl-1H-imidazol-3-ium)
bpy	2,2`-bipyridine
btp	2,6-bis(1-ethyl-1H-1,2,3-triazol-4-yl)pyridine
btz	3,3'-dimethyl-1,1'-di-*p*-tolyl[4,4'-bis-(1,2,3-triazol-5-ylidene)]
DCM	dichlormethane
dcpp	2,6-bis(2-carboxypyridinyl)pyridine
ddpd	*N,N'*-dimethyl-*N,N'*-dipyridine-2-yl-pyridine-2,6-diamine
DIPA	*N*-(Propan-2-yl)propan-2-amine
dqa	2,6-di(quinoline-8-yl)pyridine
EDTA	2,2',2'',2'''-(Ethane-1,2-diyldinitrilo)tetraacetic acid
FcH	ferrocene
ImP	1,1'-(1,3-phenylene)bis(3-methyl-1-imidazol-2-ylidene)
LiHMDS	Lithium 1,1,1-trimethyl-*N*-(trimethylsilyl)silanaminide
naph	naphthalene
n-BuLi	butyllithium
NI	naphthalimide
pdmmi	3,3'-pyridine-2,6-diyl(methylene)bis(1-methylimidazolylidene)
PEPPSI	Pyridine-Enhanced Precatalyst Preparation Stabilization and Initiation
per	perylene
phen	phenyl
phtmeimb	phenyl(tris(3-methylimidazol-1-ylidene))borate
PNI	Pyridinyl-naphthalimide
pyr	pyrene
SPhos	Dicyclohexyl(2',6'-dimethoxy[1,1'-biphenyl]-2-yl)phosphane
TBTA	Tris((1-benzyl-4-triazolyl)methyl)amine
TEA	Triethylamine
THF	Tetrahydrofuran
TMPMgCl	2,2,6,6-tetramethylpiperidinylmagnesium chloride lithium chloride complex
Tpy	2,2':6',2''-terpyridine
tri	4,4'-(pyridine-2,6-diyl)bis(1-ethyl-3-methyl-1H-1,2,3-triazol-3-ium)

1

Introduction

Scarcity of fossil fuels and global climate change raise the challenge for scientists to develop novel and sustainable methods for energy production and storage. To design resource-efficient supply chains and energy circles free from emissions is an imperative necessity for the next decades and generations. In this context, iron is in the focus of interest, as it is the most earth abundant transition metal in the earth crust. Transition metal complexes (TMCs) as molecular photosensitizers using iron as their central atom are in the focus of this thesis to enable the utilization of solar energy on a molecular scale.

1.1 Utilization of solar Energy on a Molecular Scale

The earth's climate is influenced by a wide variety of factors. To be able to specifically identify these influencing variables, the climate data of many countries and regions have long been collected by weather services and climate research institutes and made publicly available to document climate changes. For Germany, these data are provided by the German Weather Service (Deutscher Wetterdienst, DWD), including documentation of the mean annual temperature in Germany (Figure 1.1.1). Compared to the long-term mean from 1961 to 1990, the linear trend of the mean annual temperature from 1881 to 2021 in Germany is +1.6 K.[1]

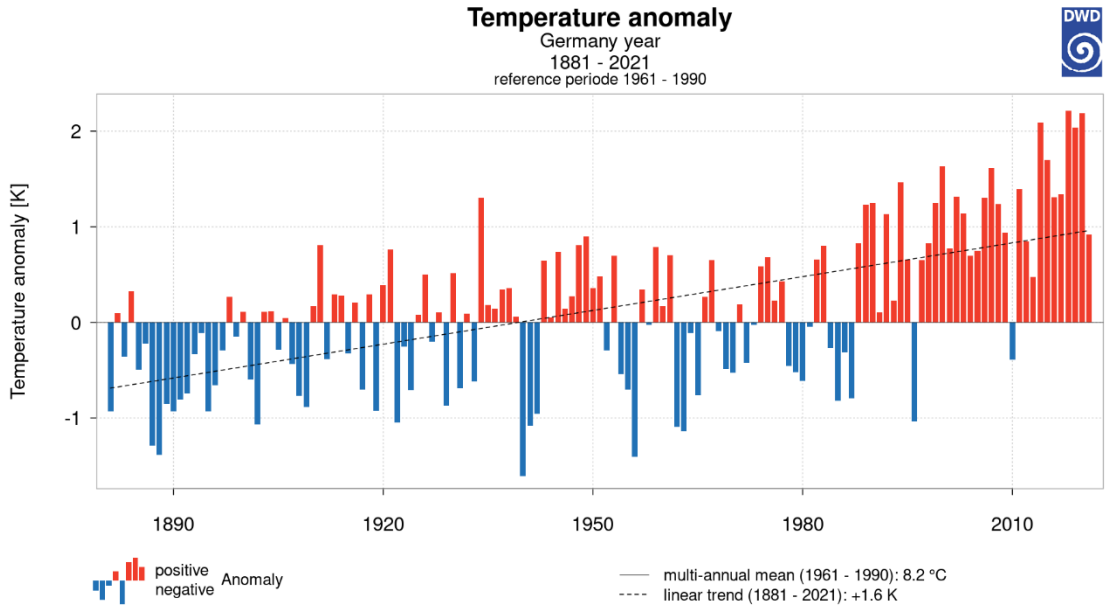

Figure 1.1.1: Annual temperature anomaly in Germany in the time period 1881-2021 with positive (red) and negative (blue) anomalies with respect to the multi-annual mean (1961-1990) of 8.2 °C. Dashed line shows the linear trend of the mean annual temperature from 1881 to 2021 of +1.6 K.[1]

It is particularly striking that, relative to the reference period, nine of the ten hottest years in Germany occurred in the last 20 years and only two below-average warm years (1996, 2010) occurred in the last 34 years.[1]

This significant increase in average annual temperatures is associated with CO_2 released into the atmosphere as a product of burning fossil fuels in combustion engines or power plants. The concentration of CO_2 in the earth's atmosphere has been recorded in the Keeling curve since 1958 (Figure 1.1.2). The curve shows a characteristic cyclic annual pattern that mirrors the vegetation cycle in the northern hemisphere. The natural process of CO_2 uptake and release by plants is a closed cycle in which the amount of CO_2 released is reabsorbed throughout the year if no human-caused (anthropogenic) events occur. The dramatic slope of the Keeling curve impressively documents the resulting anthropogenic increase in CO_2 concentration in the Earth's atmosphere due to changes in land use and the use of fossil fuels. The anthropogenic input represents a notable additional source in the CO_2 cycle, which cannot be completely absorbed by soils, plants, and oceans. The Keeling curve is thus a particularly important metrological indication of human-induced climate change.[2]

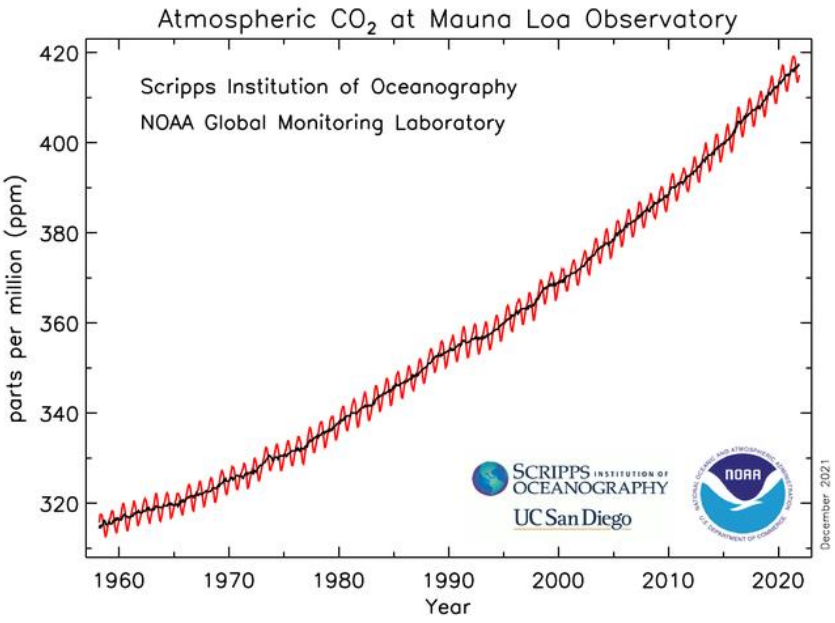

Figure 1.1.2: Atmospheric CO_2 in ppm at Mauna Loa Observatory (Keeling-Curve 1958-2021).[2]

Renewable energies offer a solution for the decoupling of increasing energy demand and the emission of CO_2 by civilization. In 2020, renewable energies had a share of 45.3 % of the total electricity consumption in Germany. This was the first time the production of renewable energies overcame the production of electricity by fossil sources. However, photovoltaics, which are the most common use of solar energy, have a share of only about 19.4 % of the total composition of renewable energy (250.2 billion kWh).[3] This corresponds to an energy of 48.6 billion kWh, whereas solar energy alone has a potential of up to 2482 TWh in our latitudes.[4]

A more dramatic situation is revealed in the global renewable energy usage data. Again, solar energy in the form of photovoltaics accounted for only 8.6% of global generation of renewable

electricity. This represents a dramatically low share of only about 2.5 % of solar energy in total global electricity generation in 2019.[5]

To exploit this enormous potential more adequately, new strategies for harnessing solar energy must be developed. These include the development of new ways to use solar energy besides photovoltaics. One possible variant may be the photocatalytic production of green hydrogen.

Green hydrogen, which is produced completely without emission of CO_2 in the production processes, is currently almost exclusively being produced through electrolysis of water by electricity from photovoltaic, hydro or wind power. Electrolysis has an efficiency of up to 85 %, resulting from losses during the two conversion processes of solar, wind or hydro energy into electricity and the subsequent conversion of the electricity into hydrogen.[6] Moreover, the local production of hydrogen in this process is always dependent on the possibility of local production of green electricity. Green hydrogen can be produced by electrolysis only in regions with the possibility to produce green electricity. Regions without this possibility must first be supplied with electricity via power lines, which often meet with widespread public opposition, or be supplied directly with green hydrogen, for which a completely new infrastructure must be built.

One possibility for the local production of green hydrogen lies in photocatalytic proton reduction. In this process, water is also split into the elements hydrogen and oxygen. In these systems, light is absorbed by special chemical compounds and the protons in the water are reduced to green hydrogen by catalysts. The advantages of photocatalytic proton reduction are the possibility of local production of green hydrogen without the need to build a supraregional hydrogen infrastructure or additional power lines. In addition, there is the possibility of a very large increase in efficiency compared to electrolysis, since the solar energy does not first have to be converted into electricity but is used directly to produce hydrogen.

Essential components in all conceivable systems to produce green hydrogen by solar energy, whether electrolytically by green electricity or photocatalytically, are photosensitizers, the sustainable conception of which is outlined in the following introductory section.

1.2 Substitution of Platinum Group Metals by Iron

Research in the field of photoactive substances plays a key role in the utilization of solar energy at the molecular level. These photosensitizers absorb the light of the solar spectrum, the solar energy is converted into chemical energy in the form of excited states of the photosensitizers. From the excited states electrons are passed onto a catalyst where the reduction of protons to hydrogen takes place. Such photosensitizers are used in photocatalytic proton reduction as well as in photovoltaics and other photochemistry. Substances that are currently frequently used are organic chromophores and transition metal complexes containing noble metals.

Since organic chromophores can absorb only a narrow range of the solar spectrum and transition metal complexes containing noble metals offer economic and ecological disadvantages, iron complexes have become the focus of research.[7] Transition metal complexes used as standard in photochemistry are based on ruthenium and iridium as central atoms. These platinum group metals (PMGs) are extremely rare and are only produced in small quantities annually worldwide.

The largest deposits are in South Africa and Russia. Together with the USA, Canada, and Zimbabwe, these five countries provide the global quantity of PMGs[8]. The total concentration of PMG ore ranges from 3-8 g/t in the deposits. The concentrations of ruthenium and iridium are varying from 0.3 g/t in the Merensky Reef to 1 g/t in the UG2 Reef, both located in South Africa.[9] The production of these metals from small total concentrations has a high degree of pollution and compounds containing ruthenium and iridium are extremely toxic to the environment, water and to humans.

To balance factors from different fields in a single indicator, Graedl *et al.* implemented the "Criticality Score" for 62 different metals and metalloids in 2015. The Criticality Score (CS) is considering 17 different subcategories from the various fields such as long- and short-term supply risks, environmental implications, and vulnerability to supply restrictions. This analysis results in the CS as an indicator for each metal or metalloid in the range from 0 (of little concern for nature and humans) to 100 (of extreme concern).[10] To illustrate the findings of Graedl *et al.* selected categories are visualized in Figure 1.2.1 for ruthenium, iridium, and iron. The global production (GP) and the global CO_2 emission (CE) is given in kilogram. The effect on climate change (CC) is given in kg CO_2 equivalents per produced kg of pure metal. The human toxicity (HT), terrestrial ecotoxicity (TE) and the marine ecotoxicity (ME) are given in equivalents to mg 1,4-dichloro-benzene (1,4-DB) per kg of pure metal. Water depletion (WD) is shown in liters. All data are taken from the work of Graedl *et al.* and are referred to the year 2008.[10]

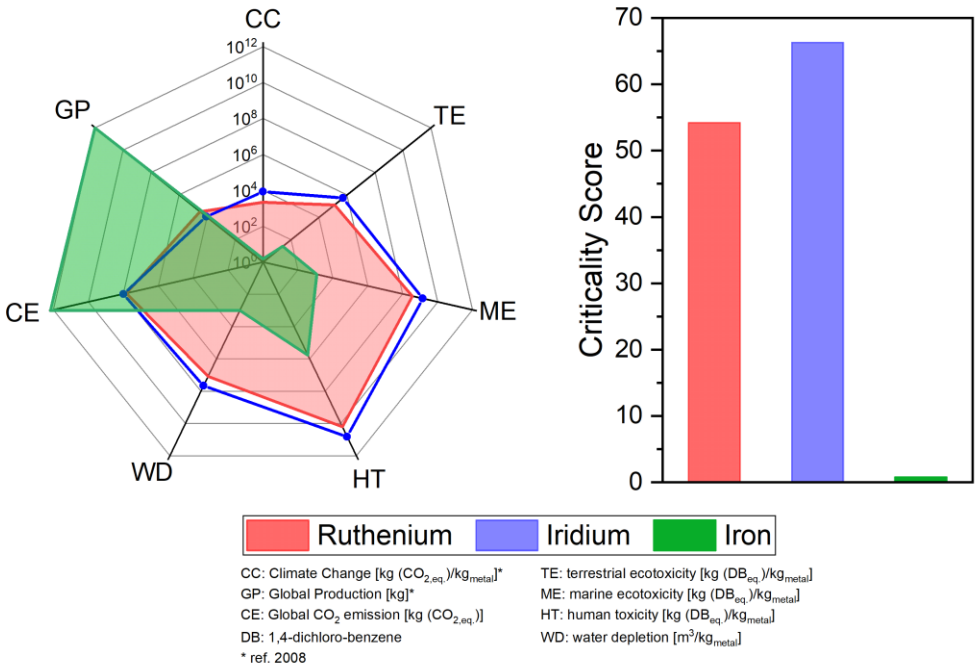

Figure 1.2.1: Diagram of selected categories included in the criticality score according to Graedl et al. and the corresponding CS for ruthenium, iridium and iron.[10,7]

The impact of the production of the pure metals is quite different. In comparison of these three metals, iron has the largest global production, which is about the factor 10^8 larger than iridium and ruthenium. Due to this fact the global CO_2 emission of iron is higher by the factor of about 10^4. Referring to the CO_2 equivalents per produced mass, the results look quite different. The kg

CO_2 equivalents per kg pure iron is smaller by a factor of 10^4. The values for terrestrial and marine ecotoxicity and human toxicity are higher by at least the factor 10^4 in iridium and ruthenium in comparison to iron. The water depletion is by about the factor 10^5 lower for iron. Combining these categories among others, results in a criticality score of 54.2 for ruthenium and 66.3 for iridium. The criticality score of iron is overwhelming 0.8. The factor of economic efficiency, namely the price is even more drastic. The prices for PGMs in general are quite high (ruthenium approx. 12.000 €/kg; iridium approx. 180.000 €/kg),[11] while iron costs around 10 €/kg.[12] Additionally, iron offers a larger molar quantity, which is important for chemical use, due to its smaller molar mass.

Given these figures, it is obvious that iron as a metal could be a much more sustainable and ecologically friendly alternative to precious metals and there is a strong need to replace PMGs in photochemical applications to yield a novel approach for a sustainable future.

1.3 Structure of this work

The introductory part of this work is schematically divided into four main sections. First, the thematic background will be described in detail. The photocatalytic production of green hydrogen will be described, which is a sustainable method for the storage of solar energy and allows a diverse and location-independent use of the stored energy. This is followed by the introduction of photosensitizers, which are required for the utilization of solar energy at the molecular level. Their necessary properties are presented based on photosensitizers containing noble metals. Subsequently, strategies are shown how noble metal-containing photosensitizers can be substituted to provide a more sustainable alternative in photocatalytic proton reduction and photocatalysis in general. For this purpose, different strategies are presented to optimize the most important properties of iron complexes in photocatalysis. Finally, the multichromophoric approach in iron complexes, which is the main aspect of this dissertation, is presented and described in detail.

2

Scientific background

Hydrogen is the fuel with the highest mass-related energy density and can be used in fuel cells without releasing greenhouse gases. For this reason, hydrogen and the fuel cell have a very high public profile and are seen by politicians, the public and business as an important building block in the energy transition. In addition to hydrogen itself, derived products made from hydrogen (ammonia, methanol, methane, etc.) are important basic materials for the chemical, agricultural and pharmaceutical industries. But regeneratively produced hydrogen is currently not available to a large extend, which is why there is great research interest in revolutionizing sustainable hydrogen production.

Photocatalytic proton reduction is a method for using solar energy to directly generate molecular hydrogen. The production of electricity from sunlight is no longer necessary for this process. Therefore, this method promises lower losses due to an omitted conversion process of the energy und possibly higher efficiencies than the production of hydrogen by electrolysis. Suitable quantum yields of the photosensitizers are prerequisite for a high efficiency. However, photosensitizers based on precious metals limit the sustainability of this method from an economic and ecological point of view. Finding sustainable alternatives as photosensitizers such as iron complexes is thus a big challenge.

2.1 Hydrogen

Hydrogen is the most abundant element in the universe. About two thirds of the total mass of the universe consists of hydrogen. In the earth's crust, every sixth atom is a hydrogen atom. Elemental hydrogen, however, only occurs in the atmosphere in traces (volume fraction: $5 \cdot 10^{-5}$ %).[13] For this reason, hydrogen for industrial applications is currently produced almost exclusively from fossil raw materials. To highlight the energy source used in the production and to label the sustainability of different hydrogen production strategies a color code is often used (Figure 2.1.1).

Grey hydrogen is based on the use of fossil hydrocarbons. The steam reforming of natural gas and higher hydrocarbons is decisive to produce grey hydrogen. Its production is associated with considerable CO_2 emissions. Blue hydrogen is hydrogen whose production is coupled with a CO_2 capture and storage process (CCS). The CO_2 produced during hydrogen production is thus not released into the atmosphere and hydrogen production can be considered CO_2-neutral in balance sheet terms. Turquoise hydrogen is hydrogen that has been produced by the thermal splitting of methane (methane pyrolysis). Instead of CO_2, solid carbon is produced. Prerequisites for the CO_2 neutrality of the process is the heat supply of the high-temperature reactor from renewable or

CO_2-neutral energy sources and the permanent binding of the carbon. Green hydrogen is produced by electrolysis of water, whereby only electricity from renewable energies is used for electrolysis.[14]

2.1.1 Production of hydrogen

The primarily used process to produce hydrogen is steam reforming. The process utilizes carbon-based energy sources and steam to generate hydrogen. This technique delivers about 70 % of the global hydrogen production. Two endothermic key steps are involved in the steam reforming process. In the first step fossil hydrocarbons and steam are reacting at the surface of a heterogeneous nickel catalyst to carbon monoxide and hydrogen (eq. 2.1). This reaction takes place at 750 °C-1000 °C and a pressure of 15 bar-20 bar.[13]

$$\mathrm{C}_n\mathrm{H}_m + n\mathrm{H}_2\mathrm{O}_{(g)} \rightleftharpoons n\mathrm{CO}_{(g)} + (n + 0.5m)\mathrm{H}_{2(g)} \tag{2.1}$$

The resulting mixture of carbon monoxide and hydrogen – called synthesis gas – is feed into a shift reactor. In this reactor, in the second step additional steam is added to oxidize the carbon monoxide to carbon dioxide and thus to increase the yield of produced hydrogen (eq. 2.2). This reaction is performed at 200 °C- 300 °C.[13]

$$\mathrm{CO} + \mathrm{H}_2\mathrm{O} \rightleftharpoons \mathrm{CO}_{2(g)} + \mathrm{H}_{2(g)} \tag{2.2}$$

Finally, the produced hydrogen is purified by adsorption. The efficiency of this process is up to 70 %. The process is limited by two different side reactions. First, in the methanation the produced hydrogen reacts with carbon monoxide to methane and reduces the overall yield of hydrogen. Second, in the Boudouard reaction carbon monoxide decomposes to carbon dioxide and carbon, reducing the overall yield of produced hydrogen by a smaller amount of carbon monoxide in eq. (2.2).[15] As fossil fuels are used, steam reforming is forming grey hydrogen. In the case of a following CO_2 capture and store (CSS) process, steam reforming is resulting in blue hydrogen.

A promising alternative to this method is methane pyrolysis (eq. 2.3). This is using methane from natural gas or biomass to produce hydrogen and elemental carbon. Methane is split in its elements in an endothermic reaction at high temperatures. Methane is added in a bubble column reactor filled with molten tin at 1000 °C heated by electricity. Produced hydrogen bubbling to the top of the column while carbon slag is deposited at the top of the column. This technique is not associated with carbon dioxide as a direct byproduct of the hydrogen production. Hydrogen produced by methane pyrolysis is claimed as turquoise hydrogen. Carbon as the resulting byproduct can be stored or used as fertilizer in agriculture for example.[16]

$$\mathrm{CH}_4 \rightarrow \mathrm{C}_{(solid)} + 2\mathrm{H}_{2(g)} \tag{2.3}$$

In principle, however, all the processes mentioned to produce hydrogen from fossil energy sources take place at high process temperatures. They require large amounts of energy. If this energy comes from fossil fuels, even more carbon dioxide emissions are associated with it. In terms of climate protection, it is usually better to burn natural gas or crude oil directly than to first produce

hydrogen at great expense and then use it in a supposedly environmentally friendly way. Other processes are therefore necessary for the climate-friendly production of hydrogen. One possibility is electrolysis with alkaline electrolysis cells.

$$2\mathrm{NaCl} + 2\mathrm{H_2O} \xrightarrow{electricity} 2NaOH + \mathrm{H_2} + Cl_2 \tag{2.4}$$

In alkaline electrolysis, water is split by applying electrical energy to two electrodes immersed in an aqueous alkaline electrolyte. At the anode hydroxide ions are oxidized to oxygen and water. At the cathode water is consumed to produce hydroxide ions and hydrogen (eq. 2.4). Both half-cells are separated by a diaphragm, which is permeable to hydroxide ions and water molecules to enable the transport of hydroxide ions from the cathode to the anode by a gradient in the osmotic pressure. The half-cells are also separated to keep the evolved gases apart from each other for safety and efficiency reasons.[13] Today, efficiencies of up to 85 % are achieved in alkaline electrolysis.[6]

In a proton exchange membrane (PEM, eq. 2.5) cell, no additional electrolyte is required like it is necessary for alkaline cells. The half cells are separated by a PEM, which is only permeable to protons. At the anode, water is oxidized to oxygen and protons. The protons pass through the membrane to the cathode at which hydrogen is evolved. The electrodes are based on noble metals. At this time, the PEM is not competitive with the alkaline cells, as no stack option is available at this stage.[17]

$$2\mathrm{H_2O} \xrightarrow{electricity} 2\mathrm{H_2} + O_2 \tag{2.5}$$

Optimally, the electrical energy for electrolysis comes from renewable power plants, so that the hydrogen is produced without carbon dioxide emissions. While electrolysis has already reached a high technical level as a climate-friendly option for hydrogen production, other alternative processes are still under development. No electricity is needed for photocatalytic proton reduction. In contrast to electrolysis, sunlight directly drives the chemical process that produces hydrogen. This method therefore has the potential to generate green hydrogen with a high degree of efficiency.

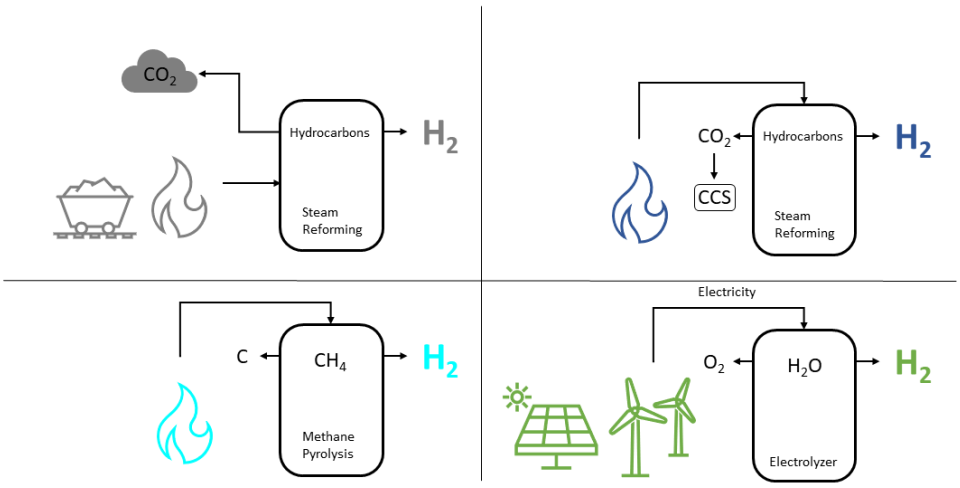

Figure 2.1.1: Schematic illustration of different colors of hydrogen including grey, blue, turquoise, and green hydrogen.

2.1.2 Photocatalytic Proton Reduction

Sustainable hydrogen production from solar energy without the use of fossil raw materials is a special challenge for the future. One of the most promising methods is the photocatalytic splitting of water into the elements hydrogen and oxygen. Due to the complexity of the individual partial reactions of photocatalytic water splitting, they are usually considered separately in research. Oxygen production is referred to as oxidative water splitting and hydrogen production as reductive water splitting.[18] When carrying out the partial reactions, an oxidizing agent is required in oxidative water splitting and a reducing agent in reductive water splitting. Therefore, the subsequent combination of the sub-processes is necessary to carry out the water splitting atom-economically and economically. Systems for the simultaneous development of hydrogen and oxygen are currently an exception.

The first results on photocatalytic water splitting were published at the end of the 1970s. Semiconducting metal compounds such as TiO_2 were used in heterogeneous systems,[19] but homogeneous systems were also developed.[20] The first homogeneous system for reductive water splitting with tris(2,2`-bipyridine)-ruthenium(II) $[Ru(bpy)_3]^{2+}$ as photosensitizer (PS) and $[CoMe_6[14]dienN_4(H_2O)_2]^{2+}$ as catalyst was published by Sutin *et al*. in 1979.[21] The used PS was already synthesized in 1936 by Burstall *et al*. and is nowadays a very intensively researched standard PS.[22] Two basic approaches for homogeneous systems are currently being in the focus of research for reductive water splitting and will be discussed in more detail below.

In general, systems for photocatalytic water splitting consist of a PS, a water reduction catalyst (WRC) and an electron donator (ED). The PS is excited by light and provides the electrons needed to reduce the protons. The WRC catalyzes the reduction of the protons to elemental hydrogen. The ED is easily oxidized and reduces the PS after electron transfer to ensure that this catalytic cycle is completed. After excitation with visible light, an electron is transferred from a metal-centered d orbital to a ligand-centered orbital of higher energy. This transfer is called metal-ligand charge transfer (MLCT) and corresponds to a formal intramolecular oxidation of the metal center and simultaneous reduction of the ligand.[23] Two different mechanisms can be described for the transfer of this excited electron to the WRC. On the one hand, the excited electron can be transferred to the WRC. The PS results in its oxidized form (oxidative quenching). It is then reduced by a reducing agent – the ED – and can be excited again by light. On the other hand, the PS can be excited, and an electron can be transferred from the ED to the formally oxidized metal center. The PS is then present in a reduced form (reductive quenching). Subsequently, the excited electron is transferred to the WRC and the PS can be excited again by light.[24] If the components described are not linked, this is called a multi-component system. In these systems, the PS, WRC, and ED are present in a mixture of solvent and water. Optionally, an electron mediator (EM) can be added to pass the electrons provided by the PS to the WRC. The mechanism by which reductive water splitting occurs in a multi-component system is shown schematically adapted from the literature (Figure 2.1.2, right panel). An exemplary and intensively researched multi-component system consists of $[Ru(bpy)_3]^{2+}$ as PS, EDTA or triethyl amine as ED (not shown), methyl viologen as EM and a Pt system as WRC.[25,24]

In addition, organized systems are used for photocatalytic water reduction. These are called molecular dyads or PHEMDs (photo-hydrogen-evolving molecular devices). In these systems, PS

and WRC are linked via a bridging ligand (BL), which transfers the electrons provided to the WRC. In dyads, an ED is also necessary to reduce the PS. As an example, a dyad and a multi-component system in which a ruthenium PS and a platinum WRC are used are shown, based on Sakai *et al.* (Figure 2.1.2, left panel).[26]

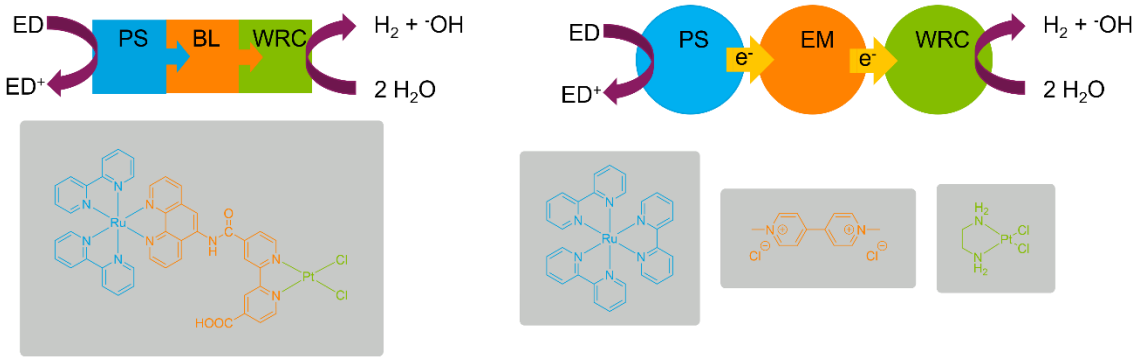

Figure 2.1.2: Schematic representation (top) and examples (bottom) of a molecular dyad (left panel)[26] and multicomponent systems (right panel) [24].

Researchers have different views on which of these basic systems achieves better results.[27,26] The expectations of some authors that dyads achieve better results can be justified with the help of direct electron transfer. The transfer of electrons through the bridging ligand is diffusion-independent and is postulated to be more efficient than the diffusion-dependent transfer of electrons through a solution.[18] In contrast, it was found that dyads are currently less active systems,[27] although they have a significantly higher long-term stability than multi-component systems.[28] For the utilization of solar energy, the PS plays a decisive role in both systems. In this work, novel concepts for photosensitizers used in multi component systems are investigated. The basic properties and the state of research on photosensitizers are described below.

2.2 Photosensitizers

Photosensitizers are needed for the application of solar energy at the molecular level, both in photocatalytic water splitting and in applications of photocatalysis in organic synthesis. For such applications, transition metal complexes containing noble metals have become established in the past. Particularly d^6 transition metals such as Ru^{2+}, Re^{+} or Ir^{3+} complexes are prominent, but also noble metal-free Cu^{+}, Co^{3+} and Fe^{2+} complexes have been described in the literature.[29,30] The following section describes the photophysical properties of d^6-TMCs and has basically been published in terms of this work.[7]

2.2.1 Photophysical properties of d^6-TMCs

Utilization of solar energy in photocatalysis with TMCs fundamentally bases on the ability of the PS to take part in energy transfer (EnT) or in electron transfer (ET) processes with organic substrates or catalysts in multicomponent systems upon photoexcitation. Effective absorption of visible light and the population of photocatalytically active excited states after the excitation

process are mandatory in TMCs suitable for photocatalysis. Efficient EnT or ET processes to substrates or catalysts need sufficiently long excited state lifetimes in these TMCs. This is important to overcome diffusion limitation in catalytic application. States fulfilling these requirements are long-lived metal-to-ligand charge-transfer (MLCT) states in complexes of noble metals (*e.g.*, Ru^{2+}, Ir^{3+}, Os^{2+}, Re^{+}) coordinated by polypyridine ligands with low-energy π* orbitals featuring a $4d^6$ or $5d^6$ electron configuration, as in $[Ru(bpy)_3]^{2+}$ (bpy = 2,2'-bipyridine) as a very prominent example.[31]

A simplified description of the photoexcitation processes in $Ru^{II}L_6$ complexes assumes an octahedral ligand field (Figure 2.2.1). It should be emphasized that of course a lower symmetry requires a slightly modified description, but due to the rather large ligand field splitting in Ru complexes the key message remains unaltered. The five metal-centered (MC) d-orbitals split into three orbitals with t_{2g} symmetry and two orbitals with e_g symmetry in an octahedral ligand field. The six valence electrons are located in the t_{2g} orbitals in the presented case. The t_{2g} orbitals are representing the highest occupied molecular orbitals (HOMOs), leading to a t_{2g}^6 low-spin ground-state configuration. The e_g orbitals remain unoccupied. Because of the strong ligand-field splitting, resulting from the effective metal–ligand interactions in the cases of 4d and 5d metal complexes, the unoccupied π* orbitals of the polypyridine ligands are lower in energy than the e_g orbitals and represent the lowest unoccupied molecular orbitals (LUMOs) of such complexes.[32] After photoexcitation, an electron from one the metal centered t_{2g}-HOMOs is excited into a π*-LUMO orbital. The lowest electronically excited state therefore has MLCT character. From the singlet ground state (^{1}GS), the singlet ^{1}MLCT state is initially populated in the Franck-Condon regime, followed by a rapid intersystem crossing (ISC), which takes typically place on the femtosecond time scale.[33] The finally populated triplet ^{3}MLCT states are quite long-lived, often emissive, and able to drive photocatalytic processes. In the case of $[Ru(bpy)_3]^{2+}$ a ^{3}MLCT lifetime of 1100 ns is sufficiently long to engage in bimolecular EnT and ET reactions with a huge variety of organic substrates in competition with its deactivation pathways to the ground state.[34]

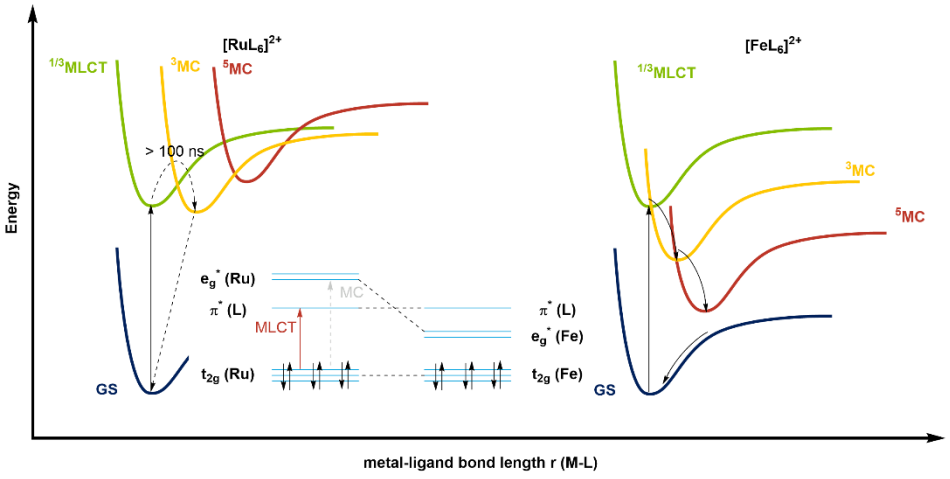

Figure 2.2.1: Schematic ground- and excited-state landscapes of ruthenium(II) (left) and iron(II) (right) polypyridine complexes. Middle: Simplified molecular orbital diagrams for the corresponding ruthenium(II) and iron(II) complexes.[35,36]

In $Fe^{II}L_6$ complexes with the $3d^6$ configuration the extension of the lifetimes of photoactive MLCT states is still a challenge. The intrinsically smaller ligand field splitting in first row transition metals

compared to their higher homologues is limiting the photofunctionality in iron complexes.[32] In iron(II) polypyridine complexes the e_g* orbitals are lower in energy than the ligand π* orbitals and are thus representing the LUMOs. Since t_{2g}-e_g transitions are Laporte forbidden, visible light absorption processes still lead to the population of ^{1}MLCT states. The ^{3}MLCT state is populated after rapid ISC in the same way as described in $[Ru(bpy)_3]^{2+}$. In contrast to the ruthenium analogues, in iron(II) complexes the ^{3}MLCT decays usually into triplet ^{3}MC states essentially without a barrier, followed by ISC and vibrational cooling. Consequently, a long-lived, non-emissive quintet ^{5}MC state is populated.[37] Relaxation from ^{5}MC into the ^{1}GS is both spin- and Laporte forbidden and therefore rather slow in comparison to the deactivation from ^{3}MLCT into ^{3}MC and from ^{3}MC into ^{5}MC states. As a result of the relaxation cascade, the ^{1}GS-^{5}MC transition can be achieved by visible light absorption and iron(II) polypyridine complexes result in a long-lived, non-emissive and non-catalytic active state. This effect is referred to as light-induced excited spin-state trapping (LIESST).[37] According to this discussion, in $[Fe(tpy)_2]^{2+}$ (tpy = 2,2′:6′,2′′-terpyridine) the populated ^{3}MLCT state relaxes ultrafast within 150 fs into the ^{3}MC. A following deactivation into the ^{5}MC state is observed, with a lifetime of 5.35 ns, which drastically limits its use in catalytic application.[38,39]

The main challenge in iron(II) complexes is to avoid the loss of photocatalytic activity following from the deactivation of ^{3}MLCT via MC states in the LIESST process. Therefore, the two main strategies to target the inversion of $^{3/5}$MC and ^{3}MLCT state energies are the stabilization of ^{3}MLCT and the destabilization of $^{3/5}$MC states. For this purpose, the ligand field splitting can be increased by the improvement of the octahedral geometry and by strong σ-donor ligands (i.e. N-heterocyclic carbenes; NHCs and mesoionic carbenes; MICs), which both leads to energetically higher MC states. Better π-acceptor ligands or by increased electronic delocalization are stabilizing the LUMO-levels, both reducing the energy of MLCT states.[7,35]

2.2.2 Strategies to improve the photophysical properties of iron(II) complexes

There are several strategies described in literature to improve the ^{3}MLCT lifetimes and catalytic properties of Fe^{2+} complexes. In numerous excellent reviews these strategies are summarized with detailed examples. In this section the most important milestones will be discussed in detail using selected examples. More comprehensive collections of strategies and examples of iron-base PS can be taken from very comprehensive reviews,[35,30,40a,29,40b–d] including the one that has been published in the frame of this work.[7]

Symmetry

A strategy to destabilize the e_g orbitals is to maximize the overlap between metal and ligand orbitals. A high local symmetry with a N-Fe-N *trans* angle as close as possible to 180° in FeN_6 ligand systems results in the maximized destabilization of the e_g levels (Figure 2.2.2). In a **$[Fe(dcpp)_2]^{2+}$** complex McCusker and coworkers achieved a N-Fe-N *trans* angle of 178.3°. Electron withdrawing carbonyl groups in the dcpp (= 2,6-bis(2-carboxypyridinyl)pyridine) ligand lead to a further destabilization of the ligands π* orbitals.[38] The lifetime of 280 ps at room temperature was assigned to have ^{5}MC character.[41]

The ddpd (= *N,N'*-dimethyl-*N,N'*-dipyridine-2-yl-pyridine-2,6-diamine) ligand is more electron rich, due to the electron amines instead of the carbonyl groups. The combination of dcpp with the electron-rich ddpd ligand by Heinze and coworkers in a heteroleptic push-pull ligand design gave a N-Fe-N *trans* angle of 178.4°. A ground state recovery within 528 ps was observed after photoexcitation. **[Fe(dcpp)(ddpd)]$^{2+}$** still exhibits a ^{3}MLCT > $^{3/5}$MC energy ordering.[42,43]

Gros and coworkers published **[Fe(dqa)$_2$]$^{2+}$** (dqa = 2,6-di(quinoline-8-yl)pyridine) – prepared using microwave techniques – with a N–Fe–N trans angle of 178.4° and a relaxation behavior, which is more like the benchmark complex **[Fe(tpy)$_2$]$^{2+}$**. A ^{3}MLCT state with a lifetime of 0.45 ps is initially populated upon photoexcitation in **[Fe(dqa)$_2$]$^{2+}$**, relaxing into a ^{5}MC state with a lifetime of 3.0 ns.[44]

The improvement of octahedral geometry has also successfully been transferred to C^N^C ligands using N-heterocyclic carbene ligands as strong σ-donors. A C-Fe-C trans angle of 176.1° is realized in **[Fe(pdmmi)$_2$]$^{2+}$** (pdmmi = 3,3'-pyridine-2,6-diyl(methylene)bis(1-methylimidazolylidene)). The lifetimes of one triplet state were determined in a range of 7-17 ps, while the lifetimes of the other range between 0.8 ps and 1.5 ps. The two proposed deactivation pathways include on the one hand a parallel decay from the ^{3}MLCT state and ^{3}MC state back into the ^{1}GS and on the other hand a mixed state decay. Longer lifetimes are most probable assigned to the ^{3}MC state. The ^{5}MC is excluded from the relaxation pathway in **[Fe(pdmmi)$_2$]$^{2+}$**, but the complete deactivation process has not fully been understood yet.[44]

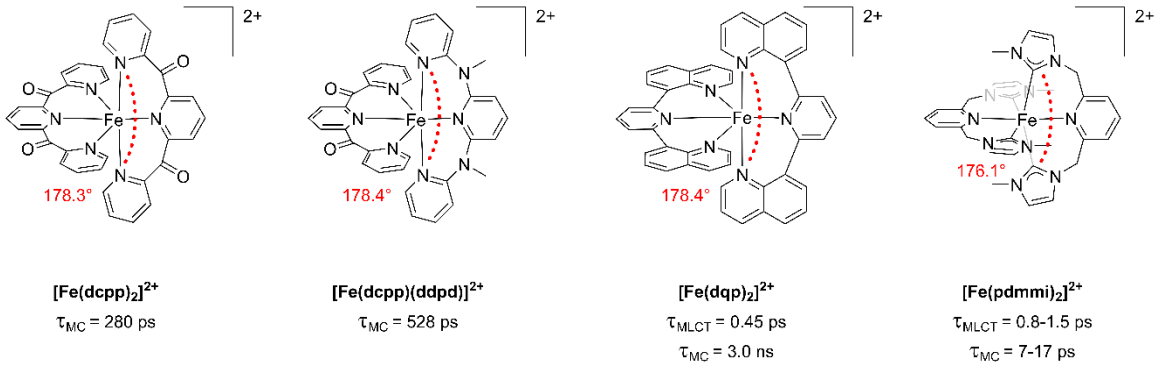

*Figure 2.2.2: Molecular structures and excited state lifetimes of **[Fe(dcpp)$_2$]$^{2+}$**,[38] **[Fe(dcpp)(ddpd)]$^{2+}$**,[42,43] **[Fe(dqp)$_2$]$^{2+}$**[44] and **[Fe(pdmmi)$_2$]$^{2+}$**[44] with optimized octahedral geometry.*

The exclusion of ^{5}MC states from the relaxation cascade is frequently reported and well understood for N-heterocyclic carbene metal complexes and further described in the following section.

Strongly σ-donating ligands

Introduction of strongly σ-donating *N*-heterocyclic carbenes (NHCs) induces a stronger ligand field and significant destabilization of the e_g orbitals (Figure 2.2.3). Ground-breaking studies on iron(II) photosensitizers with NHC ligands reported **[Fe(bim)$_2$]$^{2+}$** (bim = 1,1'-(pyridine-2,6-diyl)bis(3-methyl-1H-imidazol-3-ium) with a lifetime of 9 ps assigned to a ^{3}MLCT state.[39] A computational study confirmed the assignment of the ^{3}MLCT state and showed that the MC states are destabilized by the NHC ligands compared to **[Fe(tpy)$_2$]$^{2+}$**. To populate a ^{5}MC state, large structural

rearrangements and significant elongation of the metal-ligand bonds is necessary. Population of the ^{5}MC state is therefore unlikely and it is bypassed in the deactivation cascade.[45]

To counteract the destabilization of the ligand centered LUMO orbitals in NHCs, while achieving a maximal destabilization of the HOMO levels, expansion of the ligand π-system by benzimidazoles showed promising results in **[Fe(bbp)$_2$]$^{2+}$** (bbp = (pyridine-2,6-diyl)bis(1-methyl-benzimidazol-2-ylidene). **[Fe(bbp)$_2$]$^{2+}$** exhibits stabilized LUMO levels by the increased π-system at the benzimidazole. However, the stronger π-acceptor properties of benzimidazole also stabilize the t_{2g}-orbitals (HOMO), leading to an increased HOMO-LUMO gap. Despite this blue shift **[Fe(bbp)$_2$]$^{2+}$** exhibits an extended ^{3}MLCT lifetime of 16 ps.[46]

While NHCs are strong σ-donor ligands, their π-acceptor capability is limited. Mesoionic carbenes (MICs) carry a negative charge on the carbene carbon atom in one of their resonance structures and therefore act as stronger σ-donor ligands than classical NHCs.[47] Beside this, the π* levels are lower in energy than in NHCs by the increased number of N atoms, resulting in an improved π-acceptor capability. This concept was first used in the heteroleptic **[Fe(btz)$_2$(bpy)]$^{2+}$** complex (btz = 3,3'-dimethyl-1,1'-di-*p*-tolyl[4,4'-bis-(1,2,3-triazol-5-ylidene)]). Excited state kinetics of **[Fe(btz)$_2$(bpy)]$^{2+}$** exhibited a decay process with three different time components, all showing MLCT character by comparison with spectroelectrochemical experiments. Time constants of maximum 13 ps for the ^{3}MLCT lifetimes were reported.[48] Detailed time-resolved X-Ray spectroscopy revealed a hot branching mechanism of the relaxation cascade. This means a vibrationally excited, hot ^{3}MLCT is populated after photoexcitation by ultrafast ISC and vibrational redistribution leads then quickly to a relaxed ^{3}MLCT state. The redistribution process competes with a direct channel to the ^{3}MC state, in which a fraction of 30% of the population ends up within the first 0.15 ps. The remaining population of 70% in the relaxed ^{3}MLCT state decays comparatively slowly (7.6 ps) to the ^{3}MC state, which deactivates more rapidly (2.2 ps) back to the ^{1}GS.[49]

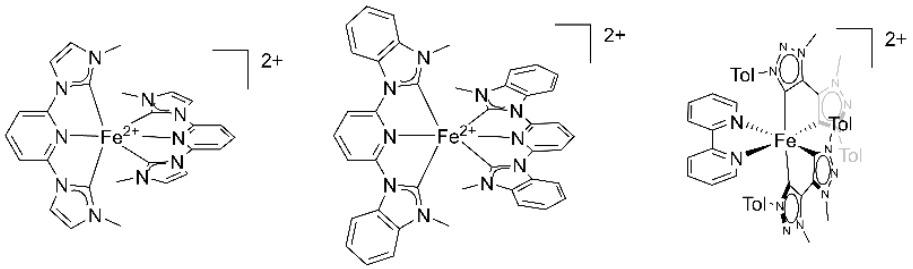

[Fe(bim)$_2$]$^{2+}$ τ_{MLCT} = 9 ps | **[Fe(bbp)$_2$]$^{2+}$** τ_{MLCT} = 16 ps | **[Fe(btz)$_2$(bpy)]$^{2+}$** τ_{MLCT} = 13 ps

*Figure 2.2.3: Molecular structures and excited state lifetimes of **[Fe(bim)$_2$]$^{2+}$**,[39] **[Fe(bbp)$_2$]$^{2+}$**[46] and **[Fe(btz)$_2$(bpy)]$^{2+}$**[48] with strongly σ-donating ligands.*

Fe^{III}-d^5 complexes

As an alternative to Fe^{II}-d^6 metal complexes remarkable advances could be achieved with Fe^{III}-d^5 compounds with respect to photochemical applications. Prominent examples with long excited state lifetimes, more complex absorptivity and emission are the three metal complexes **[Fe(btz)$_3$]$^{3+}$**, **[Fe(phtmeimb)$_2$]$^+$** (phtmeimb = phenyl(tris(3-methylimidazol-1-ylidene))borate) and **[Fe(ImP)$_2$]$^+$** (ImP = 1,1'-(1,3-phenylene)bis(3-methyl-1-imidazol-2-ylidene)). The molecular structures and excited state energy landscapes are shown in Figure 2.2.4. Progress is caused by

the distinct photophysics of Fe^{III} metal complexes. Frontier MOs are typically the same in octahedral $3d^5$ and $3d^6$ metal complexes. The MO diagrams include the same basic metal- and ligand-based orbitals. The partially filled t_{2g} orbitals in the t_{2g}^5 low-spin ground-state configuration enable LMCT (ligand to metal charge transfer) transitions from a filled π orbital of the ligands to the partially filled t_{2g} orbitals (Figure 2.2.4). Optical spectra thus consist of π-π*, MLCT and, additionally, LMCT transitions in $3d^5$ metal complexes, while LMCT bands are typically the lowest energy transition in Fe^{III} *hexa*-carbene compounds.[50] **$[Fe(btz)_3]^{3+}$** displays a ^{2}GS-^{2}LMCT charge transfer absorption band at 558 nm resulting in an emissive ^{2}LMCT excited state with a lifetime of 100 ps and a quantum yield of $3 \cdot 10^{-4}$ in MeCN. This assignment is based on transient absorption kinetics of the ground state recovery and time resolved luminescence kinetics, which exhibit identical kinetics.[51]

With **$[Fe^{III}(phtmeimb)_2]^+$** a metal complex with nearly ideal octahedral geometry and an additional negative charge on the ligand to further is improving the σ-donor properties is realized. In **$[Fe^{III}(phtmeimb)_2]^+$** a ^{2}GS-^{2}LMCT charge transfer absorption band at 502 nm and an emission with a maximum at 655 nm with a quantum yield of 2% is observed. The excited state lifetime is 2 ns following the ^{2}GS-^{2}LMCT excitation/deactivation processes.[52] After a tris(bidentate) and scorpionate ligand arrangement, a bis(tridentate) complexes was realized recently with **$[Fe^{III}(ImP)_2]^+$**. The iron center is sixfold carbon coordinated by four NHCs units and two cyclometalating phenyl rings. This ligand design leads to a dual ^{2}GS-^{2}LMCT absorption at 585 nm and a ^{2}GS-^{2}MLCT absorption at 351 nm. After ^{2}LMCT-excitation at low energies an emission with a maximum at 675 nm is observed. After ^{2}MLCT-excitation at higher energies an additional emission with a maximum at 450 nm is detected together with the 675 nm luminescence. Such a dual or two color luminescence is a rare observation and was never reported for iron compounds before. The excited state landscape is dominated by a ^{2}LMCT state with a lifetime of 0.24 ns at low energies and a ^{2}MLCT state with a lifetime of 4.2 ns at higher energies.[53]

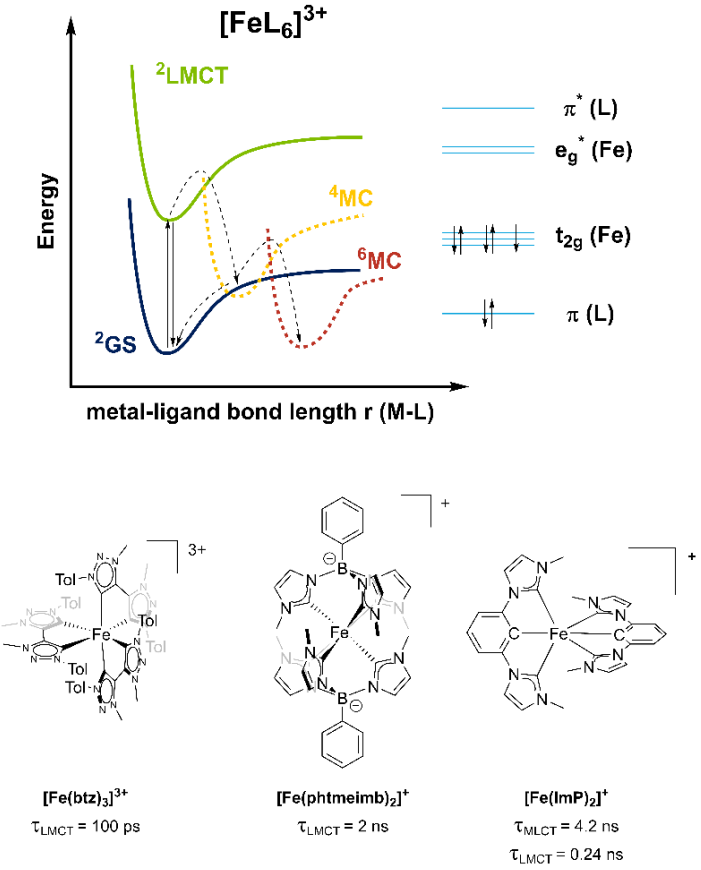

Figure 2.2.4: Schematic ground- and excited-state landscapes of iron(III) complexes (top). Molecular structures and excited state lifetimes of ***[Fe(btz)$_3$]$^{3+}$****,[51]* ***[Fe(phtmeimb)$_2$]$^+$****[52] and* ***[Fe(ImP)$_2$]$^+$****[53] with iron(III) as central atom (bottom).*

Although no experimental evidence is presented, participation of a ^{4}MC state in the deactivation path cannot be excluded so far. As lifetimes are in the picosecond or low nanosecond range and only moderate quantum yields are observed in Fe^{III} *hexa*-carbene metal complexes, non-radiative mechanisms contributing to the deactivation from the photoactive ^{2}LMCT to the ^{2}GS must be contemplated. As there is no obvious way to undergo ISC to higher spin states, there is still a limitation of the lifetimes in this type of metal complexes by the spin-allowed direct relaxation into the ^{2}GS by fluorescence or non-radiative pathways. This fact is so far limiting the promising photophysical results, and it presents a future challenge to overcome this fundamental property of Fe^{III} complexes.

2.2.3 The Multichromophoric Approach

A very promising strategy to increase the ^{3}MLCT lifetimes has been proposed for ruthenium photosensitizers. The functionalization of the coordinating ligands by a second, organic chromophore with a long triplet lifetime, leads to the so called multichromophoric approach.[54] In such multichromophoric complexes, π-extension leads to energetically lowered ^{3}MLCT states as described in the basic photophysical properties of d^6 metal complexes. Additionally, the long-lived excited triplet states of the organic chromophores can act as reservoirs for the population of the ^{3}MLCT states.[55,56–61]

The fundamental processes of this reservoir effect are depicted in Figure 2.2.5 and eq. 2.5-2.7 for the complex **[Ru(phen-pyr)$_3$]$^{2+}$** (phen-pyr = 5-(pyren-1-yl)-1,10-phenanthroline) bearing a pyrene backbone.

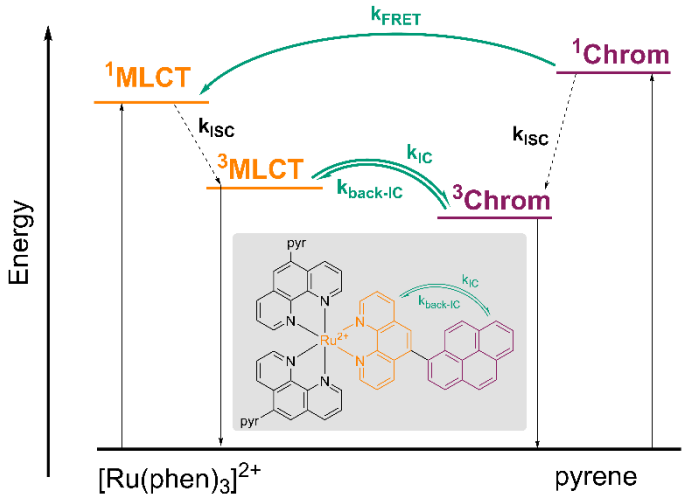

Figure 2.2.5: Effective prolongation of ^{3}MLCT lifetimes by chromophore-states populated by MLCT states and repopulation (reservoir effect) in Ru^{II} complexes according to Castellano et al.[56,57]

The initial photoexcitation of the metal complex from ^{1}GS into ^{1}MLCT state (eq. 2.6) is followed by ISC into the ^{3}MLCT state (eq. 2.7). This situation is identical to the previously described processes in d^6-TMCs. From the ^{3}MLCT state the energy can be transferred in an internal conversion (IC) step to the nearly isoenergetic triplet chromophore-state (^{3}Chrom; k_{IC}, eq. 2.8). Back-IC ($k_{back\text{-}IC}$) yields the ^{3}MLCT state, resulting in a thermal equilibrium of the ^{3}MLCT and ^{3}Chrom state (eq. 2.8). Due to this equilibrium caused by coupling with a long-lived organic chromophore, the ^{3}MLCT lifetime is significantly extended, and the organic chromophore can be described as a reservoir for the ^{3}MLCT state. Equilibration is most efficient with isoenergetic ^{3}MLCT and ^{3}Chrom states. If the triplet state of the chromophore is energetically higher than the thermal energy (k_BT), there is no energy transfer from the ^{3}MLCT to this state.[60,56,57] If the triplet state of the chromophore is significantly lower than the ^{3}MLCT state, an irreversible energy transfer takes place, resulting in the quenching of the ^{3}MLCT state.[61] These two cases show the limiting cases of the multichromophoric approach, whose efficiency is described by the Boltzmann statistics.

$$ML_n - Chrom. \xrightarrow{h \cdot \vartheta} {}^1M^*L_n - Chrom. \tag{2.6}$$

$${}^1M^*L_n - Chrom. \xrightarrow{k_{ISC}} {}^3M^*L_n - Chrom. \tag{2.7}$$

$${}^3ML_n - Chrom. \underset{k_{back-IC}}{\overset{k_{IC}}{\rightleftharpoons}} M^*L_n - {}^3Chrom^* \tag{2.8}$$

Beside the reservoir effect a second effect is observed in multichromophoric ruthenium complexes. After photoexcitation using UV light, not the ^{1}MLCT, but the ^{1}Chrom state is populated, which is higher in energy than the ^{1}MLCT state (eq. 2.9). From the ^{1}Chrom state the energy can be

transferred in an IC step to the lower lying ^{1}MLCT state (2.10). This energy transfer process on the excited singlet state hypersurface is referred to as Förster Resonance Energy Transfer (k_{FRET}; eq. 2.10). This energy transfer step from the ^{1}Chrom state to the ^{1}MLCT state is claimed as the "antenna effect" in literature. The antenna effect therefore enables the population of the ^{1}MLCT states both by visible and by UV light and enhances the more frequent population of catalytically active ^{3}MLCT states.[60]

$$ML_n - Chrom. \xrightarrow{h \cdot \vartheta} ML_n - {}^1Chrom.^* \tag{2.9}$$

$$ML_n - {}^1Chrom.^* \xrightarrow{k_{FRET}} {}^1M^*L_n - Chrom. \tag{2.10}$$

Very successful examples of using the multichromophoric approach in ruthenium-based photosensitizers are the increase of the ^{3}MLCT lifetime in **[Ru(phen)$_3$]$^{2+}$** from 510 ns to 148 µs[56] in **[Ru(phen-pyr)$_3$]$^{2+}$** and in **[Ru(tpy)$_2$]$^{2+}$** from 250 ps to 1806 ns in **[Ru(tpy-pym-ant)$_2$]$^{2+}$** using 9-anthryl-pyrimidine units (Figure 2.2.6).[62]

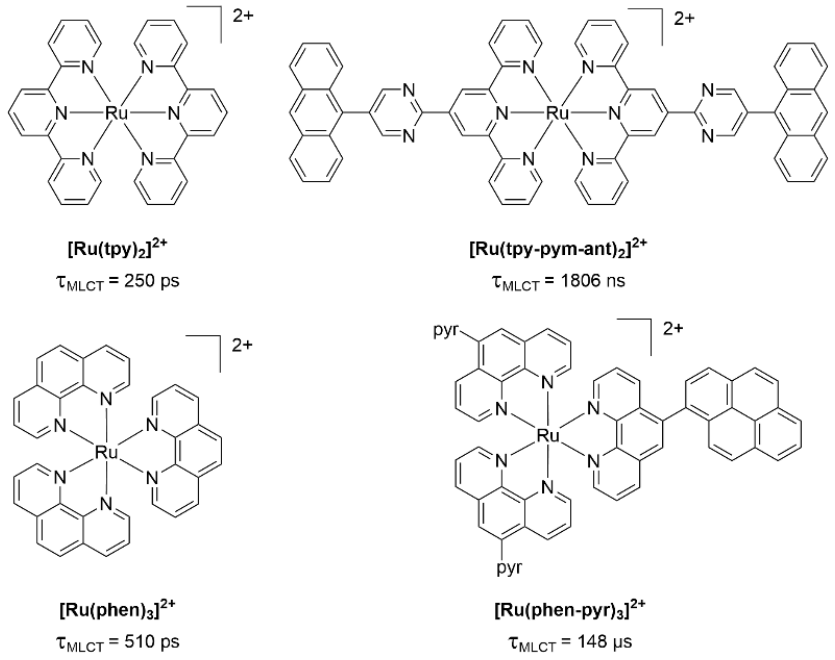

*Figure 2.2.6: Molecular structures and excited state lifetimes of **[Ru(tpy)$_2$]$^{2+}$**, **[Ru(tpy-pym-ant)$_2$]$^{2+}$**,[62] **[Ru(phen)$_3$]$^{2+}$** and **[Ru(phen-pyr)$_3$]$^{2+}$**[56] as examples of the multichromophoric approach.*

Based on a series of experiments on **[Ru(bpy)$_3$]$^{2+}$**-based multichromophoric complexes, the extension of lifetimes can be linearly correlated with the number of bound chromophores. McClenaghen *et al.* systematically increased the number of pyrene units attached to a **[Ru(bpy)$_3$]$^{2+}$** center from zero to six and found a linear correlation in the excited state lifetimes. The **[Ru(bpy)$_3$]$^{2+}$** derivative carrying zero pyrenes has a ^{3}MLCT lifetime of 0.87 µs, that is increased to 18.1 µs in the case of six pyrene units.[59] Furthermore, it was shown on **[Ru(phen)$_3$]$^{2+}$** complexes that both chromophores bound directly to the ligand – as described in the examples before – and the binding of the chromophore over longer distances (e.g.: polyethylene glycol, distance up to 1.2 nm) lead to an extension of the lifetimes.[60]

The multichromophoric approach has also been investigated for Re(I) complexes. In a first publication a single complex consisting of a [Re(phen)(CO)$_3$Cl]-center connected to *N*-(1,10-phenanthroline)-4-(1.piperidinyl)naphthalene-1,8-dicarboximide (NPI) has been reported. The resulting **[Re(NPI-phen)(CO)$_3$Cl]** has a lifetime of 651 µs, which represents an enhancement of the lifetime by a factor of 3000 in comparison to the lifetime of 197 ns in **[Re(phen)(CO)$_3$Cl]**. In this complex both the reservoir and antenna effect as described for Ru-complexes before have been identified.[63] These effects have been more extensively investigated in two different ways. In a first following work different naphthalimides (NIs) have been attached to the rhenium center **Re0** resulting in a series of complexes **Re1**-**Re5** to investigate the influence of different ^{3}NI energies (Figure 2.2.7).[64] In a second following work different ligands have been coordinated to the rhenium-center to result in the series of complexes **Re6**-**Re10**. In these complexes **Re6**-**Re10** the same pyridinyl-NI (PNI) ligand has been used as second chromophore to investigate the influence of different ^{3}MLCT energies in multichromophoric rhenium complexes (Figure 2.2.8).[65]

The investigations on different ^{3}NI energies gave insight into the excited state dynamics of the complexes **Re1**-**Re5**. In all the complexes the lifetime of the excited states is prolonged and the ^{3}NI energy is below the ^{3}MLCT state in each complex. In the complexes **Re1**-**Re3** the ^{1}LC state is initially populated after photoexcitation with UV light. An energy transfer according to the antenna effect enables the population of the ^{1}MLCT state. After rapid ISC the ^{3}MLCT is populated and a thermal equilibrium between the ^{3}MLCT and the ^{3}LC according to the reservoir effect is achieved. For **Re1**-**Re3** the excited state dynamics after photoexcitation can be described by a ^{1}LC → ^{1}MLCT → ^{3}MLCT ⇄ ^{3}LC relaxation cascade according to the description of d^6-TMCs before.[64] In the complexes **Re4** and **Re5** the difference in the triplet energies is the largest and the ^{3}NI energies are clearly below the ^{3}MLCT energy. In **Re4** and **Re5** this difference is too large to still observe black population of the ^{3}MLCT since the ^{3}LC state is once populated. The relaxation cascade in **Re4** and **Re5** the ^{1}LC → ^{1}MLCT → ^{3}MLCT → ^{3}LC relaxation cascade results in ^{3}LC state without any black population of the ^{3}MLCT state. The observed lifetime in **Re4** and **Re5** is the excited state lifetime of the ^{3}NPI states.[64]

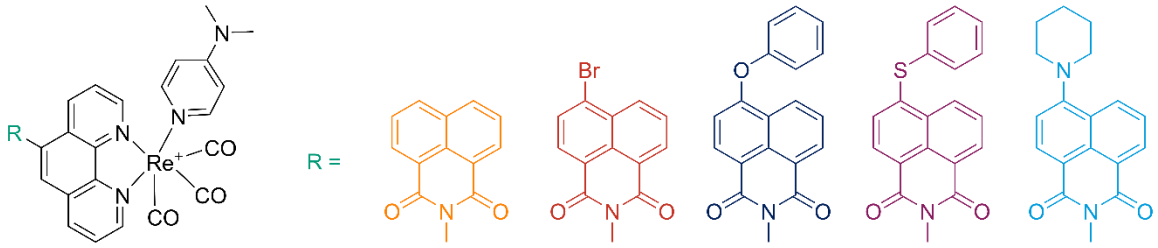

Re0	**Re1**	**Re2**	**Re3**	**Re4**	**Re5**
	$\Delta^3E_{MLCT-NI}$ =				
	2430 cm^{-1}	2800 cm^{-1}	2680 cm^{-1}	3650 cm^{-1}	3900 cm^{-1}
τ_{TA} =	τ_{TA} =				
176 ns	11.9 µs	53.7 µs	42.2 µs	116 µs	136 µs

*Figure 2.2.7: Molecular structures, triplet-energy differences of the MLCT and NI character states and excited state lifetimes of **Re0**-**Re5** as examples of Re(I)-based multichromophoric complexes.[64]*

These findings clearly indicate that a slight mismatch between the triplet energies – even if the triplet energy of the chromophore is below the ^{3}MLCT state – is suitable for the achievement of a

reservoir effect, but a clear mismatch leads into the population of the ^{3}LC state without any back population of the ^{3}MLCT state.

The investigations on different ^{3}MLCT energies gave insight into the excited state dynamics of the complexes **Re6**-**Re10**. In **Re6**-**Re8** the ^{3}MLCT states are higher in energy than the ^{3}PNI energy. In **Re9** the triplet energies are nearly isoenergetic. In **Re10** the ^{3}MLCT energy is lower than the ^{3}PNI states (Figure 2.2.8). In **Re6**-**Re8** the ^{3}MLCT lifetimes are prolonged according to an equilibrium between the ^{3}MLCT and ^{3}PNI states following the ^{1}LC → ^{1}MLCT → ^{3}MLCT ⇄ ^{3}LC relaxation cascade. Consequently, the energy difference in **Re8** results in the longest ^{3}MLCT lifetime. In **Re9** the triplet energies are nearly isoenergetic, but the ^{3}MLCT is not prolonged with the highest efficiency, as the ^{3}MLCT and ^{3}LC states do not equilibrate without a barrier. In **Re10** the ^{3}PNI is higher in energy than the ^{3}MLCT state. In this case the ^{3}LC state is excluded from the ^{1}LC → ^{1}MLCT → ^{3}MLCT deactivation cascade. These findings clearly indicate that the ^{3}LC states should be located lower in energy, but as close as possible to the ^{3}MLCT states to realize both a reservoir and an antenna effect in multichromophoric d^6-TMCs.[65]

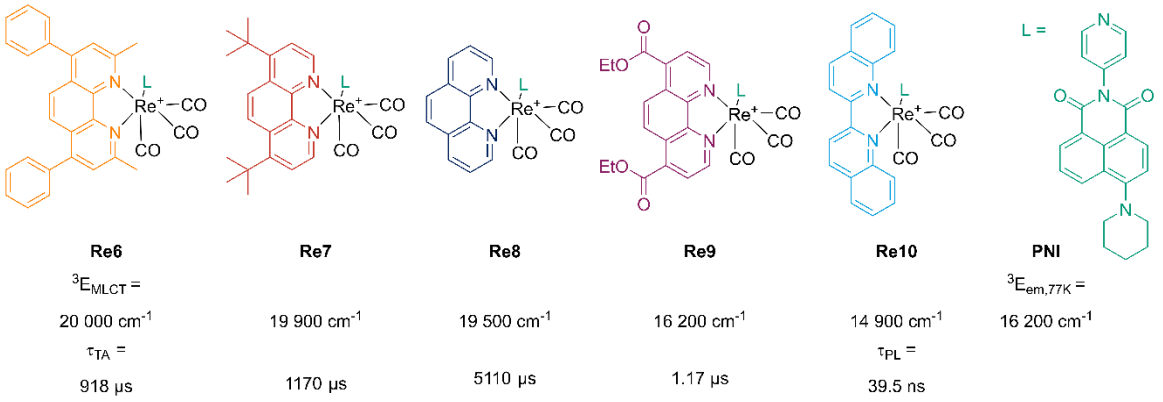

*Figure 2.2.8: Molecular structures, triplet-energy of the MLCT states and excited state lifetimes of **Re6**-**Re10** as examples of Re(I)-based multichromophoric complexes. Triplett energy of **PNI** (right side).[65]*

Additionally, to these examples of ruthenium and rhenium complexes, the multichromophoric approach has also basically been investigated for platinum and one chromium complex. Platinum(I) complexes are exclusively investigated with acetylene groups as linkers between the metal complex center and the organic chromophore.[66a–e,67,66f–o] **Pt1** is an example of multichromophoric platinum complexes (Figure 2.2.9). For chromium(0) very recently a first example **Cr1** has been published showing the potential of the multichromophoric approach also for earth abundant metal centers (Figure 2.2.9).[68]

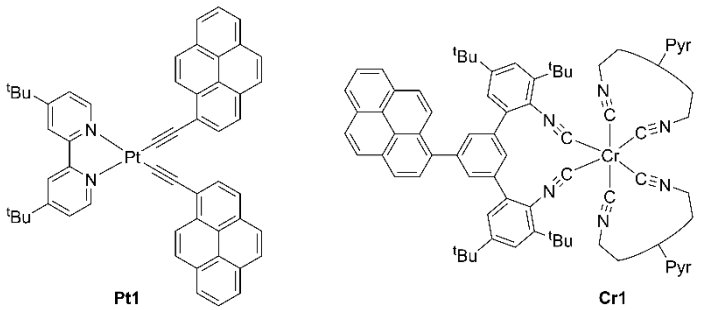

*Figure 2.2.9: Molecular structures of **Pt1** and **Cr1** as examples of platinum[67] and chromium[68] based multichromophoric complexes.*

Despite numerous examples for the application of the multichromophoric approach with TMCs, it is experimentally unexplored for iron(II) as the central atom in combination with C^N^C ligands. A recent theoretical study evaluates the potential of anthracene-functionalized **[Fe(bim)$_2$]$^{2+}$** complexes. The results show that even for the direct connection of anthracene to the bim ligand the lowest energy triplet state is localized on anthracene, which could act as a reservoir for an excited state population (Figure 2.2.10, **Fe1** and **Fe2**). The authors suggested a mitigation of the fast excited state decay of iron(II) excited states due to the attachment of anthracene.[69]

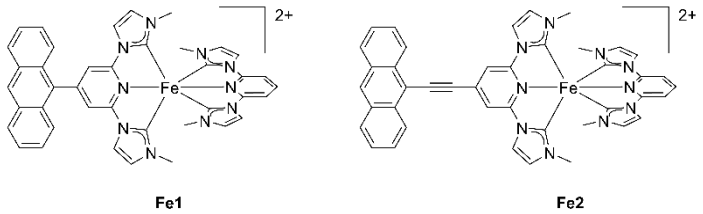

Fe1 **Fe2**

*Figure 2.2.10: Molecular structures of **Fe1** and **Fe2** predicted to have ^{3}MLCT states localized at the anthracenyl-chromophore.[69]*

For iron as the central atom, no experimental studies have been published prior to this work that address the multichromophoric approach leading to the transfer of the multichromophoric approach from noble metal d^6-TMCs to the more abundant and more sustainable iron as the central metal in multichromophoric d^6-TMCs as the aim of this work.

3

Aim of this work

In this work two key strategies to improve the photophysical properties and the catalytic activities of N^N^N- and C^N^C-coordinated iron(II) complexes are focused. All ligands designed in this work consist of a central, coordinating pyridine ring. In the first strategy the σ-donor and π-acceptor properties of the ligand motifs, laterally attached to the central pyridine ring, are investigated. Additional pyridines and triazoles are representatives of good π-acceptor ligand, while different types of NHCs are chosen as strong σ-donor ligands. In the group of NHCs imidazolium, benzimidazolium and triazolium precursors, as representatives of MICs, are the chosen to investigate the effect of different σ-donor strength.

The second main strategy targeted in this work is the introduction and variation of an organic chromophore in the 4-position of the central pyridine ring. Aromatic hydrocarbons from phenyl to perylene will be used as backbone chromophores. With this not only the size and geometry of the aromatic system varies, but also the energy and the lifetime of the ^{3}Chrom state, which could act as a “light-antenna” or as an excited state energy reservoir.

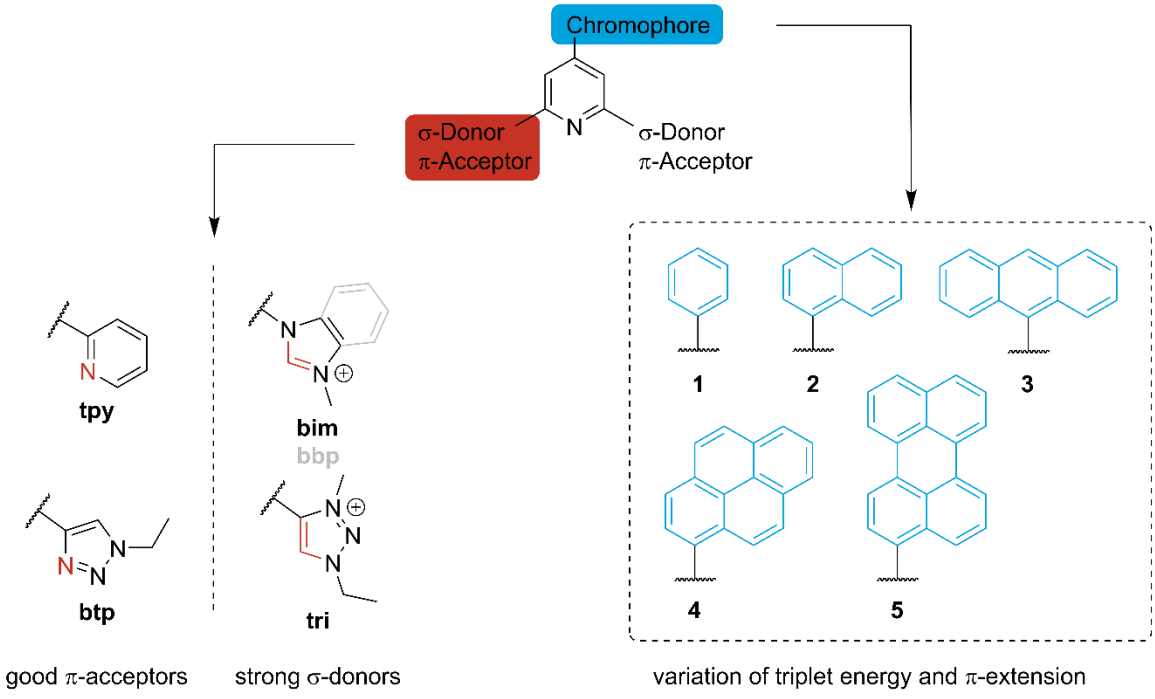

Figure 3.1.1: Schematic representation of the two main strategies to improve photophysical properties of iron(II) complexes followed in this work: The variation of σ-donor and π-acceptor properties (left side, red) and the variation of organic chromophores in 4-position of the central pyridine ring (right side, blue) of the ligands. Abbreviations used in the following in bold letters.

Prepared complexes will be intensively analyzed by advanced spectroscopic and quantum chemical techniques. The ground state properties are characterized by steady state absorption and cyclic voltammetry. The excited state properties are determined by transient absorption,

steady state, and time-resolved emission spectroscopy and spectroelectrochemical experiments. The results of ground and excited state characterization are accompanied by time-dependent density functional theory (TD-DFT) calculations. For selected complexes ruthenium analoga are prepared for comparison purposes.

In the final stage of this thesis, selected complexes, showing promising photophysical properties are used in photocatalytic experiments. Two types of possible reactions will be addressed. The possibility for these complexes to act as photosensitizers in single electron transfer reactions, in the example of proton reduction reactions to evolve hydrogen. And second the possibility of these complexes to enable energy transfer reactions will be tested. As an example, the activation of oxygen in solution to yield reactive singlet oxygen will be addressed.

To identify the ligands and chromophores in this work the following abbreviations are used: **tpy** (= 2,2’:6’,2’’-terpyridine), **bim** (= 1,1’-(pyridine-2,6-diyl)bis(3-methyl-1H-imidazol-3-ium)), **bbp** (= (pyridine-2,6-diyl)bis(1-methyl-benzimidazol-2-ylidene)), **btp** (= 2,6-bis(1-ethyl-1H-1,2,3-triazol-4-yl)pyridine), **tri** (= 4,4'-(pyridine-2,6-diyl)bis(1-ethyl-3-methyl-1H-1,2,3-triazol-3-ium)), **1** (= phen-1-yl), **2** (= naphthalen-1-yl), **3** (= anthracen-9-yl), **4** (= pyren-1-yl), **5** (= perylen-3-yl) according to Figure 3.1.1.

4

Synthesis

In this thesis five different classes of ligands were prepared to investigate the photophysical properties and catalytic activities of multichromophoric iron(II) complexes. In this section the synthetic strategies, used to prepare ligands with organic chromophores attached in their backbones, will be discussed in detail.

4.1 Synthesis of terpyridine-based ligands and complexes

The synthesis of terpyridines has been described in many forms,[70] and is discussed in the context of this work as a reaction of two equivalents of acetylpyridine and one equivalent of anthracenyl and pyrenyl aldehyde, respectively.[71–73]

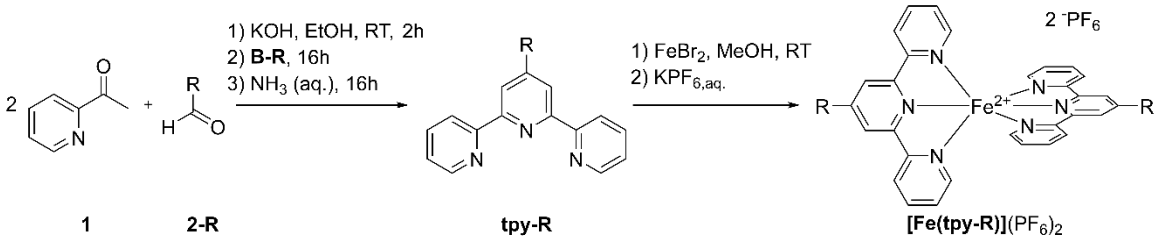

*Scheme 4.1.1: Syntheses of **tpy-R** ligands and **[Fe(tpy-R)$_2$]**(PF$_6$)$_2$ complexes.*

To optimize existing procedures, KOH and 2-acetylpyridine **1** were stirred in ethanol for 2h to achieve the most quantitative deprotonation of **1** as possible. Subsequently, the corresponding aldehyde **2-R** was added and stirred at room temperature for 16h before an ammonia solution was added. This reaction time was considerably longer than in previously described syntheses in literature. After the addition of the ammonia solution, the crude product was formed as a solid, separated from the solution and purified by recrystallization. The ligands **tpy-3** and **tpy-4**, which had previously been prepared in two-step syntheses,[71] were obtained in a single-step synthesis with yields of 53% (**tpy-3**) and 27% (**tpy-4**) in this work. The corresponding terpyridine complexes **[Fe(tpy-3)$_2$]**(PF$_6$)$_2$ and **[Fe(tpy-4)$_2$]**(PF$_6$)$_2$ were obtained by the reaction of **tpy-3** and **tpy-4** with FeBr$_2$ at room temperature in methanol. After filtration of insoluble solids, an aqueous KPF$_6$ solution was added to give the hexafluorophosphate salts **[Fe(tpy-3)$_2$]**(PF$_6$)$_2$ and **[Fe(tpy-4)$_2$]**(PF$_6$)$_2$. The resulting solids were separated and taken up in acetone. After crystallization by diffusion of *n*-pentane into acetone solution of the complexes. The compounds were obtained in 90% (**[Fe(tpy-3)$_2$]**(PF$_6$)$_2$) and 80% (**[Fe(tpy-4)$_2$]**(PF$_6$)$_2$) yield (Scheme 4.1.1).

*Table 4.1.1: Yields of the syntheses of **(tpy-R)** ligands and **[Fe(tpy-R)$_2$]**$(PF_6)_2$ complexes.*

Compound	Yield	Compound	Yield
tpy-3	53 %	**[Fe(tpy-3)$_2$]**$(PF_6)_2$	90 %
tpy-4	27 %	**[Fe(tpy-4)$_2$]**$(PF_6)_2$	80 %

According to the distinct photophysical characterization and the not promising results (section 5.1) the synthesis of a larger variety of terpyridine ligands and complexes was not performed in this work.

4.2 Syntheses of (benz)imidazole-based complexes

A more promising approach to implement the multichromophoric approach in iron complexes is the use of NHC-based ligands. They cause a stronger ligand field splitting of the d-orbitals, which leads to longer ^{3}MLCT lifetimes. This section is divided into three parts. These parts are the description of different synthetic routes for the important precursor molecule **7**, the discussion of the syntheses of imidazole and benzimidazole based pro-ligands and complexes, and the discussion of follow-up syntheses to enable further improvement of the photophysical properties and to gain a better photophysical understanding by acetylene-linked pro-ligands and complexes.

*Syntheses of precursor molecule **7***

4-iodo-2,6-dichloro-pyridine **7** is the starting point to introduce organic chromophores in the backbone of the ligands in multichromophoric carbene complexes. Three different synthetic procedures have been prepared for the synthesis of **7** (Scheme 4.2.1).

In the first multistep route 2,6-dichloropyridine **3** is oxidized to the *N*-oxide-derivative **4** and subsequently treated with nitrating acid to yield **5**.[74] After reduction using iron powder in acetic acid **6** is received.[75] Intermediate **6** is an important starting molecule for following syntheses to prepare complexes with larger distances between the metal center and the organic backbone molecule. **7** was obtained in a Sandmeyer-reaction (Scheme 4.2.1, upper reaction).[76] The overall yield of this sequence is 21 % with respect to the starting amount of **3**. Two optimization steps have been performed to improve the yield in the preparation of **7**. Nevertheless, this reaction sequence is an important part as the dibromo-derivative of **6** (later named **6-Br**) is important for follow up syntheses.

Both attempts to optimize the yield rely on a direct iodination of **3** in 4-position. In a first attempt **3** is deprotonated and metalated by *n*-butyllithium and subsequently iodinated by elemental iodine (Scheme 4.2.1, middle reaction). As *n*-butyllithium is a strong and sterically non-demanding base **3** is metalated not only in 4-, but also in 3-position. For this reason, 3-iodo-2,6-dichloropyridine is obtained as a side-product (Scheme 4.2.1, middle reaction, colored in grey). Both isomers can be separated by stepwise crystallization and **7** is obtained with a yield of 30 %.[77]

To selectively deprotonate **3** in 4-position the sterically demanding base TMPMgCl (= 2,2,6,6-tetramethylpiperidinylmagnesium chloride lithium chloride complex) – also called Turbo-Hauser base – is used (Scheme 4.2.1, lower reaction). The sterically demanding tetramethyl-piperidinyl is selectively deprotonating the 4-position and metalating by magnesium and lithium. The subsequent iodination gives **7** with a yield of 68 %.[78]

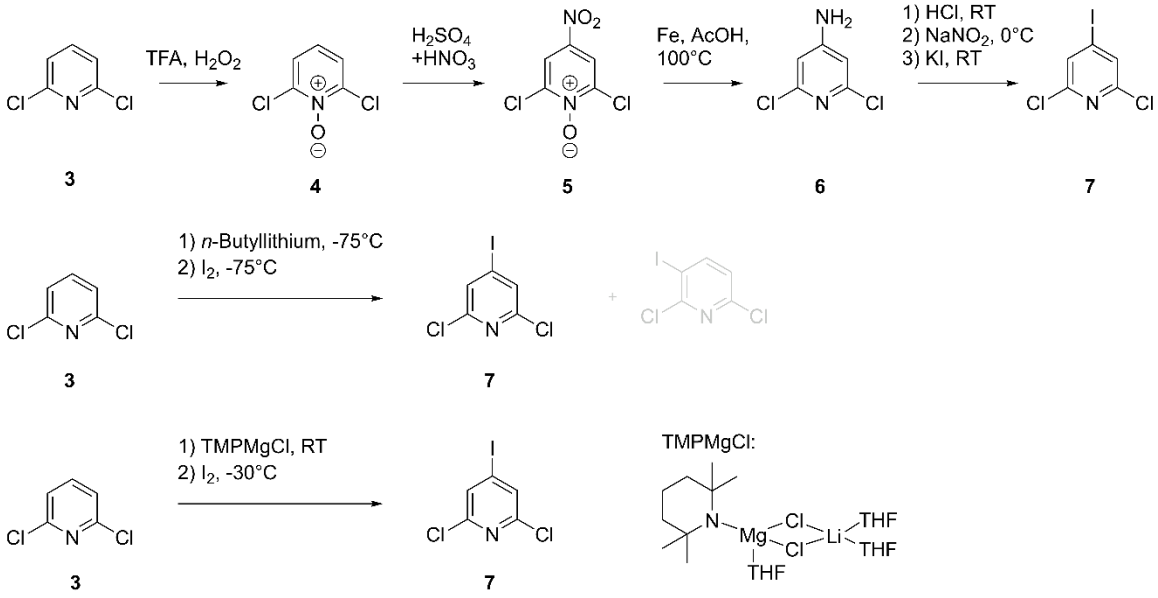

*Scheme 4.2.1: Optimization of the synthesis of **7** starting from a four-step synthesis (upper reaction)[74–76] over one-step synthesis using n-BuLi (middle reaction)[77] resulting in a more selective one-step synthesis using TMPMgCl as base (lower reaction).[78]*

*Table 4.2.1: Yields of the syntheses described in this section. *3 is commercially available [1)]Yield of the Sandmeyer reaction, [2)]Yield of deprotonation using TMPMgCl.*

Compound	Yield	Compound	Yield
3	-*	**4**	70 %
5	60 %	**6**	88 %
7[1)]	58 %	**7**[2)]	68 %

Syntheses of imidazole-based pro-ligands and complexes

The synthetic sequence developed for the syntheses of the complexes **[Fe(bim-R)$_2$]**$(PF_6)_2$ is discussed in this section (Scheme 4.2.2).

The Suzuki coupling using **7** and the corresponding chromophore-boronic-acids to introduce the organic backbone to yield in 4-chromophore-2,6-dichloro-pyridine (**8-R**) derivatives has been optimized in six steps using **8-3** as an example (Table 4.2.2).

*Table 4.2.2: Parameters in the optimization process of the Suzuki-Coupling resulting in **8-R** products. In this table the yields of **8-3** are shown.*

Catalyst	Base	Solvent	Temperature	Time	Yield
$Pd(OAc)_2$+SPhos	$NaCO_3$	THF	65 °C	24 h	27 %
$Pd(OAc)_2$+SPhos	$NaCO_3$	THF	65 °C	72 h	40 %
$Pd(OAc)_2$+$P(^tBu)_3$	$NaCO_3$	THF	65 °C	72 h	-
$Pd(OAc)_2$+SPhos	K_3PO_4	THF	65 °C	72 h	22 %
$Pd(OAc)_2$+SPhos	$NaCO_3$	THF	RT	144 h	11 %
$Pd(OAc)_2$+SPhos	$NaCO_3$	toluene	110 °C	72 h	59 %

In the beginning $Pd(OAc)_2$ as palladium source and SPhos (= dicyclohexyl(2',6'-dimethoxy[1,1'-biphenyl]-2-yl)phosphane) as ligand were chosen.[79] The increase of the reaction time from 24 h to 72 h results in an increase of the yield from 27 % to 40 %. The $P(^tBu)_3$ ligand, often chosen for Suzuki couplings using aryl-boronic acids in literature[80] did not give **8-3**. SPhos is thus kept as the supporting ligand in this reaction. The pure anthracene was found as a side product in all reactions. Therefore, a protodeboronation was assumed to be a side reaction, limiting the yields. Protodeboronation reactions can be suppressed either by using weaker bases (pK_B (K_3PO_4) = 1.68[81], pK_B (Na_2CO_3) = 3.60[81]) or by lower temperatures.[82] Using K_3PO_4 as stronger base indeed reduces the yield to 22 %. At lower temperature **8-3** was formed, but even with an increase reaction time to 144 h the yield was still low (11 %).

The most successful parameters were obtained after changing the solvent from THF to toluene and using Na_2CO_3 as base. This allows the reaction to work at a higher temperature of 110 °C. While still protodeboronation was observed, the yield was increased to 59 %.

For perylene **5** the pinacol-protected boronic acid has been used instead of the unprotected acid for the other chromophores **1**-**4**. The yield was increased to 95 % using this strategy. It can be assumed that this strategy will increase the yield for **8-1** - **8-4** as well.[83]

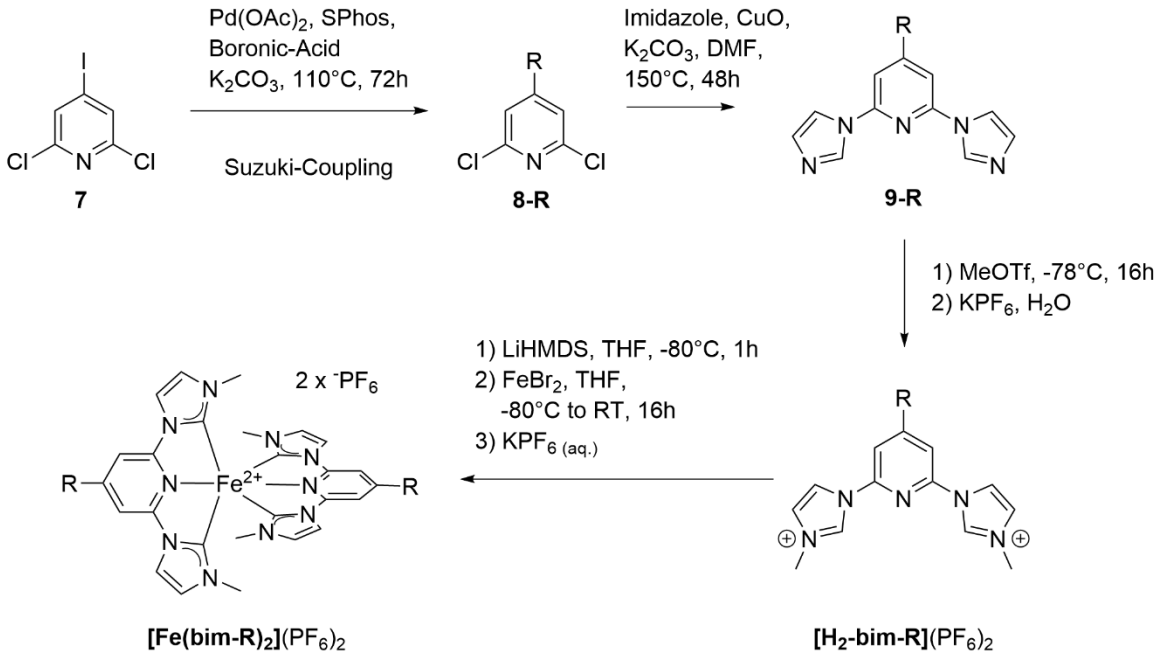

*Scheme 4.2.2: Syntheses of pro-ligands **[H_2-bim-R]**$(PF_6)_2$ and **[Fe(bim-R)$_2$]**$(PF_6)_2$ complexes.[36]*

According to literature procedures a neat coupling of **8-R** and *N*-methyl-imidazole at 150°C for 5 d was performed. This neat coupling was only successfully performed for the phenyl-derivative **8-1** to yield in **[H_2-bim-1]**$(PF_6)_2$ with a yield of 23 % after anion exchange. All other derivatives **8-2** to **8-5** decomposed under these conditions and no formation of the pro-ligands was detected.[84]

To receive the pro-ligands for the other chromophores a two-step synthesis has been developed, first the imidazole-derivatives **9-2** to **9-5** have been prepared. An attempt to deprotonated imidazole by NaH and to perform a nucleophilic aromatic substitution was not successful.[85]

The imidazole derivatives **9-2** - **9-5** finally have been synthesized by a copper-mediated Ullmann-reaction.[86] For this the **8-R** has been heated in DMF at 150°C for 48 h in the presence of imidazole, CuO and K_2CO_3. After column chromatography (stationary phase: SiO_2/ mobile phase: DCM/MeOH 9/1 V/V) the imidazole derivatives **9-2** - **9-5** have been received.[87]

In a first attempt to obtain the pro-ligands **[H_2-bim-2]**$(PF_6)_2$ - **[H_2-bim-4]**$(PF_6)_2$ the imidazole derivatives have been methylated with MeI in acetonitrile for 24 h at 80°C according to literature procedures, but methylation was incomplete.[88] To optimize this reaction the stronger methylating agent MeOTf has been used. A successful methylation with 2.2 eq. MeOTf in dry DCM at -80°C for 16 h has been observed for **[H_2-bim-2]**$(OTf)_2$-**[H_2-bim-4]**$(OTf)_2$. After anion exchange using an aqueous KPF_6 solution the final pro-ligands **[H_2-bim-2]**$(PF_6)_2$-**[H_2-bim-4]**$(PF_6)_2$ have been obtained according to Scheme 4.2.2.[36]

This strategy was not successful for **[H_2-bim-5]**$(PF_6)_2$ as not complete methylation was observed. The obtain **[H_2-bim-5]**$(OTf)_2$ 20 eq. MeOTf in dry $CHCl_3$ at 65°C were necessary. No anion-exchange was performed and **[H_2-bim-5]**$(OTf)_2$ was obtained in a yield of 79 %.

The iron complexes **[Fe(bim-R)$_2$]**$(PF_6)_2$ were prepared by deprotonation of the imidazolium pro-ligands with LiHMDS in THF followed by addition of $FeBr_2$ as the iron(II) source. The crude complexes were purified by column chromatography (stationary phase: basic AlOx/ mobile phase: acetonitrile) and subsequent crystallization using diffusion techniques (solvent: acetone/ anti-solvent: diethyl ether).[88]

*Table 4.2.3: Yields of syntheses performed according to the procedures described in this section.[1] **8-1** was not obtained without impurities. [2] Synthesis of **9-1** was not performed as **8-1** was used in a neat coupling to result in **[H_2-bim-1]$(PF_6)_2$**.*

Compound	Yield	Compound	Yield
8-1	-[1]	**9-1**	-[2]
8-2	62 %	**9-2**	83 %
8-3	58 %	**9-3**	85 %
8-4	86 %	**9-4**	92 %
8-5	94 %	**9-5**	80 %
[H_2-bim-1]$(PF_6)_2$	23 %	**[Fe(bim-1)$_2$]**$(PF_6)_2$	59 %
[H_2-bim-2]$(PF_6)_2$	83 %	**[Fe(bim-2)$_2$]**$(PF_6)_2$	71 %
[H_2-bim-3]$(PF_6)_2$	92 %	**[Fe(bim-3)$_2$]**$(PF_6)_2$	68 %
[H_2-bim-4]$(PF_6)_2$	86 %	**[Fe(bim-4)$_2$]**$(PF_6)_2$	72 %
[H_2-bim-5]$(PF_6)_2$	79 %	**[Fe(bim-5)$_2$]**$(PF_6)_2$	24 %

Syntheses of benzimidazole-based pro-ligands and complexes

In the following section the synthetic sequence developed for the syntheses of the complexes **[Fe(bbp-R)$_2$]**$(PF_6)_2$ is discussed (Scheme 4.2.3).

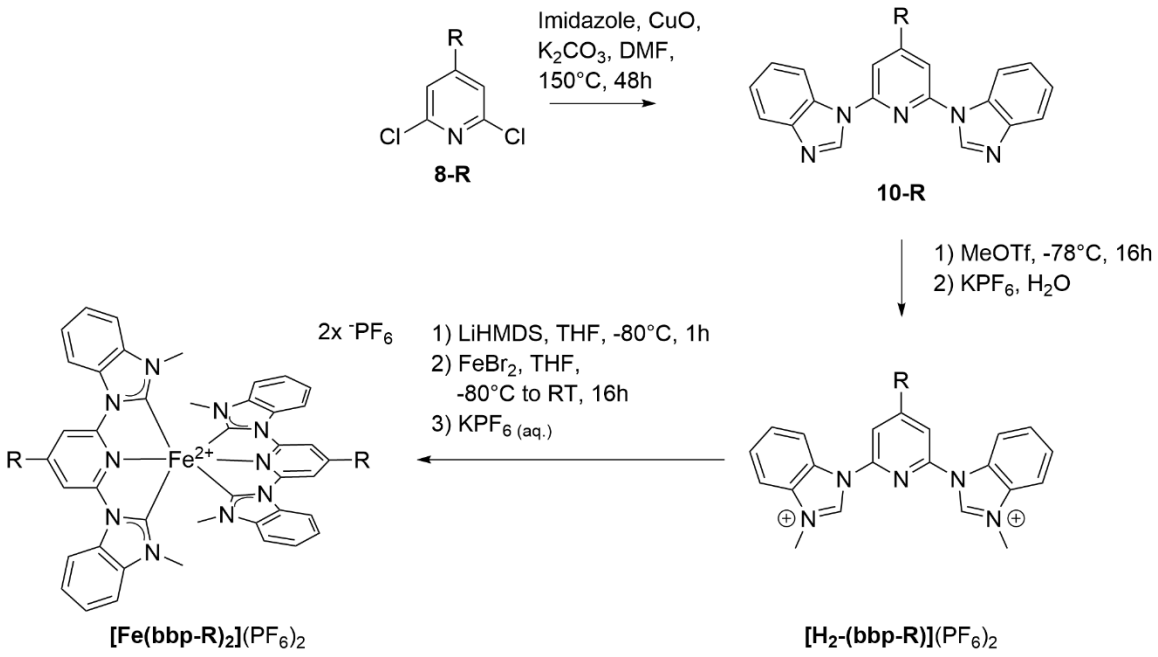

*Scheme 4.2.3: Syntheses of pro-ligands **[H$_2$-bbp-R]**$(PF_6)_2$ and **[Fe(bbp-R)$_2$]**$(PF_6)_2$ complexes.*

The synthetic procedures to prepare the **[Fe(bbp-R)$_2$]**$(PF_6)_2$ complexes are basically the same as for the preparation of the **[Fe(bim-R)$_2$]**$(PF_6)_2$ complexes.

8-R derivatives were used in an Ullmann-style coupling with benzimidazole to result in **10-R** products. The final pro-ligands **[H$_2$-(bbp-R)]**$(PF_6)_2$ were obtained after methylation with methyl triflate in DCM at -80°C. Only the perylene containing pro-ligands **[H$_2$-(bbp-5)]**$(OTf)_2$ was obtained after methylation with methyl triflate in $CHCl_3$ at 65°C. The iron complexes **[Fe(bbp-R)$_2$]**$(PF_6)_2$ were obtained by deprotonation of the benzimidazolium ligands with LiHMDS in THF followed by addition of $FeBr_2$ as the iron(II) source. The crude complexes were purified by column chromatography (stationary phase: basic AlOx/ mobile phase: acetonitrile) and subsequently following crystallization using diffusion techniques (solvent: acetone/ anti-solvent: diethyl ether).

*Table 4.2.4: Yields of syntheses of **10-R** derivatives, pro-ligands **[H$_2$-bbp-R]**$(PF_6)_2$ and **[Fe(bbp-R)$_2$]**$(PF_6)_2$ complexes performed according to the procedures described in this section.*

Compound	Yield	Compound	Yield	Compound	Yield
10-1	18 %	**[H$_2$-bbp-1]**$(PF_6)_2$	92 %	**[Fe(bbp-1)$_2$]**$(PF_6)_2$	47 %
10-2	21 %	**[H$_2$-bbp-2]**$(PF_6)_2$	95 %	**[Fe(bbp-2)$_2$]**$(PF_6)_2$	63 %
10-3	25 %	**[H$_2$-bbp-3]**$(PF_6)_2$	84 %	**[Fe(bbp-3)$_2$]**$(PF_6)_2$	56 %
10-4	23 %	**[H$_2$-bbp-4]**$(PF_6)_2$	92 %	**[Fe(bbp-4)$_2$]**$(PF_6)_2$	64 %
10-5	35 %	**[H$_2$-bbp-5]**$(PF_6)_2$	91 %	**[Fe(bbp-5)$_2$]**$(PF_6)_2$	22 %

After crystallization using diffusion technique (solvent: acetone/ anti-solvent: diethyl ether) a single crystal X-Ray structure of **[Fe(bbp-3)$_2$]**$(PF_6)_2$ is obtained. The key structural parameters of the anthracene substituted complex **[Fe(bbp-3)$_2$]**$(PF_6)_2$ are mainly described by the Fe-N and Fe-C

bond lengths, the C-Fe-C-*trans* angles and the torsion of the backbone chromophore with respect to the central pyridine ring. The Fe-N bond length has an averaged distance of 1.894(4) Å and the Fe-C bond length an averaged distance of 1.920(4) Å. The complex is spanning a distorted octahedral geometry with an averaged C-Fe-C-*trans*-angle of 159.4(2)°. The anthracene chromophore in the ligand's backbone favors two different torsion angles. One anthracene unit is twisted by 67.2(6)° and the second by 84.3(7)° with respect to the central pyridine ring. The twisting of the second anthracene backbone may possibly be due to packing effects in the crystal.

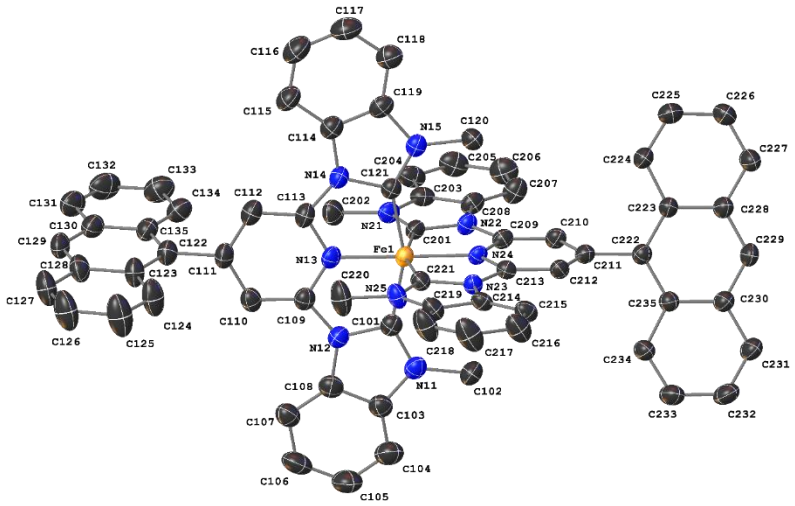

Figure 4.2.1: Single crystal X-Ray structure of ***[Fe(bbp-R)$_2$]***$(PF_6)_2$.

Syntheses of acetylene-linked imidazole-based pro-ligands and complexes

To increase the distance between the iron centre and the organic backbone an acetylene linker in the 4-position of the central pyridine unit of the ligands is introduced. With this attempt more information about the phtophysical deactivation cascade after photoexcitation should be obtained. In particular, considering that Francés-Monerris *et al*. described the lowest excited triplet state localized at the anthracenyl-backbone in the heteroleptic complex **Fe2** (Figure 2.2.10) as received from quantum chemical calculations.[69] In this section the synthetic procedures leading to the similar homoleptic complex **[Fe(bim-ac-3)$_2$]**$(PF_6)_2$ are described (Scheme 4.2.4).

The starting molecule of the synthetic sequence **6-Br** is received from 2,6-dibromo-pyridine according to the sequence described in Scheme 4.2.1 (upper reaction). An Ullmann-style coupling of **6Br** with imidazole catalyzed with CuO and K_2CO_3 as a base in DMF at 150°C leads to **11**.[87] The amino group in **11** is transferred into an iodine group in **12** by a Sandmeyer reaction, which is one of substrates needed in a Sonogashira coupling to reach **14**.[89]

9-bromoanthracene is coupled with TMS-acetylene in a Sonogashira coupling according to a literature procedure using $Pd(PPh_3)_2Cl_2$ and CuI in a mixture of diisopropylamine (DIPA) and triethylamine (TEA, NEt_3) at 110°C for 16 h. After subsequent deprotection of the TMS group by K_2CO_3 **13** is obtained, which is the second substrate needed in a Sonogashira coupling to reach **14**.[90]

In the Sonogashira coupling of **12** and **13** a very brief screening of catalysts and solvents was performed. $Pd(PPh_3)_4$ in TEA did not show any reactivity, while $Pd(PPh_3)_2Cl_2$ in TEA results in a yield of 29 %. Changing the solvent to a mixture of TEA and toluene (1/1 V/V) allows to increase the temperature of the reaction to 110°C, which results in a yield of 58 %. All these yields are reported for reaction scales of 0.1 mmol. An upscaling approach to 1 mmol results in drastically reduced yields.

*Table 4.2.5: Parameters in the optimization process of the Sonogashira-Coupling of **12** and **13** resulting in **14**.*

Catalyst	Solvent	Temperature	Time	Yield
$Pd(PPh_3)_4$	TEA	90°C	17h	No reaction
$Pd(PPh_3)_2Cl_2$	TEA	90°C	17h	29%
$Pd(PPh_3)_2Cl_2$	TEA/toluene	110°C	17h	58%

The final pro-ligands **[H_2-(bim-ac-3)]**$(PF_6)_2$ were obtained after methylation with methyl triflate in DCM at -80°C. The iron complexes **[Fe(bim-ac-3)$_2$]**$(PF_6)_2$ were obtained by deprotonation of the benzimidazolium ligands with LiHMDS in THF followed by addition of $FeBr_2$ as the iron(II) source. The crude complexes were purified by column chromatography (stationary phase: basic AlOx/ mobile phase: acetonitrile) and subsequently following crystallization using diffusion techniques (solvent: acetone/ anti-solvent: diethyl ether).[36,88]

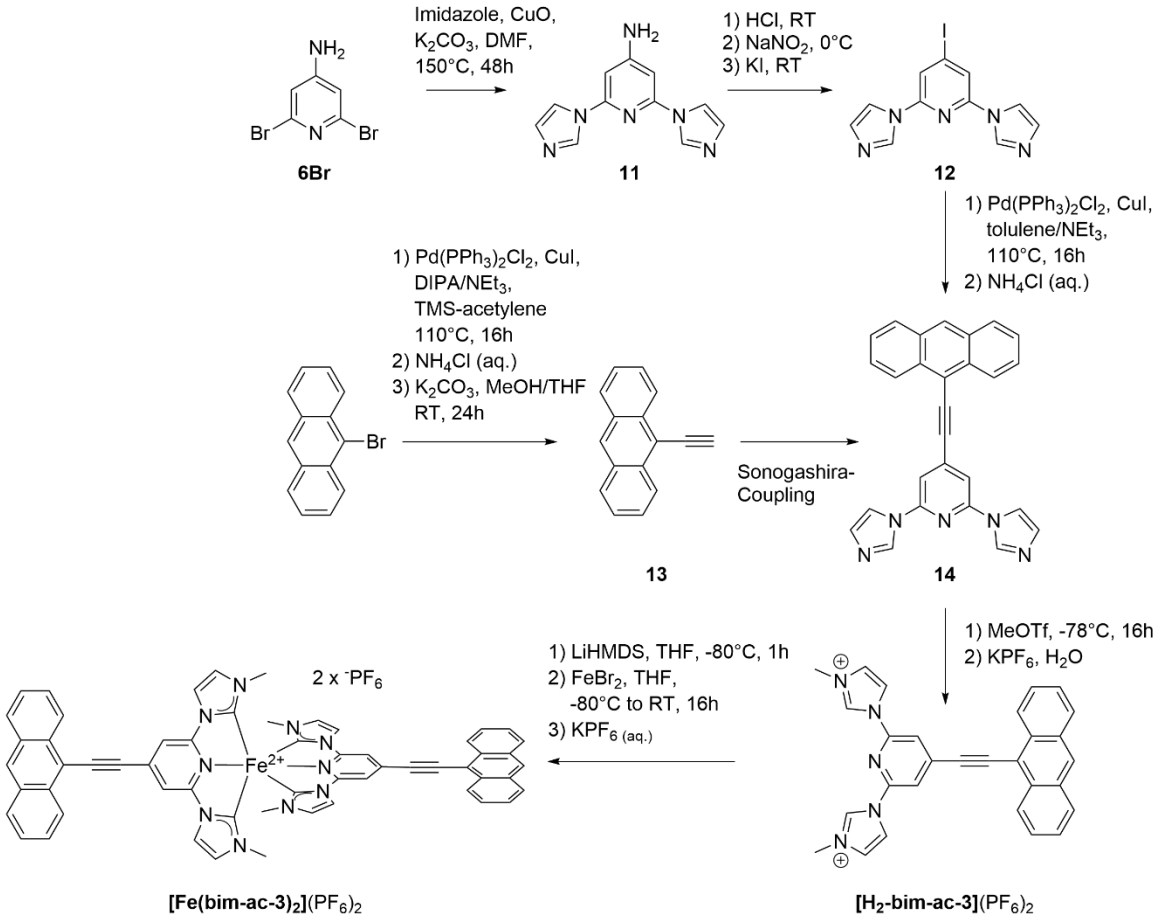

*Scheme 4.2.4: Syntheses of pro-ligand **[H_2-bim-ac-3]**$(PF_6)_2$ and **[Fe(bim-ac-3)$_2$]**$(PF_6)_2$ complex.*

In the following, the crystal structure received for **[Fe(bim-ac-3)$_2$]**$(PF_6)_2$ is compared with the geometry optimization of the analogous heteroleptic complex with an anthracene backbone by Francés-Monerris *et al*. (**Fe2**, Figure 2.2.10).[69] The spatial position of the anthracene backbone relative to the coordinating unit is the main focus. Further, the lengths of the C≡C triple bonds are compared. As this crystal structure is provisional and not published or deposited at databases, no sigma values are given for this structure. In the geometry optimization of Francés-Monerris *et al.* of **Fe2** the anthracene backbone is twisted by 2.4° relative to the coordinating unit.[69] In the crystal structure of **[Fe(bim-ac-3)$_2$]**$(PF_6)_2$, the anthracene backbone is twisted by 4.3° relative to the coordinating unit in one ligand and 24.4° relative to the coordinating unit in the other ligand. The high planarity predicted by Francés-Monerris *et al.* through geometry optimization can be confirmed experimentally for one of the two anthracene backbones in **[Fe(bim-ac-3)$_2$]**$(PF_6)_2$. Such a high planarity could result in an enlargement of the π-system due to a good orbital overlap. This could have beneficial effects on the energetic location of the π*-orbital, resulting in a red shift of the MLCT absorption and finally in a higher MLCT lifetime. The twisting of the second anthracene backbone may possibly be due to packing effects in the crystal. For the length of the C≡C triple bond, a length of 1.22 Å is reported by Francés-Monerris *et al*.[69] For **[Fe(bim-ac-3)$_2$]**$(PF_6)_2$, a bond length of 1.2006 Å and 1.2012 Å is measured, respectively. Thus, the calculated bond lengths can also be confirmed by the experimental data of X-ray structural analysis.

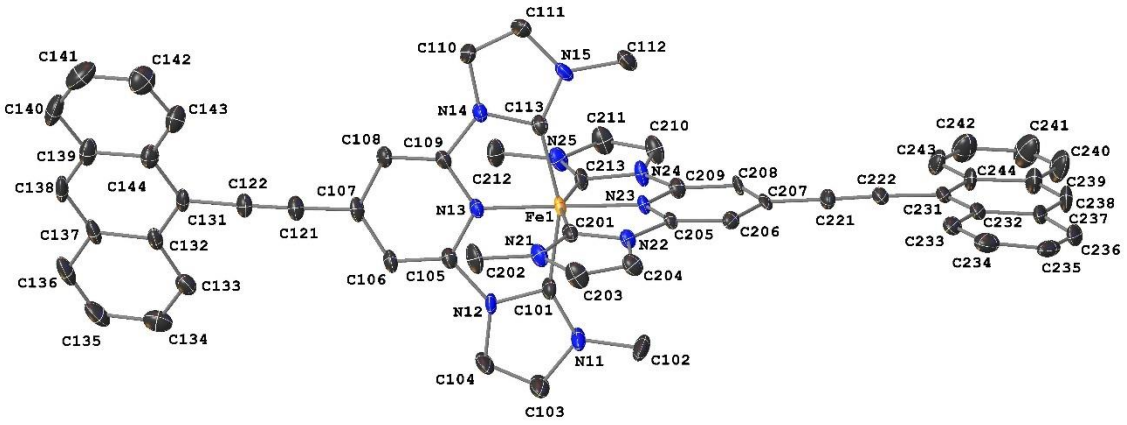

*Figure 4.2.2: Provisional single crystal X-Ray structure of **[Fe(bim-ac-3)$_2$]**$(PF_6)_2$.*

To further increase the distance between the iron center and the anthracenyl-backbone an attempt to introduce a second acetylene spacer was made, which is described in the following section (Scheme 4.2.5). Commercially available 1,4-bis-(trimethylsilyl)-butadiyne was single-deprotected by MeLi in DCM at room temperature for 24 h. The reaction was quenched by the addition of a saturated NH_4Cl solution at -80°C. Only unilaterally deprotected **15** was separated from the educt and the two-site deprotected site product by distillation.[91] **16** was obtained by Sonogashira coupling 9-bromoanthracene and **15**. Using the condition described in literature, $Pd(PPh_3)_2Cl_2$ and CuI in a mixture of DIPA and TEA at 110°C for 16 h, gave **16** with a yield of 26 %.[90] Also using PEPPSI-iPr as a catalyst more suitable for sterically demanding substrates did not significantly increase the yield.[92] To improve the yield of **16** a Hay coupling of **13** with TMS-acetylene was performed. Therefore **13** and TMS-acetylene were added to an in situ prepared Hay catalyst (CuCl·TMEDA (= N,N,N',N'-Tetramethylehane-1,2-diamine)) bubbled with O_2 for 45 min and stirred for 24 h, but **16** could not be observed in this attempt.[93]

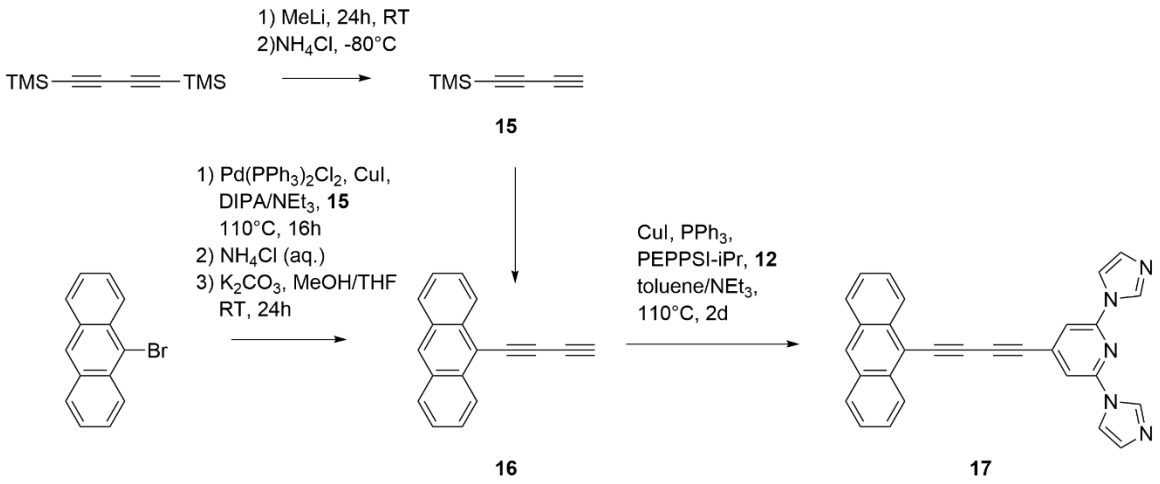

*Scheme 4.2.5: Synthetic procedure attempting to yield in **17**.*

In a Sonogashira coupling of **12** and **16** using PEPPSI-iPr as a catalyst for sterically demanding substrates and CuI in a mixture of toluene and TEA at 110°C for 16 h **17** was prepared. The presence of **17** was proved by ESI-MS data and NMR spectroscopy. In both analytical techniques the presence of unreacted **12** next to **17** was detected. It was not possible to separate **12** and **17** by column chromatography or crystallization techniques (Figure 4.2.3).

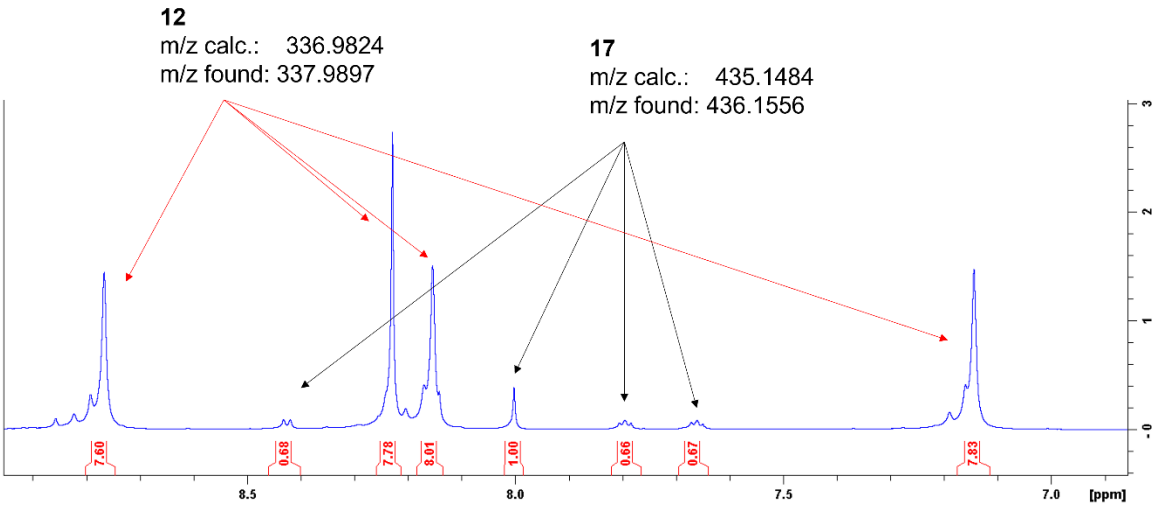

*Figure 4.2.3: NMR-spectrum and ESI-MS data proving the synthesis of **17** not separated from educt **12**.*

Therefore, is introduction of a second acetylene-linker was not performed successfully, but still is an interesting attempt to investigate the influence of the distance of the metal center and the organic chromophore backbone.

*Table 4.2.6: Yields of syntheses of **11**-**14**, pro-ligand **[H$_2$-bim-ac-3]**(PF$_6$)$_2$ and **[Fe(bim-ac-3)$_2$]**(PF$_6$)$_2$ complex performed according to the procedures described in this section. [1] **17** could not be purified.*

Compound	Yield	Compound	Yield	Compound	Yield
11	67 %	**14**	58 %	**15**	54 %
12	38 %	**[H$_2$-bim-ac-3]**(PF$_6$)$_2$	83 %	**16**	26 %
13	72 %	**[Fe(bim-ac-3)$_2$]**(PF$_6$)$_2$	46 %	**17**	-[1]

4.3 Synthesis of triazole and mesoionic-carbene based ligands and complexes

Since triazolylidenes, which represent a special class of MICs, can be synthesized via methylation of the corresponding triazoles and subsequent deprotonation of the triazolium salts. These types of ligands offer a unique possibility to address some fundamental questions in the photochemistry of Fe^{II} complexes using tridentate ligands. Although Fe^{II} triazole complexes are well-known for their spin-crossover properties their photo physics remain unexplored.

The triazole-based ligand **btp** is obtained by Sonogashira coupling of 2,6-dibromopyridine with trimethylsilyl acetylene to give **18** and a subsequent copper catalyzed azide-alkyne cyclization of **18** with *in situ* prepared ethylazide. The reaction of $FeBr_2$ in degassed ethanol with **btp** yields **[Fe(btp)$_2$]**$(PF_6)_2$. For the preparation of the mesoionic carbenes **btp** is methylated with methyl triflate in DCM at -80 °C to give the triazolium salt **[H$_2$-tri]**$(OTf)_2$. The preparation of **[Fe(tri)$_2$]**$(PF_6)_2$ requires deprotonation of **[H$_2$-tri]**$(OTf)_2$ with LiHMDS in THF at -80 °C and addition of $FeBr_2$ (Scheme 4.3.1).[94–96]

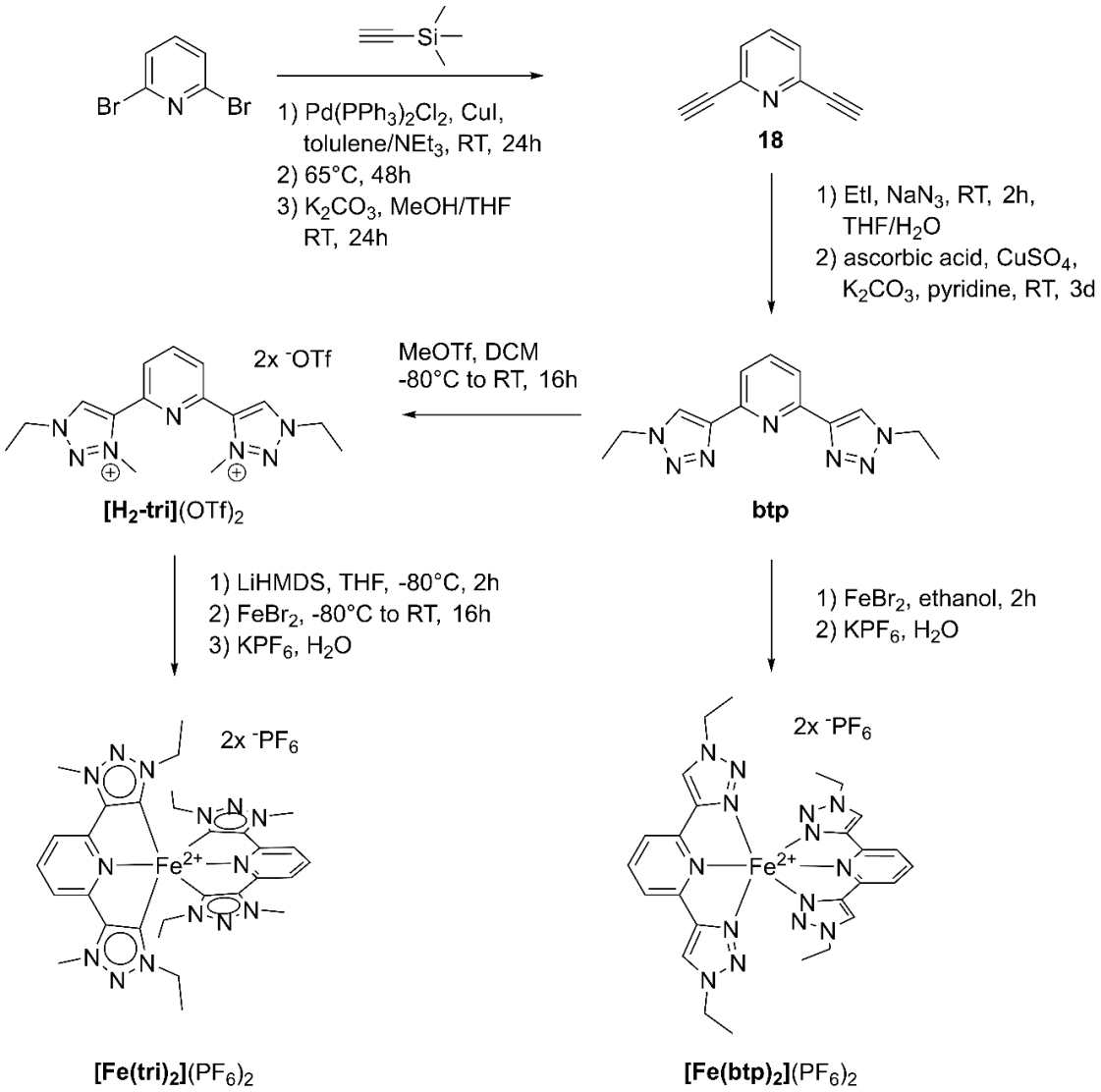

*Scheme 4.3.1: Syntheses of complexes **[Fe(btp)$_2$]**$(PF_6)_2$ and **[Fe(tri)$_2$]**$(PF_6)_2$.*[94]

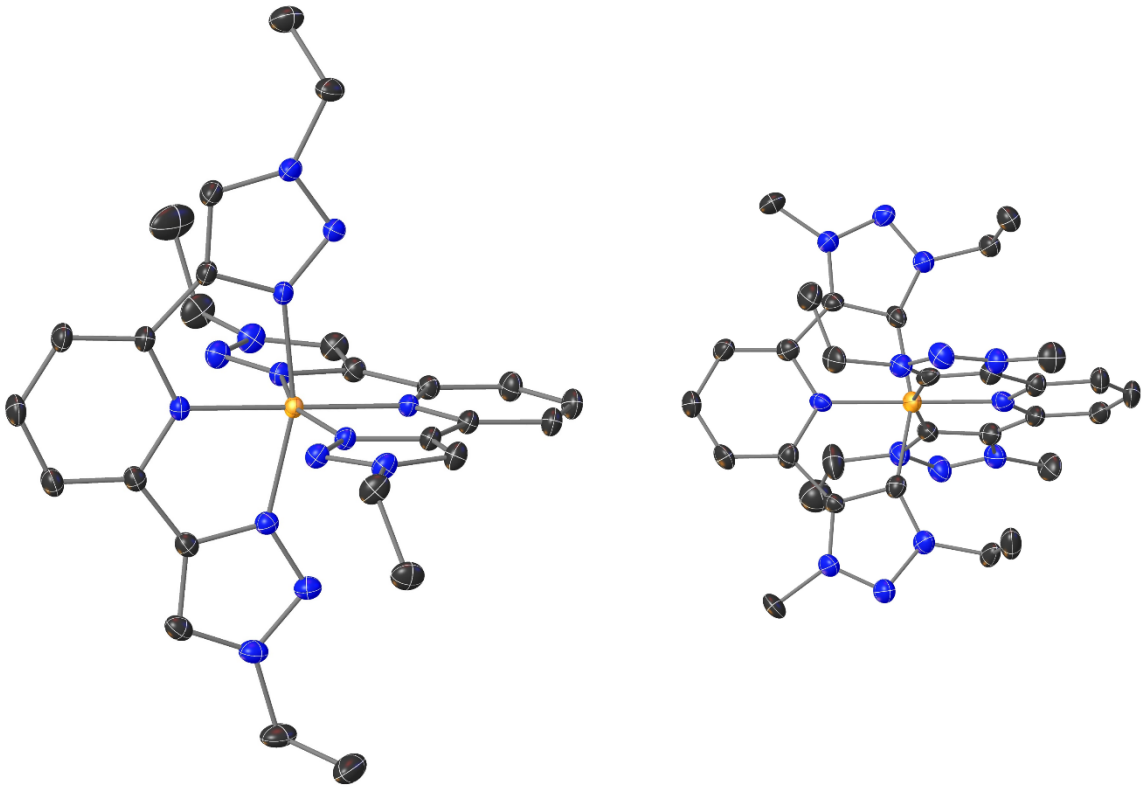

*Figure 4.3.1: Single crystal X-Ray structures of **[Fe(btp)$_2$]**(PF$_6$)$_2$ (left) and **[Fe(tri)$_2$]**(PF$_6$)$_2$ (right).*

The Fe-N bond length of 1.9539(9) Å in **[Fe(btp)$_2$]**(PF$_6$)$_2$ and the *N*-Fe-*N trans* angle of 161.06(4)° are only slightly changed with respect to 1.987(3) Å and 161.55(12)° in **[Fe(tpy)$_2$]$^{2+}$**.[97] Thus, the different electronic properties of the **btp** and **tpy** ligands only slightly affect the crystal structure parameters. A different picture can be found for **[Fe(tri)$_2$]**(PF$_6$)$_2$ in comparison to the bis(tridentate) **[Fe(bim)$_2$]$^{2+}$**. The *C*-Fe-*C trans* angle of 159.72(18)° in **[Fe(tri)$_2$]**(PF$_6$)$_2$ indicates a slightly increased octahedral symmetry in comparison to 158.32(15)° in **[Fe(bim)$_2$]**(PF$_6$)$_2$. The Fe-N$_{pyridine}$ bond length is elongated from 1.925(3) Å in **[Fe(bim)$_2$]**(PF$_6$)$_2$ to 1.958(3) Å in **[Fe(tri)$_2$]**(PF$_6$)$_2$ by stronger π-backdonation, potentially caused by a higher electron density at the iron center due to the stronger σ-donating character of the triazolylidene units.[39] This interpretation is confirmed by the shortening of the Fe-C$_{carbene}$ bond length from 1.9665(3) Å in **[Fe(bim)$_2$]**(PF$_6$)$_2$ to 1.9495(4) Å in **[Fe(tri)$_2$]**(PF$_6$)$_2$. The structural parameters, which are also in line with those reported by Iwasaki *et al.*,[98] therefore support the stronger σ-donating character of mesoionic carbene ligands in comparison to classical NHCs.

*Table 4.3.1: Yields of syntheses performed according to the procedures described in this section resulting in **[Fe(btp)$_2$]**(PF$_6$)$_2$ and **[Fe(tri)$_2$]**(PF$_6$)$_2$.*

Compound	Yield
18	85 %
btp	69 %
[H$_2$-tri](OTf)$_2$	92 %
[Fe(btp)$_2$](PF$_6$)$_2$	74 %
[Fe(tri)$_2$](PF$_6$)$_2$	46 %

Syntheses of chromophore-substituted triazolylidene-based pro-ligands and complexes

Based on the synthesis of **[Fe(btp)$_2$]**$(PF_6)_2$ and **[Fe(tri)$_2$]**$(PF_6)_2$ it was attempted to combine the strategy of using triazole and triazolylidene ligands and the multichromophoric approach. Synthetic realization of this attempt is described in this section. As a first attempt a direct iodination of **btp** in 4-position of the central pyridine ring under the conditions reported for **7** was performed.[78] In a first MS-analytic of the crude product a single-iodinated product was found, next to the educt **btp** and a two-fold iodinated product. After separation by column chromatography the products turned out to be remaining **btp**, **btp-I** and **btp-2I**. The interpretation following from these findings is, that the triazole proton is more acidic than the 4-pyridine proton and therefore no deprotonation in the 4-position is observed, but at the triazole (Scheme 4.3.2, first row). The direct iodination of **btp** thus is no suitable synthetic pathway to introduce organic backbone molecules in the backbone of **btp** and type **[H$_2$-tri]**$(OTf)_2$ ligands and complexes.

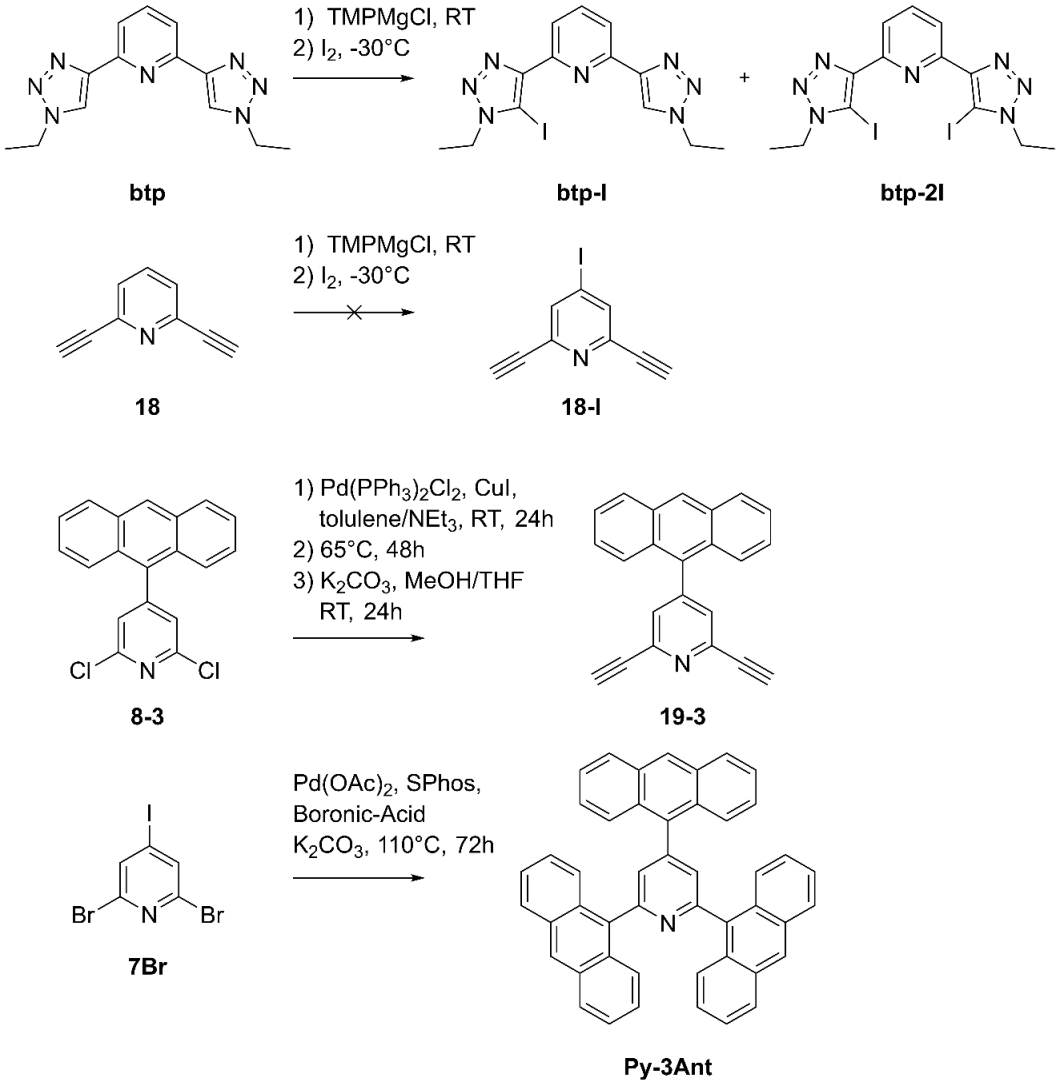

*Scheme 4.3.2: Synthetic procedure attempting to yield in **19-3**.*

A second attempt was starting at the stage of **18**. Again, an iodination in 4-position of the central pyridine ring was performed according to the procedure reported for **7**.[78] The successful synthesis of **18-I** was not observed in this attempt. Also, the use of the TMS-protected version of **18** did not lead to the formation of **18-I**. Unfortunately, no products formed in these reactions

could be identified (Scheme 4.3.2, second reaction). A completely different approach uses **8-3** in a Sonogashira reaction to introduce acetylene side chains into a molecule having an organic chromophore already attached to the backbone. In this case only traces of **19-3** have been isolated (Scheme 4.3.2, third reaction). To overcome the low yield changing the chlorine-leaving groups in **8-3** to the better leaving group of bromine has been tried. Therefore, **7-Br** was prepared according to the procedure reported for **7** using 2,6-dibromopyridine as starting material. But performing a Suzuki-coupling with **7-Br** does not lead to the analogous **8Br-3**, but a three-time functionalization leading to **Py-3Ant** was exclusively observed (Scheme 4.3.2). As a Sonogashira reaction using **8-3** is the method of choice to yield **19-3** in the end of this screening of different approaches. The Sonogashira conditions have been optimized in a catalyst screening process. The use of $Pd(PPh_3)_2Cl_2$ as catalyst in TEA/toluene gave only traces of **19-3**, while $Pd_2(dba)_3$ and Josiphos as the ligand gave no reaction. $Pd(dppf)Cl_2$ gave a yield of 6 % and $Pd(PPh_3)_4$+PPh_3 gave a yield of 10 %. The change from NEt_3/toluene to NEt_3/DMF gave a slightly increase of the yield up to 12 % but changing the solvent did not affect the yield drastically. The most successful approach was the use of a PEPPSI-iPr catalyst using additional PPh_3 as supporting ligand. PEPPSI catalysts are quite stable catalysts often used in the coupling of sterically demanding substrates.[92]

*Table 4.3.2: Parameters in the optimization process of the Sonogashira-Coupling resulting in **19-3**.*

Catalyst	Solvent	Temperature	Time	Yield
$Pd(PPh_3)_2Cl_2$	TEA/toluene	90°C	2d	Traces
$Pd(PPh_3)_4$+PPh_3	TEA/toluene	90°C	2d	10 %
$Pd_2(dba)_3$+Josiphos	TEA/toluene	90°C	2d	No reaction
$Pd(dppf)Cl_2$	TEA/toluene	90°C	2d	6%
$Pd(PPh_3)_4$+PPh_3	TEA/DMF	90°C	2d	12%
PEPPSI-IPr+PPh_3	TEA/toluene	90°C	2d	70%

The copper catalyzed [2+3]-Cycloaddition of *in situ* prepared ethyl azide with **19-3** was optimized by different approaches. The conditions used for the synthesis of **btp** gave only 6 % yield in the synthesis of **btp-3**. The increase of temperature from RT to 60°C results in the increase of the yield up to 17 %. The change of the supporting ligand from pyridine to TBTA (= tris((1-benzyl-4-triazolyl)methyl)amine) increases the yield to 35 %. In this reaction TBTA is hindering the disproportionation and the oxidation of the Cu(I) catalyst.[99] Further increase of the temperature to 100 °C further increases the yield to 55 %. And finally, the change of the copper-source from $CuSO_4$ to CuI increases the yield to 67 %.

*Table 4.3.3: Parameters in the optimization process of the Huisgen-[2+3]-cyclization resulting in **btp-3**.*

Catalyst	Ligand	Temperature	Yield
$CuSO_4$+Ascorbic Acid	Pyridine	RT	6%
$CuSO_4$+Ascorbic Acid	Pyridine	60°C	17%
$CuSO_4$+Ascorbic Acid	TBTA	60°C	35%
$CuSO_4$+Ascorbic Acid	TBTA	100°C	55%
CuI+Ascorbic Acid	TBTA	100°C	67%

The corresponding triazole complex **[Fe(btp-3)$_2$]**$(PF_6)_2$ was obtained by the reaction of **btp-3** with $FeBr_2$ at room temperature in ethanol. After filtration of insoluble solids, an aqueous KPF_6 solution was added to give the hexafluorophosphate salts and **[Fe(btp-3)$_2$]**$(PF_6)_2$ precipitated.[94]

To result in the triazolium salts as pro ligands **btp-3** was methylated using MeOTf at -80°C in DCM to give **[H$_2$-tri-3]**(OTf)$_2$. The preparation of **[Fe(tri-3)$_2$]**(PF$_6$)$_2$ requires deprotonation of **[H$_2$-tri-3]**(OTf)$_2$ with LiHMDS in THF at -80 °C and addition of FeBr$_2$. In contrast to the previously described complexes, **[Fe(tri-3)$_2$]**(PF$_6$)$_2$ was purified by column chromatography using SiO$_2$ as stationary phase and a mixture of acetone/KNO$_{3(aq.,sat.)}$/H$_2$O (10/3/1 V/V/V) and following crystallization (solvent: acetone/ antisolvent: diethyl ether).

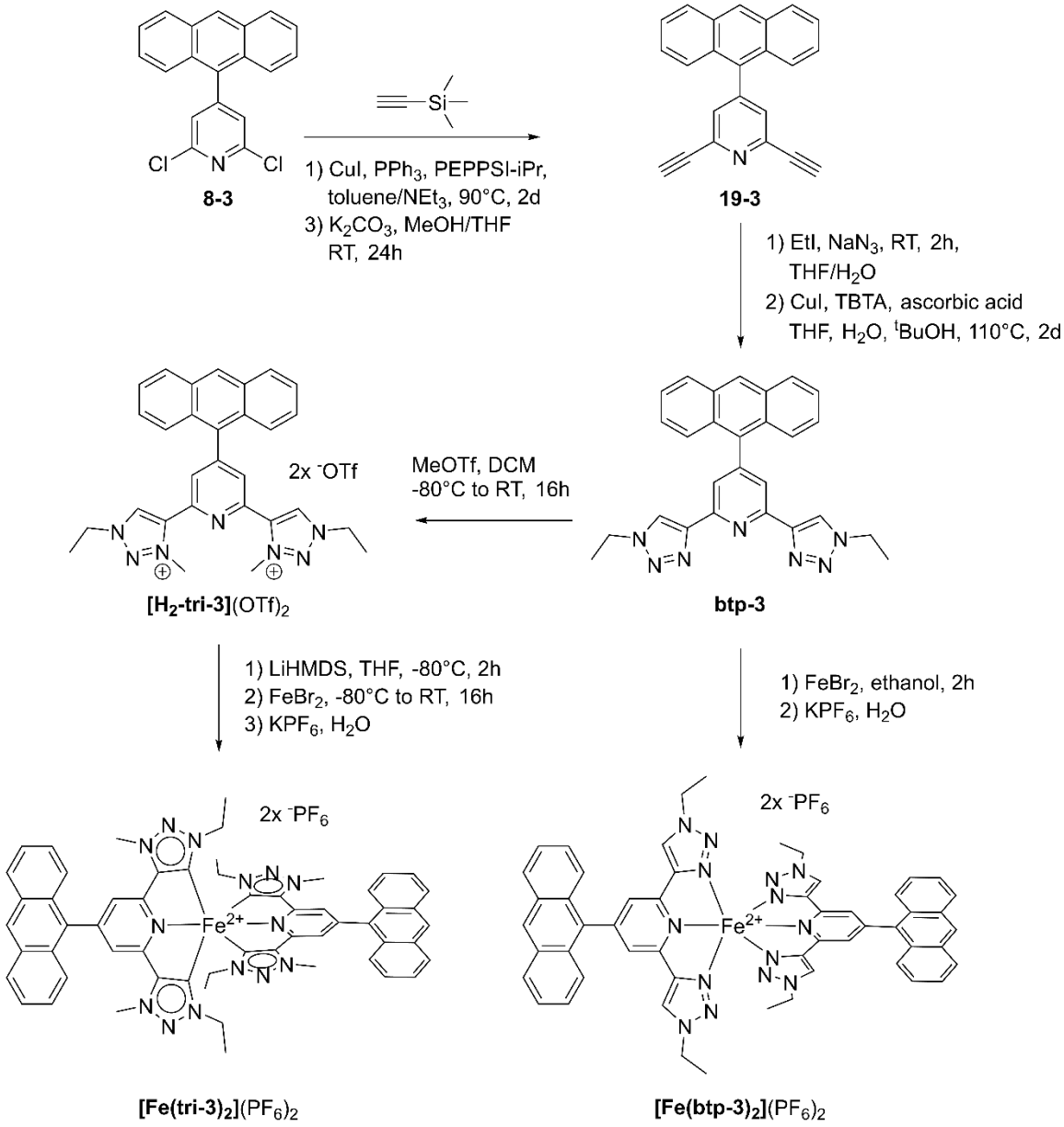

*Scheme 4.3.3: Syntheses of complexes **[Fe(btp-3)$_2$]**(PF$_6$)$_2$ and **[Fe(tri-3)$_2$]**(PF$_6$)$_2$.*

*Table 4.3.4: Yields of syntheses performed according to the procedures described in this section resulting in **[Fe(btp-3)$_2$]**(PF$_6$)$_2$ and **[Fe(tri-3)$_2$]**(PF$_6$)$_2$.*

Compound	Yield
19-3	70 %
btp-3	67 %
[H$_2$-tri-3](PF$_6$)$_2$	94 %
[Fe(btp-3)$_2$](PF$_6$)$_2$	90 %
[Fe(tri-3)$_2$](PF$_6$)$_2$	37 %

4.4 Synthesis of multichromophoric ruthenium complexes

To investigate the effect of the higher homologous Ru^{II} center on the multichromophoric effect using NHC-based ligands three different ruthenium complexes have been prepared.

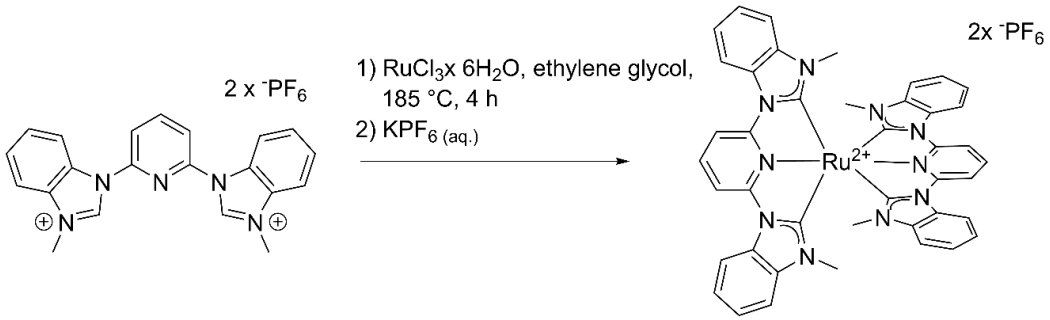

*Scheme 4.4.1: Synthetic procedure of **[Ru(bbp)$_2$]**(PF$_6$)$_2$. The same procedure results in the formation of **[Ru(bbp-1)$_2$]**(PF$_6$)$_2$ and **[Ru(bbp-3)$_2$]**(PF$_6$)$_2$.[100,101]*

To synthesize **[Ru(bbp-R)$_2$]**(PF$_6$)$_2$ complexes, RuCl$_3$·6H$_2$O as the ruthenium source is stirred in presence of the ligand in ethylene glycol for 4 h at 185 °C. In this reaction ethylene glycol is used as the solvent as well as the reductant to reduce ruthenium from the +III to the +II form. Cooling to room temperature and addition of an aqueous KPF$_6$ solution, leads to the precipitation of the **[Ru(bbp-R)$_2$]**(PF$_6$)$_2$ complexes. The phenyl-derivative **[Ru(bbp-1)$_2$]**(PF$_6$)$_2$ and anthracene-derivative **[Ru(bbp-3)$_2$]**(PF$_6$)$_2$ are prepared next to **[Ru(bbp)$_2$]**(PF$_6$)$_2$ without any backbone-functionalization for comparison purposes. The crude complexes were purified by column chromatography (stationary phase: basic AlOx/ mobile phase: acetonitrile) and subsequently following crystallization using diffusion techniques (solvent: acetone/ anti-solvent: diethyl ether).[100,101]

*Table 4.4.1: Yields of syntheses performed according to the procedures described in this section resulting in **[Ru(bbp)$_2$]**(PF$_6$)$_2$, **[Ru(bbp-1)$_2$]**(PF$_6$)$_2$ and **[Ru(bbp-3)$_2$]**(PF$_6$)$_2$.*

Compound	Yield
[Ru(bbp)$_2$](PF$_6$)$_2$	64 %
[Ru(bbp-1)$_2$](PF$_6$)$_2$	52 %
[Ru(bbp-3)$_2$](PF$_6$)$_2$	85 %

5 Characterization

The photophysical properties of the pro-ligands and complexes prepared for this thesis are characterized by advanced spectroscopic and quantum chemical techniques to reveal insights into the excited state dynamics. The ground state properties are characterized by steady state absorption and cyclic voltammetry. The excited state properties are determined by transient absorption, steady state and time-resolved emission spectroscopy and spectroelectrochemical measurements. The results of ground and excited state characterization are accompanied by time-dependent density functional theory (TD-DFT) calculations. Back coupling of the results laid the ground for the synthetic variations to further improve the photophysical and catalytical properties unveiled in the chapter before.

5.1 Photophysics of $[Fe(tpy\text{-}R)_2](PF_6)_2$ complexes

For the terpyridine-based complexes and their ligands, the ground state was first investigated by UV/Vis spectroscopy and cyclic voltammetry in comparison with the **[Fe(tpy)$_2$]**$(PF_6)_2$ complex known from literature (Figure 5.1.1; Table 5.1.1).[88] UV/Vis spectroscopy revealed characteristic absorption bands for the π-π* transitions within the respective chromophore in addition to the π-π* transitions in the terpyridine unit for the two ligands **tpy-3** and **tpy-4**. These characteristic absorption bands were also detected in the respective complexes **[Fe(tpy-3)$_2$]**$(PF_6)_2$ and **[Fe(tpy-4)$_2$]**$(PF_6)_2$. Moreover, a bathochromic shift for the absorption band with the lowest energy was detected in the UV/Vis spectra of the complexes. The absorption shifts from 552 nm (11 200 M^{-1} cm^{-1}) in **[Fe(tpy)$_2$]**$(PF_6)_2$ over 561 nm (21 500) in **[Fe(tpy-3)$_2$]**$(PF_6)_2$ to 568 nm (26 800) in **[Fe(tpy-4)$_2$]**$(PF_6)_2$. This absorption band was characterized as the MLCT absorption band based on literature comparisons[38] and using cyclic voltammetry. Cyclic voltammograms of the iron(II) complexes show no significant shift of the fully reversible Fe^{II}/Fe^{III} oxidation potentials going from **[Fe(tpy)$_2$]**$(PF_6)_2$ (0.72 V vs. FcH/FcH^+) to potentials of **[Fe(tpy-3)$_2$]**$(PF_6)_2$ (0.74 V) and **[Fe(tpy-4)$_2$]**$(PF_6)_2$ (0.68 V), indicating a similar energy of the highest occupied metal centered d-orbitals in each complex. Irreversible oxidations can be found at anodic potentials for the bichromophoric complexes that are assigned to the oxidation of the organic chromophores.[36] At cathodic potentials irreversible ligand-based reductions occur, which are assigned to the **tpy-R** moiety in each ligand. **[Fe(tpy-3)$_2$]**$(PF_6)_2$ and **[Fe(tpy-4)$_2$]**$(PF_6)_2$ are reduced irreversibly at cathodic potentials. This leads to the assumption that the lowest energy absorption in optical spectroscopy is a MLCT transition.

After excitation of the characteristic absorption bands for the π-π* transitions within the respective chromophore, emission was detected for each of the ligands and the complexes. These are independent of the excitation wavelength and exhibit an emission maximum at λ_{Em} = 420 nm for all four compounds. Strikingly, the emission quantum yield is significantly reduced in the complexes compared to the respective ligands. The emission is not sensitive to oxygen, which is indicative of a fluorescence process. After excitation of the respective MLCT absorption bands, no emission was detected for any of the complexes.

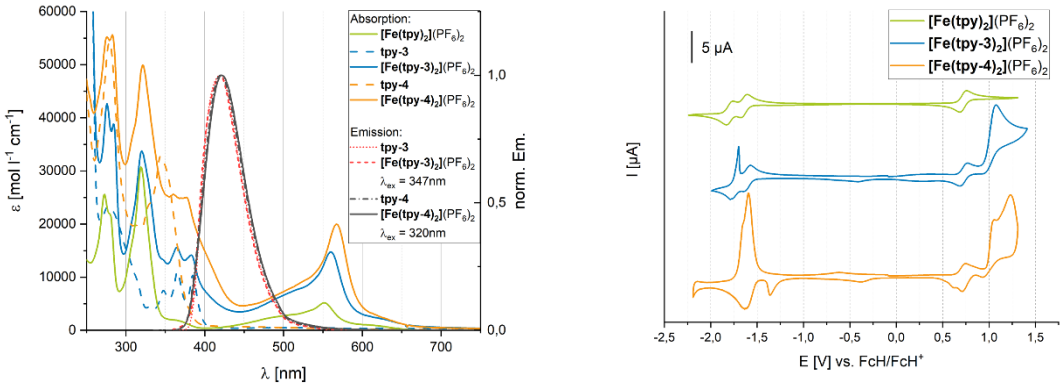

Figure 5.1.1: Optical absorption and emission spectroscopy data (left panel) and cyclic voltammograms (right panel) of ***tpy-R*** *ligands and* ***[Fe(tpy-R)$_2$]***$(PF_6)_2$ *complexes.*

To determine the dynamics of the excited states, time correlated single photon counting (TCSPC) was performed to determine the emission lifetimes after excitation of the π-π* transitions of the organic chromophores and transient absorption (TA) was performed to determine the dynamics after excitation of the MLCT absorption band (Figure 5.1.2). The results from the TCSPC show an emission lifetime in the nanosecond range. All measurements are fitted with one time component, so that in all compounds presumably the fluorescence from an excited singlet state located at the chromophore back to the ground state (^{1}Chrom → ^{1}GS) is observed. It is noticeable that for the complexes, in addition to the quantum yield, the emission lifetime is also slightly reduced, suggesting more likely non-radiative deactivation in the complexes. These non-emissive deactivation pathways were probed by ultrafast pump–probe spectroscopy. For **[Fe(tpy-3)$_2$]**$(PF_6)_2$ the TA spectra and decay associated spectra (DAS) reflect the ground state bleach (GSB) but deviate significantly from what is expected for a populated charge transfer state. The signature and the very long lifetime of the TA signal indicate that excitation of **[Fe(tpy-3)$_2$]**$(PF_6)_2$ results in an ultrafast population (τ_{MC} = 5.8 ns) of a MC or ligand field state. Similar findings related to ^{5}MC-^{1}GS ground state recovery were also reported for other $[FeN_6]^{2+}$ complexes.[38]

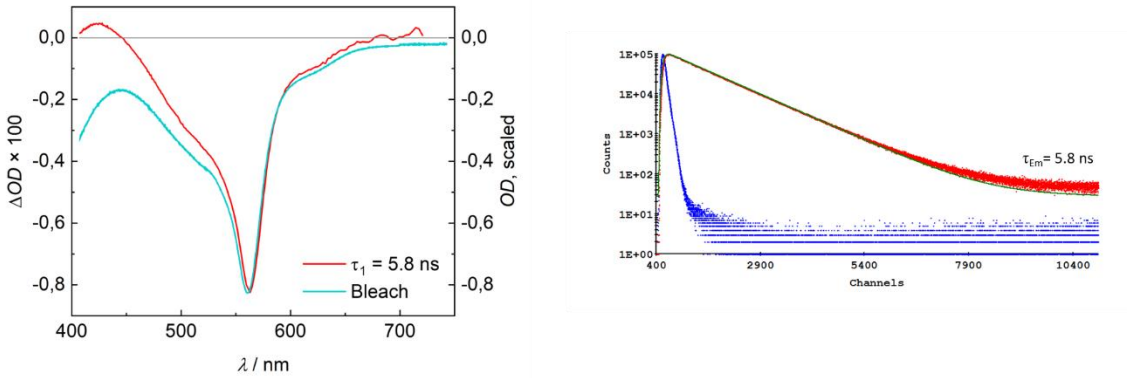

Figure 5.1.2: Decay associated spectrum (DAS; left panel) and TCSPC data (right panel) of ***[Fe(tpy-3)$_2$]***$(PF_6)_2$.

Table 5.1.1: Photo- and electrochemical properties of ***tpy-R*** *ligands and* ***[Fe(tpy-R)$_2$]***$(PF_6)_2$ *complexes.*

Compound	λ_{MLCT} [nm] (ε [M^{-1} cm^{-1}])	$Fe^{III/II}$ [V vs. FcH/FcH^+]	λ_{Em} [nm]	Φ_{Em}	τ_{Em} [ns]	τ_{MC} [ns]
[Fe(tpy)$_2$]$(PF_6)_2$	552 (11 200)	0.72	-	-	-	5.4[38]
tpy-3	-	-	420	23 %	5.9	-
[Fe(tpy-3)$_2$]$(PF_6)_2$	561 (21 500)	0.74	420	< 1 %	5.8	5.8
tpy-4	-	-	420	56 %	4.0	-
[Fe(tpy-4)$_2$]$(PF_6)_2$	568 (26 800)	0.68	420	3 %	3.3	6.4

In summary, an increase in MLCT lifetime cannot be observed in terpyridine-based Fe(II) complexes. This remains in the range of τ_{MLCT} < 100 fs and cannot be determined more precisely. The lifetime of the MC states is comparable to that of **[Fe(tpy)$_2$]**$(PF_6)_2$ (τ_{MC} = 5.4 ns)[38]. The emission quantum yields are significantly reduced in both complexes. A slight reduction was observed for the emission lifetimes in both complexes. Nevertheless, the optical properties could be improved, in terms of an MLCT absorption shifted into the visible spectrum with a significantly higher extinction coefficient than in **[Fe(tpy)$_2$]**$(PF_6)_2$. Thus, the multichromophoric approach initially represents a possibility to improve the optical properties of Fe(II) complexes with other ligand systems as well. Based on these results, the preparation of further terpyridine-based multichromophoric Fe(II) complexes was omitted.

5.2 Photophysics of [Fe(bim-R)$_2$](PF$_6$)$_2$ complexes

For all complexes **[Fe(bim-1)$_2$]**(PF$_6$)$_2$ - **[Fe(bim-5)$_2$]**(PF$_6$)$_2$, the absorption spectra are composed of three distinct spectral regions (Figure 5.2.1, left panel). The intense bands at wavelengths shorter than 320 nm correspond to π-π*-transitions within the bim moieties of the ligands[39,102,103]. In the range of 320 – 420 nm π-π*-transitions of the organic chromophores in the backbone can be found for **[Fe(bim-3)$_2$]**(PF$_6$)$_2$ - **[Fe(bim-5)$_2$]**(PF$_6$)$_2$ containing several intra-chromophore transitions.[104] The anthracenyl derivative **[Fe(bim-3)$_2$]**(PF$_6$)$_2$ show the typical vibrational fine structure of anthracene.[105] The π-π*-transitions of the organic chromophores in **[Fe(bim-1)]**(PF$_6$)$_2$ - **[Fe(bim-2)$_2$]**(PF$_6$)$_2$ are in the UV region below 350 nm. According to the results of TDDFT calculations, the low intensity band at 389 nm of **[Fe(bim)$_2$]**(PF$_6$)$_2$ has a dominant MLCT character.[106] At longer wavelengths, MLCT transitions appear for all complexes. These bands are clearly red-shifted for the bichromophoric complexes compared to **[Fe(bim)$_2$]**(PF$_6$)$_2$ and in line with the electrochemical data discussed below. The absorption bands and intensities shift from 473 nm (26 800 M^{-1} cm^{-1}) in **[Fe(bim-3)$_2$]**(PF$_6$)$_2$ to 497 nm (23 400 M^{-1} cm^{-1}) in **[Fe(bim-5)$_2$]**(PF$_6$)$_2$, which does not correlate with the size of the organic chromophore in the ligand backbone or any other attribute like the triplet energy level. The energy of the MLCT absorption is also referred to as optical energy gap (ΔE_o). The absorption maxima at longer wavelengths and the higher absorption coefficients render the bichromophoric complexes potentially more suited as photosensitizers than **[Fe(bim)$_2$]**(PF$_6$)$_2$.

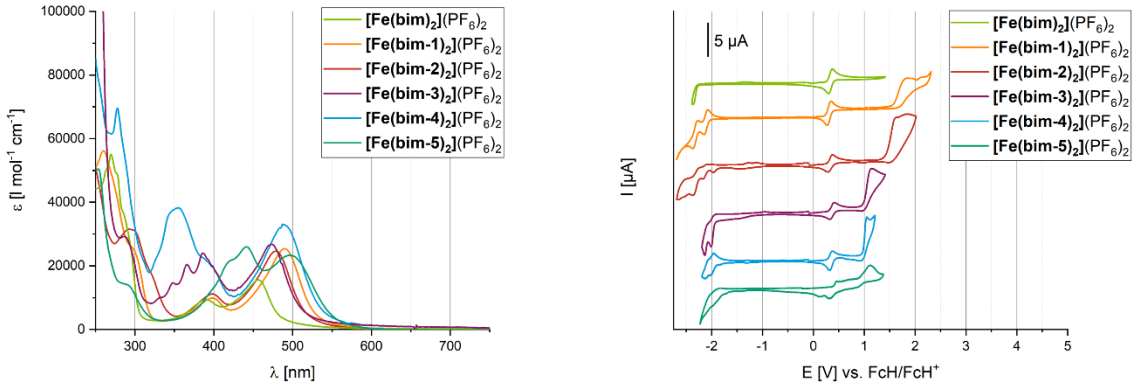

*Figure 5.2.1: Optical absorption and emission spectroscopy data (left panel) and cyclic voltammograms (right panel) of **[Fe(bim-R)$_2$]**(PF$_6$)$_2$ complexes in MeCN.*

Cyclic voltammograms of the iron(II) complexes (Figure 5.2.1, right panel) show no distinct trend in the shift of the fully reversible Fe^{II}/Fe^{III} oxidation potentials going from **[Fe(bim-1)$_2$]**(PF$_6$)$_2$ (0.32 V) to **[Fe(bim-3)$_2$]**(PF$_6$)$_2$ (0.37 V) indicating a similar energy of the HOMOs, but slightly stabilized HOMOs for larger organic chromophores in the backbones of the ligands. Irreversible oxidations can be found at anodic potentials for the multichromophoric complexes, but not for **[Fe(bim)$_2$]**(PF$_6$)$_2$. Comparison of the cyclic voltammograms of **[H$_2$-bim]**(PF$_6$)$_2$, **[H$_2$-bim-3]**(PF$_6$)$_2$ and **[H$_2$-bim-4]**(PF$_6$)$_2$ with those of pure anthracene and pyrene and with those of the complexes **[Fe(bim)$_2$]**(PF$_6$)$_2$, **[Fe(bim-3)$_2$]**(PF$_6$)$_2$ and **[Fe(bim-4)$_2$]**(PF$_6$)$_2$ – that can be found in literature[36] – reveals that the irreversible oxidation can be assigned to the oxidation of the organic chromophore.[107] At cathodic potentials irreversible ligand-based reductions occur, which are

assigned to the bim moiety in each ligand. **[Fe(bim)$_2$]**$(PF_6)_2$ is reduced irreversibly at -2.37 V vs. FcH/FcH^+, while the reduction in the multichromophoric complexes ranges from **[Fe(bim-1)$_2$]**$(PF_6)_2$ (-2.16 V) to **[Fe(bim-5)$_2$]**$(PF_6)_2$ (-1.93 V)**.** These values are in accordance with the electron-accepting properties of multichromophoric ligands and the lower energies of their π* levels in comparison to **[H$_2$-bim]**$(PF_6)_2$.[42] A similar behavior is found in bis-polypyridine iron(II) complexes where two consecutive one-electron reductions are observed for each polypyridine ligand.[108] The potential difference of Fe^{II}/Fe^{III} oxidation and ligand reduction is referred to as electrochemical energy gap. The resulting electrochemical energy gap ΔE_p roughly correlates to the optical energy gap ΔE_o. The values confirm the assignment of the lowest energy absorptions to MLCT states (Table 5.2.1).

*Table 5.2.1: Photo- and electrochemical properties of **[Fe(bim-R)$_2$]**$(PF_6)_2$ complexes.*

Compound	λ_{MLCT} [nm] (ε [M^{-1} cm^{-1}])	CV [V vs. FcH/FcH^+]	ΔE_p (eV)	ΔE_o (eV)
[Fe(bim)$_2$]$(PF_6)_2$	444 (13 200)	0.34 (rev.) -2.37 (irrev.)	2.71	2.71
[Fe(bim-1)$_2$]$(PF_6)_2$	490 (25 400)	1.82 (irrev.) 0.32 (rev.) -2.16 (rev.) -2.36 (rev.)	2.48	2.53
[Fe(bim-2)$_2$]$(PF_6)_2$	479 (24 600)	1.61 (irrev.) 0.35 (rev.) -2.16 (irrev.) -2.36 (irrev.)	2.51	2.59
[Fe(bim-3)$_2$]$(PF_6)_2$	474 (26 800)	1.15 (irrev.) 0.37 (rev.) -2.01 (irrev.)	2.38	2.62
[Fe(bim-4)$_2$]$(PF_6)_2$	489 (32 900)	1.05 (irrev.) 0.34 (rev.) -2.02 (irrev.)	2.36	2.54
[Fe(bim-5)$_2$]$(PF_6)_2$	497 (23 400)	1.05 (irrev.) 0.36 (rev.) -1.93 (irrev.)	2.29	2.49

All multichromophoric pro-ligands exhibit luminescence in solution at room temperature. Excitation at different wavelengths in the region of the π-π*-transitions of the organic chromophores (λ_{ex} = 320 – 390 nm) leads to luminescence (Table 5.2.2, example of **[H$_2$-bim-3]**$(PF_6)_2$ in Figure 5.2.2). All ligands show an emission spectrum which is independent of the excitation wavelength. This emission is assigned to the lowest electronically excited singlet states of the organic chromophores. Coupling of the organic chromophore to the (bim) pro-ligand results in a redshift of the emission in comparison to the pure chromophore.[104] This lower energy points to low lying π*-orbitals which further supports the conclusion the pro-ligands being good π-acceptor ligands. Quantum Yields have been determined for anthracene, pyrene and perylene containing ligands. Emission lifetime was determined by streak camera measurements. For **[H$_2$-bim-1]**$(PF_6)_2$ the emission intensity was too weak to perform streak camera measurements. For all pro-ligands a single exponential decay of the population of the luminescent state with a lifetime was revealed.

All complexes – except **[Fe(bim-1)$_2$]**$(PF_6)_2$ – also exhibit luminescence at room temperature in solution after excitation of the organic chromophores (λ_{ex} = 320 – 390 nm). Emission bands of the complexes are shifted to higher energies in comparison to the emission of the pro-ligands. The

emission spectra at different excitation energies match nearly perfectly. The excitation spectra recorded at the wavelength with maximum emission intensity reproduce merely the part of the absorption spectrum, which is related to the organic chromophore, but not the MLCT absorption band. Consequently, the observed emission is safely attributed to the singlet state of the appended organic chromophores. But through coordination to the iron(II) centre, this chromophore-based luminescence is shifted to higher energies. This is still in line with the interpretation of the low lying π*-orbitals of the good π-acceptor ligands. Quantum yields of the anthracene, pyrene and perylene containing complexes are drastically reduced compared to the free pro-ligands. In all complexes two exponential time constants were required to fit the emission decay. Due to the similarity of the longer lifetimes τ_1 with those of the pro-ligands and due to the fact, that excitation spectra of the complexes resemble the absorption spectra of the pro-ligands, the luminescence is more specifically assigned to the fluorescence of the organic chromophore. The complex formation by coordination of the chromophore-functionalized ligand to iron(II) results in the second, shorter lifetime τ_2 in the luminescence decay. This suggests an additional non-radiative pathway opened by the iron(II) center. The absorption and emission spectra show a broad spectral overlap between the singlet emission band of the ligand and the ^{1}MLCT absorption of the complexes. A key requirement for a Förster-Resonance-Energy-Transfer (FRET) is thus fulfilled.[109] The excited organic chromophore singlet state can therefore act as a donor in a FRET process resulting in the formation of the ^{1}MLCT state. This interpretation is supported by the drastically reduced quantum yield of the complexes in comparison to the quantum yield of the pro-ligands. Within this excited state kinetic model, the time constant of the FRET process contributes to the reduced luminescence quantum yields of complexes with respect to their pro-ligands. The ^{1}MLCT state populated by FRET decays rapidly to the ^{3}MLCT and further to the non-luminescent ^{3}MC states. Following the discussion above, attachment of an organic chromophore to a photoactive iron(II) complex shows unprecedented and so far unreported luminescence results.[110] No MLCT emission is observed, but the emission wavelength of the organic chromophore can be tuned by coupling to the bim ligand motif and coordination to an iron(II) centre over a large range.

According to the preceding discussion, luminescence measurements cannot access the photochemically relevant MLCT states. Therefore, fs-TA measurements with excitation pulses at 480 nm were used to track the early excited state dynamics of the complexes. The TA spectra are analyzed together with DAS resulting from a global multi-exponential fit of the data. For all complexes, a pronounced excited state absorption (ESA) is found at wavelengths larger than 500 nm beside the GSB at 480 nm. The kinetics can be fitted with two time constants, which are similar in each complex. In all compounds a very short lifetime of 0.1 ps is found and a longer one which differs slightly with 12.8 ps in **[Fe(bim-4)$_2$]**$(PF_6)_2$ and 14.4 ps in **[Fe(bim-1)$_2$]**$(PF_6)_2$.

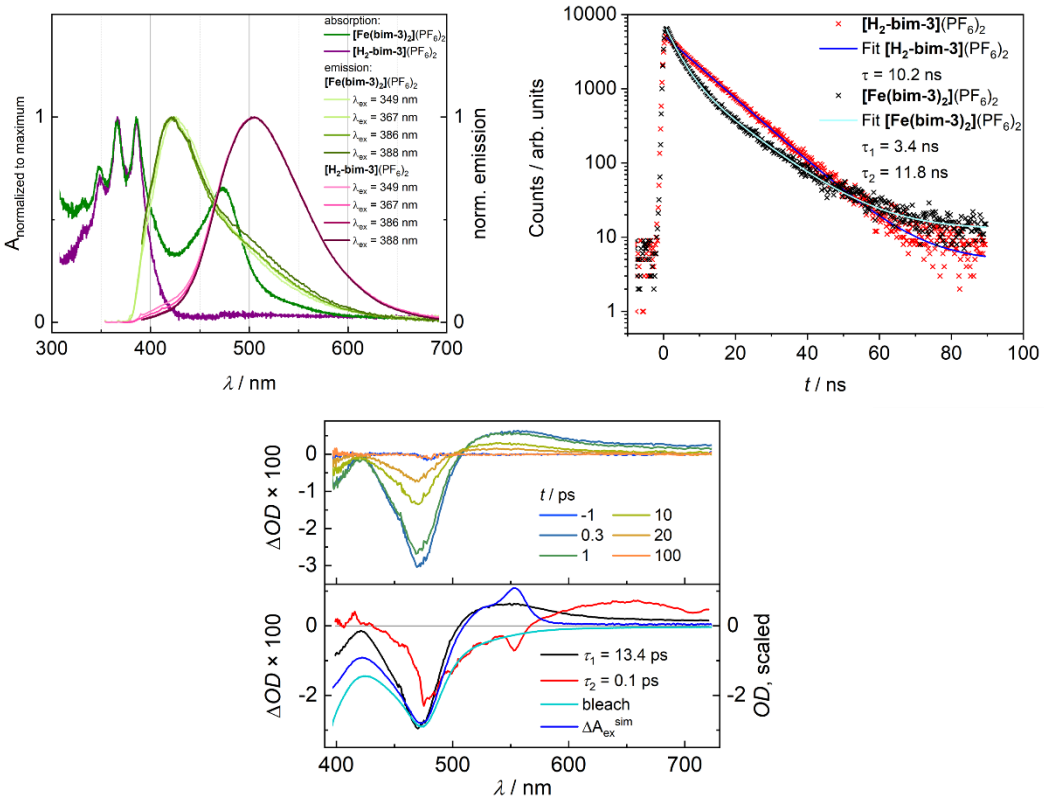

*Figure 5.2.2: Steady state absorption and emission spectroscopy (top left panel), experimental data and analysis of time resolved emission spectroscopy performed by streak camera measurements (top right panel) and transient absorption and decay associated spectra including results of spectroelectrochemical experiments ΔA_{ex}^{sim} (bottom panel). These experimental data are shown for **[H$_2$-bim-3]**(PF$_6$)$_2$ and **[Fe(bim-3)$_2$]**(PF$_6$)$_2$ as examples.*

The DAS of the long-lived component shows two ESA signals. One in the blue and one in the red spectral region, respectively. This feature is very similar to the reported TA spectra for the ^{3}MLCT state of **[Fe(bim)$_2$]**(PF$_6$)$_2$ and different from the characteristic ESA of $^5T_2$ states, observed for example in **[Fe(tpy)$_2$]**(PF$_6$)$_2$.[39] Moreover, the difference spectra $\mathbf{\Delta A_{ex}^{sim}}$ obtained by spectroelectrochemistry reproduce the ESA reasonably well, except for a sharp signal at about 560 nm in each case assigned to a reduced ligand. Consequently, the longer time constant is assigned to the ^{3}MLCT lifetime. The fast decay component with a time constant of 0.1 ps shows in both complexes sharp features, which are typical for Raman artefacts at time zero, and red shifted replica of the main ESA and bleach bands pointing to contributions of vibrational redistribution.[46,111] Therefore, this component is not further considered in the analysis. Since no feature in the TA points to population of MC states, the ^{3}MC lifetimes in the complexes are supposed to be much shorter than the ^{3}MLCT-lifetimes. In this case, the observed dynamics lead to negligible population of the MC states and repopulation of the electronic ground states from the ^{3}MLCT states occurs essentially within the ^{3}MLCT lifetime. This behavior is frequently reported for Fe-NHC-complexes with ^{3}MLCT-lifetimes in the ps range.[46,112,48]

*Table 5.2.2: Excited state properties of **[H₂-bim-R]**$(PF_6)_2$ pro-ligands and **[Fe(bim-R)₂]**$(PF_6)_2$ complexes. [a] Data not collected due to weak emission. [b] Measurements still in progress.*

Compound	λ_{Em} [nm]	τ_{em} [ns]	Φ_{Em} [%]	τ_{MLCT} [ps]
[H₂-bim]$(PF_6)_2$	-[a]	-[a]	-[a]	-
[Fe(bim)₂]$(PF_6)_2$	-[a]	-[a]	-[a]	9[39]
[H₂-bim-1]$(PF_6)_2$	330	-[b]	-[b]	-
[Fe(bim-1)₂]$(PF_6)_2$	-[a]	-[a]	-[a]	14.4
[H₂-bim-2]$(PF_6)_2$	429	7.6	-[b]	-
[Fe(bim-2)₂]$(PF_6)_2$	408	4.0 10.7	-[b]	13.5
[H₂-bim-3]$(PF_6)_2$	502	10.2	37	-
[Fe(bim-3)₂]$(PF_6)_2$	421	3.4 11.8	6	13.4
[H₂-bim-4]$(PF_6)_2$	492	5.9	79	-
[Fe(bim-4)₂]$(PF_6)_2$	468	3.4 6.9	2	12.8
[H₂-bim-5]$(OTf)_2$	545	-[c]	90	-
[Fe(bim-5)₂]$(PF_6)_2$	478	-[c]	5	13.0

Long-lived triplet states can undergo energy transfer to $^3O_2$ and generate highly reactive $^1O_2$.[113] To finally complement the model for the excited state dynamics, the existence of long-lived triplet states is chemically probed by the reaction of luminescent **DPBF** (1,3-diphenylisobenzofuran) with reactive singlet oxygen to non-luminescent *ortho*-dibenzoylbenzene.[114] In none of the probed **[Fe(bim-R)₂]**$(PF_6)_2$ complexes reactive $^1O_2$ was detected after irradiation with λ_{ir} = 480 nm. **[Ru(bpy)₃]**$(PF_6)_2$ as a reference for effective oxygen sensitization is selected for comparison. This result is expected for **[Fe(bim)₂]**$(PF_6)_2$ since in this compound the only possible triplet states are the short lived ^{3}MLCT and ^{3}MC states. In contrast, the excited state landscapes in the multichromophoric **[Fe(bim-R)₂]**$(PF_6)_2$ could in principle include triplet chromophore states (^{3}Chrom) in addition to the ^{3}MLCT states. The lifetimes of anthracene and pyrene triplet states are typically in the µs range and therefore able to sensitize the formation of singlet oxygen.[115] Accordingly, the lack of $^1O_2$ formation after irradiation of **[Fe(bim-R)₂]**$(PF_6)_2$ suggests that there is no appreciable population of ^{3}Chrom states in these complexes. Consequently, no equilibrium between ^{3}Chrom and ^{3}MLCT states - which is found in ruthenium complexes that exhibit the "reservoir" effect[57,60,58,61] – is present in **[Fe(bim-R)₂]**$(PF_6)_2$. Rather, rapid deactivation of the ^{3}MLCT state occurs (Figure 5.2.3).

The energy of the lowest excited ^{3}MLCT state is 2.447 eV according to literature.[116] The lowest excited triplet states of the chromophores have been calculated by quantum chemical calculations by the research group of Prof. Dr. Oliver Kühn to be 4.1789 eV (^{3}phen), 2.9746 eV (^{3}naph), 2.3340 eV (^{3}pyr), 2.0319 eV (^{3}ant) and 1.7391 eV (^{3}per). Literature values from spectroscopic experiments reveal triplet chromophore energies of 3.66 eV (^{3}phen), 2.64 eV (^{3}naph), 2.09 eV (^{3}pyr), 1.85 eV (^{3}ant) and 1.52 eV (^{3}per).[115] In both cases – according to quantum chemical calculations and according to spectroscopic experiments – the ^{3}MLCT and the ^{3}Chrom states are most isoenergetic in **[Fe(bim-2)₂]**$(PF_6)_2$ and in **[Fe(bim-4)₂]**$(PF_6)_2$ in the class of **[Fe(bim-R)₂]**$(PF_6)_2$ complexes. Nevertheless, those complexes do not show more prolonged lifetimes than the other **[Fe(bim-R)₂]**$(PF_6)_2$ complexes.

Summarizing, these results indicate the absence of observable ISC from the ^{1}Chrom to the ^{3}Chrom state due to the spin-orbit coupling imposed by iron(II) in **[Fe(bim-R)$_2$]**$(PF_6)_2$ (Figure 5.2.3). Accordingly, the triplet chromophore state cannot act as reservoir for emission originating from the ^{3}MLCT state. Instead, emission can only be observed from the states that are dominated by the singlet chromophore states, which are quenched by internal conversion into the ^{1}MLCT states in **[Fe(bim-R)$_2$]**$(PF_6)_2$. Although the discussed iron(II) complexes are indeed luminescent, the emission properties result from a metal-modified emission from the organic chromophore. It has to be emphasized that the separation between the **[Fe(bim)$_2$]**$(PF_6)_2$ core complex and the chromophore constituents in the discussion and in the graphic representation of the result (like in Figure 5.2.3) is somewhat artificial and used for better clarity and comparison with Ru-based work. The involved chromophore transitions are likely to be delocalized onto the bim ligand (CT type) such that a strict separation does not reflect reality. High energy irradiation causes an excitation of the appended chromophore connected to the NHC-pyridine ligand directly populating the singlet state of the chromophore. Intersystem crossing into the low-lying chromophore localized triplet state does not occur to a significant observable extent. Instead, either fluorescence or an internal conversion (FRET type) from the chromophore-dominated ligand states to the ^{1}MLCT state occurs. The ^{1}MLCT state undergoes fast ISC into the ^{3}MLCT state as deduced from the fs-TA data. In contrast to chromophore-functionalized ruthenium(II)-polypyridine complexes, no reservoir effect, allowing for a ^{3}MLCT ⇌ ^{3}Chrom equilibrium resulting in long-lived MLCT states is observed here. Two reasons might be speculated for this observation: on the one hand, the mismatch between the ^{3}MLCT and ^{3}Chrom state energies for the substituents; on the other hand, the very short lifetime of the ^{3}MLCT state precluding back-IC to chromophore-dominated triplet states.

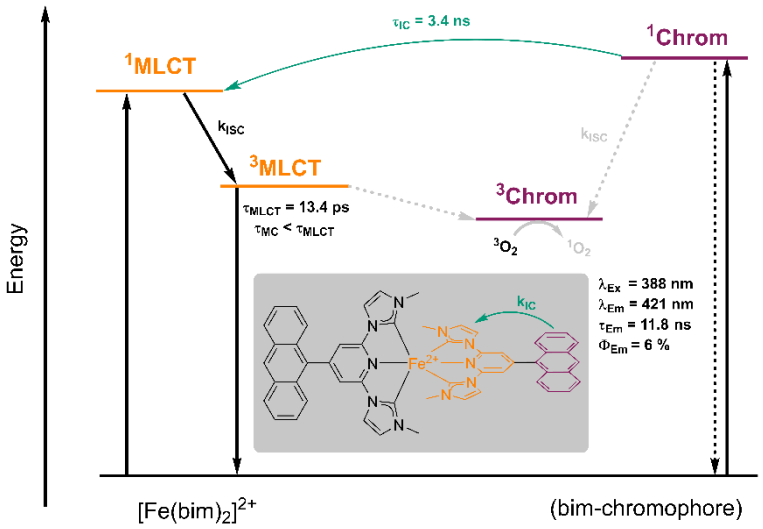

*Figure 5.2.3: Schematic representation of excited-state dynamics in **[Fe(bim-3)$_2$]**$(PF_6)_2$ as example. ^{3}MLCT lifetime as seen by transient absorption spectroscopy (black arrow). ^{1}Chrom lifetime and IC time as deduced from streak camera measurements (black dotted/green arrow). ^{3}Chrom is not effectively populated by ^{1}Chrom or ^{3}MLCT state according to $^1O_2$ experiments (gray dotted arrows). The nomenclature ^{3}Chrom indicates a chromophore-dominated electronic state within the bim-chromophore ligand assembly.*

Photophysics of acetylene-linked molecules

The idea of the preparation of the acetylene-linked complex **[Fe(bim-ac-3)$_2$]**$(PF_6)_2$ is to earn more information about the proposed FRET in **[Fe(bim-R)$_2$]**$(PF_6)_2$ type complexes. The efficiency of the FRET (η_{FRET}) is very high, if the distance between the energy donor and the energy acceptor is very small and gets weaker with an increased distance. The efficiency is calculated by the fraction of the emission quantum yield of the donor acceptor pair (ϕ_{DA}) and the quantum yield of the donor itself (ϕ_D) or by the fraction of the emission lifetime of the donor acceptor pair (τ_{DA}) and the emission quantum yield of the donor itself (τ_D), respectively. In the case of the multichromophoric approach the donor is the pro-ligand and the donor acceptor pair is the complex (eq. 5.1).[109,117,105]

$$\eta_{FRET} = 1 - \frac{\Phi_{DA}}{\Phi_D} = 1 - \frac{\tau_{DA}}{\tau_D} \quad (5.1)$$

In the complex **[Fe(bim-ac-3)$_2$]**$(PF_6)_2$, the distance between the between the chromophore and the metal center is increased, which should decrease η_{FRET}. The fraction of ϕ_{DA} and ϕ_D should increase as well as the fraction of τ_{DA} and τ_D. This unique possibility to gain insights into the intramolecular excited state dynamics in this class of complexes makes **[Fe(bim-ac-3)$_2$]**$(PF_6)_2$ a very interesting compound.

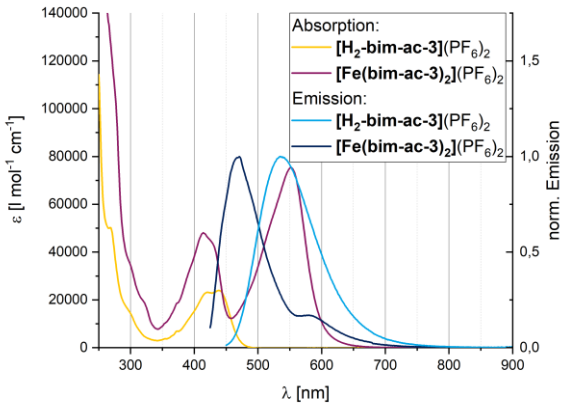

*Figure 5.2.4: Steady state absorption and emission spectroscopy of **[H$_2$-bim-ac-3]**$(PF_6)_2$ pro-ligand and **[Fe(bim-ac-3)$_2$]**$(PF_6)_2$ complex.*

The ground state absorption spectra of **[H$_2$-bim-ac-3]**$(PF_6)_2$ and **[Fe(bim-ac-3)$_2$]**$(PF_6)_2$ differ distinctly from those of the analogous pro-ligand **[H$_2$-bim-3]**$(PF_6)_2$ and **[Fe(bim-3)$_2$]**$(PF_6)_2$ without an acetylene linker (Figure 5.2.4). In **[H$_2$-bim-ac-3]**$(PF_6)_2$ π-π*-transitions show two absorption maxima at 439 nm (23 900 M^{-1} cm^{-1}) and 417 nm (22 700 M^{-1} cm^{-1}), which is red-shifted and shows stronger extinction in comparison to the absorption of free anthracene and **[H$_2$-bim-3]**$(PF_6)_2$. This bathochromic shift can be explained by the enlargement of the π-system by the introduction of the acetylene linker. In **[Fe(bim-ac-3)$_2$]**$(PF_6)_2$ the π-π*-transitions can be found at similar energies (417 nm; 48 200 M^{-1} cm^{-1}). The MLCT absorption is at 554 nm (74 100 M^{-1} cm^{-1}), which is also drastically red-shifted and stronger in extinction in comparison to the data of the complex without acetylene linker.[36] This is also explained by the enlargement of the π-system and is in line with quantum chemical calculations performed by Francés-Monerris *et al.* who predict a large bathochromic shift and a stronger extinction in the heteroleptic complex **Fe2**, as discussed in the introduction.[69] A distinct photophysical analysis of the excited state dynamics and the following possibility to discuss the influence on the FRET is still in progress.

5.3 Photophysics of $[Fe(bbp\text{-}R)_2](PF_6)_2$ complexes

Simplified, the absorption spectra of **[Fe(bbp-R)$_2$]**$(PF_6)_2$ complexes consist of three distinct spectral regions (Figure 5.3.1, left panel). The intense bands at wavelengths shorter than 300 nm correspond to π-π* transitions within the bbp moieties in the ligands with some transitions within the chromophore moieties and intrachromophore transitions.[103,36,39,102] In the range of 300-420 nm π-π* transitions of the organic chromophores in the backbone of the ligands containing several intrachromophore transitions as well as MLCT transitions can be found. The anthracenyl derivatives **[H$_2$-bbp-3]**$(PF_6)_2$ and **[Fe(bbp-3)$_2$]**$(PF_6)_2$ show the typical vibrational fine structure of anthracene.[105] At longer wavelengths, MLCT transitions appear for all complexes. This is indicated by electrochemical experiments and optical ground state spectra of the ligands, which do not show the specific MLCT absorption feature. The bands are clearly red-shifted for the bichromophoric complexes compared to **[Fe(bbp)$_2$]**$(PF_6)_2$ and is in line with the electrochemical data discussed before. The absorption bands and intensities shift from 444 nm (13 200 cm^{-1} M^{-1}) in **[Fe(bbp)$_2$]**$(PF_6)_2$ to a range of 459 nm (20 200 cm^{-1} M^{-1}) in **[Fe(bbp-3)$_2$]**$(PF_6)_2$ to 478 nm (53 500 cm^{-1} M^{-1}) in **[Fe(bbp-5)$_2$]**$(PF_6)_2$ within the bichromophoric complexes. The HOMO and HOMO-1 levels are quite close in energy for **[Fe(bbp-3)$_2$]**$(PF_6)_2$, **[Fe(bbp-4)$_2$]**$(PF_6)_2$ and **[Fe(bbp-5)$_2$]**$(PF_6)_2$ as predicted by quantum chemical calculations by the group of Prof. Dr. Oliver Kühn. Those predict the HOMOs to be located at the chromophores. This HOMO-Inversion is not realized according to optical ground state spectra and electrochemical experiments.

Cyclic voltammograms of **[Fe(bbp-R)$_2$]**$(PF_6)_2$ complexes show no distinct trend in the shift of the fully reversible Fe^{II}/Fe^{III} oxidation potentials going from **[Fe(bbp)$_2$]**$(PF_6)_2$ (0.62 V vs. FcH/FcH^+) to potentials between **[Fe(bbp-1)$_2$]**$(PF_6)_2$ (0.59 V) and **[Fe(bbp-4)$_2$]**$(PF_6)_2$ (0.64 V), indicating a similar energy of the highest occupied metal centered d-orbitals in each complex (Figure 5.3.1, right panel). This finding is in line with the TD-DFT calculations, giving similar d_π(Fe) energies for each complex.

Irreversible oxidations can be found at anodic potentials for the bichromophoric complexes that are assigned to the oxidation of the organic chromophores.[36] The chromophore oxidation potential decreases with an increasing size of the ring starting at 1.98 V in **[Fe(bbp-1)$_2$]**$(PF_6)_2$ ending at 0.75 V in **[Fe(bbp-5)$_2$]**$(PF_6)_2$. This is indicating a shift of the chromophore-based π-levels closer to the metal-centered t_{2g}-levels and make them energetically better aligned, causing an increase in the t_{2g}-π-mixing. This might result in multiple mixed MLCT/ILCT transition and in strong increase and red shift in the absorption spectra. These findings are not completely in line with the findings of the TD-DFT calculations. In TD-DFT calculations the d_π(Fe) energies of **[Fe(bbp)$_2$]**$(PF_6)_2$, **[Fe(bbp-1)$_2$]**$(PF_6)_2$ and **[Fe(bbp-2)$_2$]**$(PF_6)_2$ are higher in energy than the highest occupied chromophore-based orbitals. This energy ordering is confirmed by electrochemical experiments. In TD-DFT calculations the d_π(Fe) energies are lower in energy than the highest occupied chromophore-based orbitals in **[Fe(bbp-3)$_2$]**$(PF_6)_2$, **[Fe(bbp-4)$_2$]**$(PF_6)_2$ and **[Fe(bbp-5)$_2$]**$(PF_6)_2$. This inversion of d_π(Fe)-HOMOs to chromophore-based-HOMOs found in TD-DFT calculations for **[Fe(bbp-3)$_2$]**$(PF_6)_2$, **[Fe(bbp-4)$_2$]**$(PF_6)_2$ and **[Fe(bbp-5)$_2$]**$(PF_6)_2$ cannot be found in electrochemical experiments. At this point TD-DFT calculations and electrochemical data are contradicting. The similarity in energy of the highest occupied d_π(Fe)- and chromophore-based-orbitals found in

electrochemical experiments as well as in TD-DFT calculations might result in multiple mixed MLCT/ILCT transition and in strong increase and red shift in the absorption spectra.[118]

At cathodic potentials irreversible ligand-based reductions occur, which are assigned to the bbp moiety in each ligand. **[Fe(bbp)$_2$]**$(PF_6)_2$ is reduced irreversibly at -2.18 V, while the bichromophoric complexes are reduced between -2.04 V in **[Fe(bbp-2)$_2$]**$(PF_6)_2$ and -1.80 V in **[Fe(bbp-5)$_2$]**$(PF_6)_2$. These values are in accordance with the estimated electron-accepting properties of the ligand with extended π-systems and the lower energies of their π*-levels in comparison to **[H$_2$-bbp]**$(PF_6)_2$.[36] The resulting electrochemical energy gap ΔE_p roughly correlates to the optical energy gap ΔE_o (Table 5.3.1). The values indicate the lowest energy absorptions to be MLCT transitions.

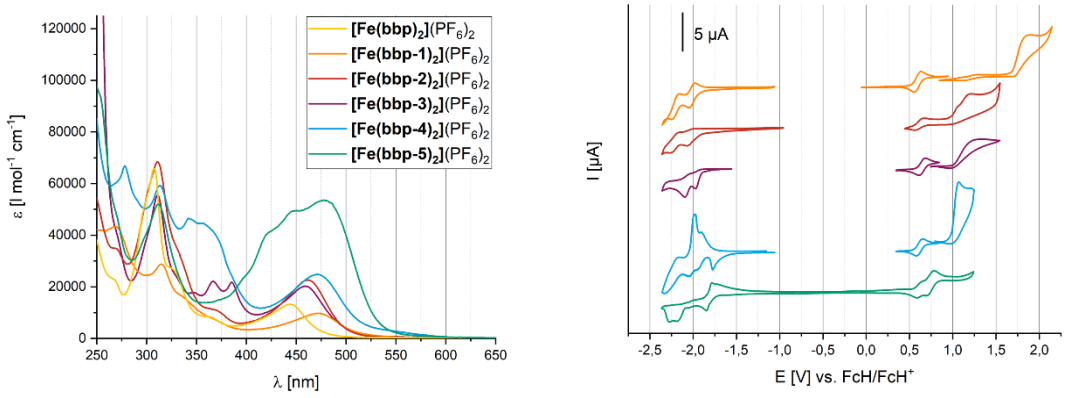

*Figure 5.3.1: Optical absorption and emission spectroscopy data (left panel) and cyclic voltammograms (right panel) of **[Fe(bbp-R)$_2$]**$(PF_6)_2$ complexes.*

*Table 5.3.1: Photo- and electrochemical properties of **[Fe(bbp-R)$_2$]**$(PF_6)_2$ complexes.*

Compound	λ_{MLCT} [nm] (ε [M^{-1} cm^{-1}])	CV [V vs. FcH/FcH$^+$]	ΔE_p (eV)	ΔE_o (eV)
[Fe(bbp)$_2$]$(PF_6)_2$	444 (13 200)	0.62 (rev.) -2.18 (irrev.)	2.80	2.79
[Fe(bbp-1)$_2$]$(PF_6)_2$	473 (9 700)	1.98 (irrev.) 0.59 (rev.) -2.01 (irrev.)	2.60	2.62
[Fe(bbp-2)$_2$]$(PF_6)_2$	461 (22 700)	1.12 (irrev.) 0.61 (rev.) -2.04 (irrev.)	2.65	2.69
[Fe(bbp-3)$_2$]$(PF_6)_2$	459 (20 200)	1.06 (irrev.) 0.62 (rev.) -2.01 (irrev.)	2.63	2.70
[Fe(bbp-4)$_2$]$(PF_6)_2$	471 (24 900)	1.06 (irrev.) 0.64 (rev.) -1.97 (irrev.)	2.61	2.63
[Fe(bbp-5)$_2$]$(PF_6)_2$	478 (53 500)	0.75 (irrev.) 0.61 (rev.) -1.80 (irrev.)	2.42	2.59

In contrast to **[Fe(bim-R)$_2$]**$(PF_6)_2$ type complexes, the **[Fe(bbp-R)$_2$]**$(PF_6)_2$ type complexes are only weak emissive at room temperature as well as at 77 K (Figure 5.3.2, bottom panel). For this reason, it is not possible to give any lifetime or interpretation regarding the "antenna effect" as discussed for **[Fe(bim-R)$_2$]**$(PF_6)_2$ type complexes.

Photochemically relevant MLCT states in the iron complexes are inaccessible by luminescence spectroscopy as they are non-luminescent neither at room temperature nor at 77 K. Therefore, femtosecond (fs)-TA measurements were used to track the early excited state dynamics of the iron(II) complexes (Figure 5.3.2, top left and right panel, Table 5.3.2). The transient spectra of the various complexes exhibit a very similar behavior. After optical excitation at 490 nm, intense negative signals are detected in a range from 415-505 nm that are caused by ground state bleach (GSB). The GSB mirrors nearly perfectly the ground state MLCT absorption. Positive bands are visible above 505 nm, corresponding to an ESA. A second ESA band below 415 nm is indicated with a maximum at about 390 nm for each complex. In general, two components are found, one with a short time constant of a few picoseconds and a dominant one with a decay time of about 20 ps. A very similar behavior was found by Haacke and Gros *et al*. for iron(II) complexes with benzimidazole-2-ylidene-based ligands.[46,106] They observed dynamics, which they also characterized by two time constants. The short component was assigned to the relaxation of a hot ^{3}MLCT state, directly populated by an ultrafast intersystem crossing from the ^{1}MLCT state into the ^{3}MLCT state. The second one varying between 19 and 23 ps was attributed to the ^{3}MLCT lifetime.[119] In the present case, the short time constant varies between 1.5 and 2.0 ps depending on the complex, which seems to be too long for ultrafast intersystem crossing from the ^{1}MLCT to the ^{3}MLCT state. Probably this component is due to vibrational redistribution and cooling which is often reported to occur on the picosecond time scale[120] representing the relaxation of a hot ^{3}MLCT state.[46] The assignment is supported by the shape of the corresponding DAS. They correlate with the slope of the DAS of the second component and have minima and maxima where this slope is particularly steep. This behavior reflects a blueshift of the transient spectra during the first picoseconds, which is expected in the case of vibrational relaxation processes.

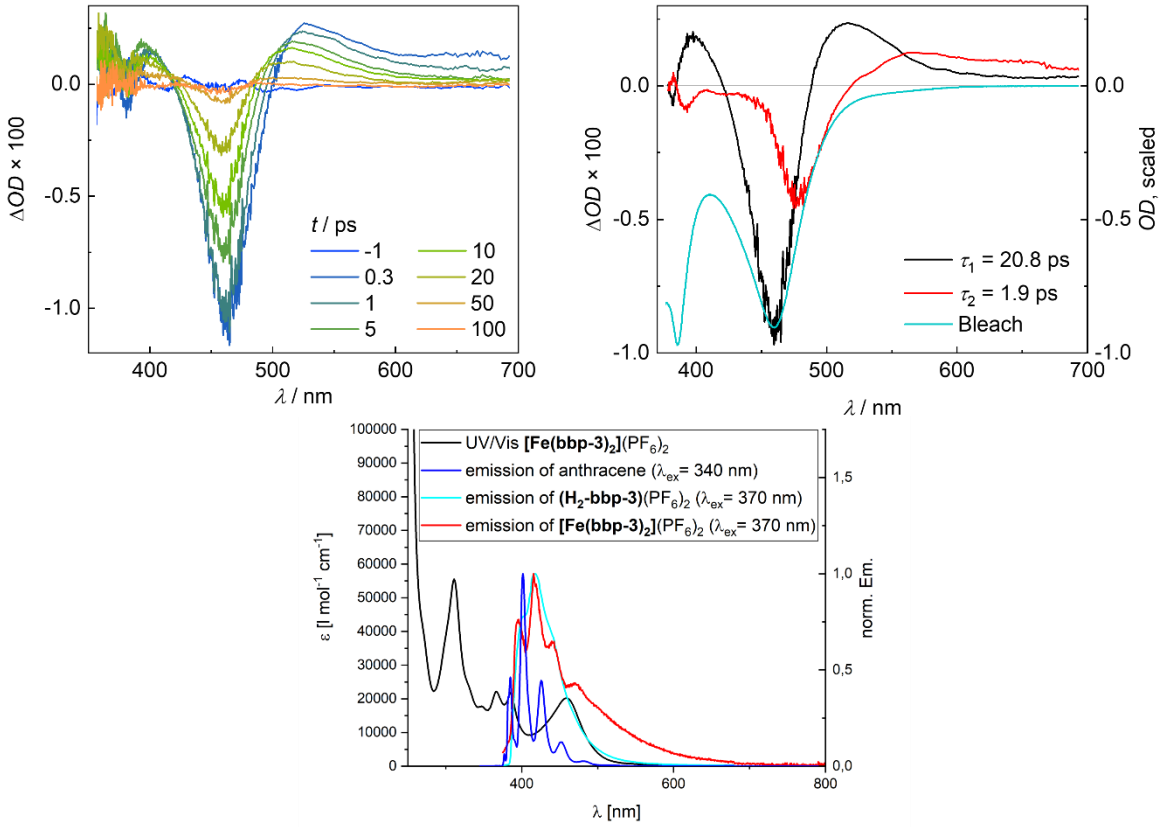

Figure 5.3.2: absorption (top left panel) and decay associated spectra (top right panel) of ***[Fe(bbp-3)$_2$]***$(PF_6)_2$ *and emission of anthracene,* ***[H$_2$-bbp-3]***$(PF_6)_2$ *and* ***[Fe(bbp-3)$_2$]***$(PF_6)_2$ *at 77 K (bottom panel).*

Table 5.3.2: Excited state properties of ***[Fe(bbp-R)$_2$]***$(PF_6)_2$ *complexes.*

Compound	τ_1 [ps]	τ_2 [ps]	$\lambda_{Em,\ Chromophore}$ [nm]	$\lambda_{Em,\ Complex}$ [nm]	$\lambda_{Em,Pro\text{-}ligand}$ [nm]
[Fe(bbp)$_2$]$(PF_6)_2$	16.4[46]	0.2[46]	-	-	-
[Fe(bbp-1)$_2$]$(PF_6)_2$	21.6	1.5	276 (358)	297 (405)	322 (450)
[Fe(bbp-2)$_2$]$(PF_6)_2$	19.6	1.6	320	403	367
[Fe(bbp-3)$_2$]$(PF_6)_2$	20.8	1.9	402	416	417
[Fe(bbp-4)$_2$]$(PF_6)_2$	20.1	1.9	371	403	410
[Fe(bbp-5)$_2$]$(PF_6)_2$	23.0	2.0	442 (469) (500)	463 (494) (531)	473 (500) (535)

Calculation of the triplet energies gave a value of 1.1416 eV for the lowest excited triplet state in **[Fe(bbp)$_2$]**$(PF_6)_2$, which has MC character. The energy of the lowest excited ^{3}MLCT state is 2.2460 eV. The lowest excited triplet states of the chromophores have been calculated to be 4.1789 eV (^{3}phen), 2.9746 eV (^{3}naph), 2.3340 eV (^{3}pyr), 2.0319 eV (^{3}ant) and 1.7391 eV (^{3}per). For reasons of comparability the triplet states have been calculated using the same methods and basis sets.

The two complexes with the most isoenergetic ^{3}MLCT and triplet chromophore states are **[Fe(bbp-4)$_2$]**$(PF_6)_2$ and **[Fe(bbp-3)$_2$]**$(PF_6)_2$. The triplet energy of pyrene is 0.0980 eV higher than the ^{3}MLCT of **[Fe(bbp)$_2$]**$(PF_6)_2$. The triplet energy of anthracene is 0.2141 eV lower than the ^{3}MLCT of **[Fe(bbp)$_2$]**$(PF_6)_2$. Thermal energy at room temperature approximately values $k_BT \approx 0.025$ eV,

which gives a hint to the energy match between the triplet energies that should be received. Experimental reports by Castellano *et al*. covering Re(I) complexes bearing a naphthalimide-backbone-chromophores gave an achievement of a reservoir effect even with a triplet energy of the chromophore 0.3472 eV lower than the ^{3}MLCT energy of the corresponding Re(I) complex.[65,64] The findings by Castellano *et al*. clearly indicate that a slight mismatch between the triplet energies – even if the triplet energy of the chromophore is below the ^{3}MLCT state – is suitable for the achievement of a reservoir effect. This indicates the possibility to find a reservoir effect at least in **[Fe(bbp-3)$_2$]**$(PF_6)_2$.

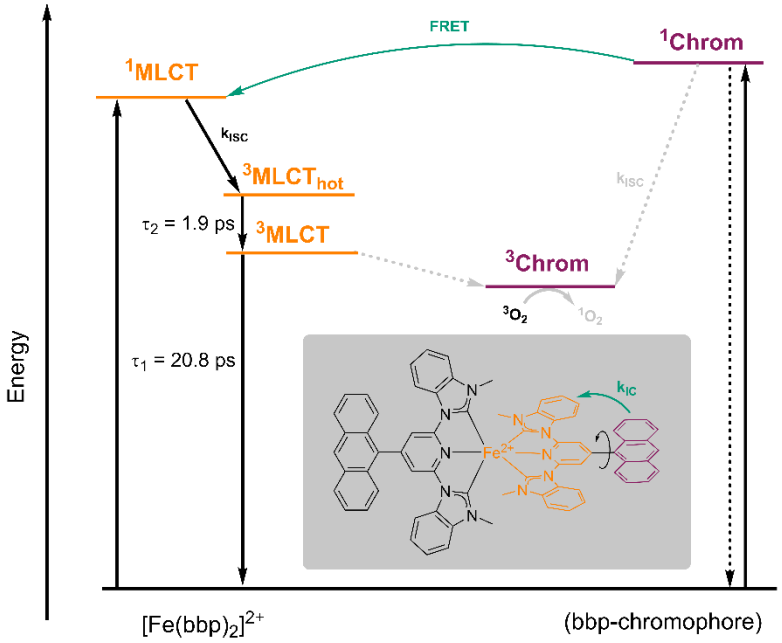

*Figure 5.3.3: Schematic representation of excited-state dynamics in **[Fe(bbp-3)$_2$]**$(PF_6)_2$ as example. ^{3}MLCT lifetime as seen by transient absorption spectroscopy (black arrow). ^{1}Chrom lifetime and FRET time could not be deduced by streak camera measurements due to weak emission (black dotted/green arrow). ^{3}Chrom is not effectively populated by ^{1}Chrom or ^{3}MLCT state according to $^1O_2$ experiments (gray dotted arrows). The nomenclature ^{3}Chrom indicates a chromophore-dominated electronic state within the bbp-chromophore ligand assembly.*

In general, the chromophores discussed in this section cover a large variety of triplet energies and therefore allows to discuss the impact of nearly isoenergetic triplet states and the possibility to reach a reservoir effect. Furthermore, the impact of chromophores having clearly higher (^{3}phen and ^{3}naph) or lower (^{3}per) triplet energies than the ^{3}MLCT of **[Fe(bbp)$_2$]**$(PF_6)_2$ can be discussed.

Summarizing, a reservoir effect could not be observed in one of the complexes (Figure 5.3.3). This is expected for **[Fe(bbp-1)$_2$]**$(PF_6)_2$ and **[Fe(bbp-2)$_2$]**$(PF_6)_2$ as the triplet chromophore energy is significantly higher than the ^{3}MLCT energy. But also, in **[Fe(bbp-2)$_2$]**$(PF_6)_2$, **[Fe(bbp-4)$_2$]**$(PF_6)_2$ and **[Fe(bbp-5)$_2$]**$(PF_6)_2$ no population of the triplet chromophore states is observed, although these states are nearly isoenergetic or lower in energy than the ^{3}MLCT states. The absence of long-lived spectroscopically inaccessible states was probed by NIR-$^1O_2$-phosphoresence. Accordingly, no reservoir for MLCT states exists.

With this series of complexes, the absorption properties can be turned and the MLCT absorption maximum is shifted towards the red part of the spectrum. While converging a HOMO inversion the extinction can drastically be optimized[118], which is promising for following catalytic applications, as well as increased MLCT lifetimes. Still no reservoir effect is achieved, although the energy match at least between ^{3}MLCT and ^{3}pyrene/^{3}anthracene should be sufficient for electron transfer and back transfer. Nevertheless, an increase of the MLCT lifetimes is achieved. What remains open is the role of the spin-orbit coupling via the heavy atom effect imposed by iron, which can be addressed by the investigation of analogous ruthenium complexes in one of the following sections.

5.4 Photophysics of [Fe(btp-R)$_2$](PF$_6$)$_2$ complexes

In the optical absorption spectra of **[Fe(btp)$_2$]**(PF$_6$)$_2$ and **[Fe(btp-3)$_2$]**(PF$_6$)$_2$ the intense bands below 340 nm are dominated by ligand π-π*-transitions (Figure 5.4.1, left panel and Table 5.4.1). In **[Fe(btp-3)$_2$]**(PF$_6$)$_2$ and the corresponding **btp-3** ligand the typical vibronic fine structure of the anthracene backbone is detected in the range of 340-400 nm. **[Fe(btp)$_2$]**(PF$_6$)$_2$ exhibits a sharp absorption maximum at 444 nm (11 500 M^{-1} cm^{-1}) with an additional shoulder at higher energies. These features are assigned to MLCT transitions with some admixture of MC character, which is also known for **[Fe(tpy)$_2$]**(PF$_6$)$_2$.[103] In **[Fe(btp-3)$_2$]**(PF$_6$)$_2$ the MLCT absorption maximum in the visible is shifted to 456 nm (14 700 M^{-1} cm^{-1}). These findings are supported by TD-DFT calculations, which are not discussed in further detail in this work.[94] This red-shift and the increase of the extinction **[Fe(btp-3)$_2$]**(PF$_6$)$_2$ can be explained by improved π-acceptor properties. The MC-character admixture as described for **[Fe(btp)$_2$]**(PF$_6$)$_2$ cannot be separately detected in **[Fe(btp-3)$_2$]**(PF$_6$)$_2$ as it is overlapping with the anthracene absorption.

The cyclic voltammogram of **[Fe(btp)$_2$]**(PF$_6$)$_2$ shows a reversible wave at 0.74 V (vs. FcH/FcH$^+$), which is assigned to the $Fe^{III/II}$ couple (Figure 5.4.1, right panel and Table 5.4.1).[36,103] The shift to more anodic potentials compared to **[Fe(tpy)$_2$]**(PF$_6$)$_2$ (0.72 V) indicates a slightly reduced HOMO energy. The HOMO in **[Fe(btp)$_2$]**(PF$_6$)$_2$ has a distinct d_π(Fe) character. This points to similar π-acceptability of **btp** in comparison to **tpy**. At cathodic potentials, two reversible reductions at -1.79 V and -2.11 V are detected. In analogy to **[Fe(tpy)$_2$]**(PF$_6$)$_2$, they are assigned to a stepwise reduction of the two ligands. In **[Fe(btp-3)$_2$]**(PF$_6$)$_2$ the reversible $Fe^{III/II}$ couple is at an anodic potential of 0.76 V. At more anodic potentials the partially irreversible oxidation of anthracene (1.05 V) is detected. At cathodic potentials to reductions at -1.77 V and -2.00 V are observed, which are not fully reversible. In analogy to **[Fe(btp)$_2$]**(PF$_6$)$_2$ and **[Fe(tpy)$_2$]**(PF$_6$)$_2$ these reductions are assigned to a stepwise reduction of the two ligands. The electrochemical band gaps are in line with the absorption maximum in the MLCT region for both complexes. These findings point to a very similar electrochemical behavior of the two complexes **[Fe(btp)$_2$]**(PF$_6$)$_2$ and **[Fe(btp-3)$_2$]**(PF$_6$)$_2$.

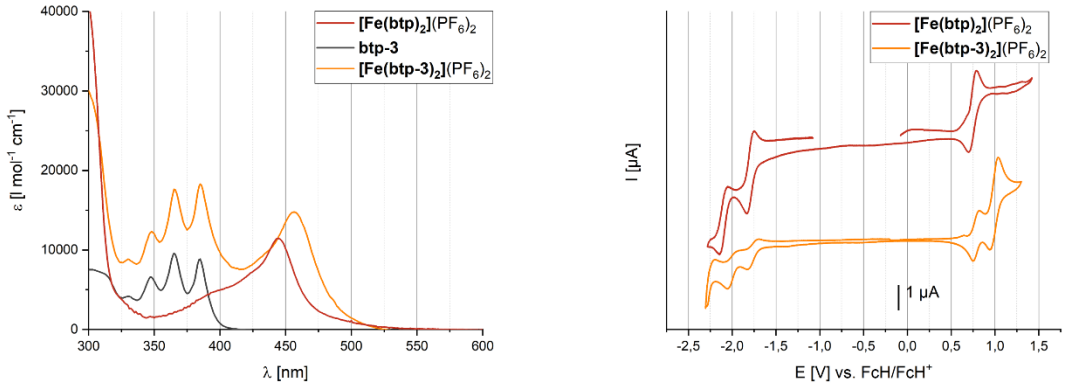

*Figure 5.4.1: Optical absorption spectroscopy data of **[Fe(btp)$_2$]**(PF$_6$)$_2$, **btp-3** and **[Fe(btp-3)$_2$]**(PF$_6$)$_2$ (left panel) and cyclic voltammograms of **[Fe(btp)$_2$]**(PF$_6$)$_2$ and **[Fe(btp-3)$_2$]**(PF$_6$)$_2$ (right panel).*

Non emissive states are probed by ultrafast pump-probe spectroscopy (Figure 5.4.2, left panel). For **[Fe(btp)$_2$]**(PF$_6$)$_2$ a step-like absorption change at time zero is observed, which persists beyond the experimental time window of 1.6 ns. The TA spectra reflect the GSB but deviate significantly

from what is expected for a populated charge transfer state. Beside the dominant GSB signature, ESA should be detected, which is missing in the TA spectra of **[Fe(btp)$_2$]**$(PF_6)_2$. This and the very long lifetime of the TA signal indicate that excitation of **[Fe(btp)$_2$]**$(PF_6)_2$ in the MLCT absorption results in an ultrafast population of a ligand field MC state (Figure 5.4.2, right panel). Similar findings relate to $^{3/5}$MC → ^{1}GS ground state recovery were also reported for other $[FeN_6]^{2+}$ complexes.[38,121] For **[Fe(btp-3)$_2$]**$(PF_6)_2$ TA experiments are still under investigation. From the findings of **[Fe(btp)$_2$]**$(PF_6)_2$ and the multichromophoric **[Fe(tpy-R$_2$]**$(PF_6)_2$ complexes, it is expected that **[Fe(btp-3)$_2$]**$(PF_6)_2$ also has a quite long $^{3/5}$MC lifetime.

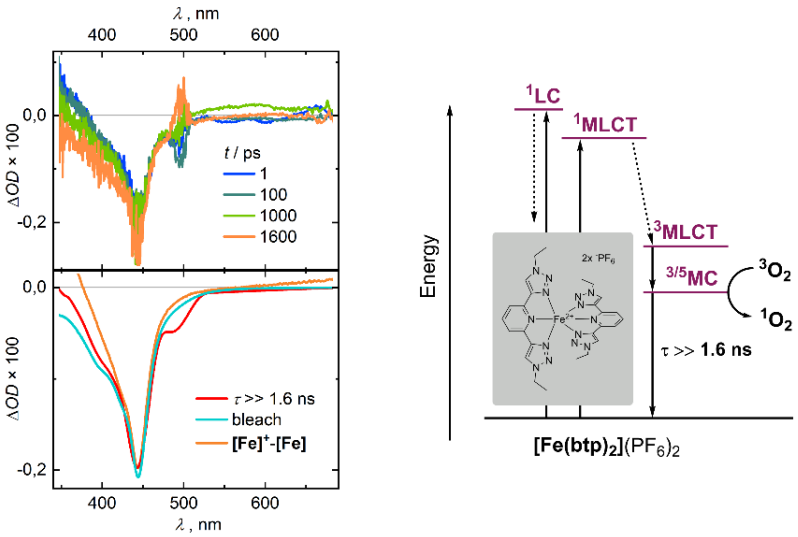

*Figure 5.4.2: Transient absorption and decay associated spectra including results of spectroelectrochemical experiments **[Fe]$^+$-[Fe]** (left panel) and schematic representation of excited-state dynamics in **[Fe(btp)$_2$]**$(PF_6)_2$ (right panel).*

After excitation in the π-π* transitions emission is observed in the ligands **btp** and **btp-3** as well as the complexes **[Fe(btp)$_2$]**$(PF_6)_2$ and **[Fe(btp-3)$_2$]**$(PF_6)_2$. In **btp** and **[Fe(btp)$_2$]**$(PF_6)_2$ emission with λ_{em} = 334 nm is observed after excitation at λ_{ex} = 295 nm. The emission lifetime in the complex is 2.9 ns as determined by TCSPC.[94] In **[Fe(btp)$_2$]**$(PF_6)_2$ the emission was found to be sensitive against oxygen and $^1O_2$-phophorescence was observed after excitation with λ_{ex} = 295 nm. This behavior makes **[Fe(btp)$_2$]**$(PF_6)_2$ a very promising candidate as a photosensitizer in oxidation reactions, which is discussed in Section 6.2 in more detail.

*Table 5.4.1: Ground and excited state properties of **[Fe(btp)$_2$]**$(PF_6)_2$, **btp-3** and **[Fe(btp-3)$_2$]**$(PF_6)_2$.[a] MC lifetime of **[Fe(btp-3)$_2$]**$(PF_6)_2$ has not been determined yet.*

Compound	λ_{MLCT} [nm] (ε [M^{-1} cm^{-1}])	CV [V vs. FcH/FcH$^+$]	λ_{Em} [nm]	τ_{Em} [ns]	τ_{MC} [ns]
[Fe(btp)$_2$]$(PF_6)_2$	444 (11 500)	0.74 (rev.) -1.79 (rev.) -2.11 (rev.)	334	2.9	> 1.6
btp-3	-	-	420	5.0	-
[Fe(btp-3)$_2$]$(PF_6)_2$	456 (14 700)	1.06 (irrev.) 0.76 (rev.) -1.77 (irrev.) -2.00 (irrev.)	420	6.7	-[a]

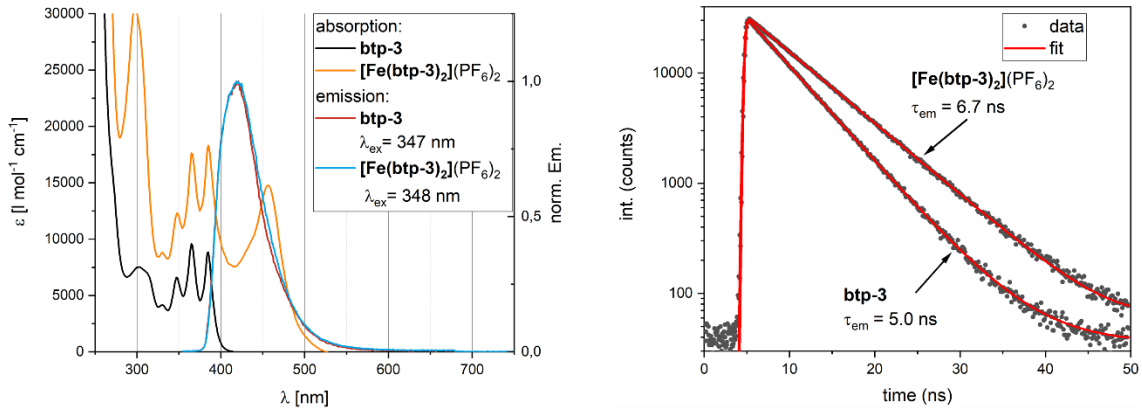

*Figure 5.4.3: Steady state emission spectroscopy (left panel) and time streak camera measurements (right panel) of **btp-3** and **[Fe(btp-3)$_2$]**$(PF_6)_2$.*

In **btp-3** and **[Fe(btp-3)$_2$]**$(PF_6)_2$ emission with λ_{em} = 420 nm after excitation with λ_{ex} = 348 nm. The lifetime of the ligand emission was found to be τ_{em}(**btp-3**) = 5.0 ns and τ_{em}(**[Fe(btp-3)$_2$]**$(PF_6)_2$) = 6.7 ns as determined by streak camera measurements (Figure 5.4.3). In **btp** and **[Fe(btp-3)$_2$]**$(PF_6)_2$ the emissive state is the ^{1}anthracene state, as deduced from excitation spectra.

5.5 Photophysics of [Fe(tri-R)$_2$](PF$_6$)$_2$ complexes

The optical absorption spectra of **[Fe(tri)$_2$]**(PF$_6$)$_2$ and **[Fe(tri-3)$_2$]**(PF$_6$)$_2$ show a very similar behavior as the previously described multichromophoric complexes (Figure 5.5.1, left panel and Table 5.5.1). Both complexes show intense bands below 340 nm, which are dominated by ligand π-π*-transitions. **[Fe(tri)$_2$]**(PF$_6$)$_2$ shows a more red-shifted MLCT absorption than the previously described complexes with a maximum at 593 nm (21 000 M^{-1} cm^{-1}). A second maximum at 411 nm (11 200) also has a predominant MLCT character as deducted from quantum chemical calculations. The lowest energy MLCT transition in **[Fe(tri-3)$_2$]**(PF$_6$)$_2$ is found at 607 nm (23 500), while the MLCT transition with higher energy is overlapping with the vibronic fine structure of anthracene in the range of 340 – 400 nm. In **[Fe(tri)$_2$]**(PF$_6$)$_2$ the lowest adiabatic triplet state has MC character with an energy of 1.62 eV. The excitation from the ground state to the lowest triplet state is accompanied by an elongation of the central Fe-N bond by 0.28 Å, which is forcing a rearrangement of the ligand shell after photoexcitation. The lowest ^{3}MLCT state has an energy of 1.88 eV according to quantum chemical calculations.[94]

The $Fe^{III/II}$ couple in **[Fe(tri)$_2$]**(PF$_6$)$_2$ is found at a low cathodic potential of -0.15 V (vs. FcH/FcH$^+$) (Figure 5.5.1, right panel and Table 5.5.1). This significant shift in comparison to **[Fe(bim)$_2$]**(PF$_6$)$_2$ (0.34 V) is connected to the MIC coordination and agrees with reported trends.[103] The HOMO has dominating d_π(Fe) character and is destabilized by weaker π-acceptability of the triazolylidenes in comparison to triazoles.[122,48] In comparison to imidazolylidene ligands in **[Fe(bim)$_2$]**(PF$_6$)$_2$, the triazolylidene ligands in **[Fe(tri)$_2$]**(PF$_6$)$_2$ might have a better π-acceptability, as the two irreversible reduction steps of the ligands occur at potentials of -1.91 V and -2.15 V. In **[Fe(tri-3)$_2$]**(PF$_6$)$_2$ the reversible $Fe^{III/II}$ couple is found at -0.05 V and two irreversible ligand reduction steps are found at -2.05 V and -2.24 V. Additionally, the irreversible anthracene oxidation is observed at 1.00 V. The electrochemical band gaps are in line with the absorption maximum in the MLCT region for both complexes.

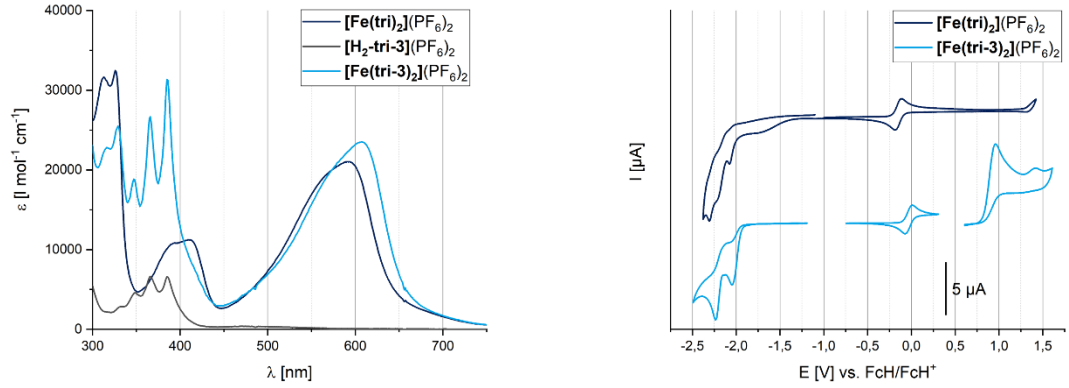

*Figure 5.5.1: Optical absorption spectroscopy data of **[Fe(tri)$_2$]**(PF$_6$)$_2$, **[H$_2$-tri-3]**(PF$_6$)$_2$ and **[Fe(tri-3)$_2$]**(PF$_6$)$_2$ (left panel) and cyclic voltammograms of **[Fe(tri)$_2$]**(PF$_6$)$_2$ and **[Fe(tri-3)$_2$]**(PF$_6$)$_2$ (right panel).*

The TA of **[Fe(tri)$_2$]**(PF$_6$)$_2$ is dominated by GSB causing a strong negative band around 600 nm and a less intense one around 420 nm (Figure 5.5.2, right panel). In addition, two ESA features are observed, one at about 455 nm and another one in the red spectral region. The TA disappears in less than 50 ps with an evolution which has to be described by four exponential decay

components. One component of 5 fs is an artefact at time zero. The component with a time constant of $\tau_1 = 0.1$ ps is slightly red-shifted compared to the longer living contributions, suggesting an ultrafast relaxation like vibrational redistribution or intersystem crossing (ISC). The DAS of the dominating decay component with $\tau_2 = 2.7$ ps and the weaker one with $\tau_3 = 8.7$ ps consist both of the described GSB and ESA features in the blue and red of the GSB, most probably a feature of ^{3}MLCT contributions.[48] This conclusion is supported by the difference spectrum of **[Fe]$^+$-[Fe]**. It reproduces the ESA in the blue at 455 nm and the GSB of the two decay components very well. In contrast, the ESA in the red is only insufficiently reflected. This may result from the fact, that for a more realistic description of the MLCT spectrum the difference spectrum **[Fe]$^+$** + **[Fe]$^-$** - **[Fe]** should be considered[121], which is impossible due to the irreversible ligand reduction.

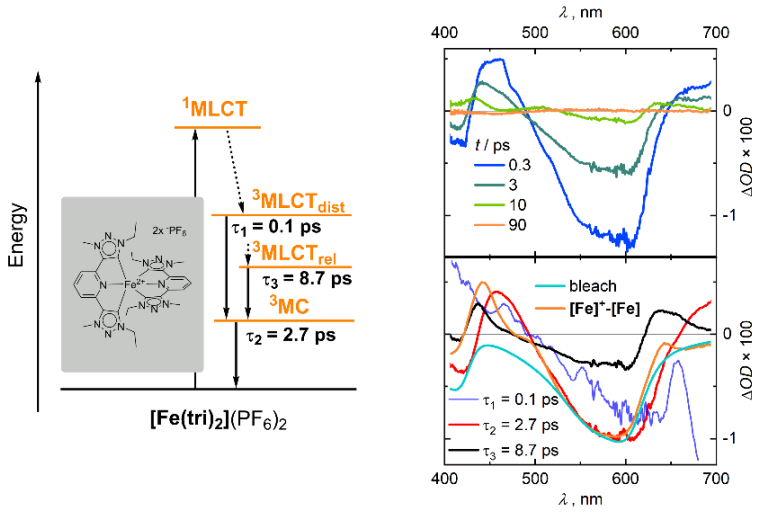

*Figure 5.5.2: Schematic representation of excited-state dynamics in **[Fe(tri)$_2$]**(PF$_6$)$_2$ (left panel) and transient absorption and decay associated spectra including results of spectroelectrochemical experiments **[Fe]$^+$-[Fe]** (right panel).*

Analogous behavior of the TA is observed in **[Fe(btz)$_2$(bpy)]**(PF$_6$)$_2$ and the spectral components were assigned to multiple MLCT states (Figure 5.5.2, left panel).[48] The analysis of data from time-resolved X-Ray spectroscopy on this tris(bidentate) reference associated the time constants to different transitions in a hot branching scenario.[49] Transferred to **[Fe(tri)$_2$]**(PF$_6$)$_2$ this means a vibrationally hot ^{3}MLCT state is populated after photoexcitation by the ultrafast ISC and vibrational redistribution leads within 0.1 ps to a relaxed ^{3}MLCT state. In case of hot branching, the redistribution process competes with a direct channel to the ^{3}MC state in which a large fraction of the population ends up within the first 0.1 ps. The remaining population in the relaxed ^{3}MLCT state decays comparatively slowly (8.7 ps) to the ^{3}MC state, which deactivates more rapidly (2.7 ps) back to the ^{1}GS. This relaxation scenario is supported by the observation that the DAS of both, the 2.7 ps and the 8.7 ps component exhibit a strong GSB contribution. Although it is not in line with the current literature reports on similar complexes, the following second scenario could also explain the reported findings. The ^{3}MLCT state exhibits two parallel relaxation channels one leading directly back to the ^{1}GS and the second one to the ^{3}MC state. Then the 2.7 ps have to be assigned to the lifetime of the ^{3}MLCT state and the 8.7 ps to that of the ^{3}MC state.

Table 5.5.1: Ground and excited state properties of ***[Fe(tri)$_2$]***$(PF_6)_2$ *and* ***[Fe(tri-3)$_2$]***$(PF_6)_2$.[a)] *Transient absorption of* ***[Fe(tri-3)$_2$]***$(PF_6)_2$ *has not been determined yet.*

Compound	λ_{MLCT} [nm] (ε [M^{-1} cm^{-1}])	CV [V vs. FcH/FcH^+]	λ_{Em} [nm]	τ_{TA} [ps]
[Fe(tri)$_2$]$(PF_6)_2$	593 (21 000) 411 (11 500)	-0.15 (rev.) -1.91 (irrev.) -2.15 (irrev.)	-	τ_1 = 0.1 τ_2 = 2.7 τ_3 = 8.7
[Fe(tri-3)$_2$]$(PF_6)_2$	607 (23 500)	1.00 (irrev.) -0.05 (rev.) -2.05 (irrev.) -2.24 (irrev.)	582	-[a)]

As **[Fe(tri-3)$_2$]**$(PF_6)_2$ is carrying anthracene as backbone chromophore **[H$_2$-tri-3]**$(PF_6)_2$ and **[Fe(tri-3)$_2$]**$(PF_6)_2$ are luminescent at room temperature after excitation with λ_{ex} = 348 nm. **[H$_2$-tri-3]**$(PF_6)_2$ has an emission maximum at λ_{em} = 420 nm, while **[Fe(tri-3)$_2$]**$(PF_6)_2$ has an emission maximum at λ_{em} = 582 nm. A more detailed interpretation of this data has not been performed yet. For **[Fe(tri-3)$_2$]**$(PF_6)_2$ TA and time resolved emission spectroscopy experiments are still under investigation. This specific complex **[Fe(tri-3)$_2$]**$(PF_6)_2$ is a very promising candidate in this multichromophoric approach as the energy of the lowest ^{3}MLCT was calculated to 1.88 eV.[94] The triplet energy of anthracene is given in the literature with 1.85 eV.[115] The resulting difference between the triplet energies is 0.03 eV, very close to the value of the thermal energy at room temperature $k_BT \approx 0.025$ eV. Quantum chemical calculations using the same functionals for **[Fe(tri-3)$_2$]**$(PF_6)_2$ and anthracene gave a triplet energy of anthracene of 2.0319 eV.

5.6 Photophysics of $[Ru(bbp\text{-}R)_2](PF_6)_2$ complexes

In the ruthenium complexes a similar picture as observed in multichromophoric iron complexes can be drawn. The intense bands at wavelengths shorter than 320 nm correspond to π-π* transitions within the bbp moieties in the ligands. In the range of 320-420 nm π-π* the typical vibrational fine structure of anthracene can be found in **[Ru(bbp-3)$_2$]**$(PF_6)_2$. At longer wavelengths MLCT transitions appear for all complexes. The MLCT absorption band is more intense and red-shifted to 403 nm (37 100 cm^{-1} M^{-1}) in **[Ru(bbp-1)$_2$]** $(PF_6)_2$ and 393 nm (33 700 cm^{-1} M^{-1}) in **[Ru(bbp-3)$_2$]**$(PF_6)_2$ in comparison to 378 nm (16 600 cm^{-1} M^{-1}) in **[Ru(bbp)$_2$]**$(PF_6)_2$. These findings are in line with those reported in multichromophoric iron complexes.

In **[Ru(bbp)$_2$]**$(PF_6)_2$ the reversible Ru^{III}/Ru^{II} oxidation is at 0.92 V (vs. FcH/FcH^+) and thus is shifted to more anodic potentials compared to **[Fe(bbp)$_2$]**$(PF_6)_2$. Due to the intrinsically large ligand field splitting in ruthenium complexes the metal-centered t_{2g}-HOMO levels are stabilized in energy compared to iron complexes.[32] In **[Ru(bbp-1)$_2$]**$(PF_6)_2$ the Ru^{III}/Ru^{II} oxidation is at 0.87 V, which shows a slight stabilization of the t_{2g}-HOMO by the multichromophoric ligand design. At 1.72 V the irreversible oxidation of the phenyl-backbone is observed. A more complex interpretation can be drawn in **[Ru(bbp-3)$_2$]**$(PF_6)_2$. The metal- (0.93 V) and ligand based (1.02 V) oxidations are as close in energy, that these oxidations cannot be completely distinguished. In a square wave voltammetry experiment it is possible to separate these oxidations and to identify two different oxidation processes. This is indicating a shift of the ruthenium-centered t_{2g}-HOMO levels closer to the energetically stabilized anthracene-based π-levels and make them energetically better aligned, causing an increase in the t_{2g}-π-mixing.[118] Its not possible to clearly figure out the reversibility of the reduction and oxidation events in **[Ru(bbp-3)$_2$]**$(PF_6)_2$.

The irreversible ligand-based reduction at cathodic potentials is at -2.17 V in **[Ru(bbp)$_2$]**$(PF_6)_2$ and thus not significantly different than in **[Fe(bbp)$_2$]**$(PF_6)_2$. In **[Ru(bbp-1)$_2$]**$(PF_6)_2$ and **[Ru(bbp-3)$_2$]**$(PF_6)_2$ the situation at cathodic potentials is similar. The ligand-based reduction is shifted slightly to more anodic potential of -1.95 V (**[Ru(bbp-3)$_2$]**$(PF_6)_2$) and -1.88 V (**[Ru(bbp-1)$_2$]**$(PF_6)_2$), which is in line with the interpretation of the more π-accepting character of the multichromophoric ligands.[36]

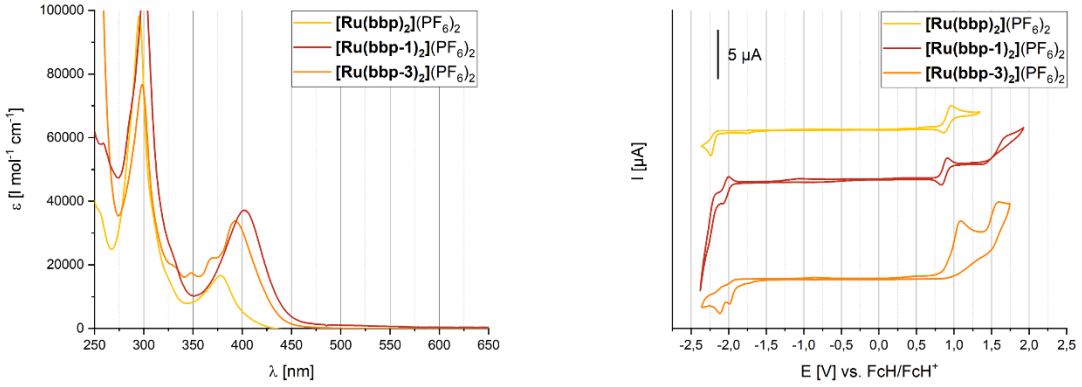

Figure 5.6.1: Optical absorption spectroscopy data (left panel) and cyclic voltammograms (right panel) of ***[Ru(bbp)$_2$]***$(PF_6)_2$, ***[Ru(bbp-1)$_2$]***$(PF_6)_2$ *and* ***[Ru(bbp-3)$_2$]***$(PF_6)_2$.

In **[Ru(bbp)$_2$]**$(PF_6)_2$ an emission with a maximum at 525 nm after MLCT excitation can be detected at room temperature and at 77 K (Figure 5.6.2, top panel). The quantum yield was determined to be $\Phi = (0.9 \pm 0.2) \cdot 10^{-3}$ at room temperature. This emission originates from the ^{3}MLCT state populated after ultrafast ISC from the initially excited ^{1}MLCT state. This interpretation is substantiated by excitation spectra. These are resembling the MLCT absorption band in the complexes nearly perfectly. In **[Ru(bbp-1)$_2$]**$(PF_6)_2$ an emission with a maximum at 585 nm after MLCT excitation can be detected at room temperature and at 77 K (Figure 5.6.2, bottom left panel). Also, this emission originates from the ^{3}MLCT state populated after ultrafast ISC from the initially excited ^{1}MLCT state. This interpretation is substantiated by excitation spectra as they are tracking the MLCT absorption band nearly perfectly.

In **[Ru(bbp-3)$_2$]**$(PF_6)_2$ at room temperature an only slightly weaker emission with a maximum at 535 nm and a shoulder at 430 nm is observed (Figure 5.6.2, bottom right panel). The quantum yield of the maximum at 535 nm was determined to be $\Phi = (0.8 \pm 0.2) \cdot 10^{-3}$ at room temperature. As in the excitation spectra using λ_{em} = 430 nm, only the vibrational fine structure of the anthracene motif is reproduced and the stokes shift is rather small, this emission is assigned to the ^{1}Anthracene emission. As the ^{1}Anthracene emission still has an overlap with the ^{1}MLCT emission with a maximum at 393 nm a FRET on the singlet hypersurface is possible. In the excitation spectra using λ_{em} = 535 nm, mainly the lowest energy absorption band is reproduced, which is assigned to the MLCT absorption band. The emission at λ_{em} = 535 nm is therefore ascribed to the ^{3}MLCT phosphorescence in **[Ru(bbp-3)$_2$]**$(PF_6)_2$**.** At 77 K only the phosphorescence resulting from the ^{3}MLCT state is detected, but with a very weak intensity. From the very weak ^{3}MLCT phosphorescence in **[Ru(bbp-3)$_2$]**$(PF_6)_2$ at 77 K, while the ^{1}Ant and ^{3}MLCT states are emissive at room temperature, it is deduced, that the ^{1}Ant states decays into the ^{3}MLCT followed by rapidly decay into the ^{3}Anthracene state, which is non-luminescent and energetically stabilized relative to the ^{3}MLCT state.[54] The ^{1}Ant emission is quenched due to the population of lower lying ^{3}Ant or ^{3}MLCT states in **[Ru(bbp-3)$_2$]**$(PF_6)_2$.[123]

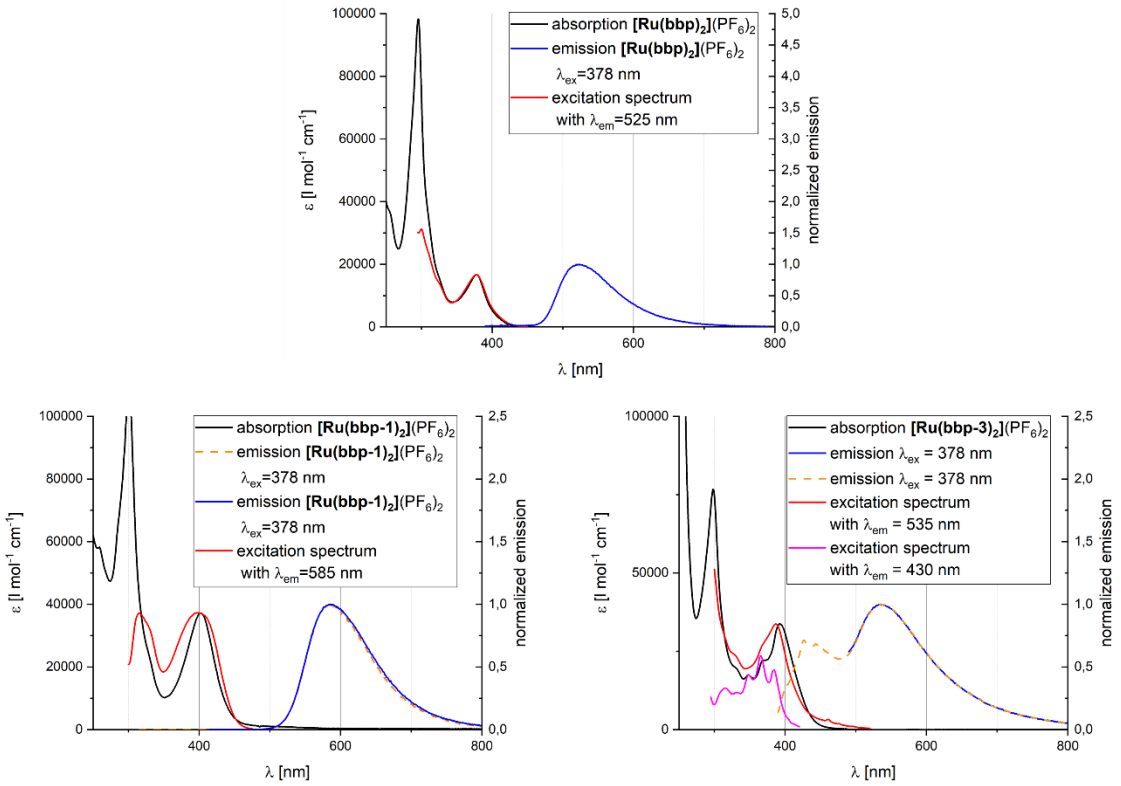

Figure 5.6.2: Steady state absorption (black), emission (blue/orange dotted) and excitation spectra (red/pink) of ***[Ru(bbp)$_2$]***$(PF_6)_2$ *(top panel),* ***[Ru(bbp-1)$_2$]***$(PF_6)_2$ *(bottom left panel) and* ***[Ru(bbp-3)$_2$]***$(PF_6)_2$ *(bottom right panel).*

Photochemically relevant ^{3}MLCT states in both ruthenium complexes are investigated in more detail by time resolved emission spectroscopy using streak camera measurements. The emission of **[Ru(bbp)$_2$]**$(PF_6)_2$ was fitted with a lifetime of $\tau = 0.9$ µs. Streak camera measurements of **[Ru(bbp-1)$_2$]**$(PF_6)_2$ are still in progress. For the emission analysis of **[Ru(bbp-3)$_2$]**$(PF_6)_2$, the two different emissive features must be discussed separately. The emission at $\lambda_{em} = 430$ nm assigned to the ^{1}Ant-state before, are also found in the streak camera measurements. The lifetime is drastically shorter than the lifetime of the emission at $\lambda_{em} = 535$ nm assigned to the ^{3}MLCT state and cannot be revealed more precisely by streak camera measurements. To fit the emission at $\lambda_{em} = 535$ nm, three different time components were necessary. Differential associated amplitude spectra (DAS) were generated to investigate the spectral shapes. The global fits of the DASs reveal only two different time components. The shortest time component of the streak camera measurement fit of $\tau_1 = 1.5$ µs is reproduced in the DAS. The second time component of the DAS is 8.21 µs, which exactly is averaged lifetime of the lifetimes fitted in the streak camera measurements of $\tau_2 = 6.4$ µs and of $\tau_3 = 14.5$ µs. The similar spectral shapes of the DASs assume that the emission described with two respectively three exponential decays is originating from the same emissive state, which is assigned to the ^{3}MLCT state. The averaged lifetime of the three different lifetimes in the streak camera measurements fit is 5.96 µs.

Table 5.6.1: Ground and excited state properties of ***[Ru(bbp)$_2$]***$(PF_6)_2$, ***[Ru(bbp-1)$_2$]***$(PF_6)_2$ *and* ***[Ru(bbp-3)$_2$]***$(PF_6)_2$. [a)]*Streak camera experiments of* ***[Ru(bbp-1)$_2$]***$(PF_6)_2$ *have not been performed yet.*

Compound	λ_{MLCT} [nm] (ε [M^{-1} cm^{-1}])	CV [V vs. FcH/FcH$^+$]	λ_{Em} [nm]	τ_{Em} [µs]
[Ru(bbp)$_2$]$(PF_6)_2$	378 (16 600)	0.92 (rev.) -2.17 (irrev.)	525	0.9
[Ru(bbp-1)$_2$]$(PF_6)_2$	403 (37 100)	1.72 (irrev.) 0.87 (rev.) -1.95 (irrev.)	585	-[a)]
[Ru(bbp-3)$_2$]$(PF_6)_2$	393 (33 700)	1.02 (irrev.) 0.93 (rev.) -1.88 (irrev.)	535	τ_1 = 1.5 τ_2 = 6.4 τ_3 = 14.5

After excitation of the MLCT states in all three ruthenium complexes $^1O_2$ phosphorescence has been detected. In all complexes this is straight forward to the interpretation of the emission originating from a ^{3}MLCT state. As long-lived ^{3}MLCT states are promising candidates in photo redox catalysis, catalytic proton reduction experiments have been performed.

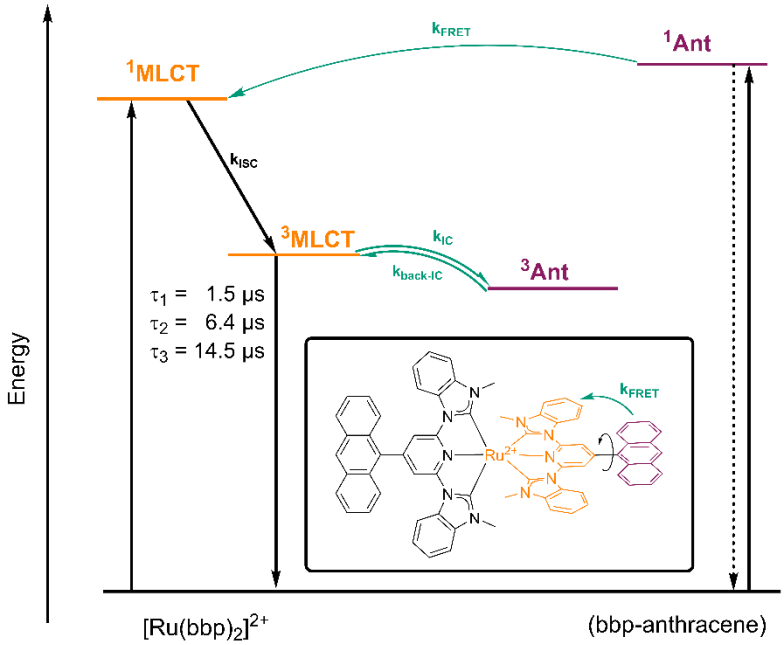

Figure 5.6.3: Provisional schematic representation of excited-state dynamics in ***[Ru(bbp-3)$_2$]***$(PF_6)_2$. *^{3}MLCT lifetime as seen by streak camera measurements (black arrow). Relaxation cascade from ^{1}Ant into ^{1}MLCT by FRET and from ^{3}MLCT into ^{3}Ant is deduced by emission spectroscopy at room temperature and at 77 K. Back-IC ($k_{back-IC}$) seems not to be possible at 77 K. This representation bases on the current results and might be completed by further detailed spectroscopic investigations and quantum chemical calculations.*

6

Catalytic Experiments

In this section, two photocatalytic applications of the prepared photosensitizers are discussed in detail. First, the proton reduction to elemental hydrogen, which was already explained in detail in the introduction, is carried out with the ruthenium photosensitizers presented. In another section, the possibility of energy transfer in triazole complexes to produce reactive oxygen is discussed and the produced reactive oxygen species is used to oxidize diene systems.

6.1 Photocatalytic Protonreduction

For the photocatalytic proton reduction experiments, the multicomponent system approach was chosen. For this purpose, the ruthenium-based **[Ru(bbp-R)$_2$]**$(PF_6)_2$ photosensitizer was placed together with the cobalt-based water reduction catalyst **[Co(dmgH)$_2$pyCl]** (dmgH = *N*,*N*'-Dihydroxy-2,3-butanediimine ; py = pyridine) in a solvent system based on acetonitrile or THF. Acetonitrile was combined with triethanolamine (TEOA) as an electron donator (ED) and HBF_4 as a proton source (0.5 M TEOA; 0.05 M HBF_4 in MeCN). The second solvent mixture used, was THF combined with triethylamine (TEA) as ED and water as proton source (THF/H_2O/TEA: 8/1/1 V/V/V).[24,124] The use of an electron mediator was omitted. In the photocatalytic proton reduction, an electron from the excited ^{3}MLCT state is transferred to the WRC and it reduces protons to elemental hydrogen (Figure 6.1.1).

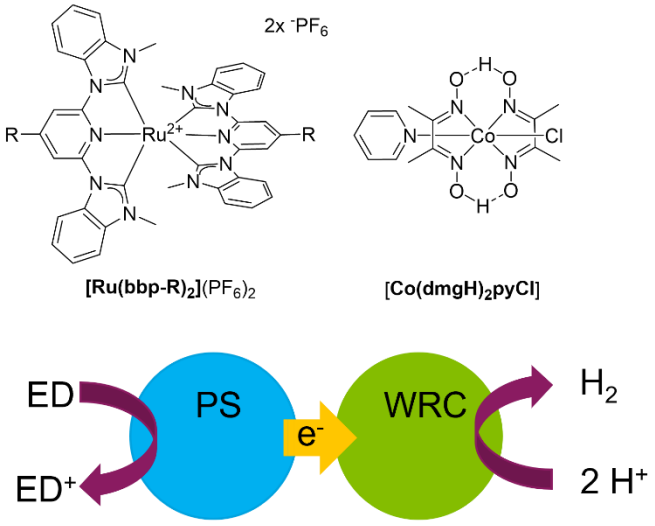

*Figure 6.1.1: Molecular structures of used photosensitizer **[Ru(bbp-R)$_2$]**$(PF_6)_2$ and **[Co(dmgH)pyCl]** as water reduction catalyst (top) and schematic representation of the catalytic mechanism (bottom).*

Catalytic samples have a volume of 3.6 ml containing 1 µmol PS, 1 µmol **[Co(dmgH)$_2$pyCl]** and 4 µmol dmgH as supporting ligand. Samples have been illuminated at a constant temperature of 25 °C of the sample. While illumination the change in pressure was detected in the catalytic experiments. In each of the experiments, four samples of each PS together with the WRC and one sample of each PS without catalyst were performed. The pressure difference of the sample without catalyst was used as a reference value and subtracted from the pressure differences of the catalyst systems. The pressure differences of the combination of the PS and WRC were averaged and plotted against time after the start of irradiation (Figure 6.1.2).

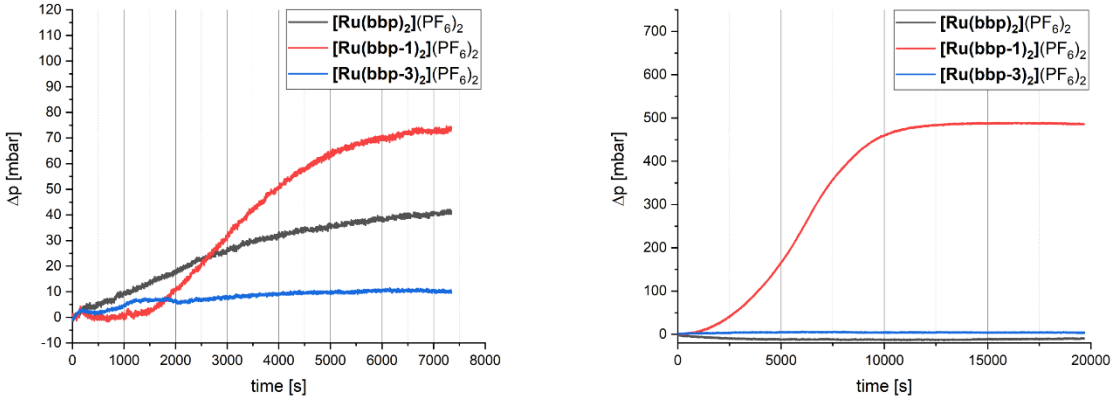

Figure 6.1.2: Pressure differences in photocatalytic proton reduction in acetonitrile (left panel) and THF (right panel).

These experiments are analyzed in detail according to the ideal gas law (eq. 6.1). In this equation *p* is the pressure measured in this set up. *V* is the volume of the gas phase in the reactor set up, consisting of the gas volume inside the reactor (1 ml) and inside the pressure sensor (0.594 ml). *R* is the gas constant (*R* = 8.314 J K^{-1} mol^{-1}) and *T* is the temperature, which is 25 °C in this set up. This equation is enabling the calculation of produced hydrogen in this run.

$$p \cdot V = n \cdot R \cdot T \tag{6.1}$$

As the run in MeCN did not give large quantities of hydrogen, only the run in THF is analyzed in this section. The detected difference in pressure is 487.25 mbar. According to the ideal gas law, the produced amount of hydrogen is 31.3 µmol (H_2). To produce one hydrogen molecule, two protons are reduced by 1 µmol of the PS inside the reactor. This is resulting in a turnover number (TON) of 62.6 with respect to the PS (Table 6.1.1).

Table 6.1.1: Parameters used to calculate the TON in photocatalytic proton reduction in THF/H_2O/TEA (8/1/1 V/V/V).

p [mbar]	V [ml]	T [K]	n_{PS} [µmol]	$n_{Hydrogen}$ [µmol]	TON
487.25	1.594	298.15	1	31.3	62.6

The TON of **[Ru(bbp-1)$_2$]**(PF$_6$)$_2$ is in the range of noble metal based multicomponent systems, tested in this working group before.[125]

The prepared iron complexes have not been tested in detail but the complexes **[Fe(bbp)$_2$]**(PF$_6$)$_2$ and **[Fe(bbp-3)$_2$]**(PF$_6$)$_2$ did not show significant activity. The photocatalytic behavior of especially **[Ru(bbp-1)$_2$]**(PF$_6$)$_2$ shows the potential of the multichromophoric approach in catalysis. Not only the ground and excited state properties of multichromophoric ruthenium and iron-based PSs are

improved, but also the catalytic applications. This development is also promising for the photocatalytic application of iron complexes, which is still limited in the moment.

6.2 Sensitization of oxygen

Catalytic processes initiated by photoinduced electron transfer are well studied. Currently, there is growing interest in triplet energy transfer, also known as sensitization, because it can be used to achieve high selectivity in photochemical reactions.[126] Oxygen is one of the few molecules with triplet ground state $^3O_2$. It can quench almost any excited triplet state of a photosensitizer. Often, the energy transfer is from the excited triplet state of PS (^{3}MLCT) to the triplet ground state of molecular oxygen, producing high-energy $^1O_2$ with lifetimes of 3 µs to 300 ms.[127] In chemical quenching $^1O_2$ reacts with another molecule to form various products. $^1O_2$ reacts preferentially with nucleophilic compounds. Synthetically known $^1O_2$ reactions to generate oxygen-containing compounds include [2+2] and [4+2] cycloadditions, which work with a variety of substrates.[128] In this work, the [4+2] cycloaddition of reactive oxygen to three different organic diene systems was investigated.

The reaction of 1,3-diphenyl-isobenzofuran (**DPBF**) with $^1O_2$ was used to indirectly detect the presence of non-luminescent high spin states and was investigated most detailed in this work. The measurements were carried out at room temperature in MeOH under ambient conditions. 2.5 ml **DPBF** (20 µM in MeOH) were mixed with 0.5 ml of the triazole-based complex **[Fe(btp)$_2$]**$(PF_6)_2$ (10^{-4} M in MeOH) in a fluorescence cuvette and illuminated with λ = 480±5 nm. The consumption of **DPBF** was detected by monitoring the decreasing luminescence intensity at 475 nm. **[Ru(bpy)$_3$]**$(PF_6)_2$ with an $^1O_2$ quantum yield of 0.86 in ambient MeOH was used as a reference. The decomposition reaction of **DPBF** is effectively initialized by **[Ru(bpy)$_3$]**$(PF_6)_2$ and **[Fe(btp)$_2$]**$(PF_6)_2$. The effectivity of **[Ru(bpy)$_3$]**$(PF_6)_2$ is about twice as high as the effectivity of **[Fe(btp)$_2$]**$(PF_6)_2$. Therefore, singlet oxygen sensitization for these two complexes is assumed. **DPBF** without any additional photosensitizer and **DPBF** + **[Fe(btp)$_2$]**$(PF_6)_2$ in a degassed solution show no decomposition of **DPBF**. Additionally, the ability of **[Fe(tpy)$_2$]**$(PF_6)_2$ to sensitize oxygen was tested, but no decomposition of **DPBF** was detected. This leads to the interpretation, that **[Fe(btp)$_2$]**$(PF_6)_2$ could be ending up in a long-lived triplet state after photoexcitation in the MLCT band and is probably not resulting in a long-lived ^{5}MC state like **[Fe(tpy)$_2$]**$(PF_6)_2$. This interpretation needs to be clarified by further investigations (Figure 6.2.1).[94]

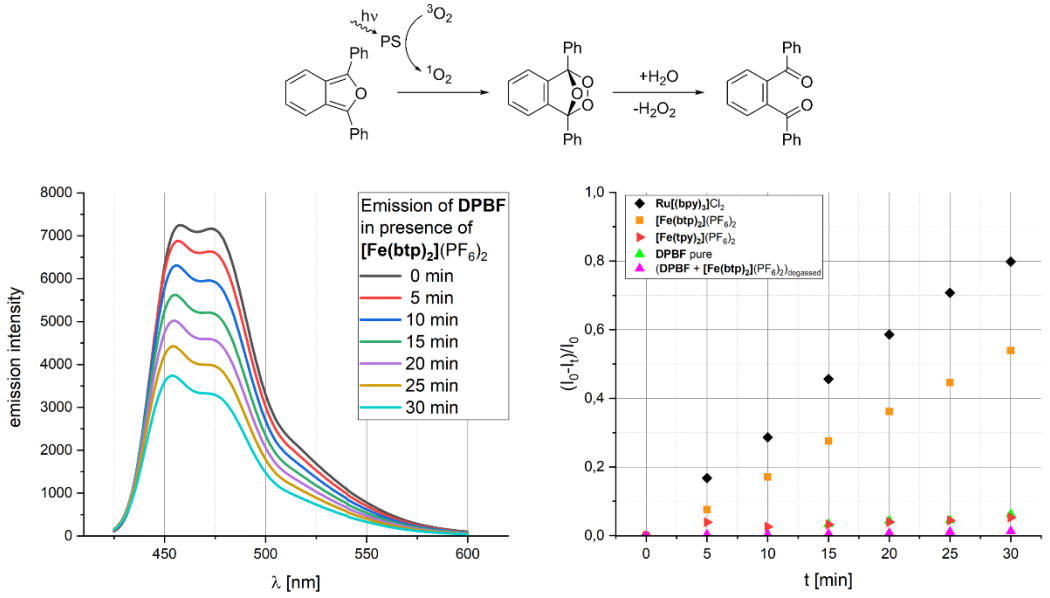

*Figure 6.2.1: [4+2] cycloaddition of **DPBF** and $^1O_2$ (top) and resulting change in emission intensities of **DPBF** in presence of **[Fe(btp)$_2$]**$(PF_6)_2$ (bottom left panel). Analysis for different conditions and with **[Ru(bpy)$_3$]**Cl_2 as reference plotted at different reaction times (bottom right panel).*

The cycloaddition of reactive oxygen with anthracene was detected by absorption and luminescence spectroscopy (Figure 6.2.2).[128] Therefore 2.5 ml of 200 µM solution of anthracene in $CHCl_3$ was mixed with 0.5 ml of a 100 µM **[Fe(btp)$_2$]**$(PF_6)_2$ solution in MeOH and irradiated using a long-pass filter (λ > 400 nm). Progress of the reaction was probed each 60 min. The EI-MS data were calculated for $C_{14}H_8O_2$ to be 208.0524 (m/z). After irradiation 207.9863 (m/z) was found. The peroxo-species was not detected in EI-MS. The decrease of absorbance and emission in the sample without PS, can be explained by photodimerization of anthracene at λ > 300 nm. In the blank samples a decrease of the intensities is observed, but the shapes of the signals stay the same. This is not the case while anthraquinone is formed.

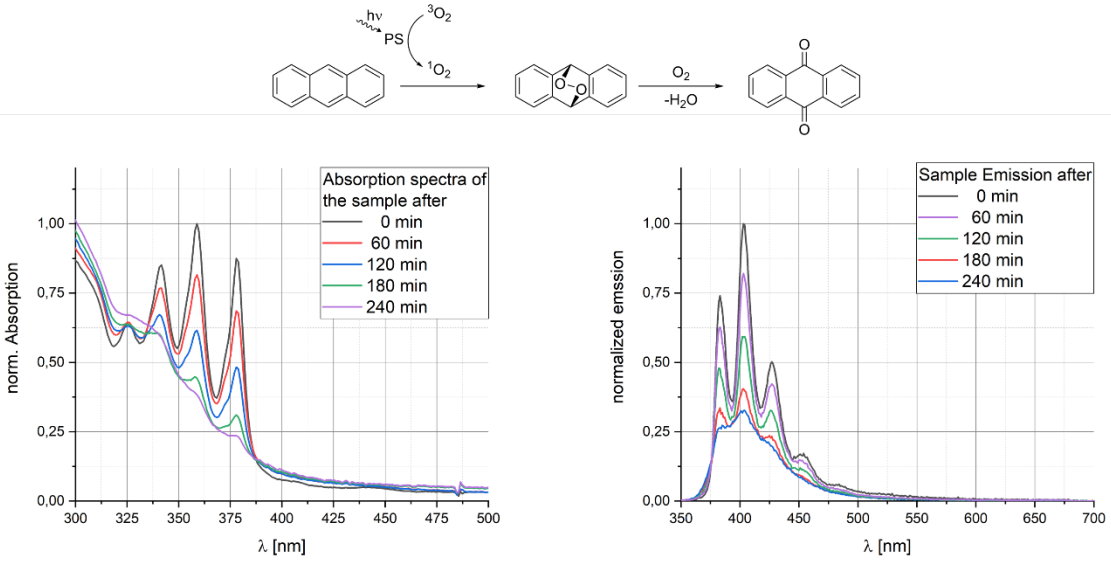

*Figure 6.2.2: [4+2] cycloaddition of anthracene and $^1O_2$ (top) and resulting change in absorption (left bottom) and emission (right bottom) at different reaction times for a mixture of anthracene and **[Fe(btp)$_2$]**$(PF_6)_2$.*

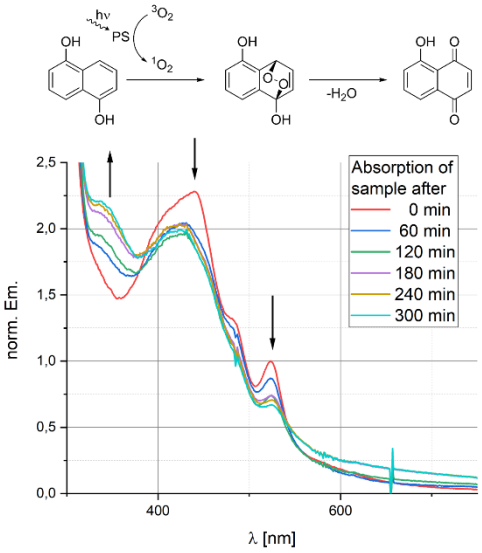

*Figure 6.2.3: [4+2] cycloaddition of naphthalene-1,5-diole and $^1O_2$ (top) and resulting changes in absorption intensities of the mixture of naphthalene-1,5-diole and **[Fe(btp)$_2$]**$(PF_6)_2$ at different reaction times (bottom).*

The cycloaddition of reactive oxygen with naphthalene-1,5-diole was detected by absorption spectroscopy (Figure 6.2.3).[129] Therefore 2.5 ml of 200 µM solution of naphthalene-1,5-diole in $CHCl_3$ was mixed with 0.5 ml of a 100 µM **[Fe(btp)$_2$]**$(PF_6)_2$ solution in MeOH an irradiated using a long-pass filter (λ > 400 nm).

Progress of the reaction was probed each 60 min. In the absorption, three different regions with a change in the absorption are detected. The absorption is decreasing at around λ = 340 nm. A small decrease is also found for pure naphthalene-1,5-diole at this wavelength. Furthermore, the absorption is increasing at around λ = 440 nm and λ = 520 nm because of the formation of juglone (5-hydroxynaphthalene-1,4-dione). In the sample without any photosensitizer no change in the absorption at these wavelengths is detected. The EI-MS data calculated for $C_{10}H_6O_3$ to be 174.0317 (m/z). After irradiation 173.9510 (m/z) was found. The peroxo-species was not detected in EI-MS.

In summary, this type of oxygen sensitization represents a reactivity not yet described for iron complexes. Through the different experiments and substrates, it could be shown that the oxygen sensitization is induced by light in the visible spectral range, although it can be assumed by the spectroscopic data that it is not an active MLCT state. A possible suggestion would be a ^{3}MC reactivity in this complex, which is not proven yet. A detailed mechanistic elucidation of this reactivity is still in progress.

7

Summary and Conclusion

In addition to the development of new sustainable processes to achieve the climate targets the further development of existing processes plays an important role. From this point of view, iron has become established as an ecological alternative in photocatalysis, and there have been pioneering advances in tuning of the photophysical properties of iron complexes in the recent years. The multichromophoric approach, which is the first time investigated for iron(II) complexes in the frame of this work is a further step to make the application of iron complexes in photocatalysis increasingly efficient. The multichromophoric approach leads to a red shift and an increase in the extinction coefficient of the MLCT absorption bands. The lifetime of the catalytically active MLCT states increases. All multichromophoric complexes show an antenna effect, which results in a larger occupation of MLCT states. The effects elucidated in this work make multichromophoric complexes very important key components in the development of iron(II) photosensitizers and the understanding of fundamental excited state properties after photoexcitation, which are groundbreaking in the implementation of iron(II) photosensitizers in photo redox catalysis.

The preparative aim of this work was the preparation and characterization of novel multichromophoric Fe(II) complexes for use as molecular photosensitizers. In this work, the preparation of five different multichromophoric ligand classes is discussed in detail. Multichromophoric complexes based on **tpy** (= 2,2':6',2''-terpyridine), **bim** (= 1,1'-(pyridine-2,6-diyl)bis(3-methyl-1H-imidazol-3-ium)), **bbp** (= (pyridine-2,6-diyl)bis(1-methyl-benzimidazol-2-ylidene)), **btp** (= 2,6-bis(1-ethyl-1H-1,2,3-triazol-4-yl)pyridine), **tri** (= 4,4'-(pyridine-2,6-diyl)bis(1-ethyl-3-methyl-1H-1,2,3-triazol-3-ium)) ligands and pro-ligands were successfully synthesized. In addition, problems and difficulties in selected synthesis steps were presented and possible solutions were discussed in detail.

After successful synthesis of terpyridine complexes, the synthesis of the important intermediate **7** was first discussed. Selective deprotonation of **3** in 4-position and subsequent iodination with elemental iodine turned out to be most effective. Starting from **7**, the synthesis of **8-R** was developed, which is a splitting point in the synthetic routes of **[Fe(bim-R)$_2$]**$(PF_6)_2$/**[Fe(bbp-R)$_2$]**$(PF_6)_2$ and **[Fe(btp-R)$_2$]**$(PF_6)_2$/**[Fe(tri-R)$_2$]**$(PF_6)_2$ complexes. **9-R**/**10-R** was prepared by the Suzuki coupling of **8-R** and the respective chromophore boronic acids.

[Fe(bim-R)$_2$]$(PF_6)_2$/**[Fe(bbp-R)$_2$]**$(PF_6)_2$ were prepared by a sequence of one Ullmann coupling followed by methylation of the imidazole groups. Complexes were prepared by subsequent coordination of the ligands to Fe(II). For comparison purposes **[Ru(bbp-1)$_2$]**$(PF_6)_2$ and **[Ru(bbp-3)$_2$]**$(PF_6)_2$ have been prepared as well. **[Fe(btp-R)$_2$]**$(PF_6)_2$/**[Fe(tri-R)$_2$]**$(PF_6)_2$ were prepared

by a sequence of a Sonogashira coupling, a [2+3]-cycloaddition and subsequent methylation. The complexes were prepared by subsequent coordination of the ligands to Fe(II).

Detailed photophysical investigations were carried out for all substance classes with various cooperation partners. The most detailed investigations were carried out for the group of **[Fe(bim-R)$_2$]**$(PF_6)_2$ complexes. Three main findings were obtained. Firstly, an increase in the extinction coefficient and a red shift of the MLCT absorption maximum were observed. This can be explained by the increase in the π-system of the ligands. This observation was confirmed by electrochemical characterization. Secondly, an increase in MLCT lifetime was observed by TA spectroscopy. Confirmation that these are indeed MLCT lifetimes was provided by spectroelectrochemical experiments. Thirdly, both the pro-ligands and the final complexes show emission upon excitation into the π-π* transitions of the chromophores. Through time-dependent fluorescence spectroscopy and TDDFT calculations, a FRET between a photo-excited ^{1}Chromophore state to a ^{1}MLCT state is assumed. This effect is called the "antenna effect" following the literature. In addition, the photosensitizers were investigated for long-lived ^{3}Chromophore states. For this purpose, the energy transfer to oxygen was studied indirectly. By reactivity of reactive $^1O_2$ with organic diene systems and by direct observation of $^1O_2$ phosphorescence, the presence of long-lived triplet states was indirectly investigated. No energy transfer to oxygen was observed for any of the multichromophoric complexes presented, leading to the interpretation that no long-lived ^{3}Chromophore states exist. This also means that the originally targeted "reservoir effect" could not be realized.

The increase of the extinction coefficient and a red shift of the MLCT absorption maximum were observed for all multichromophoric iron complexes prepared in this work. An increase in MLCT lifetimes was also found for all fully characterized multichromophoric complexes. Not all complexes have yet been investigated for an "antenna effect". Detailed investigations are currently underway.

Besides the fundamental understanding of the dynamics of the photoexcited states in the multichromophoric complexes, some properties remain poorly understood. One of the most important properties that remains to be investigated is the lack of correlations of both the redshift and the increase in extinction coefficients of the MLCT absorptions and the increased MLCT lifetimes with other properties of the complexes. So far, it has not been possible to correlate any of these properties with properties of the chromophores. There is no clear correlation with, for example, the size, singlet or triplet energies, or intrinsic lifetimes of the chromophores.

Besides numerous activities to understand and improve the photophysics of iron complexes following visible light absorption, applications of iron complexes to initiate and enable chemical reactions are still rarely reported and the mechanistic details for the photocatalytic processes remain mainly unexplored, although iron-mediated photo redox chemistry is surely an emerging field. The photochemical applications as photosensitizers based on the multichromophoric design approach investigated in terms of this work are summarized in the following.

Of particular interest in this work is complex **[Fe(btp)$_2$]**$(PF_6)_2$, as it exhibits a never described reactivity with oxygen that could be used, for example, in [4+2] cycloadditions with organic diene systems. In terms of this work the [4+2] cycloadditions of reactive oxygen with **DPBF**, anthracene and naphthalene-1,5-diole after photoexcitation of the MLCT transition in **[Fe(btp)$_2$]**$(PF_6)_2$ was

investigated. The most detailed analysis was performed for the oxidation of **DPBF**. In this case the activity was found to be even half of the activity of **[Ru(bpy)$_3$]**Cl_2. Through detailed photophysical studies, it is hypothesized that this complex relaxes into a long-lived ^{3}MC state capable of oxygen sensing upon excitation into the MLCT absorption transitions. More detailed photophysical evidence for this interpretation has yet to be provided.

The use of the iron-based multichromophoric complexes as photosensitizers in the photocatalytic proton reduction did not provide any activity of the complexes. However, the use of ruthenium-based multichromophoric complexes **[Ru(bbp-1)$_2$]**$(PF_6)_2$ showed increased activity compared to **[Ru(bbp)$_2$]**$(PF_6)_2$, which has no additional chromophore in the backbone of the ligand. This increased activity shows the potential of the multichromophoric approach also in electron transfer reactions, even if some basic research is still needed especially in the field of iron-based multichromophoric complexes to increase the MLCT lifetimes to a point where electron transfer processes can also take place with these complexes.

The ability of the class of multichromophoric complexes to undergo both energy transfer reactions to singlet oxygen and electron transfer to a water reduction catalyst for proton reduction demonstrates the potential for a wide range of photocatalytic applications.

An outlook on possible further research questions in the field of multichromophoric iron complexes, which will be discussed below, points to the possibility of understanding the photophysical processes within the complexes and optimizing the complex properties with respect to photocatalytic applications.

8

Perspectives

The long term perspective of this thesis is to be a part of the deep understanding and to enable the rational tuning of excited state energy landscapes of iron(II) and iron(III) complexes to devise (photo)stable complexes for applications, e.g. in dye-sensitized solar cells, light-emitting electrochemical cells, organic light-emitting diodes, bioanalytics or photo(redox) chemistry to replace and complement noble metal sensitizers based on e.g. ruthenium(II) or iridium(III) in these applications.

8.1 Short-, medium-, and long-term perspectives

For this purpose, different targets with different - short-, medium- and long-term - perspectives of success are described. As a first target with short-term prospects of success, the already presented complex **[Fe(tri-3)$_2$]**$(PF_6)_2$ should be completely investigated in terms of its photophysical behavior by spectroscopic and quantum chemical techniques (Figure 8.1.1). This one is particularly interesting because in this compound the energy difference between the ^{3}MLCT and the ^{3}Ant state are almost isoenergetic. The energy of the ^{3}MLCT state of the unsubstituted complex **[Fe(tri)$_2$]**$(PF_6)_2$ has already been calculated quantum mechanically in the context of this work. The calculated energy value of the ^{3}MLCT state is 1.88 eV.[94] The literature value of the ^{3}Ant energy is 1.85 eV.[115]. The resulting difference between the triplet energies is 0.03 eV, very close to the value of the thermal energy at room temperature $k_BT \approx 0.025$ eV. This energy difference is the smallest for all complexes described in this work and significantly lower than the energy differences for which a reservoir effect is described in various publications on noble metal complexes and a back-population of initially occupied states is described for rare earth complexes. Calculated in the context of this work was a ^{3}Ant energy with a value of 2.0319 eV. With the precise photophysical description of complex **[Fe(tri-3)$_2$]**$(PF_6)_2$, it allows the influence on the relative energetic position between the ^{3}MLCT and ^{3}Chrom states to be studied in detail.

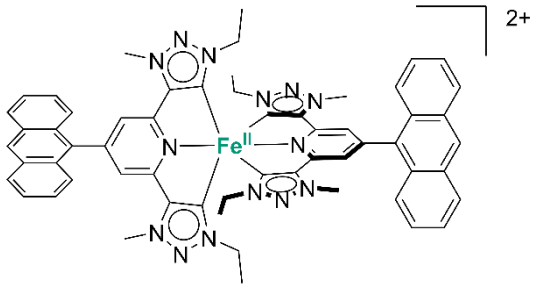

[Fe(tri-3)$_2$]$(PF_6)_2$

*Figure 8.1.1: Molecular structure of **[Fe(tri-3)$_2$]**$(PF_6)_2$ which is a promising candidate as multichromophoric photosensitizer due to the small energy gap between ^{3}MLCT and ^{3}Chromophore states.*

As a project with medium-term prospects of success, the antenna effect discovered for multichromophoric iron complexes can be applied in molecular dyads (Figure 8.1.2).[130] Molecular dyads with an iron complex as the photoactive moiety and a cobalt complex as the catalytic active site have already been successfully used in photocatalytic proton reduction.[125] In this process, an electron is transferred from the ^{3}MLCT state of the iron complex to the cobalt catalyst, from where it is utilized in the proton reduction. The antenna effect described in this work implies an energy transfer on the singlet hypersurface from the ^{1}Chrom state to the ^{1}MLCT state. This is a second pathway of the population of MLCT states besides direct population by the absorption of light in the visible region and broadens the spectral range suitable in photocatalytic application. The antenna effect has been interpreted to mean that the MLCT state is more frequently populated as a result. In such dyads, electron transfer to the cobalt center, which is the catalytically active center of the dyads, initialized by the MLCT state. A more frequent population of the iron center is followed by a more frequent population of catalytically active cobalt states, promising an increase in activity. A possible design of a **Dyad** with a multichromophoric photosensitizer is shown in Figure 8.1.2. For the photoactive iron complex with the anthracene in the backbone of the outer ligand, the antenna effect due to the more frequent population of the MLCT state ensures that the ^{3}MLCT state is populated more frequent. The catalytically active cobalt complex is also excited more frequently, because of the electron transfer from the iron to the cobalt center. This is a possible variant to further enhance the catalytic activity of a Fe-Co dyad that already shows catalytic activity.

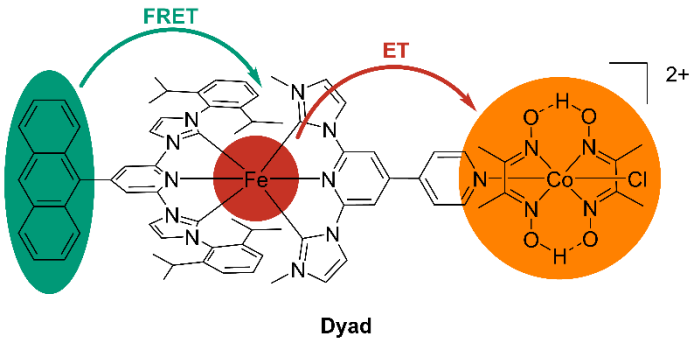

*Figure 8.1.2: Molecular structure of a **Dyad** carrying an aromatic chromophore at one ligand. The antenna effect might increase the population of the ^{3}MLCT state by the proposed Förster Resonance Energy Transfer. This could increase the photocatalytic properties of this type of molecular dyads.*

A long-term perspective is the transfer of the multichromophoric approach from iron(II) complexes to iron(III) complexes bearing a slightly different type of photophysical behavior as discussed in detail in the introduction. After a tris(bidentate) and scorpionate ligand arrangement, a bis(tridentate) version of hexa-carbene complexes was realized recently with **[Fe^{III}(ImP)$_2$]**PF_6.[53] The iron center is coordinated by four NHCs units and two cyclometalating phenyl rings. This ligand design leads to a dual ^{2}GS-^{2}LMCT absorption at 585 nm and a ^{2}GS-^{2}MLCT absorption at 351 nm. After ^{2}LMCT-excitation at low energies an emission with a maximum at 675 nm is observed. After ^{2}MLCT-excitation at higher energies an additional emission with a maximum at 450 nm is detected together with the 675 nm luminescence. Such a dual or two color luminescence is a rare observation and was never reported for iron complexes before. The excited state landscape is dominated by a ^{2}LMCT state with a lifetime of 0.24 ns at low energies and a ^{2}MLCT state with a lifetime of 4.2 ns at higher energies. In this type of iron(III) complexes, the bichromophoric approach will be used to increase the absorptivity of both the MLCT and LMCT bands caused for

example by a cyclometalated ligand in the proposed complex **[Fe^{III}(ImP-3)$_2$]**PF_6 (Figure 8.1.3). Further ligand tuning with electron donating and withdrawing groups and carbene variations will allow to tune the energy of the characteristic (dual) emission and to optimize the luminescence quantum yields as well as the photochemical and photocatalytic behavior.

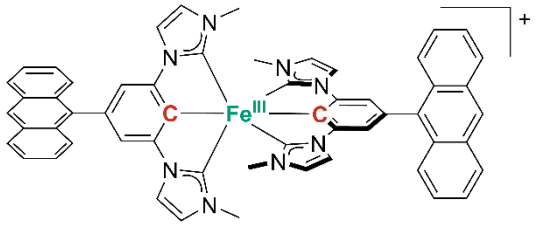

[Fe(ImP-3)$_2$]PF_6

*Figure 8.1.3: Molecular structure of **[Fe^{III}(ImP-3)$_2$]**PF_6. The multichromophoric approach could help to increase the photophysical properties of iron(III) complexes.*

The general overview (Figure 8.1.4) of possible deactivation processes and the influence of the multichromophoric approach on iron(II) and iron(III) complexes, shows which questions about this approach are still open and which still have to be addressed. In addition, the possible structural design concepts of the complexes are generically presented. The synthetic approaches rely on tridentate ligands with iron(II) and iron(III) centers in 5-ring chelates in a classical C^N^C and C^C^C arrangement to ensure a very high octahedrality and rigidity. It is possible to introduce different types of carbenes, from classical NHC, over mesoionic to cyclometalated carbenes in all these concepts. The number of different carbenes with N-donors can be optimized with respect to the photophysical (tuning of the energy of different states and luminescence) and photochemical (reactivity) properties. The generic Figure 8.1.4 shows the full potential that can be covered by the multichromophoric approach in iron photosensitizers.

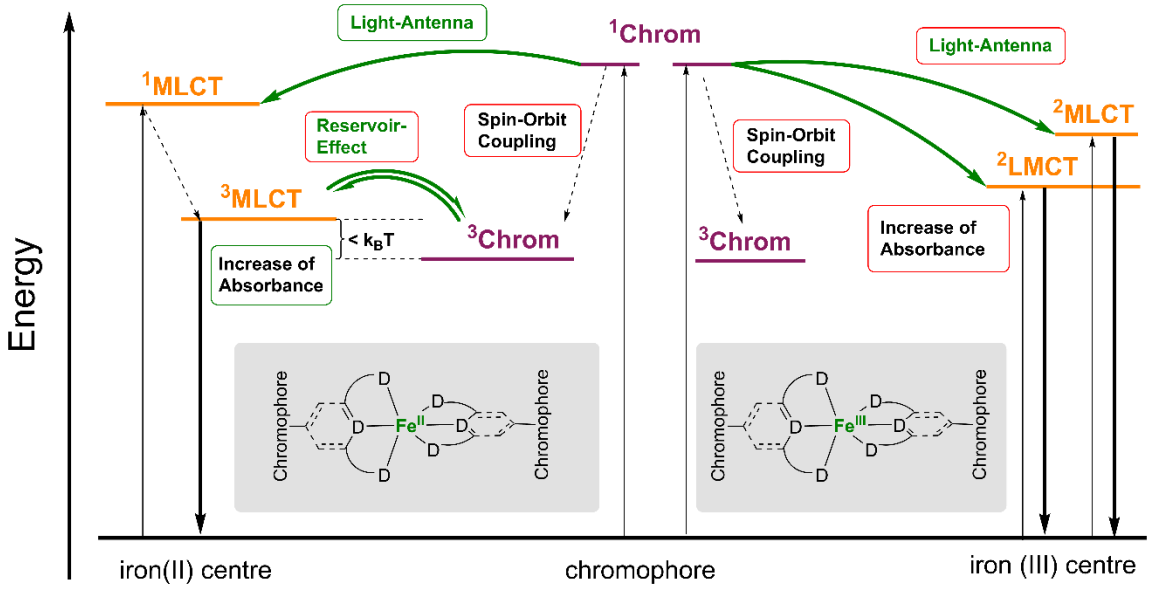

Figure 8.1.4: Schematic representation of photophysical processes in multichromophoric iron (II) complexes (left side) and multichromophoric iron (III) complexes (right side). Effects that have been found and discussed in terms of this work are highlighted in green boxes. Effects that are still under investigation and of huge interest for following projects are highlighted in red boxes.

9

Experimental Details

In this section, experimental details of analytical and spectroscopic methods and published and unpublished syntheses are described. A more detailed insight into the methods of the published results can be found in the corresponding publications and their supplementary information.[36,94]

9.1 General information on equipment and chemicals

The synthesis of all compounds is performed due to sensitivity against air or humidity of chemicals used under inert and anhydrous conditions. Therefore, standard Schlenk conditions are applied, and the used glass equipment is baked out at least three times and filled with pre-dried argon. All synthesis under inert conditions were carried out using water free solvents, which either were dried by literature references[131] or picked from a solvent-drying plant by the firm *MBraun* model *MB SPS 800.*

The used chemicals were commercially purchased by following providers: *Sigma-Aldrich*, *abcr*, *TCI* and *Fisher Scientific*. All Chemicals were used for synthesis without further purification unless otherwise noted.

9.2 Annotations to the used analytical and spectroscopic techniques

Nuclear Magnetic Resonance Spectroscopy:

^{1}H-, ^{13}C-, ^{19}F- and ^{31}P-Spectra of the different substances were recorded. These spectra are recorded by NMR-spectrometer type Avance 500 or and Ascent 700 of company *Bruker* at the University of Paderborn by the team of PD Dr. Hans Egold. ^{1}H-NMR-spectra are measured at a frequency of 500 MHz and the ^{13}C-measurements are recorded at a frequency of 125 MHz by the *Bruker* Avance 500. ^{1}H-NMR-spectra are measured at a frequency of 700 MHz, the ^{13}C-measurements are recorded at a frequency of 176 MHz, the ^{31}P-spectra are recorded at 283.5 MHz and the ^{19}F-spectra are recorded at 659 MHz by the *Bruker* Ascent 700. For measurement of the spectra the relevant substance is dissolved in an appropriate deuterated solvent which is specifically listed for each compound. The chemical shifts used indicated in ppm are related to the δ-scale.[132] For analysis of the spectra the software Topspin (version 4.0.6) by *Bruker* is used. For correlation of the different signals to the belonging molecular parts two-dimensional NMR-spectra (COSY, HMBC, HMQC, HSQC) are used.[133]

Mass Spectrometry:

The ESI-mass spectra were recorded using a quadrupole-time of flight-mass spectrometer (QTOF) type *Synapt 2G* by the firm *Waters* by the team of Dr. Adam Neuba. The solvents used in each case are listed for each compound. EI-mass spectra were recorded using a DFS sector field spectrometer by *Thermo Scientific*.

Elemental Analysis:

The measurements of elemental analysis were realized with a device of type vario MICRO Cube of the company *Elementar*. WO_3 was added as an oxidation catalyst to specified samples.[134]

Single Crystal X-Ray Diffraction:

The X-ray single crystal data were recorded by Dr. Roland Schoch on a Bruker Venture D8 diffractometer, equipped with a Mo K_α IμS 3.0-source (λ=0.71073 Å) and a Photon III area detector at 120 K. The obtained data were integrated with SAINT and a multi-scan absorption correction was carried out by SADABS.[135] The structure solution by direct methods and the refinement of the structures using full-matrix least squares method based on F^2 were achieved in SHELX – all three software programs are parts of the Bruker APEX III package.[136] All non-hydrogen-atoms were refined anisotropically and the hydrogen atom positions at idealized positions residing on the carbon atoms with isotropic displacement parameters Uiso(H)=1.2 Ueq(C) resp. 1.5 Ueq(-CH_3) and C-H bond lengths of 0.93-0.96 Å. All CH_3 hydrogen atoms were allowed to rotate but not to tip. If needed due to significant disorders of solvent molecules, those were treated using SQUEEZE from the Platon software package.[137]

IR Spectroscopy:

The infrared spectra were measured with an IR-spectrometer Vertex 70 by *Bruker*. Solid compounds were measured as pure powders using the ATR-technique. IR data were used in TD-DFT calculations for comparison pursoses and are not shown in this thesis.

UV/Vis Spectroscopy:

Absorption spectra were recorded at concentrations of 10^{-5} M on a *PerkinElmer* Lambda 465 single beam spectrophotometer. Spectroscopy grade solvents from VWR and quartz cuvettes by Hellma with a pathlength of 1 cm were used.

Transient Absorption Spectroscopy:

Transient absorption spectroscopy was performed and analyzed by the group of Prof. Dr. Stefan Lochbrunner at the University of Rostock. Transient absorption spectra were measured with a time resolution of about 100 fs by means of a pump-probe setup in which a non-collinear optical parametric amplifier (NOPA) tuned to a center a specified wavelength for each complex was used for exciting the sample and a white light continuum generated in a CaF_2 crystal for probing.[138] Both, the NOPA and the white light stage were pumped by a regenerative Ti:sapphire laser system (CPA 2001, Clark MXR, Inc.) operating at a center wavelength of 775 nm and a repetition rate of 1 kHz. The dispersion of the NOPA pulses was minimized by a compressor based on fused silica prisms and the polarizations of the pump and probe pulses were set to magic angle with respect to each other to avoid effects caused by orientational relaxation. Pump and probe beam were

focused onto the sample to overlapping spots with diameters of approximately 200 µm and 100 µm, respectively. After the sample, the probe was dispersed by a prism and transient absorption changes were spectrally resolved recorded by a photodiode array detector. Transient absorption spectra with an excitation wavelength of 400 nm were recorded with a similar setup using another Ti:sapphire laser system (Spitfire Ace PA, spectra physics). The compounds were dissolved in MeCN under argon and the sample solution was filled into a fused silica cuvette with a thickness of 1 mm.

Luminescence Spectroscopy:

The emission spectra were recorded using the fluorometer FluoroMax-4 from *Horiba Scientific* by the research group of Prof. Dr. Stefan Lochbrunner at the University of Rostock. Emission and excitation spectra were also recorded at the University of Paderborn with a *Jasco* FP-8300 fluorometer and an *Edinburgh Instruments* FLS1000. Low temperature emission spectra at 77 K were recorded on an *Edinburgh Instruments* FLS1000 while cooling with liquid nitrogen.

Time-resolved Emission Measurements:

Time-resolved luminescence measurements were carried out by means of a streak camera system (C10627, Hamamatsu Photonics) using ultrashort excitation pulses at 388 nm by the research group of Prof. Dr. Stefan Lochbrunner at the University of Rostock. The latter were generated by frequency doubling the output of a regenerative Ti:sapphire laser system (CPA 2001, Clark MXR, Inc.) which provides 160 fs long laser pulses with a center wavelength of 775 nm at a repetition rate of 1 kHz. MeCN solutions of the compounds were prepared under argon and measured in 1 cm thick fused silica cuvette.

Luminescence lifetimes were measured on a Horiba Ultima-01-DD (HORIBA Jobin Yvon GmbH) applying the time-correlated single photon counting (TCSPC) technique at the Paderborn University. Samples were excited at specified wavelengths (Horiba DeltaDiode-300 LED, 20 MHz, HORIBA Jobin Yvon GmbH) and the emission was recorded at the given luminescence maximum until the peak signal reached a specified count. Decay data analysis was performed using the DAS6 software (version v 6.8, HORIBA Scientific). The goodness of the fits was evaluated by χ^2 values.

Cyclic Voltammetry:

Potentiometric measurements were performed in deoxygenated MeCN at room temperature using a *PGSTAT 101* potentiostat from *Metrohm-Autolab*. An analyte concentration of 10^{-3} M and a [*n*-Bu_4N][PF_6] concentration of 0.1 M as inert electrolyte were used. In a three-electrode configuration, a Pt working electrode (1 mm diameter), Ag/0.01 M $AgNO_3$, 0.1 M [*n*-Bu_4N][PF_6] in MeCN as reference electrode, and a Pt pin as a counter electrode were applied. After the measurements, ferrocene FcH was added as an internal standard to reference against the FcH/FcH^+ redox couple. The resulting voltammograms were analyzed using the software Nova 2.1.3. The reversibility of the redox couples was checked by using the criteria from Nicholson[139] and the Randles-Sevcik-equation.[140]

Spectroelectrochemistry:

Spectroelectrochemical and coulometric measurements were performed by Dr. Adam Neuba at room temperature in an optically transparent cell (d = 1 mm) using a deoxygenated MeCN/0.1 M [*n*-Bu_4N][PF_6] solution and a Pt wire mesh working electrode (counter electrode: Pt wire). Spectral changes during oxidations/reductions were recorded on a *Varian Cary 50* spectrophotometer.

Photocatalytic Experiments:

The reaction of 1,3-diphenyl-isobenzofuran (**DPBF**) with reactive oxygen $^1O_2$ was carried out at room temperature in MeOH under ambient conditions. 2.5 m **DPBF** (20 µM) were mixed with 0.5 ml complex (10^{-4} M) in a 1 cm path Hellma fluorescence cuvette and illuminated with λ = 480±5 nm in a *Jasco FP-8300* fluorescence spectrophotometer. The consumption of **DPBF** was detected by monitoring the decreasing luminescence intensity at 475 nm.

The reaction of anthracene and naphthalene-1,5-diole with reactive oxygen was carried out at room temperature in a mixture of $CHCl_3$ and MeOH. 2.5 ml of the substrate (200 µM in $CHCl_3$) were mixed with 0.5 ml of the complex (100 µM in MeOH) and irradiated by 300 W Xenon light source equipped with a long-pass filter (λ > 400 nm) to cut of short wavelengths. The progress of the reaction was tracked by absorption and emission spectroscopy.

Protonreduction was carried out in a homemade catalytic set up. 15 samples were irradiated in parallel by LEDs simulating a solar spectrum. The samples cooled by an *IKA HRC 2 control* thermostat. The temperature of the solution was controlled by a temperature sensor placed directly in a vial, which is containing the solvent used for catalysis. While illumination the change in pressure was detected in the catalytic experiments.

Computational Methods:

Quantum chemical calculations have been performed by the research group of Prof. Dr. Oliver Kühn at the University of Rostock. Absorption spectra were computed with linear-response time-dependent density functional theory (TD-DFT) using the optimally-tuned LC-BLYP functional together with the polarizable continuum model (PCM) to account for solvent effects (acetonitrile). The two-parameter optimal tuning of LC-BLYP was done via the ΔSCF method,[141] the details of the present setup can be found in the literature.[142] The 6-31G(d) basis set was used for the tuning procedure, while a larger basis set (def2-TZVP on Fe, 6-311G(d,p) on other atoms) was employed for calculations of absorption spectra. The broadening of the resulting stick spectra was done by Gaussians with a width (FWHM) of 0.15 eV. All calculations were performed with the Gaussian16 suite of programs.[143] Excited state analysis was performed using the TheoDORE package,[144] which enables automatic quantitative wavefunction analysis and localization of excitations at predefined molecular moieties. Pre- and post-processing of the data was done with homemade programs.

9.3 Syntheses

4'-(anthracen-9-yl)-2,2':6',2''-terpyridine **tpy-3:**

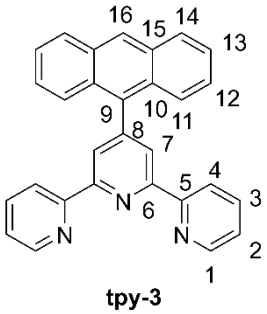

tpy-3

KOH (2.1 g, 37.5 mmol, 7.5 eq.) was suspended in ethanol (20 ml) and 2-acetylpyridine (2.8 ml, 25 mmol, 5 eq.) was added.[73] The reaction was stirred for 2 h at room temperature. 9-anthracenecarboxaldehyde **2-3** (1.031 g, 5 mmol, 1 eq.) was dissolved in THF (5 ml) and transferred to the previously described solution and stirred for 16 h at room temperature. Aqueous NH_3 (25 %, 15 ml) was added and stirred for additional 16 h. Precipitate was filtered, washed with water and methanol, and recrystallized with methanol from chloroform. Final **tpy-3** was obtained as yellow solid (53 %).

^{1}H-NMR (500 MHz, $CDCl_3$): δ (ppm) = 8.80 (dt, J = 8.5 Hz; J = 0.7 Hz, 2H, H_4); 8.64 (m, 2H, H_1); 8.62 (s, 2H, H_7); 8.55 (s, 1H, H_{16}); 8.07 (d, J = 8.5 Hz, 2H, H_{14}); 7.91 (dt, J = 7.8 Hz, J = 1.8, 2H, H_3); 7.72 (dd, J = 8.8 Hz, J = 0.7 Hz, 2H, H_{11}); 7.47 (m, 2H, H_{13}); 7.38 – 7.31 (m, 4H, H_{12} & H_2).

^{13}C-NMR (125 MHz, $CDCl_3$): δ (ppm) = 156.6 (s, 2C, C_5); 156.1 (s, 2C, C_6); 149.9 (s, 1C, C_8); 149.6 (s, 2C, C_1); 137.2 (s, 2C, C_3); 134.8 (s, 1C, C_9); 131.7 (s, 2C, C_{15}); 130.0 (s, 2C, C_{10}); 128.8 (s, 2C, C_{14}); 127.8 (s, 1C, C_{16}); 126.8 (s, 2C, C_{11}); 126.2 (s, 2C, C_{12}); 125.6 (s, 2C, C_{13}); 124.3 (s, 2C, C_7); 124.2 (s, 2C, C_2); 121.8 (s, 2C, C_4).

ESI-MS (pos) (m/z in MeCN) calculated for $C_{29}H_{19}FeN_3$: 409.1657; found: 410.1682$[M+H]^+$.

Elemental analysis calculated for $C_{29}H_{19}N_3$: C = 85.06 %, H = 4.68 %, N = 10.26 %.

Found: C = 84.46 %, H = 4.76 %, N = 10.33 %.

[Fe(tpy-3)$_2$](PF$_6$)$_2$:

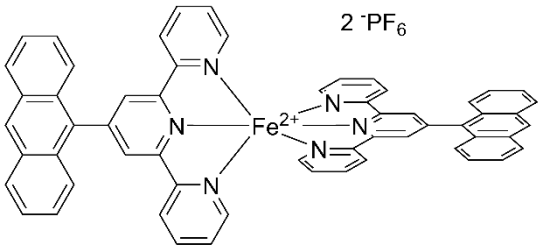

[Fe(typ-3)$_2$](PF$_6$)$_2$

tpy-3 (2 eq.) and $FeBr_2$ (1 eq.) were stirred in MeOH for 16 h. Insolouble solid was filtered, the filtrate was concentrated and dropped in an aqueous KPF_6 solution. Arising precipitate was filtered and washed with water. The crude product was dissolved in acetone and precipitated in diethylether.[71] After filtering, the product was purified by crystallization (solvent: acetone/anti-solvent: diethyl ether). **[Fe(tpy-3)$_2$]**$(PF_6)_2$ was obtained as violet crystals (90 %).

^{1}H-NMR (500 MHz, d_6-acetone): δ (ppm) = 9.44 (s, 4H, H_{tpy}); 8.99 (s, 2H, H_{ant}); 8.94 (d, 4H, $^3J_{HH}$ = 7.9 Hz, H_{tpy}); 8.38 (d, 4H, $^3J_{HH}$ = 8.4 Hz, H_{ant}); 8.34 (d, 4H, $^3J_{HH}$ = 8.4 Hz, H_{ant}); 8.10 (dt, 4H, $^3J_{HH}$ = 7.7 Hz, $^3J_{HH}$ = 1.3 Hz, H_{tpy}); 7.86 (d, 4H,$^3J_{HH}$ = 5.1 Hz, H_{tpy}); 7.75-7.70 (m, 4H, H_{ant}); 7.69-7.65 (m, 4H, H_{ant}); 7.44-7.39 (m, 4H, H_{tpy}).

^{13}C-NMR (125 MHz, d_6-acetone): δ (ppm) = 162.0 (s, C_q, 4C, C_{tpy}); 159.5 (s, C_q, 4C, C_{tpy}); 154.8 (s, 4C, C_{tpy}); 150.7 (s, C_q, 2C, C_{ant}); 140.0 (s, 4C, C_{tpy}); 133.1 (s, C_q, 2C, C_{tpy}); 132.6 (s, C_q, 4C, C_{ant}); 130.9 (s, C_q, 4C, C_{ant}); 130.0 (s, 2C, C_{ant}); 129.9 (s, 4C, C_{ant}); 128.8 (s, 4C, C_{tpy}); 128.1 (s, 4C, C_{ant}); 127.8 (s, 4C, C_{tpy}); 127.1 (s, 4C, C_{ant}); 126.8 (s, 4C, C_{ant}); 125.4 (s, 4C, C_{tpy}).

ESI-MS (pos) (m/z in MeCN) calculated for $C_{58}H_{38}N_6Fe^{2+}$ $[M]^{2+}$:437.1248; found: 437.1274 $[M]^{2+}$.

Elemental analysis calculated for $C_{58}H_{38}N_6F_{12}FeP_2$: C = 59.81 %, H = 3.29 %, N = 7.22 %.

Found: C = 59.67 %, H = 3.42 %, N = 7.38 %.

4'-(pyren-1-yl)-2,2':6',2''-terpyridine **tpy-4:**

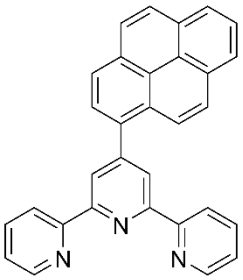

tpy-4

KOH (0.842 g, 15 mmol, 7.5 eq.) was suspended in ethanol (15 ml) and 2-acetylpyridine (1.1 ml, 10 mmol, 5 eq.) was added.[73] The reaction was stirred for 2 h at room temperature. 1-pyrenecarboxaldehyde **2-4** (465 mg, 2 mmol, 1 eq.) was dissolved in THF (5 ml) and transferred to the previously described solution and stirred for 16 h at room temperature. Aqueous NH_3 (25 %, 15 ml) was added and stirred for additional 16 h. Precipitate was filtered, washed with water and methanol, and resolved in a minimal amount of hot chloroform. Addition of methanol forced the precipitation of a green solid, which was filtered. The remaining solution was cooled to 0 °C for 1 h and precipitating yellow **tpy-4** was filtered (27 %).

^{1}H-NMR (500 MHz, $CDCl_3$): δ (ppm) = 8.79 (s, 2H, H_{tpy}); 8.76 (d, 2H, $^3J_{HH}$ = 8.0 Hz, H_{tpy}); 8.70 (d, 2H, $^3J_{HH}$ = 4.7 Hz, H_{tpy}); 8.28-8.05 (m, 8H, H_{pyrene}); 8.03 (t, 1H, $^3J_{HH}$ = 7.6 Hz, H_{pyrene}); 7.91 (dt, $^3J_{HH}$ = 7.8 Hz, $^3J_{HH}$ = 1.8 Hz, H_{tpy}); 7.35 (ddd, 2H, $^3J_{HH}$ = 7.5 Hz, $^3J_{HH}$ = 4.7 Hz, $^3J_{HH}$ = 1.2 Hz, H_{tpy}).

^{13}C-NMR (125 MHz, $CDCl_3$): δ (ppm) = 156.5 (s, C_q, 2C, C_{tpy}); 155.8 (s, C_q, 2C, C_{tpy}); 151 (s, C_q, 1C, C_{pyrene}); 149.4 (s, 2C, C_{tpy}); 137.0 (s, 2C, C_{tpy}); 135.4 (s, C_q, 1C, C_{tpy}); 131.6 (s, C_q, 1C, C_{pyrene}); 131.5 (s, C_q, 1C, C_{pyrene}); 131.1 (s, C_q, 1C, C_{pyrene}); 128.5 (s, C_q, 1C, C_{pyrene}); 128.3 (s, 1C, C_{pyrene}); 128.0 (s, 1C, C_{pyrene}); 127.6 (s, 1C, C_{pyrene}); 127.4 (s, 1C, C_{pyrene}); 126.2 (s, 1C, C_{pyrene}); 125.5 (s, 1C, C_{pyrene}); 125.3 (s, 1C, C_{pyrene}); 125.1(s, C_q, 1C, C_{pyrene}); 125.0 (s, C_q, 1C, C_{pyrene}); 124.9 (s, 1C, C_{pyrene}); 124.0 (s, 1C, C_{pyrene}); 124.0 (s, 2C, C_{tpy}); 123.0 (s, 2C, C_{tpy}); 121.6 (s, 2C, C_{tpy}).

ESI-MS (pos) (m/z in MeCN) calculated for $C_{31}H_{19}N_3$ [M]: 433.1579; found: 434.1756 $[M+H]^+$

Elemental analysis calculated for $C_{31}H_{19}N_3$: C = 85.89 %, H = 4.42 %, N = 9.69 %.

Found: C = 84.93 %, H = 4.46 %, N = 9.68 %.

[Fe(tpy-4)$_2$](PF$_6$)$_2$:

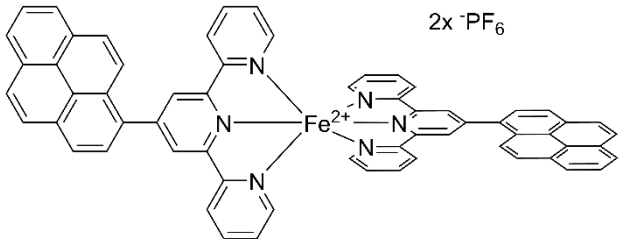

[Fe(tpy-4)$_2$](PF$_6$)$_2$

tpy-4 (2 eq.) and $FeBr_2$ (1 eq.) were stirred in MeOH for 16 h. Insolouble solid was filtered, the filtrate was concentrated and dropped in a aqueous KPF_6 solution. Arising precipitate was filtered and washed with water. The crude product was dissolved in acetone and precipitated in diethylether.[71] After filtering, the product was purified by crystallization (solvent: acetone/anti-solvent: diethyl ether). **[Fe(tpy-4)$_2$](PF$_6$)$_2$** was obtained as violet crystals (80 %).

^{1}H-NMR (500 MHz, d_6-acetone): δ (ppm) = 9.63 (s, 4H, H_{tpy}); 9.03 (d, 4H, $^3J_{HH}$ = 7.9 Hz, H_{tpy}); 8.88 (d, 2H, $^3J_{HH}$ = 9.2 Hz, H_{pyrene}); 8.67 (q, 4H, $^3J_{HH}$ = 3.0 Hz, H_{pyrene}); 8.49 (q, 4H, $^3J_{HH}$ = 7.6 Hz, H_{pyrene}); 8.42 (t, 6H, $^3J_{HH}$ = 8.5 Hz, H_{pyrene}); 8.24 (t, 2H, $^3J_{HH}$ = 7.5 Hz, H_{pyrene}); 8.11 (t, 4H, $^3J_{HH}$ = 7.5 Hz, H_{tpy}); 7.81 (d, 4H, $^3J_{HH}$ = 5.2 Hz, H_{tpy}); 7.36 (t, 4H, $^3J_{HH}$ = 6.4 Hz, H_{tpy}).

^{13}C-NMR (125 MHz, d_6-acetone): δ (ppm) = 160.6 (s, C_q, 4C, C_{tpy}); 158.6 (s, C_q, 4C, C_{tpy}); 153.6 (s, 4C, C_{tpy}); 151.4 (s, C_q, 2C, C_{pyrene}); 139.0 (s, 4C, C_{tpy});133.3 (s, C_q, 2C, C_{tpy}); 132.5 (s, C_q, 2C, C_{pyrene}); 131.6 (s, C_q, 2C, C_{pyrene}); 131.1 (s, C_q, 2C, C_{pyrene}); 129.1 (s, 2C, C_{pyrene}); 128.9 (s, 2C, C_{pyrene}); 128.7 (s, C_q, 2C, C_{pyrene}); 128.3 (s, 2C, C_{pyrene}); 127.7 (s, 4C, C_{tpy}); 127.5 (s, 2C, C_{pyrene}); 126.9 (s, 2C, C_{pyrene}); 126.3 (s, 2C, C_{pyrene}); 125.9 (s, 2C, C_{pyrene}); 125.6 (s, 4C, C_{tpy}); 125.3 (s, 2C, C_{pyrene}); 124.9 (s, C_q, 2C, C_{pyrene}); 124.5 (s, C_q, 2C, C_{pyrene}); 124.5 (s, 2C, C_{pyrene}); 124.3 (s, 4C, C_{tpy}).

ESI-MS (pos) (m/z in MeCN) calculated for $C_{62}H_{38}N_6Fe^{2+}$ $[M]^{2+}$:461.1248; found: 461.1332 $[M]^{2+}$.

Elemental analysis calculated for $C_{62}H_{38}N_6F_{12}FeP_2$: C = 61.40 %, H = 3.16 %, N = 6.93 %.

Found: C = 60.57 %, H = 4.06 %, N = 6.41 %.

2,6-dichloropyridine 1-oxide **4**:

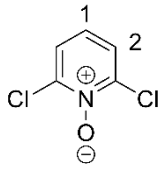

4

2,6-dichloropyridine **3** (11.1 g, 75 mmol, 1 eq.) was dissolved in trifluoroacetic acid (90 ml). Aqueous H_2O_2 (35 %, 20 ml) was added dropwise while stirring. The solution was heated to 100 °C for 4 h. The yellow solution was cooled to room temperature and water (30 ml) was added dropwise. The resulting solid was filtered, and the remaining solution was extracted with DCM (10 x 30 ml). The combined organic layers were washed by an aqueous K_2CO_3-solution (3 x 30 ml). n-hexane was added, and the volume was reduced. Precipitated solid was filtered and **4** was obtained as colorless solid (70 %).[74]

^{1}H-NMR (500 MHz, $CDCl_3$): δ (ppm) = 7.44 (d, $^3J_{HH}$ = 8.2 Hz, 2H, H_2); 7.11 (t, $^3J_{HH}$ = 8.2 Hz, 1H, H_1).

ESI-MS (pos) (m/z in MeCN) calculated for $C_5H_3Cl_2NO$: 162.9670; found: 163.9675 $[M+H]^+$.

2,6-dichloro-4-nitropyridine 1-oxide **5**:

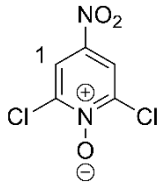

5

4 (8.64 g, 52.5 mmol, 1 eq.) was dissolved in concentrated H_2SO_4 (50 ml) and red fuming HNO_3 (20 ml) and stirred 20 h at 60 °C. The resulting yellow solution was cooled to room temperature and neutralized by aqueous NH_3 (25 %, 100 ml) while cooling in an ice bath. The precipitating solid was filtered and **5** was obtained as colorless crystals (60 %).[74]

^{1}H-NMR (500 MHz, $CDCl_3$): δ (ppm) = 8.31 (s, 2H, H_1).

ESI-MS (pos) (m/z in MeOH) calculated for $C_5H_2Cl_2N_2O_3$: 207.9521; found: 208.9508 $[M+H]^+$.

2,6-dichloropyridin-4-amine **6**:

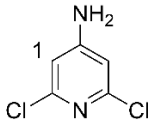

6

5 (6.52 g, 31.2 mmol, 1 eq.) was suspended in concentrated acetic acid (100 ml) and heated to 100 °C. Iron powder (8.68 g, 156 mmol, 5 eq.) was added in portions within 15 min, while evolution of gases was obtained. The dark red suspension was stirred for 24 h at 100 °C. After cooling to room temperature, the suspension was neutralized by concentrated NaOH (200 ml) and extracted with diethyl ether (5 x 50 ml).[75] The crude product was recrystallized in chloroform. **6** was obtained as colorless crystals (88 %).

^{1}H-NMR (500 MHz, DMSO-d_6): δ (ppm) = 6.73 (s, H_{amin}, 2H); 6.50 (s, H_1, 2H).

ESI-MS (pos) (m/z in MeOH) calculated for $C_5H_4Cl_2N_2$: 161.9830; found: 162.9835 $[M+H]^+$.

2,6-dichloro-4-iodopyridine **7**:

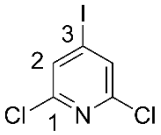

7

Synthetic procedure 1: Sandmeyer reaction

6 (815 mg, 5 mmol, 1 eq.) was suspended in HCl (37 %, 20 ml) and stirred for 24 h at room temperature. It was cooled to 0 °C and $NaNO_2$ (690 mg, 10 mmol, 2 eq.) dissolved in 5 ml water was added dropwise. KI (2075 mg, 12.5 mmol, 2.5 eq.) was dissolved in 10 ml water and was added to the previously described suspension. It was stirred until no further gas evolution was observed. The suspension was dissolved in THF (15 ml) and extracted with diethyl ether (5 x 30 ml). The combined organic layers were washed in saturated NaS_2O_3-solution, until no color-change was observed. The organic layer was dried over Na_2SO_4, and the crude product was obtained by removing the solvent. It was purified by column chromatography (stationary phase: SiO_2/ mobile phase: n-hexane) and **7** was obtained as orange solid (58 %).[76]

Synthetic procedure 2: Deprotonation by n-butyllithium

6 (1 eq.) was dissolved in dry THF (20 ml) and cooled to -78 °C. n-butyllithium (1 eq., 1M in THF) was added dropwise and it was stirred for 45 min. Iodine (1.1 eq.) dissolved in dry THF (10 ml) was added dropwise and it was stirred for 1 h at -78 °C and 1 h at room temperature. The reaction was stopped by the addition of saturated aqueous NaS_2O_3-solution. The mixture was extracted by diethyl ether. The combined organic layers were dried over Na_2SO_4. The crude product was obtained after removing the solvent. **7** was purified by fractional crystallization from ethanol (30 %).[77]

Synthetic procedure 3: Deprotonation by TMPMgCl

3 (1 eq.) dissolved in THF was added dropwise to a solution of tetramethylpiperidine-magnesium/lithium-chloride (1M in THF, 1.05 eq.) and stirred for 1 h at room temperature. The solution was cooled down to -30 °C and iodine (1.1 eq. in THF) was added dropwise. After stirring for 30 min the remaining iodine was deactivated by adding a saturated aqueous $Na_2S_2O_4$ solution. The aqueous layer was extracted with dichloromethane and the combined organic layers were dried over Na_2SO_4. While removing the solvent under reduced pressure the product precipitated as a colorless solid (68 %).[78]

^{1}H-NMR (700 MHz, $CDCl_3$): δ (ppm) = 7.68 (s, 2H, H_2).

^{13}C-NMR (176 MHz, $CDCl_3$): δ (ppm) = 150.7 (s, 2C, C_q, C_1); 131.5 (s, 2C, C_2); 107.6 (s, 1C, C_q, C_3).

ESI-MS (pos) (m/z in MeCN) calculated for $C_5H_2Cl_2IN$: 272.8609; found: 273.8671 $[M+H]^+$.

Elemental analysis calculated for $C_5H_2Cl_2IN$: C = 21.93 %, H = 0.74 %, N = 5.11 %.

Found: C = 22.88 %, H = 1.19 %, N = 5.22 %.

General procedure for 4-chromophore-2,6-dichloropyridine **8-R**:

Palladium acetate (0.05 eq.) and SPhos (0.22 eq.) were stirred in degassed toluene under inert conditions for 30 min. In parallel 4-iodo-2,6-dichloropyridine **7** (1 eq.) and the corresponding boronic acid (1.2 eq.) were suspended in degassed toluene under inert conditions. Solution containing the Pd-catalyst was transferred to the reactants' suspension. K_2CO_3 (2.4 eq.) was solved in water and degassed by argon and transferred to the reaction mixture. The mixture was stirred at 105 °C for three days. Reaction was cooled down to room temperature and extracted with DCM. Combined organic layers were washed with water and dried over Na_2SO_4. The solvent was removed under reduced pressure and the product was obtained after flash chromatography.[36]

2,6-dichloro-4-phenylpyridine **8-1**:

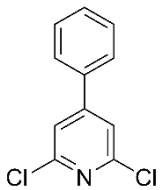

8-1

8-1 is obtained as colorless oil. The product could not be obtained without impurities (The yield of the crude product is 58 %).

2,6-dichloro-4-(naphthalene-1-yl)pyridine **8-2**:

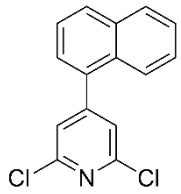

8-2

Following the general procedure, the product was obtained as a colorless solid (62 %).

^{1}H-NMR (700 MHz, $CDCl_3$): δ (ppm) = 7.97-7.93 (m, 2H, $H_{naphthalene}$); 7.79-7.76 (m, 1H, $H_{naphthalene}$); 7.58-7.52 (m, 3H, $H_{naphthalene}$); 7.42 (s, 2H, $H_{pyridine}$); 7.40 (dd, 1H, $^{3}J_{HH}$ = 7.7 Hz, $^{3}J_{HH}$ = 0.6 Hz, $H_{naphthalene}$).

^{13}C-NMR (176 MHz, $CDCl_3$): δ (ppm) = 154.7 (s, C_q, 1C, $C_{naphthalene}$); 151.0 (s, C_q, 2C, $C_{pyridine}$); 135.1 (s, C_q, 1C, $C_{pyridine}$); 134.1 (s, C_q, 1C, $C_{naphthalene}$); 130.7 (s, C_q, 1C, $C_{naphthalene}$); 130.3 (s, 1C, $C_{naphthalene}$); 129.1 (s, 1C, $C_{naphthalene}$); 127.6 (s, 1C, $C_{naphthalene}$); 127.4 (s, 1C, $C_{naphthalene}$); 126.9 (s, 1C, $C_{naphthalene}$); 125.6 (s, 1C, $C_{naphthalene}$); 124.9 (s, 1C, $C_{naphthalene}$); 124.4 (s, 2C, $C_{pyridine}$).

ESI-MS (pos) (m/z in MeCN) calculated for $C_{15}H_9Cl_2N$: 273.0112; found: 274.0211 $[M+H]^+$.

4-(anthracen-9-yl)-2,6-dichloropyridine **8-3**:

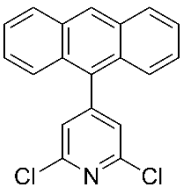

8-3

Following the general procedure, the product was obtained as a bright yellow solid (58 %).

^{1}H-NMR (700 MHz, $CDCl_3$): δ (ppm) = 8.57 (s, 1H, $H_{anthracene}$); 8.07 (d, 2H, $^{3}J_{HH}$ = 8.4 Hz, $H_{anthracene}$); 7.51-7.47 (m, 4H, $H_{anthracene}$); 7.47-7.45, 2H, $H_{anthracene}$); 7.39 (s, 2H, $H_{pyridine}$).

^{13}C-NMR (176 MHz, $CDCl_3$): δ (ppm) = 153.5 (C_q, 1C, $C_{anthracene}$); 151.2 (C_q, 2C, $C_{pyridine}$); 131.3 (C_q, 2C, $C_{anthracene}$); 130.7 (C_q, 1C, $C_{pyridine}$); 129.4 (C_q, 2C, $C_{anthracene}$); 128.9 (s, 2C, $C_{anthracene}$); 128.8 (s, 1C, $C_{anthracene}$); 126.9 (s, 2C, $C_{anthracene}$); 125.8 (s, 2C, $C_{pyridine}$); 125.7 (s, 2C, $C_{anthracene}$); 125.4 (s, 2C, $C_{anthracene}$).

ESI-MS (pos) (m/z in MeCN) calculated for $C_{19}H_{11}Cl_2N$: 323.0269; found: 324.0336 $[M+H]^+$.

2,6-dichloro-4-(pyren-1-yl)pyridine **8-4**:

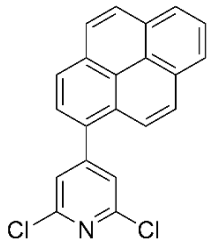

8-4

Following the general procedure, the product was obtained as a bright yellow solid (86 %).

^{1}H-NMR (700 MHz, $CDCl_3$): δ (ppm) = 8.27 (d, 1H, $^{3}J_{HH}$ = 7.6 Hz, H_{pyrene}); 8.24 (d, 2H, $^{3}J_{HH}$ = 7.8 Hz, H_{pyrene}); 8.18-8.04 (m, 5H, H_{pyrene}); 7.90 (d, 1H, $^{3}J_{HH}$ = 7.8 Hz, H_{pyrene}); 7.56 (s, 2H, $H_{pyridine}$).

^{13}C-NMR (176 MHz, $CDCl_3$): δ (ppm) = 155.2 (s, 1C, C_q, C_{pyrene}); 151.1 (s, 2C, C_q, $C_{pyridine}$); 132.4 (s, 1C, C_q, C_{pyrene}); 131.9 (s, 1C, C_q, $C_{pyridine}$); 131.7 (s, 1C, C_q, C_{pyrene}); 131.1 (s, 1C, C_q, C_{pyrene}); 129.4 (s, 1C, C_{pyrene}); 129.1 (s, 1C, C_{pyrene}); 128.5 (s, 1C, C_q, C_{pyrene}); 127.6 (s, 1C, C_{pyrene}); 127.1 (s, 1C, C_{pyrene}); 126.9 (s, 1C, C_{pyrene}); 126.4 (s, 1C, C_{pyrene}); 126.1 (s, 1C, C_{pyrene}); 125.3 (s, 1C, C_q, C_{pyrene}); 125.2 (s, 1C, C_{pyrene}); 124.9 (s, 1C, C_q, C_{pyrene}); 124.8 (s, 2C, $C_{pyridine}$); 123.8 (s, 1C, C_{pyrene}).

ESI-MS (pos) (m/z in MeCN) calculated for $C_{19}H_{11}Cl_2N$: 347.0269; found: 348.0432 $[M+H]^+$.

2,6-dichloro-4-(perylen-3-yl)pyridine **8-5**:

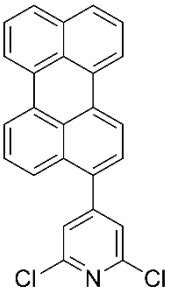

8-5

In contrast to the general procedure the corresponding 4,4,5,5-tetramethyl-2-(perylen-3-yl)-1,3,2-dioxaborolane has been used instead of the boronic acid. All other parameters are the same as described in the general procedure. **8-5** has been obtained as yellow solid (94 %).

^{1}H-NMR (700 MHz, $CDCl_3$): δ (ppm) = 8.27 (d, 1H, $^{3}J_{HH}$ = 7.3 Hz, $H_{perylene}$); 8.24 (t, 1H, $^{3}J_{HH}$ = 7.6 Hz, $H_{perylene}$); 7.76-7.74 (m, 2H, $H_{perylene}$); 7.64-7.63 (m, 1H, $H_{perylene}$); 7.53 (t, 3H, $^{3}J_{HH}$ = 7.8 Hz, $H_{perylene}$); 7.46 (s, 2H, $H_{pyridine}$); 7.40 (d, 1H, $^{3}J_{HH}$ = 7.7 Hz, $H_{perylene}$).

^{13}C-NMR (176 MHz, $CDCl_3$): δ (ppm) = 154.5 (s, C_q, 1C, $C_{perylene}$); 151.0 (s, C_q, 2C, $C_{pyridine}$); 134.8 (s, C_q, 1C, $C_{perylene}$); 134.2 (s, C_q, 1C, $C_{pyridine}$); 133.2 (s, C_q, 1C, $C_{perylene}$); 132.1 (s, C_q, 1C, $C_{perylene}$); 132.0 (s, C_q, 1C, $C_{perylene}$); 131.0 (s, C_q, 1C, $C_{perylene}$); 130.7 (s, C_q, 1C, $C_{perylene}$); 129.3 (s, C_q, 1C, $C_{perylene}$); 129.0 (s, 1C, $C_{perylene}$); 128.7 (s, C_q, 1C, $C_{perylene}$); 128.6 (s, 1C, $C_{perylene}$); 128.0 (s, 1C, $C_{perylene}$); 127.9 (s, 1C, $C_{perylene}$); 127.0 (s, 1C, $C_{perylene}$); 126.9 (s, 1C, $C_{perylene}$); 124.5 (s, 1C, $C_{perylene}$); 124.1 (s, 2C, $C_{pyridine}$); 121.2 (s, 1C, $C_{perylene}$); 121.1 (s, 1C, $C_{perylene}$); 121.0 (s, 1C, $C_{perylene}$); 119.8 (s, 1C, $C_{perylene}$).

General Procedure for 2,6-di(1*H*-imidazol-1-yl)-4-(chromophore)pyridine **9-R**:

Corresponding 4-chromophore-2,6-dichloropyridine **8-R** (1 eq.), imidazole (2.4 eq.), potassium carbonate (2.4 eq.) and copper(I)oxide (0.2 eq.) were suspended in DMF (10 ml/mmol), degassed by bubbling through with argon and stirred at 150°C for 48 h. DMF was removed under reduced pressure. Flash chromatography with pure DCM gave not reacted educt and incompletely coupled 4-chromophore-2,6-dichloropyridine and imidazole. Corresponding 2,6-di(1*H*-imidazol-1-yl)-4-(chromophore)pyridine **9-R** was obtained by flash chromatography with DCM/MeOH (9/1 V/V) afterwards. If the product was containing imidazole, the mixture was dissolved in DCM and extracted with water to transfer residual imidazole to the aqueous phase.[36]

2,6-di(1H-imidazol-1-yl)pyridine **9-0**:

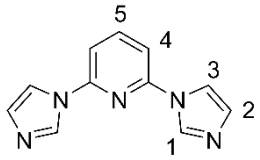

9-0

In contrast to the general procedure 2,6-dibromopyridine **3Br** was used instead of the dichloro-derivate **3**. The product **9-0** was obtained as colorless solid (82 %).

^{1}H-NMR (700 MHz, d_6-DMSO): δ (ppm) = 8.77 (s, 2H, $H_{imidazole}$); 8.18 (t, 1H, $^{3}J_{HH}$ = 8.01 Hz, H_5); 8.15 (s, 2H, $H_{imidazole}$); 7.75 (d, 2H, $^{3}J_{HH}$ = 8.01 Hz, H_4); 7.18 (s, 2H, $H_{imidazole}$).

^{13}C-NMR (176 MHz, d_6-DMSO): δ (ppm) = 109.9 (C_4); 117.0 ($C_{imidazole}$); 130.4 ($C_{imidazole}$); 135.8 ($C_{imidazole}$); 143.0 (C_5); 147.7 (C_q).

ESI-MS (pos) (m/z in MeCN): calculated for $C_{11}H_9N_5$: 211.0850; found: 212.0960 $[M+H]^+$.

2,6-di(1*H*-imidazol-1-yl)-4-(naphthalen-1-yl)pyridine **9-2**:

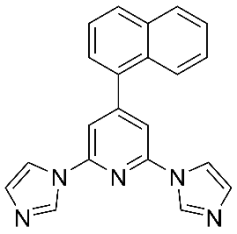

9-2

The product was obtained according to general procedure as colorless solid. **9-2** was not obtained without small amount of impurities, therefore no NMR analytic is given. The yield is calculated referring to the crude product (83 %).

ESI-MS (pos) (m/z in MeCN): calculated for $C_{21}H_{15}N_5$: 337.1327; found: 338.1436 $[M+H]^+$.

4-(anthracen-9-yl)-2,6-di(1*H*-imidazol-1-yl)pyridine **9-3**:

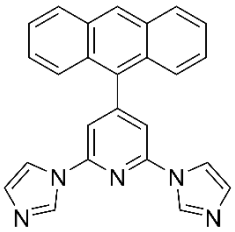

9-3

In contrast to the general procedure the reaction mixture was stirred for 72 h at 150°C to optimize yield. Product **9-3** was obtained as bright yellow solid (85 %).

^{1}H-NMR (700 MHz, d_6-DMSO): δ (ppm) = 8.87 (t, 2H, $^{3}J_{HH}$ = 1.0 Hz, $H_{imidazole}$); 8.82 (s, 1H, $H_{anthracene}$); 8.24 (t, 2H, $^{3}J_{HH}$ = 1.3 Hz, $H_{imidazole}$); 8.22 (d, 2H, $^{3}J_{HH}$ = 8.5 Hz, $H_{anthracene}$); 7.96 (s, 2H, $H_{pyridine}$); 7.71 (d, 2H, $^{3}J_{HH}$ = 8.4 Hz, $H_{anthracene}$); 7.60-7.57 (m, 2H, $H_{anthracene}$); 7.53-7.48 (m, 2H, $H_{anthracene}$); 7.16 (t, 2H, $^{3}J_{HH}$ = 1.1 Hz, $H_{imidazole}$).

^{13}C-NMR (176 MHz, d_6-DMSO): δ (ppm) = 153.8 (s, C_q, 1C, $C_{anthracene}$); 148.1 (s, C_q, 2C, $C_{pyridine}$); 135.8 (s, 2C, $C_{imidazole}$); 132.5 (s, C_q, 1C, $C_{pyridine}$); 130.7 (s, C_q, 2C, $C_{anthracene}$); 130.4 (s, 2C, $C_{imidazole}$); 128.8 (s, C_q, 2C, $C_{anthracene}$); 128.5 (s, 2C, $C_{anthracene}$); 127.8 (s, 1C, $C_{anthracene}$); 126.7 (s, 2C, $C_{anthracene}$); 125.7 (s, 2C, $C_{anthracene}$); 125.6 (s, 2C, $C_{anthracene}$); 116.9 (s, 2C, $C_{imidazole}$); 112.0 (s, 2C, $C_{pyridine}$).

ESI-MS (pos) (m/z in MeCN): calculated for $C_{25}H_{17}N_5$: 387.1484; found: 388.1566 $[M+H]^+$.

2,6-di(1*H*-imidazol-1-yl)-4-(pyren-1-yl)pyridine **9-4**:

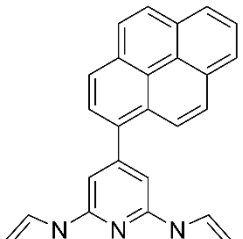

9-4

The product **9-4** was obtained as bright yellow solid (92 %).

^{1}H-NMR (700 MHz, $CDCl_3$): δ (ppm) = 8.48 (t, 2 H, $^{3}J_{HH}$ = 1.1 Hz, $H_{imidazole}$); 8.32-8.25 (m, 3H, H_{pyrene}); 8.21-8.08 (m, 5H, H_{pyrene}); 8.01 (d, 1H, $^{3}J_{HH}$ = 7.8 Hz, H_{pyrene}); 7.75 (t, 2H, $^{3}J_{HH}$ = 1.4 Hz, $H_{imidazole}$); 7.55 (s, 2H, $H_{pyridine}$); 7.27 (m, 2H, $H_{imidazole}$).

^{13}C-NMR (176 MHz, $CDCl_3$): δ (ppm) = 156.4 (s, 1C, C_q, C_{pyrene}); 148.7 (s, 2C, C_q, $C_{pyridine}$); 135.4 (s, 2C, $C_{imidazole}$); 132.7 (s, 1C, C_q, $C_{pyridine}$); 132.4 (s, 1C, C_q, C_{pyrene}); 131.6 (s, 1C, C_q, C_{pyrene}); 131.4 (s, 2C, $C_{imidazole}$); 130.9 (s, 1C, C_q, C_{pyrene}); 129.4 (s, 1C, C_{pyrene}); 129.0 (s, 1C, C_{pyrene}); 128.4 (s, 1C, C_q, C_{pyrene}); 127.4 (s, 1C, C_{pyrene}); 126.9 (s, 1C, C_{pyrene}); 126.7 (s, 1C, C_{pyrene}); 126.4 (s, 1C, C_{pyrene}); 126.0 (s, 1C, C_{pyrene}); 125.2 (s, 1C, C_q, C_{pyrene}); 125.1 (s, 1C, C_{pyrene}); 124.8 (s, 1C, C_q, C_{pyrene}); 123.6 (s, 1C, C_{pyrene}); 116.5 (s, 2C, $C_{imidazole}$); 111.7 (s, 2C, $C_{pyridine}$).

ESI-MS (pos) (m/z in MeCN): calculated for $C_{27}H_{17}N_5$: 411.1484; found: 412.1675 $[M+H]^+$.

2,6-di(1*H*-imidazol-1-yl)-4-(perylen-3-yl)pyridine **9-5**:

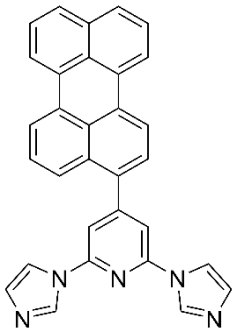

9-5

The product **9-5** was obtained as yellow solid (80 %).

^{1}H-NMR (700 MHz, d_6-DMSO): δ (ppm) = 8.86 (t, 2H, J = 1.0 Hz, $H_{imidazole}$); 8.53 (d, 1H, J = 7.9 Hz, $H_{perylene}$); 8.49-8.47 (m, 2H, $H_{perylene}$); 8.44 (d, 1H, J = 7.2 Hz, $H_{perylene}$); 8.24 (t, 2H, J = 1.4 Hz, $H_{imidazole}$); 7.98 (s, 2H, $H_{pyridine}$); 7.87-7.84 (m, 2H, $H_{perylene}$); 7.79 (d, 1H, J = 8.5 Hz, $H_{perylene}$); 7.68 (d, 1H, J = 7.7 Hz; $H_{perylene}$); 7.61-7.58 (m, 3H, $H_{perylene}$); 7.17 (t, 2H, J = 1.0 Hz, $H_{imidazole}$).

^{13}C-NMR (176 MHz, d_6-DMSO): δ (ppm) = 154.8 (s, C_q, $C_{perylene}$, 1C); 148.0 (s, C_q, $C_{pyridine}$, 2C); 135.8 (s, $C_{imidazole}$, 2C); 135.7 (s, C_q, $C_{pyridine}$, 1C); 134.3 (s, C_q, $C_{perylene}$, 1C); 131.7 (s, C_q, $C_{perylene}$, 1C); 130.9 (s, C_q, $C_{perylene}$, 1C); 130.3 (s, C_q, $C_{perylene}$, 1C); 130.3 (s, $C_{imidazole}$, 2C); 130.0 (s, C_q, $C_{perylene}$, 1C); 128.6 (s, $C_{perylene}$, 1C); 128.3 (s, $C_{perylene}$, 1C); 128.2 (s, $C_{perylene}$, 1C); 128.1 (s, $C_{perylene}$, 1C); 127.9 (s, $C_{perylene}$, 1C); 127.8 (s, C_q, $C_{perylene}$, 1C); 127.1 (s, $C_{perylene}$, 1C); 125.3 (s, $C_{perylene}$, 1C); 121.4 (s, $C_{perylene}$, 1C); 121.3 (s, $C_{perylene}$, 1C); 121.2 (s, $C_{perylene}$, 1C); 120.3 (s, $C_{perylene}$, 1C); 117.0 (s, $C_{imidazole}$, 2C); 116.8 (s, C_q, $C_{perylene}$, 1C); 110.9 (s, $C_{pyridine}$, 2C).

ESI-MS (pos) (m/z in MeCN) calculated for $C_{31}H_{19}N_5$: 461.1640; found: 462.1725 $[M+H]^+$.

1,1‘-(4-phenylpyridine-2,6-diyl)bis(3-methyl-1*H*-imidazol-3-ium) **[H_2-bim-1](PF_6)$_2$**:

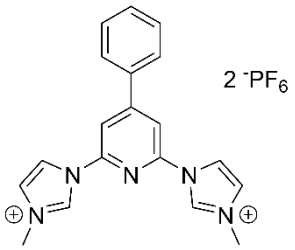

[H_2-bim-1](PF_6)$_2$

2,6-dichloro-4-phenylpyridine **8-1** (1 eq.) was suspended in *N*-methylimidazole (10 eq.) under reduced pressure in a small vial and heated to 150°C for 5 d. After cooling down to room temperature and precipitation was forced by adding acetone. Precipitate was filtered, dissolved in a small MeOH, and added dropwise to an aqueous solution of KPF_6 (10 eq.). After cooling in an ice bath, the precipitate was filtered, washed by cold water and dissolved in a small amount of acetone. The solution was added dropwise to an ice-cold diethyl ether and the product was filtered (23 %). Crystals could be obtained by diffusion of *n*-pentane in a solution of the product in acetone. This synthetic procedure could only be successfully transferred to unfunctionalized ligand.[39]

ESI-MS (pos) (m/z in MeCN): calculated for $C_{19}H_{19}N_5^{2+}$: 158.5815; found: 158.5846 $[M\text{-}2\ ^-PF_6]^{2+}$.

^{1}H-NMR (700 MHz, d_6-acetone): δ (ppm) = 10.09 (s, 2H, $H_{imidazole}$); 8.80 (t, 2H, J = 1.9 Hz, $H_{imidazole}$); 8.61 (s, 2H, $H_{pyridine}$); 8.08-8.07 (m, 2H, H_{phenyl}); 8.06 (t, 2H, J = 1.8 Hz, $H_{imidazole}$); 7.66-7.65 (m, 3H, H_{phenyl}); 4.26 (s, 6H, H_{methyl}).

^{13}C-NMR (176 MHz, d_6-acetone): δ (ppm) = 158.0 (s, C_q, 1C, C_{phenyl}); 147.5 (s, C_q, 2C, $C_{pyridine}$); 137.0 (s, 2C, $C_{imidazole}$); 136.3 (s, C_q, 1C, $C_{pyridine}$); 132.3 (s, 1C, C_{phenyl}); 130.5 (s, 2C, C_{phenyl}); 128.7 (s, 2C, C_{phenyl}); 126.4 (s, 2C, $C_{imidazole}$); 120.8 (s, 2C, $C_{imidazole}$); 113.3 (s, 2C, $C_{pyridine}$); 37.7 (s, 2C, C_{methyl}).

General procedure for 1,1‘-(4-Chromophore-pyridine-2,6-diyl)bis(3-methyl-1*H*-imidazol-3-ium) **[H_2-bim-R](PF_6)$_2$**:

The corresponding 2,6-di(1*H*-imidazol-1-yl)-4-(chromophore)pyridine **9-R** (1 eq.) was suspended in DCM under inert conditions and cooled down to -78°C. Methyl trifluoromethanesulfonate (MeOTf; 2.05 eq.) was added dropwise. The suspension was stirred for 16 h while slowly getting up to room temperature. It was cooled in an ice bath again and *n*-pentane was added. The product **[H_2-bim-R]**(OTf)$_2$ was obtained as unsolved particles, filtered and if necessary, washed again by cold *n*-pentane.[36]

1,1’-(pyridine-2,6-diyl)bis(3-methyl-1H-imidazol-3-ium) **[H_2-bim](OTf)$_2$**:

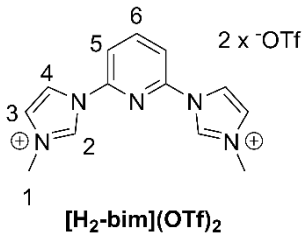

[H_2-bim](OTf)$_2$

The product was obtained as colorless solid (95 %).

^{1}H-NMR (700 MHz, d_6-acetone): δ (ppm) = 10.22 (s, 2H, H_2); 8.67 (t, 2H, $^3J_{HH}$ = 1.9 Hz, H_4); 8.36 (t, 1H, $^3J_{HH}$ = 8.1 Hz, H_6); 8.19 (d, 2H, $^3J_{HH}$ = 8.1 Hz, H_5); 7.96 (t, 2H, $^3J_{HH}$ = 3.6 Hz, H_3); 4.19 (s, 6H, H_1).

^{13}C-NMR (176 MHz, d_6-acetone): δ (ppm) = 37.5 (C_1); 115.5 (C_5); 120.5 (C_4); 126.4 (C_3); 137.3 (C_2); 146.0 (C_6); 146.8 (C_q). (quartet-signal of triflate- anions!)

ESI-MS (pos) (m/z in MeCN): calculated for $C_{13}H_{15}N_5^{2+}$: 120.5658; found: 120.5680 [M-2 $^-$OTf]$^{2+}$.

1,1‘-(4-(naphthalen-1-yl)pyridine-2,6-diyl)bis(3-methyl-1*H*-imidazol-3-ium) **[H_2-bim-2](PF_6)$_2$**:

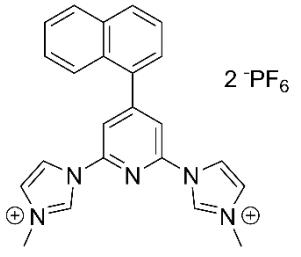

[H_2-bim-2](PF_6)$_2$

The obtained triflate salt was dissolved in a small amount of acetone and dropped into an aqueous solution of KPF_6 (10 eq.). The precipitate was filtered and purified by diffusion techniques. The product was obtained as colorless solid (83 %).

^{1}H-NMR (700 MHz, d_6-acetone): δ (ppm) = 10.41 (s, 2H, $H_{imidazole}$); 8.81 (t, 2H, $^3J_{HH}$ = 2.0 Hz, $H_{imidazole}$); 8.84 (s, 2H, $H_{pyridine}$); 8.16 (d, 1H, $^3J_{HH}$ = 8.0 Hz, $H_{naphthalene}$); 8.10 (d, 1H, $^3J_{HH}$ = 8.2 Hz, $H_{naphthalene}$); 8.05 (t, 2H, $^3J_{HH}$ = 1.9 Hz, $H_{imidazole}$); 8.00 (dd, 1H, $^3J_{HH}$ = 8.8 Hz, $^3J_{HH}$ = 0.4 Hz, $H_{naphthalene}$); 7.76-7.69 (m, 2H, $H_{naphthalene}$); 7.66-7.63 (m, 1H, $H_{naphthalene}$); 7.58-7.55 (m, 1H, $H_{naphthalene}$); 4.27 (s, 6H, H_{methyl}).

^{13}C-NMR (176 MHz, d_6-acetone): δ (ppm) = 158.6 (s, C_q, 1C, $C_{naphthalene}$); 147.2 (s, C_q, 2C, $C_{pyridine}$); 137.7 (s, 2C, $C_{carbene}$); 135.8 (s, C_q, 1C, $C_{pyridine}$); 135.0 (s, C_q, 1C, $C_{naphthalene}$); 131.5 (s, 1C, $C_{naphthalene}$); 131.3 (s, 1C, $C_{naphthalene}$); 129.8 (s, 1C, $C_{naphthalene}$); 128.9 (s, 1C, $C_{naphthalene}$); 128.6 (s, 1C, $C_{naphthalene}$); 127.8 (s, 1C, $C_{naphthalene}$); 126.6 (s, 1C, $C_{naphthalene}$); 126.5 (s, 2C, $C_{imidazole}$); 125.7 (s, 1C, $C_{naphthalene}$); 120.9 (s, 2C, $C_{imidazole}$); 116.7 (s, 2C, $C_{pyridine}$); 37.7 (s, 2C, C_{methyl}).

ESI-MS (pos) (m/z in MeCN): calculated for $C_{23}H_{21}N_5^{2+}$: 183.5893; found: 183.5947 $[M\text{-}2PF_6]^{2+}$.

1,1‘-(4-(anthracen-9-yl)pyridine-2,6-diyl)bis(3-methyl-1*H*-imidazol-3-ium) **[H_2-bim-3](PF_6)$_2$**:

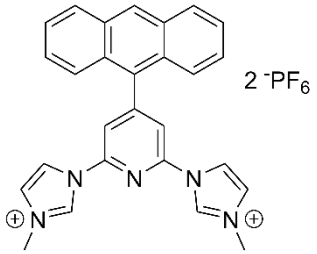

[H_2-bim-3](PF_6)$_2$

The obtained triflate salt was dissolved in a small amount of acetone and dropped into an aqueous solution of KPF_6 (10 eq.). The precipitate was filtered and purified by diffusion techniques. The product was obtained as bright yellow solid (92 %).

^{1}H-NMR (700 MHz, d_6-DMSO): δ (ppm) = 10.32 (s, 2H, $H_{imidazole}$); 8.91 (s, 1H, $H_{anthracene}$); 8.81 (s, 2H, $H_{imidazole}$); 8.43 (s, 2H, $H_{pyridine}$); 8.27 (d, 2H, $^3J_{HH}$ = 8.5 Hz, $H_{anthracene}$); 8.06 (s, 2H, $H_{imidazole}$); 7.68 (d, 2H, $^3J_{HH}$ = 8.8 Hz, $H_{anthracene}$); 7.65-7.61 (m, 2H, $H_{anthracene}$); 7.56-7.52 (m, 2H, $H_{anthracene}$); 4.01 (s , 6H, H_{methyl}).

^{13}C-NMR (176 MHz, d_6-DMSO): δ (ppm) = 155.1 (s, C_q, 1C, $C_{anthracene}$); 145.8 (s ,C_q, 2C, $C_{pyridine}$); 136.5 (s, 2C, $C_{carbene}$); 130.7 (s, C_q, 1C, $C_{pyridine}$); 130.6 (s, C_q, 2C, $C_{anthracene}$); 128.7 (s, 1C, $C_{anthracene}$); 128.6 (s, 2C, $C_{anthracene}$); 127.0 (s, 2C, $C_{anthracene}$); 125.8 (s, 2C, $C_{anthracene}$); 125.3 (s, 2C, $C_{anthracene}$); 125.0 (s, 2C, $C_{imidazole}$); 119.8 (s, C_q, 2C, $C_{anthracene}$); 1119.2 (s, 2C, $C_{imidazole}$); 116.4 (s, 2C, $C_{pyridine}$); 36.6 (s, 2C, C_{methyl}).

ESI-MS (pos) (m/z in MeCN): calculated for $C_{27}H_{23}N_5^{2+}$: 208.5971; found: 208.5984 $[M\text{-}2^{-}PF_6]^{2+}$.

Elemental analysis calculated for $C_{27}H_{23}F_{12}N_5P_2$: C = 45.84 %, H = 3.28 %, N = 9.90 %.

Found: C = 45.64 %, H = 3.59 %, N = 9.57 %.

1,1‘-(4-(pyren-1-yl)pyridine-2,6-diyl)bis(3-methyl-1*H*-imidazol-3-ium) **[H_2-bim-4](PF_6)$_2$**:

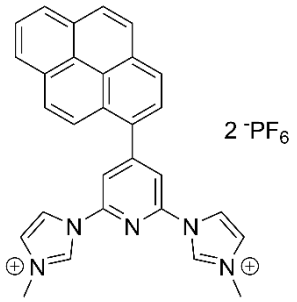

[H_2-bim-4](PF_6)$_2$

The obtained triflate salt was dissolved in a small amount of acetone and dropped into an aqueous solution of KPF_6 (10 eq.). The precipitate was filtered and purified by diffusion techniques. The product was obtained as bright yellow solid (86 %).

^{1}H-NMR (700 MHz, d_6-acetone): δ (ppm) = 10.18 (s, 2H, $H_{imidazole}$); 8.82 (t, 2H, $^3J_{HH}$ = 1.8 Hz; $H_{imidazole}$); 8.61 (s, 2H, $H_{pyridine}$); 8.50-8.18 (m, 9H, H_{pyrene}); 8.08 (t, 2H, $^3J_{HH}$ = 1.7 Hz, $H_{imidazole}$); 4.27 (s, 6H, H_{methyl}).

^{13}C-NMR (176 MHz, d_6-acetone): δ (ppm) = 157.9 (s, 1C, C_q, C_{pyrene}); 146.2 (s, 2C, C_q, $C_{pyridine}$); 136.1 (s, 2C, $C_{imidazole}$); 132.6 (s, 1C, C_q, C_{pyrene}); 131.6 (s, 1C, C_q, C_{pyrene}); 131.4 (s, 1C, C_q, $C_{pyridine}$); 130.8 (s, 1C, C_q, C_{pyrene}); 129.3 (s, 1C, C_{pyrene}); 129.1 (s, 1C, C_{pyrene}); 128.2 (s, 1C, C_q, C_{pyrene}); 127.4 (s, 1C, C_{pyrene}); 127.3 (s, 1C, C_{pyrene}); 126.9 (s, 1C, C_{pyrene}); 126.4 (s, 1C, C_{pyrene}); 125.9 (s, 2C, $C_{imidazole}$); 125.5 (s, 1C, C_{pyrene}); 125.1 (s, 1C, C_{pyrene}); 124.6 (s, 1C, C_q, C_{pyrene}); 124.2 (s, 1C, C_q, C_{pyrene}); 123.6 (s, 1C, C_{pyrene}); 119.9 (s, 2C, $C_{imidazole}$); 116.3 (s, 2C, $C_{pyridine}$), 36.7 (s, 2C, C_{methyl}).

ESI-MS (pos) (m/z in MeCN): calculated for $C_{29}H_{23}N_5^{2+}$: 220.5971; found: 220.5985 $[M\text{-}2^-PF_6]^{2+}$.

Elemental analysis calculated for $C_{29}H_{23}F_{12}N_5P_2$: C = 47.62 %, H = 3.17 %, N = 9.57 %.

Found: C = 48.29 %, H = 3.51 %, N = 9.67 %.

1,1‘-(4-(perylen-3-yl)pyridine-2,6-diyl)bis(3-methyl-1*H*-imidazol-3-ium) **[H_2-bim-5](OTf)$_2$**:

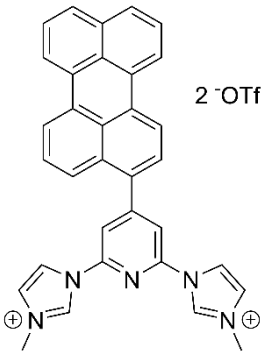

[H_2-bim-5](OTf)$_2$

2,6-di(1*H*-imidazol-1-yl)-4-(perylen-3-yl)pyridine **9-5** (1 eq.) was dissolved in $CHCl_3$ (20 ml/mmol) under inert conditions at room temperature. MeOTf (20 eq.) was added dropwise, and the reaction was stirred for 16 h at 60 °C. The reaction mixture was cooled down to room temperature while the product started to precipitate. Product remaining in solution was precipitated by adding *n*-pentane and cooling in an ice bath. The crude product was filtered and washed with *n*-pentane. The ligand precursor was purified by diffusion crystallization (solvent: acetone/ antisolvent: *n*-pentane) and the product was obtained as yellow powder (79 %).

^{1}H-NMR (700 MHz, d_6-acetone): δ (ppm) = 10.25 (s, 2H, $H_{imidazole}$); 8.72 (s, 2H, $H_{imidazole}$); 8.46-8.39 (m, 4H, $H_{perylene}$); 8.35 (s, 2H, $H_{pyridine}$); 7.99 (s, 2H, $H_{imidazole}$); 7.92-7.89 (m, 3H, $H_{perylene}$); 7.69 (d, 1H, $^3J_{HH}$ = 7.6 Hz, $H_{perylene}$); 7.63-7.58 (m, 3H, $H_{perylene}$); 4.23 (s, 6H, H_{methyl}).

^{13}C-NMR (176 MHz, d_6-acetone): δ (ppm) = 158,06 (s, C_q, 1C, $C_{perylene}$), 146,99 (s, C_q, 1C, $C_{perylene}$), 137,25(s, 2C, $C_{imidazole}$), 135,70 (s, C_q, 1C, $C_{perylene}$), 134,94 (s, C_q, 2C, $C_{pyridine}$), 134,13 (s, C_q, 1C, $C_{pyridine}$), 132,62 (s, C_q, 1C, $C_{perylene}$), 132,52 (s, C_q, 1C, $C_{perylene}$), 131,42 (s, C_q, 1C, $C_{perylene}$), 131,00 (s, C_q, 1C, $C_{perylene}$), 130,13 (s, 1C, $C_{perylene}$), 130,09 (s, 1C, $C_{perylene}$), 129,69 (s, C_q, 1C, $C_{perylene}$), 129,62 (s, 1C, $C_{perylene}$), 129,16 (s, 1C, $C_{perylene}$), 129,13 (s, C_q, 1C, $C_{perylene}$), 128,05 (s, 1C, $C_{perylene}$), 127,96 (s, 1C, $C_{perylene}$), 126,29 (s, 2C, $C_{imidazole}$), 125,64 (s, 1C, $C_{perylene}$), 123,19 (s, 1C, $C_{perylene}$), 122,30 (s, 1C, $C_{perylene}$), 122,21 (s, 1C, $C_{perylene}$), 121,37 (s, 1C, $C_{perylene}$), 120,65 (s, 2C, $C_{imidazol}$), 116,05 (s, 2C, $C_{pyridine}$), 37,54 (s, 2C, C_{methyl}), 121,8 (q, 2C, $C_{triflate-anion}$).

ESI-MS (pos) (m/z in MeCN) calculated for $C_{33}H_{25}N_5^{2+}$: 491.2099; found: 245.6048 $[M]^{2+}$.

General procedure of complexation **[Fe(bim)$_2$](PF$_6$)$_2$:**

Ligand **[H$_2$-bim-R]**(PF$_6$)$_2$ (2 eq.) was suspended in THF under inert conditions and cooled down to -78°C. LiHMDS (6 eq., 1M in THF) was added dropwise. Successful deprotonation can be seen by getting from a suspension of the imidazolium salt to a complete solution of the free carbene. After complete deprotonation $FeBr_2$ (1 eq.) was dissolved in THF under inert conditions and added dropwise to the carbene solution. The mixture instantly turned into a dark red suspension, which was stirred for 16 h while slowly getting to room temperature. The solvent was removed, and the residue was dissolved in acetone. Not soluble residue was filtered off. Acetone was removed to a minimum amount and added dropwise to a solution of KPF_6 (10 eq.) in water cooled by an ice bath and stirred for 15 min. Precipitate was filtered of and rinsed with cold water. The crude complex was dissolved in acetone, dropped into diethyl ether cold by an ice bath, filtered, dissolved in acetone again and finally purified by column chromatography (stationary phase: basic aluminum oxide/mobile phase: acetonitrile) crystallization methods.[36]

[Fe(bim)$_2$](PF$_6$)$_2$:

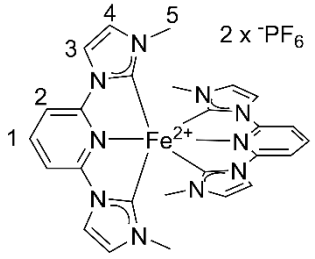

[Fe(bim)$_2$](PF$_6$)$_2$

The complex was obtained as red crystals (86 %).

^{1}H-NMR (700 MHz, d$_6$-acetone): δ (ppm) = 8.40 (d, $^3J_{HH}$ = 2.1 Hz, 4H, H_4); 8.38 (t, $^3J_{HH}$ = 8.1 Hz, 2H H_1); 8.09 (d, $^3J_{HH}$ = 8.1 Hz, 4H, H_2); 7.29 (d, $^3J_{HH}$ = 2.1 Hz, 4H, H_4); 2.74 (s, 12H, H_5).

^{13}C-NMR (176 MHz, d$_6$-acetone): δ (ppm) = 210.3 ($C_{carbene}$, 4C); 155.3 (C_q, 4C); 139.7 (C_1, 2C); 127.7 (C_4, 4C); 117.6 (C_3, 4C); 106.5 (C_2, 4C); 35.3 (C_5, 4C).

ESI-MS (pos) (m/z in MeCN): calculated for $C_{26}H_{30}FeN_{10}^{2+}$: 538.1193; found: 267.0905 $[M\text{-}2^-PF_6]^{2+}$.

Elemental analysis calculated for C$_{26}$H$_{26}$F$_{12}$FeN$_{10}$P$_2$: C = 37.88 %, H = 3.18 %, N = 16.99 %.

Found: C = 38.09 %, H = 3.33 %, N = 16.86 %.

[Fe(bim-1)$_2$](PF$_6$)$_2$:

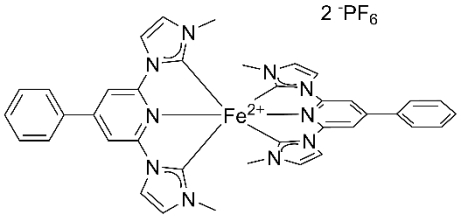

[Fe(bim-1)$_2$](PF$_6$)$_2$

The complex was obtained as red powder (59 %).

^{1}H-NMR (700 MHz, d$_6$-acetone): δ (ppm) = 8.58 (d, 4H, $^3J_{HH}$ = 2.1 Hz, H$_{imidazole}$); 8.53 (s, 4H, H$_{pyridine}$); 8.18-8.16 (m, 4H, H$_{phenyl}$); 7.68-7.60 (m, 6H, H$_{phenyl}$); 7.33 (d, 4H, $^3J_{HH}$ = 2.1 Hz, H$_{imidazole}$); 2.85 (s, 12H, H$_{methyl}$).

^{13}C-NMR (176 MHz, d$_6$-acetone): δ (ppm) = 201.5 (s, C$_q$, 4C, C$_{carbene}$); 155.6 (s, C$_q$, 4C, C$_{pyridine}$); 152.0 (s, C$_q$, 2C, C$_{phenyl}$); 137.6 (s, C$_q$, 2C, C$_{pyridine}$); 131.4 (s, 2C, C$_{phenyl}$); 130.4 (s, 4C, C$_{phenyl}$); 128.5 (s, 4C, C$_{phenyl}$); 127.7 (s, 4C, C$_{imidazole}$); 117.7 (s, 4C, C$_{imidazole}$); 104.1 (s, 4C, C$_{pyridine}$); 35.5 (s, 4C, C$_{methyl}$).

ESI-MS (pos) (m/z in MeCN): calculated for $C_{38}H_{34}FeN_{10}^{2+}$: 343.1153; found: 343.1213 $[M\text{-}2PF_6]^{2+}$.

[Fe(bim-2)$_2$](PF$_6$)$_2$:

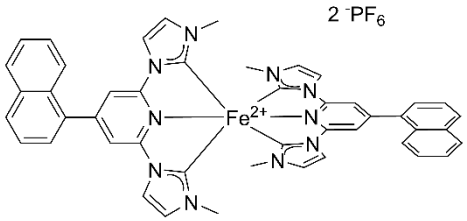

[Fe(bim-2)$_2$](PF$_6$)$_2$

The complex was obtained as red powder (71 %).

^{1}H-NMR (700 MHz, d$_6$-acetone): δ (ppm) = 8.55 (d, 4H, $^3J_{HH}$ = 2.1 Hz, H$_{imidazole}$); 8.33 (s, 4H, H$_{pyridine}$); 8.17 (d, 4H, $^3J_{HH}$ = 8.2 Hz, H$_{naphthalene}$); 8.14 (d, 2H, $^3J_{HH}$ = 8.0 Hz, H$_{naphthalene}$); 7.88 (dd, 2H, $^3J_{HH}$ = 6.9 Hz, $^3J_{HH}$ = 0.9 Hz, H$_{naphthalene}$); 7.76-7.74 (m, 2H, H$_{naphthalene}$); 7.69-7.67 (m, 2H, H$_{naphthalene}$); 7.63-7.60 (m, 2H, H$_{naphthalene}$); 7.37 (d, 4H, $^3J_{HH}$ = 2.1 Hz, H$_{imidazole}$); 3.00 (s, 12H, H$_{methyl}$).

^{13}C-NMR (176 MHz, d$_6$-acetone): δ (ppm) = 200.9 (s, C$_q$, 4C, C$_{carbene}$); 154.6 (s, C$_q$, 4C, C$_{pyridine}$); 151. 9 (s, C$_q$, 2C, C$_{naphthalene}$); 136.6 (s, C$_q$, 2C, C$_{pyridine}$); 134.4 (s, C$_q$, 2C, C$_{naphthalene}$); 130.9 (s, C$_q$, 2C, C$_{naphthalene}$); 130.3 (s, 2C, C$_{naphthalene}$); 129.2 (s, 2C, C$_{naphthalene}$); 128.5 (s, 2C, C$_{naphthalene}$); 127.7 (s, 2C, C$_{naphthalene}$); 127.2 (s, 4C, C$_{imidazole}$); 126.9 (s, 2C, C$_{naphthalene}$); 125.9 (s, 2C, C$_{naphthalene}$); 125.3 (s, 2C, C$_{naphthalene}$); 117.3 (s, 4C, C$_{imidazole}$); 107.3 (s, 4C, C$_{pyridine}$); 35.0 (s, 4C, C$_{methyl}$).

ESI-MS (pos) (m/z in MeCN): calculated for $C_{46}H_{38}FeN_{10}^{2+}$: 393.1310; found: 393.1346 $[M\text{-}2^{-}PF_6]^{2+}$.

Elemental analysis calculated for $C_{54}H_{42}F_{12}FeN_{10}P_2$: C = 51.32 %, H = 3.56 %, N = 13.01 %.

Found: C = 51.26 %, H = 3.59 %, N = 12.32 %.

[Fe(bim-3)$_2$](PF$_6$)$_2$:

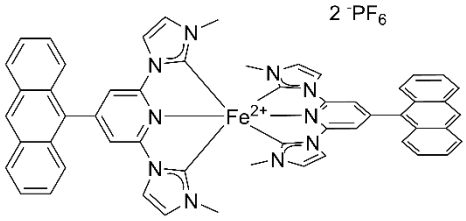

[Fe(bim-3)$_2$](PF$_6$)$_2$

The complex was obtained as red powder (68 %).

^{1}H-NMR (700 MHz, d$_6$-acetone): δ (ppm) = 8.89 (s, 2H, H$_{anthracene}$); 8.52 (d, 4H, ^{3}J$_{HH}$ = 2.1 Hz, H$_{imidazole}$); 8.31 (s, 4H, H$_{pyridine}$); 8.29 (d, 4H, ^{3}J$_{HH}$ = 8.6 Hz, H$_{anthracene}$); 7.81 (d, 4H, ^{3}J$_{HH}$ = 8.8 Hz, H$_{anthracene}$); 7.66-7.62 (m, 4H, H$_{anthracene}$); 7.57-7.53 (m, 4H, H$_{anthracene}$); 7.43 (d, 4H, ^{3}J$_{HH}$ = 2.0 Hz, H$_{imidazole}$); 3.20 (s, 12H, H$_{methyl}$).

^{13}C-NMR (176 MHz, d$_6$-acetone): δ (ppm) = 200.6 (s, C$_{q,}$ 4C, C$_{carbene}$); 154.7 (s, C$_{q,}$ 4C, C$_{pyridine}$); 149.9 (s, C$_{q,}$ 2C, C$_{pyridine}$); 132.1 (s, C$_{q,}$ 2C, C$_{anthracene}$); 131.4 (s, C$_{q,}$ 4C, C$_{anthracene}$); 129.4 (s, C$_{q,}$ 4C, C$_{anthracene}$); 128.9 (s, 2C, C$_{anthracene}$); 128.7 (s, 4C, C$_{anthracene}$); 127.0 (s, 4C, C$_{anthracene}$); 126.9 (s, 4C, C$_{imidazole}$); 125.7 (s, 4C, C$_{anthracene}$); 125.3 (s, 4C, C$_{anthracene}$); 117.1 (s, 4C, C$_{imidazole}$); 108.6 (s, 4C, C$_{pyridine}$); 34.7 (s, 4C, C$_{methyl}$).

ESI-MS (pos) (m/z in MeCN): calculated for $C_{54}H_{42}FeN_{10}^{2+}$: 443.1466; found: 4431478 $[M\text{-}2^{-}PF_6]^{2+}$.

Elemental analysis calculated for C$_{54}$H$_{42}$F$_{12}$FeN$_{10}$P$_2$: C = 55.12 %, H = 3.60 %, N = 11.90 %.

Found: C = 55.24 %, H = 4.22 %, N = 11.39 %.

[Fe(bim-4)$_2$](PF$_6$)$_2$:

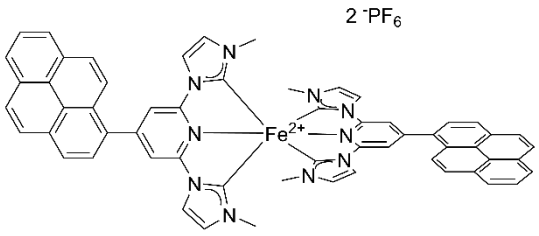

[Fe(bim-4)$_2$](PF$_6$)$_2$

The complex was obtained as red powder (72 %).

^{1}H-NMR (700 MHz, d$_6$-acetone): δ (ppm) = 8.62 (d, 4H, ^{3}J$_{HH}$ = 2.0 Hz, H$_{imidazole}$); 8.54 (d, 2H, ^{3}J$_{HH}$ = 7.7 Hz, H$_{pyrene}$); 8.52 (s, 4H, H$_{pyridine}$); 8.49 (d, 2H, ^{3}J$_{HH}$ = 9.2 Hz, H$_{pyrene}$); 8.45 (d, 2H, ^{3}J$_{HH}$ = 7.6 Hz, H$_{pyrene}$); 8.43-8.40 (m, 4H, H$_{pyrene}$); 8.38-8.32 (m, 4H, H$_{pyrene}$); 8.29 (d, 2H, ^{3}J$_{HH}$ = 9.3 Hz, H$_{pyrene}$); 8.20 (t, 2H, ^{3}J$_{HH}$ = 7.5 Hz, H$_{pyrene}$); 7.43 (d, 4H, ^{3}J$_{HH}$ = 2.0 Hz, H$_{imidazole}$); 3.09 (s, 12H, H$_{imidazole}$).

^{13}C-NMR (176 MHz, d_6-acetone): δ (ppm) = 201.6 (s, C_q, 4C, $C_{carbene}$); 155.3 (s, C_q, 4C, $C_{pyridine}$); 152.8 (s, C_q, 2C, $C_{pyridine}$); 134.4 (s, C_q, 2C, C_{pyrene}); 133.2 (s, C_q, 2C, C_{pyrene}); 132.5 (s, C_q, 2C, C_{pyrene}); 131.8 (s, C_q, 2C, C_{pyrene}); 129.9 (s, 2C, C_{pyrene}); 129.7 (s, 2C, C_{pyrene}); 129.2 (s, C_q, 2C, C_{pyrene}); 128.9 (s, 2C, C_{pyrene}); 128.4 (s, 2C, C_{pyrene}); 127.84 (s, 4C, $C_{imidazole}$); 127.83 (s, 2C, C_{pyrene}); 127.3 (s, 2C, C_{pyrene}); 126.7 (s, 2C, C_{pyrene}); 126.1 (s, 2C, C_{pyrene}); 125.8 (s, C_q, 2C, C_{pyrene}); 125.4 (s, C_q, 2C, C_{pyrene}); 125.1 (s, 2C, C_{pyrene}); 117.9 (s, 4C, $C_{imidazole}$); 108.4 (s, 4C, $C_{pyridine}$); 35.7 (s, 4C, C_{methyl}).

ESI-MS (pos) (m/z in MeCN): calculated for $C_{58}H_{42}FeN_{10}^{2+}$: 467.1466; found: 467.1528 $[M\text{-}2^{-}PF_6]^{2+}$.

Elemental analysis calculated for $C_{58}H_{42}F_{12}FeN_{10}P_2$: C = 56.88 %, H = 3.46 %, N = 11.44 %.

Found: C = 56.78 %, H = 3.97 %, N = 10.81 %.

<u>[Fe(bim-5)$_2$](PF$_6$)$_2$:</u>

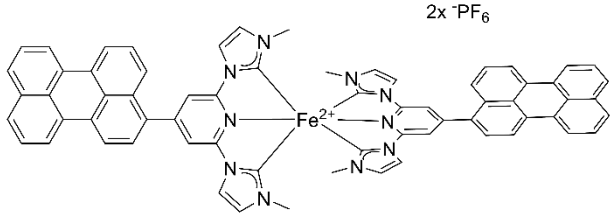

[Fe(bim-5)$_2$](PF$_6$)$_2$

The complex was obtained as red powder (24 %).

^{1}H-NMR (700 MHz, d_6-acetone): δ (ppm) = 8.61-8.60 (m, $H_{perylene}$ & $H_{imidazole}$, 4H) 8.84 (d, J = 7.2 Hz, $H_{perylene}$, 2H); 8.51 (d, J = 7.2 Hz, $H_{perylene}$, 2H); 8.48 (d, J = 7.2 Hz, $H_{perylene}$, 2H); 8.40 (s, $H_{pyridine}$, 4H); 8.07 (d, J = 8.5 Hz, $H_{perylene}$, 2H); 7.92-7.89 (m, $H_{perylene}$, 6H); 7.64-7.62 (m, $H_{perylene}$, 6H); 7.41 (d, J = 2.0 Hz, $H_{imidazole}$, 4H); 3.03 (s, H_{methyl}, 12H).

^{13}C-NMR (176 MHz, d_6-acetone): δ (ppm) = 201.5 (s, C_q, $C_{imidazole}$, 4C); 155.4 (s, C_q, $C_{pyridine}$, 4C); 152.3 (s, C_q, $C_{pyridine}$, 2C); 136.7 (s, C_q, $C_{perylene}$, 2C); 135.9 (s, C_q, $C_{perylene}$, 2C); 133.9 (s, C_q, $C_{perylene}$, 2C); 133.1 (s, C_q, $C_{perylene}$, 2C); 132.8 (s, C_q, $C_{perylene}$, 2C); 131.7 (s, C_q, $C_{perylene}$, 2C); 131.4 (s, C_q, $C_{perylene}$, 2C); 130.1 (s, C_q, $C_{perylene}$, 2C); 130.0 (s, $C_{perylene}$, 2C); 129.9 (s, $C_{perylene}$, 2C); 129.6 (s, $C_{perylene}$, 2C); 129.4 (s, $C_{perylene}$, 2C); 128.9 (s, $C_{perylene}$, 2C); 128.1 (s, $C_{perylene}$, 2C); 128.0 (s, $C_{perylene}$, 2C); 127.8 (s, $C_{imidazole}$, 2C); 126.0 (s, $C_{perylene}$, 2C); 122.5 (s, $C_{perylene}$, 2C); 122.3 (s, $C_{perylene}$, 2C); 122.2 (s, $C_{perylene}$, 2C); 121.1 (s, $C_{perylene}$, 2C); 117.9 (s, $C_{imidazole}$, 4C); 107.8 (s, $C_{pyridine}$, 4C); 35.7 (s, C_{methyl}, 4C).

ESI-MS (pos) (m/z in MeCN) calculated for $C_{66}H_{46}FeN_{10}^{2+}$: 517.1623; found: 517.1678 $[M]^{2+}$.

General procedure for 2,6-bis(1*H*-benzo[*d*]imidazol-1-yl)pyridines **10-R**:

The corresponding 4-chromophore-2,6-dichlorpyridine **8-R** (1 eq.), benzimidazole (2.4 eq.), copper oxide (0.5 eq.) and potassium carbonate (2.4 eq.) were suspended in DMF and heated to 150 °C for 3 d. After cooling down to room temperature, it was suspended with DCM and residue was filtered off. The solution was extracted with water to remove DMF and remaining benzimidazole. The product was purified by washing with methanol and ethyl acetate.[36]

2,6-bis(1*H*-benzo[*d*]imidazol-1-yl)pyridine **10-0**:

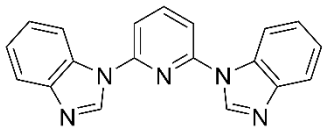

10-0

The product was obtained as a colorless solid (20 %).

^{1}H-NMR (700 MHz, DMSO-d_6): δ (ppm) = 9.10 (s, 2H, $H_{benzimidazole}$); 8.34 (t, 1H, J = 8.00 Hz, $H_{pyridine}$); 8.27-8.23 (m, 2H, $H_{benzimidazole}$); 7.97 (d, 2H, J = 8.00 Hz, $H_{pyridine}$); 7.84-7.84 (m, 2H, $H_{benzimidazole}$); 7.39-7.36 (m, 4H, $H_{benzimidazole}$).

^{13}C-NMR (176 MHz, DMSO-d_6): δ (ppm) = 148.8 (s, C_q, 2C, $C_{pyridine}$); 144.4 (s, C_q, 2C, $C_{benzimidazole}$); 142.9 (s, 1C, $C_{pyridine}$); 142.6 (s, 2C, $C_{benzimidazole,\ N\text{-}C\text{-}N}$); 131.8 (s, C_q, 2C, $C_{benzimidazole}$); 124.2 (s, 2C, $C_{benzimidazole}$); 123.3 (s, 2C, $C_{benzimidazole}$); 120.1 (s, 2C, $C_{benzimidazole}$); 113.6 (s, 2C, $C_{benzimidazole}$);112.3 (s, 2C, $C_{pyridine}$).

ESI-MS (pos) (m/z in MeCN) calculated for $C_{19}H_{13}N_5$: 311.1171; found: 312.1350 $[M+H]^+$.

1,1'-(4-phenylpyridine-2,6-diyl)bis(1*H*-benzo[*d*]imidazole) **10-1**:

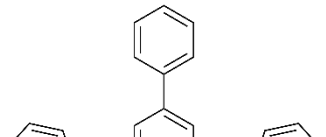

10-1

The product was obtained as colorless solid (18 %).

^{1}H-NMR (700 MHz, DMSO-d_6): δ (ppm) = 9.25 (s, 2H, $H_{benzimidazole}$); 8.33-8.31 (m, 2H, $H_{benzimidazole}$); 8.25 (s, 2H, $H_{pyridine}$); 8.19-8.16 (m, 2H, H_{phenyl}); 7.85-7.82 (m, 2H, $H_{benzimidazole}$); 7.66-7.59 (m, 3H, H_{phenyl}); 7.40-7.37 (m, 4H, $H_{benzimidazole}$).

^{13}C-NMR (176 MHz, DMSO-d_6): δ (ppm) = 153.9 (s, C_q, 1C, $C_{pyridine}$); 149.6 (s, C_q, 2C, $C_{pyridine}$); 144.3 (s, C_q, 2C, $C_{benzimidazole}$); 142.85 (s, 2C, $C_{benzimidazole,\ N\text{-}C\text{-}N}$); 136.3 (s, C_q, 1C, C_{phenyl}); 131.9 (s, C_q, 2C, $C_{benzimidazole}$); 130.3 (s, 1C, C_{phenyl}); 129.2 (s, 2C, C_{phenyl}); 127.8 (s, 2C, C_{phenyl}); 124.1 (s, 2C, $C_{benzimidazole}$); 123.3 (s, 2C, $C_{benzimidazole}$); 120.0 (s, 2C, $C_{benzimidazole}$); 114.0 (s, 2C, $C_{benzimidazole}$); 109.9 (s, 2C, $C_{pyridine}$).

ESI-MS (pos) (m/z in MeCN) calculated for $C_{25}H_{17}N_5$: 387.1484; found: 388.1672 $[M+H]^+$.

1,1'-(4-naphthalene-1-yl)pyridine-2,6-diyl)bis(1*H*-benzo[*d*]imidazole) **10-2**:

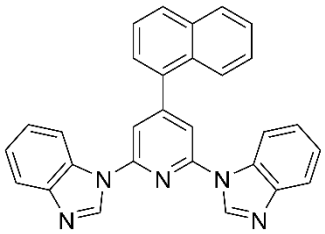

10-2

The product was obtained as colorless solid (21 %).

^{1}H-NMR (700 MHz, DMSO-d_6): δ (ppm) = 9.18 (s, 2H, $H_{benzimidazole}$); 8.36-8.35 (m, 2H, $H_{benzimidazole}$); 8.15-8.10 (m, 3H, $H_{naphthalene}$); 8.13 (s, 2H, $H_{pyridine}$); 7.84-7.83 (m, 2H, $H_{benzimidazole}$); 7.81 (dd, 1H, J = 7.0 Hz, J = 0.9 Hz, $H_{naphthalene}$); 7.73 (dd, 1H, J = 8.1 Hz, J = 7.1 Hz, $H_{naphthalene}$); 7.64-7.61 (m, 2H, $H_{naphthalene}$); 7.40-7.38 (m, 4H, $H_{benzimidazole}$).

^{13}C-NMR (176 MHz, DMSO-d_6): δ (ppm) = 154.4 (s, 1C, C_q, $C_{pyridine}$); 149.1 (s, 2C, C_q, $C_{pyridine}$); 144.3 (s, 2C, C_q, $C_{benzimidazole}$); 142.9 (s, 2C, $C_{benzimidazole,\ N\text{-}C\text{-}N}$); 135.9 (s, 1C, C_q, $C_{naphthalene}$); 133.4 (s, 1C, C_q, $C_{naphthalene}$); 132.0 (s, 2C, C_q, $C_{benzimidazole}$); 130.1 (s, 1C, C_q, $C_{naphthalene}$); 129.5 (s, 1C, $C_{naphthalene}$); 128.5 (s, 1C, $C_{naphthalene}$); 127.5 (s, 1C, $C_{naphthalene}$); 127.3 (s, 1C, $C_{naphthalene}$); 126.5 (s, 1C, $C_{naphthalene}$); 125.6 (s, 1C, $C_{naphthalene}$); 125.1 (s, 1C, $C_{naphthalene}$); 124.2 (s, 2C, $C_{benzimidazole}$); 123.4 (s, 2C, $C_{benzimidazole}$); 120.1 (s, 2C, $C_{benzimidazole}$); 1114.0 (s, 2C, $C_{benzimidazole}$); 113.3 (s, 2C, $C_{pyridine}$);

ESI-MS (pos) (m/z in MeCN) calculated for $C_{29}H_{19}N_5$: 437.1640; found: 438.1767 $[M+H]^+$.

1,1'-(4-(anthracene-9-yl)pyridine-2,6-diyl)bis(1*H*-benzo[*d*]imidazole) **10-3**:

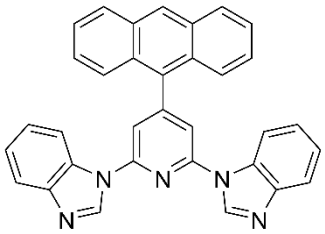

10-3

The product was obtained as bright yellow solid (25 %).

^{1}H-NMR (700 MHz, DMSO-d_6): δ (ppm) = 9.13 (s, 2H, $H_{benzimidazole}$); 8.84 (s, 1H, $H_{anthracene}$); 8.43-8.40 (m, 2H, $H_{benzimidazole}$); 8.24 (d, J = 8.6 Hz; $H_{benzimidazole}$); 8.14 (s, 2H, $H_{pyridine}$); 7.87 (dd, 2H, J = 9.2 Hz, J = 0.4 Hz, $H_{anthracene}$); 7.85-7.82 (m, 2H, $H_{benzimidazole}$); 7.62-7.58 (m, 2H, $H_{anthracene}$); 7.55-7.52 (m, 2H, $H_{anthracene}$); 7.42-7.37 (m, 4H, $H_{benzimidazole}$).

^{13}C-NMR (176 MHz, DMSO-d_6): δ (ppm) = 153.2 (s, C_q, 1C, $C_{pyridine}$); 149.4 (s, C_q, 2C, $C_{pyridine}$); 144.3 (s, C_q, 2C, $C_{benzimidazole}$); 142.6 (s, 2C, $C_{benzimidazole,\ N\text{-}C\text{-}N}$); 132.4 (s, C_q, 1C, $C_{anthracene}$); 131.9 (s, C_q, 2C, $C_{benzimidazole}$); 130.8 (s, C_q, 2C, $C_{anthracene}$); 128.9 (s, C_q, 2C, $C_{anthracene}$); 128.5 (s, 2C, $C_{anthracene}$); 127.9 (s, 1C, $C_{anthracene}$); 126.7 (s, 2C, $C_{anthracene}$); 125.9 (s, 2C, $C_{anthracene}$); 125.6 (s, 2C, $C_{anthracene}$); 124.2 (s, 2C, $C_{benzimidazole}$); 123.4 (s, 2C, $C_{benzimidazole}$); 120.1 (s, 2C, $C_{benzimidazole}$); 114.2 (s, 2C, $C_{benzimidazole}$); 114.2 (s, 2C, $C_{pyridine}$).

ESI-MS (pos) (m/z in MeCN) calculated for $C_{33}H_{21}N_5$: 487.1797; found: 488.1997 $[M+H]^+$.

1,1'-(4-(pyren-1-yl)pyridine-2,6-diyl)bis(1H-benzo[d]imidazole) **10-4**:

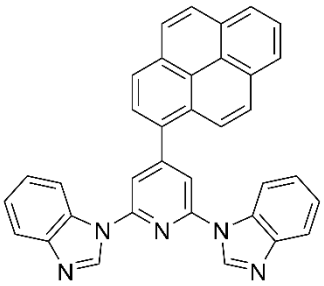

10-4

The product was obtained as yellow solid (23 %).

^{1}H-NMR (700 MHz, $CDCl_3$): δ (ppm) = 8.80 (s, 2H, $H_{benzimidazole}$); 8.33 (d, 1H, J = 7.8 Hz, H_{pyrene}); 8.29 (d, 1H, J = 7.6 Hz, H_{pyrene}); 8.27-8.24 (m, 2H, H_{pyrene}); 8.21-8.14 (m, 5H, $H_{benzimidazole}$ & H_{pyrene}); 8.11-8.07 (m, 2H, H_{pyrene}); 7.94-7.91 (m, 2H, $H_{benzimidazole}$); 7.85 (s, 2H, $H_{pyridine}$); 7.42-7.39 (m, 4H, $H_{benzimidazole}$).

^{13}C-NMR (176 MHz, $CDCl_3$): δ (ppm) = 156.2 (s, C_q, 1C, C_{pyrene}); 149.7 (s, C_q, 2C, $C_{pyridine}$); 144.9 (s, C_q, 2C, $C_{benzimidazole}$); 141.5 (s, 2C, $C_{benzimidazole,\ N\text{-}C\text{-}N}$); 132.8 (s, C_q, 1C, $C_{pyridine}$); 132.4 (s, C_q, 1C, C_{pyrene}); 132.2 (s, C_q, 2C, $C_{benzimidazole}$); 131.6 (s, C_q, 1C, C_{pyrene}); 130.9 (s, C_q, 1C, C_{pyrene}); 129.4 (s, 1C, C_{pyrene}); 129.0 (s, 1C, C_{pyrene}); 128.4 (s, C_q, 1C, C_{pyrene}); 127.4 (s, 1C, C_{pyrene}); 126.8 (s, 2C, C_{pyrene}); 126.4 (s, 1C, C_{pyrene}); 126.0 (s, 1C, C_{pyrene}); 125.2 (s, C_q, 1C, C_{pyrene}); 125.2 (s, 1C, C_{pyrene}); 125.0 (s, 2C, $C_{benzimidazole}$); 124.8 (s, C_q, 1C, C_{pyrene}); 124.1 (s, 2C, $C_{benzimidazole}$); 123.6 (s, 1C, C_{pyrene}); 121.1 (s, 2C, $C_{benzimidazole}$); 113.2 (s, 2C, $C_{pyridine}$); 113.2 (s, 2C, $C_{benzimidazole}$).

ESI-MS (pos) (m/z in MeOH) calculated for $C_{35}H_{21}N_5$: 511.1797; found: 512.1951 $[M+H]^+$.

1,1'-(4-(perylen-3-yl)pyridine-2,6-diyl)bis(1*H*-benzo[d]imidazole) **10-5**:

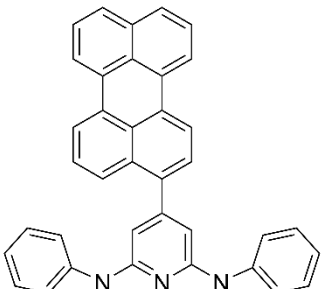

10-5

The product was obtained as orange solid (35 %).

^{1}H-NMR (700 MHz, d_6-DMSO): δ (ppm) = 9.19 (s, 2H, $H_{benzimidazole}$); 8.58 (d, 1H, $^{3}J_{HH}$ = 8.0 Hz, $H_{perylene}$); 8.52 (t, 2H, $^{3}J_{HH}$ = 7.2 Hz, $H_{perylene}$); 8.46 (d, 2H, $^{3}J_{HH}$ = 7.2 Hz, $H_{perylene}$); 8.37-8.36 (m, 2H, $H_{benzimidazole}$); 8.18 (s, 2H, $H_{pyridine}$); 7.88 (d, 1H, $^{3}J_{HH}$ = 8.0 Hz, $H_{perylene}$); 7.86 (d, 1H, $^{3}J_{HH}$ = 8.1 Hz, $H_{perylene}$); 7.58-7.83 (m, 2H, $H_{benzimidazole}$); 7.65-7.59 (m, 2H, $H_{perylene}$); 7.42-7.38 (m, 4H, $H_{benzimidazole}$).

^{13}C-NMR (176 MHz, d_6-DMSO): δ (ppm) = 161.54 (s, C_q, 1C, $C_{perylene}$); 154.29 (s, C_q, 1C, $C_{perylene}$); 149.21 (s, C_q, 2C, $C_{pyridine}$); 144.34 (s, C_q, 2C, $C_{benzimidazole}$); 142.80 (s, 2C, $C_{imidazole}$); 135, 63 (s, C_q, 1C, $C_{pyridine}$); 134.28 (s, C_q, 1C, $C_{pyridine}$); 131.91 (s, C_q, 2C, $C_{benzimidazole}$); 131.82 (s, C_q, 1C, $C_{pyridine}$); 131.69 (s, C_q, 1C, $C_{pyridine}$); 131.00 (s, C_q, 1C, $C_{pyridine}$); 130.36 (s, C_q, 1C, $C_{pyridine}$); 130.05 (s, C_q, 1C, $C_{pyridine}$); 128.62 (s, 1C, $C_{perylene}$); 128.52 (s, 1C, $C_{perylene}$); 128.31 (s, 1C, $C_{perylene}$); 127.95 (s, 1C, $C_{perylene}$); 127.80 (s, C_q, 1C, $C_{pyridine}$); 127.11 (s, 1C, $C_{perylene}$); 127.09 (s, 1C, $C_{perylene}$); 125.32 (s, 1C, $C_{perylene}$); 124.21 (s, 2C, $C_{benzimidazole}$); 123.40 (s, 2C, $C_{benzimidazole}$); 121.49 (s, 1C, $C_{perylene}$); 121.34 (s, 1C, $C_{perylene}$); 121.31 (s, 1C, $C_{perylene}$); 120.40 (s, 1C, $C_{perylene}$); 120.09 (s, 2C, $C_{benzimidazole}$); 114.02 (s, 2C, $C_{benzimidazole}$); 113.19 (s, 2C, $C_{pyridine}$).

ESI-MS (pos) (m/z in MeCN) calculated for $C_{39}H_{23}N_5$: 561.1953; found: 562.2087 $[M+H]^+$.

General procedure for the synthesis of the pro-ligands **[H_2-bbp-R](PF_6)$_2$**:

The corresponding 2,6-bis(1*H*-benzo[*d*]midazol-1-yl)-4-chromophore-pyridine **10-R** (1 eq.) was dissolved in dry DCM (10 ml/mmol) and cooled to -80 °C. Methyl trifluoromethanesulfonate (MeOTf; 2.05 eq.) was added dropwise. The solution was stirred for 16 h while slowly getting up to room temperature. It was again cooled in an ice bath, and *n*-pentane was added. The product was obtained as a solid precipitate, filtered, and, if necessary, washed again by cold *n*-pentane. The obtained triflate salt was dissolved in a small amount of acetone and added dropwise into an aqueous solution of KPF_6 (10 eq.). The precipitate was filtered and purified by recrystallization via solvent diffusion (acetone/diethyl ether).[36]

1,1'-(pyridine-2,6-diyl)bis(3-methyl-1*H*-benzo[*d*]imidazol-3-ium) **[H_2-bbp](PF_6)$_2$**:

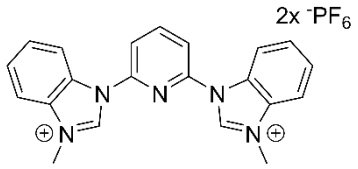

[H_2-bbp](PF_6)$_2$

Product was obtained was colorless solid (87 %).

^{1}H-NMR (700 MHz, d_6-acetone): δ (ppm) = 10.37 (s, 2H, $H_{benzimidazole}$); 8.79 (t, 1H, J = 8.0 Hz, $H_{pyridine}$); 8.54 (d, 2H, J = 8.5 Hz, $H_{benzimidazole}$); 8.45 (d, 2H, J = 8.0 Hz, $H_{pyridine}$); 8.24 (d, 2H, J = 8.3 Hz, $H_{benzimidazole}$); 7.90 (t, 2H, J = 7.8 Hz, $H_{benzimidazole}$); 7.83 (t, 2H, J = 7.9 Hz, $H_{benzimidazole}$); 4.48 (s, 6H, H_{methyl}).

^{13}C-NMR (176 MHz, d_6-acetone): δ (ppm) = 147.9 (s, C_q, 2C, $C_{pyridine}$); 146.2 (s, 1C, $C_{pyridine}$); 143.4 (s, 2C, $C_{benzimidazole,\ N\text{-}C\text{-}N}$); 133.9 (s, C_q, 2C, $C_{benzimidazole}$); 131.0 (s, C_q, 2C, $C_{benzimidazole}$); 129.4 (s, 2C, $C_{benzimidazole}$); 119.3 (s, 2C, $C_{pyridine}$); 116.4 (s, 2C, $C_{benzimidazole}$); 115.0 (s, 2C, $C_{benzimidazole}$); 34.9 (s, 2C, C_{methyl}).

ESI-MS (pos) (m/z in MeCN) calculated for $C_{21}H_{19}N_5^{2+}$: 170.5815; found: 170.5833 $[M]^{2+}$.

1,1'-(4-phenylpyridine-2,6-diyl)bis(3-methyl-1*H*-benzo[*d*]imidazol-3-ium) **[H_2-bbp-1](PF_6)$_2$**:

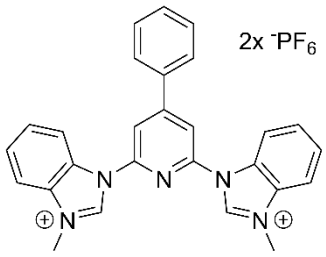

[H_2-bbp-1](PF_6)$_2$

The product was obtained as colorless solid (92 %).

^{1}H-NMR (700 MHz, d_6-acetone): δ (ppm) = 10.51 (s, 2H, $H_{benzimidazole}$); 8.72 (s, 2H, $H_{pyridine}$); 8.63 (dt, 2H, J = 8.5 Hz, J = 0.8 Hz, $H_{benzimidazole}$); 8.26 (dt, 2H, J = 8.4 Hz, J = 0.8 Hz, $H_{benzimidazole}$); 8.15-8.12 (m, 2H, H_{phenyl}); 7.91 (ddd, 2H, J = 8.4 Hz, J = 7.3 Hz, J = 1.0 Hz, $H_{benzimidazole}$); 7.83 (ddd, 2H, J = 8.4 Hz, J = 7.3 Hz, J = 1.0 Hz, $H_{benzimidazole}$); 7.69-7.67 (m, 3H, H_{phenyl}); 4.51 (s, 6H, H_{methyl}).

^{13}C-NMR (176 MHz, d_6-acetone): δ (ppm) = 157.9 (s, C_q, 1C, C_{phenyl}); 148.7 (s, C_q, 2C, $C_{pyridine}$); 143.5 (s, 2C, $C_{benzimidazole,\ N\text{-}C\text{-}N}$); 136.3 (s, C_q, 1C, $C_{pyridine}$); 133.9 (s, 2C, C_q, $C_{benzimidazole}$); 132.3 (s, 1C, C_{phenyl}); 131.2 (s, 2C, C_q, $C_{benzimidazole}$); 130.7 (s, 2C, C_{phenyl}); 129.4 (s, 2C, $C_{benzimidazole}$); 128.9 (s, 2C, $C_{benzimidazole}$); 128.8 (s, 2C, C_{phenyl}); 116.9 (s, 2C, $C_{pyridine}$); 116.8 (s, 2C, $C_{benzimidazole}$); 115.0 (s, 2C, $C_{benzimidazole}$); 35.0 (s, 2C, C_{methyl}).

ESI-MS (pos) (m/z in MeCN) calculated for $C_{27}H_{23}N_5^{2+}$: 208.5971; found: 208.5971 $[M]^{2+}$.

1,1'-(4-(naphthalen-1-yl)pyridine-2,6-diyl)bis(3-methyl-1*H*-benzo[*d*]imidazol-3-ium) **[H_2-bbp-2](PF_6)$_2$**:

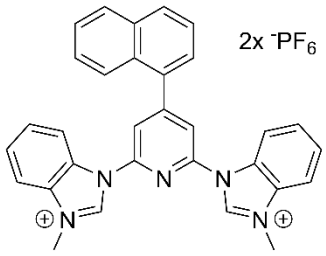

[H_2-bbp-2](PF_6)$_2$

The product was obtained as colorless solid (95 %).

^{1}H-NMR (700 MHz, d_6-acetone): δ (ppm) = 10.54 (s, 2H, $H_{benzimidazole}$); 8.65 (d, 2H, J = 8.5 Hz, $H_{benzimidazole}$); 8.61 (s, 2H, $H_{pyridine}$); 8.26 (d, 2H, J = 8.3 Hz, $H_{benzimidazole}$); 8.19 (d, 1H, J = 8.3 Hz, $H_{naphthalene}$); 8.14-8.12 (m, 2H, $H_{naphthalene}$); 7.92 (m, 2H, $H_{benzimidazole}$); 7.85-7.83 (m, 3H, 2$H_{benzimidazole}$ & 1$H_{naphthalene}$); 7.75-7.73 (m, 1H, $H_{naphthalene}$); 7.68-7.66 (m, 1H, $H_{naphthalene}$); 7.62-7.60 (m, 1H, $H_{naphthalene}$); 4.50 (s, 6H, H_{methyl}).

^{13}C-NMR (176 MHz, d_6-acetone): δ (ppm) =157.6 (s, 1C, C_q, $C_{naphthalene}$); 147.5 (s, 2C, C_q, $C_{pyridine}$); 142.9 (s, 2C, $C_{benzimidazole,\ N\text{-}C\text{-}N}$); 134.9 (s, 1C, C_q, $C_{pyridine}$); 134.2 (s, 1C, C_q, $C_{naphthalene}$); 133.1 (s, 2C, C_q, $C_{benzimidazole}$); 130.8 (s, 1C, $C_{naphthalene}$); 130.5 (s, 1C, $C_{naphthalene}$); 130.4 (s, 2C, C_q, $C_{benzimidazole}$); 129.0 (s, 1C, $C_{naphthalene}$); 128.7 (s, 2C, $C_{benzimidazole}$); 128.2 (s, 1C, $C_{naphthalene}$); 128.1 (s, 2C, $C_{benzimidazole}$); 127.8 (s, 1C, $C_{naphthalene}$); 127.0 (s, 1C, $C_{naphthalene}$); 125.8 (s, 1C, $C_{naphthalene}$); 124.8 (s, 1C, $C_{naphthalene}$); 119.5 (s, 2C, $C_{pyridine}$); 116.0 (s, 2C, $C_{benzimidazole}$); 114.3 (s, 2C, $C_{benzimidazole}$); 34.2 (s, 2C, C_{methyl}).

ESI-MS (pos) (m/z in MeCN) calculated for $C_{31}H_{25}N_5^{2+}$: 233.6050; found: 233.6089 $[M]^{2+}$.

1,1'-(4-(anthracen-9-yl)pyridine-2,6-diyl)bis(3-methyl-1*H*-benzo[*d*]imidazol-3-ium) **[H_2-bbp-3](PF_6)$_2$**:

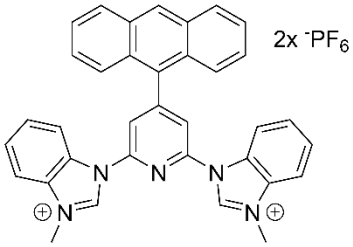

[H_2-bbp-3](PF_6)$_2$

The product was obtained as yellow solid (84 %).

^{1}H-NMR (700 MHz, d_6-acetone): δ (ppm) = 10.53 (s, 2H, $H_{benzimidazole}$); 8.88 (s, 1H, $H_{anthracene}$); 8.68 (d, 2H, J = 8.5 Hz, $H_{anthracene}$); 8.59 (s, 2H, $H_{pyridine}$); 8.27 (t, 4H, J = 7.0 Hz, $H_{benzimidazole}$); 7.91 (t, 2H, J = 7.8 Hz, $H_{benzimidazole}$); 7.87 (d, 2H, J = 8.8 Hz, $H_{anthracene}$); 7.84 (t, 2H, J = 7.9 Hz, $H_{anthracene}$); 7.62 (t, 2H, J = 7.4 Hz, $H_{benzimidazole}$); 7.53 (t, 2H, J = 7.6 Hz, $H_{anthracene}$); 4.49 (s, 6H, H_{methyl}).

^{13}C-NMR (176 MHz, d_6-acetone): δ (ppm) = 157.4 (s, 1C, C_q, $C_{anthracene}$); 148.7 (s, 2C, C_q, $C_{pyridine}$); 143.7 (s, 2C, $C_{benzimidazole,\ N\text{-}C\text{-}N}$); 133.9 (s, 2C, C_q, $C_{benzimidazole}$); 132.3 (s, 2C, C_q, $C_{anthracene}$); 131.6 (s, 1C, C_q, $C_{pyridine}$); 131.1 (s, 2C, C_q, $C_{benzimidazole}$); 130.3 (s, 2C, C_q, $C_{anthracene}$); 130.1 (s, 1C, $C_{anthracene}$); 129.8 (s, 2C, $C_{benzimidazole}$); 129.5 (s, 2C, $C_{anthracene}$); 128.9 (s, 2C, $C_{benzimidazole}$); 128.1 (s, 2C, $C_{anthracene}$); 126.7 (s, 2C, $C_{benzimidazole}$); 126.3 (s, 2C, $C_{anthracene}$); 121.5 (s, 2C, $C_{pyridine}$); 116.9 (s, 2C, $C_{anthracene}$); 115.0 (s, 2C, $C_{benzimidazole}$); 35.0 (s, 2C, C_{methyl}).

ESI-MS (pos) (m/z in MeCN) calculated for $C_{35}H_{27}N_5^{2+}$: 258.6128; found: 258.6122 $[M]^{2+}$.

1,1'-(4-(pyren-1-yl)pyridine-2,6-diyl)bis(3-methyl-1*H*-benzo[*d*]imidazol-3-ium) **[H_2-bbp-4](PF_6)$_2$**:

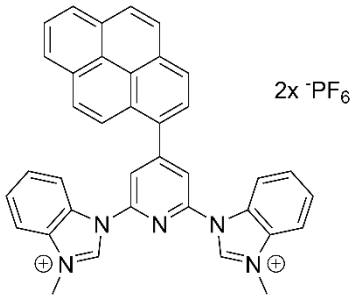

[H_2-bbp-4](PF_6)$_2$

The product was obtained as yellow solid (92 %).

^{1}H-NMR (700 MHz, d_6-acetone): δ (ppm) = 10.56 (s, 2H, $H_{benzimidazole}$); 8.74 (s, 2H, $H_{pyridine}$); 8.68 (d, 2H, J = 8.4 Hz, $H_{benzimidazole}$); 8.51 (d, 1H, J = 7.8 Hz, H_{pyrene}); 8.46 (d, 1H, J = 9.2 Hz, H_{pyrene}); 8.42 (d, 1H, J = 7.6 Hz, H_{pyrene}); 8.39-8.36 (m, 2H, H_{pyrene}); 8.34 (d, 1H, J = 8.9 Hz, H_{pyrene}); 8.31-8.29 (m, 2H, H_{pyrene}); 8.26 (d, 2H, J = 8.3 Hz, $H_{benzimidazole}$); 8.17 (t, 1H, J = 7.6 Hz, H_{pyrene}); 7.91 (t, 2H, J = 7.8 Hz, $H_{benzimidazole}$); 7.85 (t, 2H, J = 7.9 Hz, $H_{benzimidazole}$); 4.50 (s, 6H, H_{methyl}).

^{13}C-NMR (176 MHz, d_6-acetone): δ (ppm) = 158.7 (s, 1C, C_q, C_{pyrene}); 148.3 (s, 2C, C_q, $C_{pyridine}$); 143.6 (s, 2C, $C_{benzimidazole,\ N\text{-}C\text{-}N}$); 133.9 (s, 2C, C_q, $C_{benzimidazole}$); 133.6 (s, 1C, C_q, C_{pyrene}); 132.6 (s, 1C, C_q, $C_{pyridine}$); 132.4 (s, 1C, C_q, C_{pyrene}); 131.8 (s, 1C, C_q, C_{pyrene}); 131.2 (s, 2C, C_q, $C_{benzimidazole}$); 130.4 (s, 1C, C_{pyrene}); 130.0 (s, 1C, C_{pyrene}); 129.5 (s, 2C, $C_{benzimidazole}$); 129.2 (s, 1C, C_q, C_{pyrene}); 128.9 (s, 2C, $C_{benzimidazole}$); 128.6 (s, 1C, C_{pyrene}); 128.3 (s, 1C, C_{pyrene}); 127.9 (s, 1C, C_{pyrene}); 127.4 (s, 1C, C_{pyrene}); 126.9 (s, 1C, C_{pyrene}); 126.2 (s, 1C, C_{pyrene}); 125.6 (s, 1C, C_q, C_{pyrene}); 125.2 (s, 1C, C_q, C_{pyrene}); 124.6 (s, 1C, C_{pyrene}); 120.6 (s, 2C, $C_{pyridine}$); 116.8 (s, 2C, $C_{benzimidazole}$); 115.0 (s, 2C, $C_{benzimidazole}$); 34.9 (s, 2C, C_{methyl}).

ESI-MS (pos) (m/z in MeCN) calculated for $C_{37}H_{27}N_5^{2+}$: 270.6128; found: 270.6227 $[M]^{2+}$.

1,1‘-(4-(perylen-3-yl)pyridine-2,6-diyl)bis(3-methyl-1*H*-benzo[d]imidazol-3-ium) **[H_2-bbp-5](OTf)$_2$**:

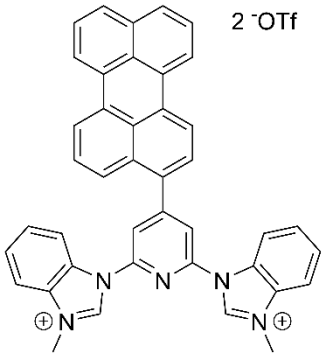

[H_2-bbp-5](OTf)$_2$

1,1‘-(4-(perylen-3-yl)pyridine-2,6-diyl)bis(1*H*-benzo[d]imidazole) **10-5** (1 eq.) was dissolved in $CHCl_3$ (20 ml/mmol) under inert conditions at room temperature. MeOTf (20 eq.) was added dropwise, and the reaction was stirred for 16 h at 60 °C. The reaction mixture was cooled down to room temperature while the product started to precipitate. Product remaining in solution was precipitated by adding n-pentane and cooling in an ice bath. The crude product was filtered and washed with n-pentane. The ligand precursor was purified by diffusion crystallization (solvent: acetone/ antisolvent: n-pentane) and the product was obtained as yellow powder (91 %).

^{1}H-NMR (700 MHz, d_6-acetone): δ (ppm): 10.49 (s, 2H, $H_{benzimidazole}$); 8.51 (d, 2H, $^3J_{HH}$ = 8.4 Hz, $H_{benzimidazole}$); 8.48 (s, 2H, $H_{pyridine}$); 8.38 (d, 1H, $^3J_{HH}$ = 7.6 Hz, $H_{perylene}$); 8.34 (d, 1H, $^3J_{HH}$ = 7.5 Hz, $H_{perylene}$); 8.33 (d, 1H, $^3J_{HH}$ = 7.5 Hz, $H_{perylene}$); 8.27 (d, 1H, $^3J_{HH}$ = 7.3 Hz, $H_{perylene}$); 8.13 (d, 2H, $^3J_{HH}$ = 8.3 Hz, $H_{benzimidazole}$); 8.04 (d, 1H, $^3J_{HH}$ = 8.04 Hz, $H_{perylene}$); 7.83 (d, 1H, $^3J_{HH}$ = 7.6 Hz, $H_{perylene}$); 7.79 (t, 2H, $^3J_{HH}$ = 7.8 Hz, $H_{benzimidazole}$); 7.78-7.74 (m, 2H, $H_{perylene}$); 7.73 (t, 2H, $^3J_{HH}$ = 7.8 Hz, $H_{benzimidazole}$); 7.62 (t, 1H, $^3J_{HH}$ = 7.8 Hz, $H_{perylene}$); 7.51 (q, 2H, $^3J_{HH}$ = 7.5 Hz, $H_{perylene}$); 4.44 (s, 6H, H_{methyl}).

^{13}C-NMR (176 MHz, d_6-acetone): δ (ppm): 157.74 (s, 1C, C_q, $C_{perylene}$); 148.17 (s, 2C, C_q, $C_{pyridine}$); 143.55 (s, 2C, $C_{benzimidazole}$); 135.59 (s, 1C, C_q, $C_{perylene}$); 134.88 (s, 1C, C_q, $C_{pyridine}$); 134.07 (s, 1C, C_q, $C_{perylene}$); 133.77 (s, 2C, C_q, $C_{benzimidazole}$); 132.65 (s, 1C, C_q, $C_{perylene}$); 132.47 (s, 1C, C_q, $C_{perylene}$); 131.31 (s, 1C, C_q, $C_{perylene}$); 130.85 (s, 2C, C_q, $C_{benzimidazole}$); 130.83 (s, 1C, C_q, $C_{perylene}$); 130.42 (s, 1C, $C_{perylene}$); 130.02 (s, 1C, $C_{perylene}$); 129.60 (s, 1C, C_q, $C_{perylene}$); 129.46 (s, 1C, $C_{perylene}$); 129.36 (s, 1C, $C_{perylene}$); 129.32 (s, 2C, $C_{benzimidazole}$); 128.93 (s, 1C, C_q, $C_{perylene}$); 128.72 (s, 2C, $C_{benzimidazole}$); 127.94 (s, 1C, $C_{perylene}$); 127.84 (s, 1C, $C_{perylene}$); 125.55 (s, 1C, $C_{perylene}$); 122.44 (s, 1C, $C_{perylene}$); 122.26 (s, 1C, $C_{perylene}$); 122.21 (s, 1C, $C_{perylene}$); 120.99 (s, 1C, $C_{perylene}$); 119.45 (s, 2C, $C_{pyridine}$); 116.72 (s, 2C, $C_{benzimidazole}$); 114.79 (s, 2C, $C_{benzimidazole}$); 34.84 (s, 2C, C_{methyl}).

ESI-MS (pos) (m/z in MeCN) calculated for $C_{41}H_{29}N_5^{2+}$: 591.2412; found: 295.6222 $[M]^{2+}$.

General procedure for the synthesis of the iron complexes:

For the synthesis of complexes, the respective pro-ligand (2 eq.) was suspended in tetrahydrofuran (THF) and cooled to −78 °C. Lithium bis(trimethylsilyl)amide (LiHMDS; 6 eq., 1 M, in THF) was added dropwise. After complete deprotonation, evidenced by a clear solution, $FeBr_2$ (1 eq.) was dissolved in THF and added dropwise to the carbene solution. The mixture instantly turned into a dark-red suspension, which was stirred for 16 h while slowly getting up to room temperature. The solvent was removed, and the residue was dissolved in acetone. Residues were filtered off. Acetone was removed to a minimum amount and added dropwise to a solution of KPF_6 (10 eq.) in water cooled by an ice bath, and stirred for 15 min. The resulting precipitate was filtered off and rinsed with cold water. The crude complex was first purified by column chromatography (stationary phase: basic aluminum oxide/ mobile phase: acetonitrile) finally purified by recrystallization via solvent diffusion (acetone/diethyl ether).[36]

$[Fe(bbp)_2](PF_6)_2$:

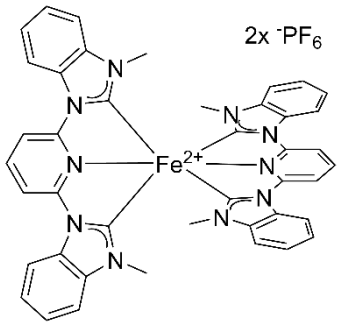

$[Fe(bbp)_2](PF_6)_2$

The complex was obtained as red crystals (54 %).

^{1}H-NMR (700 MHz, d_6-acetone): δ (ppm) = 8.73-8.67 (m, 6H, $H_{pyridine}$); 8.49 (d, 4H, $^3J_{HH}$ = 8.4 Hz, $H_{benzimidazole}$); 7.53 (quint., 4H, $^3J_{HH}$ = 4.2 Hz, $H_{benzimidazole}$); 7.44 (d, 8H, $^3J_{HH}$ = 4.0 Hz, $H_{benzimidazole}$).

^{13}C-NMR (176 MHz, d_6-acetone): δ (ppm) = 212.0 (s, C_q, 4C, $C_{carbene}$); 155.8 (s, C_q, 2C, $C_{pyridine}$); 141.5 (s, 2C, $C_{pyridine}$); 139.0 (s, C_q, 4C, $C_{benzimidazole}$); 132.1 (s, C_q, 4C, $C_{benzimidazole}$); 125.7 (s, 4C, $C_{benzimidazole}$); 125.0 (s, 4C, $C_{benzimidazole}$); 112.8 (s, 4C, $C_{benzimidazole}$); 111.4 (s, 4C, $C_{benzimidazole}$); 107.9(s, 4C, $C_{pyridine}$); 32.1 (s, 4C, C_{methyl}).

ESI-MS (pos) (m/z in MeCN) calculated for $C_{42}H_{34}FeN_{10}^{2+}$: 367.1153; found: 367.1203 $[M]^{2+}$.

Elemental analysis calculated for $(C_{54}H_{42}F_{12}FeN_{10}P_2)_2(C_4H_{10}O)$: C = 49.78 %, H = 3.70 %, N = 13.19 %.

Found: C = 49.69 %, H = 3.99 %, N = 13.10 %.

[Fe(bbp-1)$_2$](PF$_6$)$_2$:

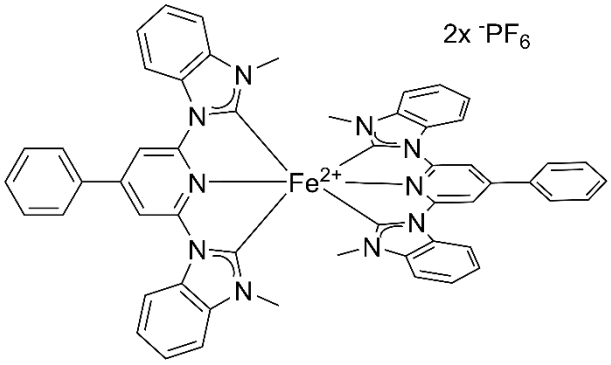

[Fe(bbp-1)$_2$](PF$_6$)$_2$

The complex was obtained as red crystals (47 %).

^{1}H-NMR (700 MHz, d$_6$-acetone): δ (ppm) = 8.80 (s, 4H, H$_{pyridine}$); 8.71 (d, 4H, J = 8.4 Hz, H$_{benzimidazole}$); 8.39 (d, 4H, J = 7.1 Hz, H$_{benzimidazole}$); 7.78-7.76 (m, 4H, H$_{benzimidazole}$); 7.74-7.71 (m, 2H, H$_{phenyl}$); 7.56-7.54 (m, 4H, H$_{benzimidazole}$); 7.46-7.44 (m, 8H, H$_{phenyl}$); 3.10 (s, 12H, H$_{methyl}$).

^{13}C-NMR (176 MHz, d$_6$-acetone): δ (ppm) = 211.5 (s, 4C, C$_q$, C$_{benzimidazole,\ N\text{-}C\text{-}N}$); 155.2 (s, 4C, C$_q$, C$_{pyridine}$); 153.4 (s, 2C, C$_q$, C$_{pyridine}$); 138.3 (s, 4C, C$_q$, C$_{benzimidazole}$); 137.1 (s, 2C, C$_q$, C$_{phenyl}$); 131.3 (s, 4C, C$_q$, C$_{benzimidazole}$); 130.9 (s, 2C, C$_{phenyl}$); 129.7 (s, 4C, C$_{benzimidazole}$); 128.6 (s, 4C, C$_{benzimidazole}$); 124.9 (s, 4C, C$_{phenyl}$); 124.2 (s, 4C, C$_{benzimidazole}$); 112.6 (s, 4C, C$_{benzimidazole}$); 110.6 (s, 4C, C$_{phenyl}$); 104.9 (s, 4C, C$_{phenyl}$); 31.6 (s, 4C, C$_{methyl}$).

ESI-MS (pos) (m/z in MeCN) calculated for $C_{54}H_{42}FeN_{10}^{2+}$: 443.1466; found: 443.1541 $[M]^{2+}$.

Elemental analysis calculated for $C_{54}H_{42}F_{12}FeN_{10}P_2$: C = 55.12 %, H = 3.60 %, N = 11.90 %.

Found: C = 54.83 %, H = 3.46 %, N = 12.01 %.

[Fe(bbp-2)$_2$](PF$_6$)$_2$:

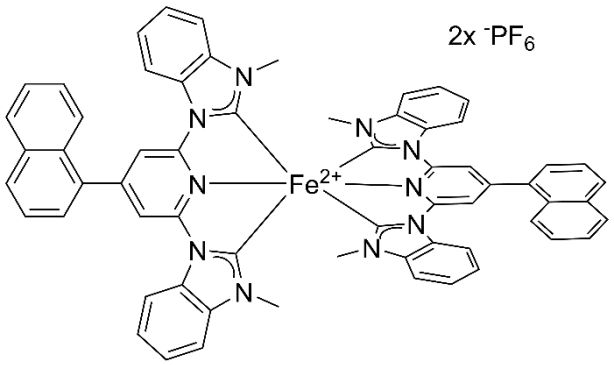

[Fe(bbp-2)$_2$](PF$_6$)$_2$

The complex was obtained as red crystals (63 %).

^{1}H-NMR (700 MHz, d$_6$-acetone): δ (ppm) = 8.79 (s, 4H, H$_{pyridine}$); 8.60-8.59 (m, 4H, H$_{benzimidazole}$); 8.28 (d, 2H, J = 8.5 Hz, H$_{naphthalene}$); 8.26 (d, 2H, J = 8.3 Hz, H$_{naphthalene}$); 8.21 (d, 2H, J = 8.2 Hz, H$_{naphthalene}$);8.06-8.05 (m, 2H, H$_{naphthalene}$); 7.86-7.83 (m, 2H, H$_{naphthalene}$); 7.74-7.72 (m, 2H, H$_{naphthalene}$); 7.67-7.66 (m, 2H, H$_{naphthalene}$); 7.51-7.49 (m, 4H, H$_{benzimidazole}$); 7.47-7.43 (m, 8H, H$_{benzimidazole}$); 3.27 (s, 12H, H$_{methyl}$).

^{13}C-NMR (176 MHz, d$_6$-acetone): δ (ppm) = 211.5 (s, 4C, C$_q$, C$_{benzimidazole,\ N\text{-}C\text{-}N}$); 154.9 (s, 4C, C$_q$, C$_{pyridine}$); 153.7 (s, 2C, C$_q$, C$_{naphthalene}$); 138.3 (s, 4C, C$_q$, C$_{benzimidazole}$); 136.5 (s, 2C, C$_q$, C$_{pyridine}$); 134.3 (s, 2C, C$_q$, C$_{naphthalene}$); 131.4 (s, 4C, C$_q$, C$_{benzimidazole}$); 131.2 (s, 2C, C$_q$, C$_{naphthalene}$); 130.3 (s, 2C, C$_{naphthalene}$); 129.1 (s, 2C, C$_{naphthalene}$); 128.5 (s, 2C, C$_{naphthalene}$); 127.7 (s, 2C, C$_{naphthalene}$); 126.8 (s, 2C, C$_{naphthalene}$); 125.8 (s, 2C, C$_{naphthalene}$); 125.2 (s, 2C, C$_{naphthalene}$); 125.0 (s, 4C, C$_{benzimidazole}$); 124.2 (s, 4C, C$_{benzimidazole}$); 112.6 (s, 4C, C$_{benzimidazole}$); 110.6 (s, 4C, C$_{benzimidazole}$); 108.5 (s, 4C, C$_{pyridine}$); 31.7 (s, 4C, C$_{methyl}$).

ESI-MS (pos) (m/z in MeCN) calculated for $C_{62}H_{46}FeN_{10}^{2+}$: 493.1623; found: 493.1644 $[M]^{2+}$.

Elemental analysis calculated for $C_{62}H_{46}F_{12}FeN_{10}P_2$: C = 58.32 %, H = 3.63 %, N = 10.97 %.

Found: C = 57.89 %, H = 3.91 %, N = 10.91 %.

[Fe(bbp-3)$_2$](PF$_6$)$_2$:

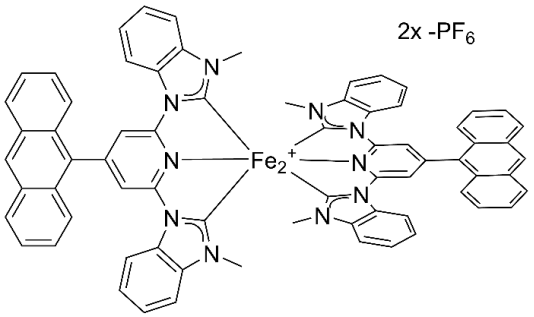

[Fe(bbp-3)$_2$](PF$_6$)$_2$

The complex was obtained as red crystals (56 %).

^{1}H-NMR (700 MHz, d_6-acetone): δ (ppm) = 8.97 (s, 2H, $H_{anthracene}$); 8.86 (s, 4H, $H_{pyridine}$); 8.55 (d, 4H, J = 8.4 Hz, $H_{benzimidazole}$); 8.36 (d, 4H, J = 8.6 Hz, $H_{anthracene}$); 7.98 (d, 4H, J = 8.9 Hz, $H_{anthracene}$); 7.71-7.68 (m, 4H, $H_{anthracene}$); 7.63-7.61 (m, 4H, $H_{anthracene}$); 7.57 (d, 4H, J = 8.0 Hz, $H_{benzimidazole}$); 7.44 (t, 4H, J = 7.6 Hz, $H_{benzimidazole}$); 7.37 (t, 4H, J = 7.5 Hz, $H_{benzimidazole}$); 3.48 (s, 12H, H_{methyl}).

^{13}C-NMR (176 MHz, d_6-acetone): δ (ppm) = 212.4 (s, 4C, C_q, $C_{benzimidazole,\ N\text{-}C\text{-}N}$); 156.1 (s, 4C, C_q, $C_{pyridine}$); 153.3 (s, 2C, C_q, $C_{anthracene}$); 139.1 (s, 4C, C_q, $C_{benzimidazole}$); 133.3 (s, 2C, C_q, $C_{pyridine}$); 132.6 (s, 4C, C_q, $C_{anthracene}$); 132.3 (s, 4C, C_q, $C_{benzimidazole}$); 130.7 (s, 4C, C_q, $C_{anthracene}$); 129.9 (s, 4C, $C_{anthracene}$); 129.8 (s, 2C, $C_{anthracene}$); 128.0 (s, 4C, $C_{anthracene}$); 126.7 (s, 4C, $C_{anthracene}$); 126.6 (s, 4C, $C_{anthracene}$); 125.8 (s, 4C, $C_{benzimidazole}$); 125.0 (s, 4C, $C_{benzimidazole}$); 113.5 (s, 4C, $C_{benzimidazole}$); 111.4 (s, 4C, $C_{benzimidazole}$); 32.6 (s, 4C, C_{methyl}).

ESI-MS (pos) (m/z in MeCN) calculated for $C_{70}H_{50}FeN_{10}^{2+}$: 543.1779; found: 543.1745 $[M]^{2+}$.

Elemental analysis calculated for $C_{70}H_{50}F_{12}FeN_{10}P_2$: C = 61.06 %, H = 3.66 %, N = 10.17 %.

Found: C = 61.17 %, H = 4.01 %, N = 10.16 %.

[Fe(bbp-4)$_2$](PF$_6$)$_2$:

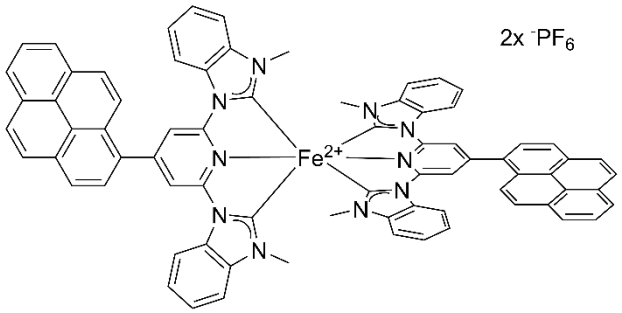

[Fe(bbp-4)$_2$](PF$_6$)$_2$

The complex was obtained as red crystals (64 %).

^{1}H-NMR (700 MHz, d$_6$-acetone): δ (ppm) = 8.97 (s, 4H, H$_{pyridine}$); 8.66-8.65 (m, 4H, H$_{benzimidazole}$); 8.62-8.61 (m, 4H, H$_{pyrene}$); 8.50 (d, 2H, J = 7.7 Hz, H$_{pyrene}$); 8.44 (d, 2H, J = 7.3 Hz, H$_{pyrene}$); 8.42 (d, 4H, J = 2.3 Hz, H$_{pyrene}$); 8.35 (d, 2H, J = 9.3 Hz, H$_{pyrene}$); 8.24 (t, 2H, J = 7.5 Hz, H$_{pyrene}$); 7.55-7.54 (m, 4H, H$_{benzimidazole}$); 7.47-7.45 (m, 8H, H$_{benzimidazole}$); 3.36 (s, 12H, H$_{methyl}$).

^{13}C-NMR (176 MHz, d$_6$-acetone): δ (ppm) = 212.4 (s, 4C, C$_q$, C$_{benzimidazole,\ N\text{-}C\text{-}N}$); 155.7 (s, 4C, C$_q$, C$_{pyridine}$); 154.9 (s, 2C, C$_q$, C$_{pyrene}$); 139.1 (s, 4C, C$_q$, C$_{benzimidazole}$); 134.4 (s, 2C, C$_q$, C$_{pyridine}$); 133.3 (s, 2C, C$_q$, C$_{pyrene}$); 132.5 (s, 2C, C$_q$, C$_{pyrene}$); 132.3 (s, 4C, C$_q$, C$_{benzimidazole}$); 131.9 (s, 2C, C$_q$, C$_{pyrene}$); 130.1 (s, 2C, C$_{pyrene}$); 129.8 (s, 2C, C$_{pyrene}$); 129.7 (s, 2C, C$_q$, C$_{pyrene}$); 129.2 (s, 2C, C$_{pyrene}$); 128.4 (s, 2C, C$_{pyrene}$); 127.8 (s, 2C, C$_{pyrene}$); 127.3 (s, 2C, C$_{pyrene}$); 126.8 (s, 2C, C$_{pyrene}$); 126.0 (s, 2C, C$_{pyrene}$); 125.8 (s, 4C, C$_{benzimidazole}$); 125.8 (s, 2C, C$_q$, C$_{pyrene}$); 125.5 (s, 2C, C$_q$, C$_{pyrene}$); 125.1 (s, 2C, C$_{pyrene}$); 125.0 (s, 4C, C$_{benzimidazole}$); 113.4 (s, 4C, C$_{benzimidazole}$); 111.4 (s, 4C, C$_{benzimidazole}$); 109.7 (s, 4C, C$_{pyridine}$); 32.6 (s, 4C, C$_{methyl}$).

ESI-MS (pos) (m/z in MeCN) calculated for $C_{74}H_{50}FeN_{10}^{2+}$: 597.1779; found: 597.1828 $[M]^{2+}$.

Elemental analysis calculated for $C_{74}H_{50}F_{12}FeN_{10}P_2+H_2O$: C = 61.59 %, H = 3.63 %, N = 9.71 %.

Found: C = 61.67 %, H = 3.71 %, N = 9.56 %.

[Fe(bbp-5)$_2$](PF$_6$)$_2$:

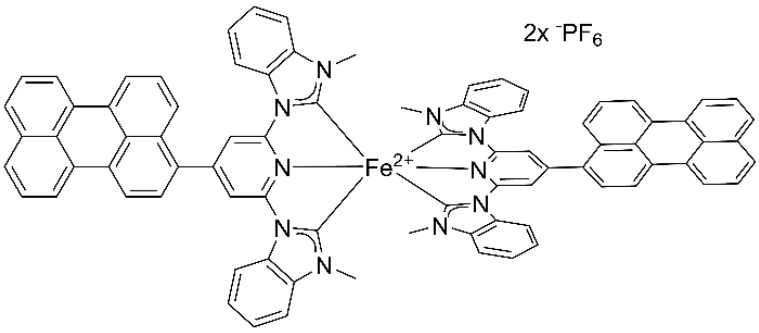

[Fe(bbp-5)$_2$](PF$_6$)$_2$

The complex was obtained as red crystals (22 %).

^{1}H-NMR (700 MHz, d$_6$-acetone): δ (ppm) = 8.86 (s, 4H, H$_{pyridine}$); 8.69 (d, 2H, $^3J_{HH}$ = 8.1 Hz, H$_{perylene}$); 8.66 (dd, $^3J_{HH}$ = 1.7 Hz, $^3J_{HH}$ = 7.3 Hz, H$_{benzimidazole}$); 8.59 (d, 4H, $^3J_{HH}$ = 7.2 Hz, H$_{perylene}$); 8.53 (d, 2H, $^3J_{HH}$ = 7.2 Hz, H$_{perylene}$); 8.18 (d, 2H, $^3J_{HH}$ = 8.4 Hz, H$_{perylene}$); 8.08 (d, 2H, $^3J_{HH}$ = 7.4 Hz, H$_{perylene}$); 7.96 (d, 2H, $^3J_{HH}$ = 8.1 Hz, H$_{perylene}$); 7.94 (d, 2H, $^3J_{HH}$ = 8.1 Hz, H$_{perylene}$); 7.70-7.66 (m, 6H, H$_{perylene}$); 7.53-7.51 (s, 4H, H$_{benzimidazole}$); 7.49-7.45 (m, 8H, H$_{benzimidazole}$); 2.82 (s, 12H, H$_{methyl}$).

^{13}C-NMR (176 MHz, d$_6$-acetone): δ (ppm) = 212.27 (s, 4C, C$_q$, C$_{carbene}$); 155.81 (s, 4C, C$_q$, C$_{pyridine}$); 154.38 (s, 2C, C$_q$, C$_{perylene}$); 139.08 (s, 4C, C$_q$, C$_{benzimidazole}$); 136.82 (s, 2C, C$_q$, C$_{pyridine}$); 135.93 (s, 2C, C$_q$, C$_{perylene}$); 133.94 (s, 2C, C$_q$, C$_{perylene}$); 133.58 (s, 2C, C$_q$, C$_{perylene}$); 132.90 (s, 2C, C$_q$, C$_{perylene}$); 132.21 (s, 4C, C$_q$, C$_{benzimidazole}$); 131.73 (s, 2C, C$_q$, C$_{perylene}$); 131.43 (s, 2C, C$_q$, C$_{perylene}$); 130.27 (s, 2C, C$_{perylene}$); 130.05(s, 2C, C$_q$, C$_{perylene}$); 129.96 (s, 2C, C$_{perylene}$); 129.61 (s, 2C, C$_{perylene}$); 129.40 (s, 2C, C$_q$, C$_{perylene}$); 129.03 (s, 2C, C$_{perylene}$); 128.13 (s, 2C, C$_{perylene}$); 128.07 (s, 2C, C$_{perylene}$); 126.01 (s, 2C, C$_{perylene}$); 125.78 (s, 4C, C$_{benzimidazole}$); 125.02 (s, 4C, C$_{benzimidazole}$); 122.43 (s, 2C, C$_{perylene}$); 122.35 (s, 2C, C$_{perylene}$); 122.21 (s, 2C, C$_{perylene}$); 121.13 (s, 2C, C$_{perylene}$); 113.39 (s, 4C, C$_{benzimidazole}$); 111.38 (s, 4C, C$_{benzimidazole}$); 109.17 (s, 4C, C$_{pyridine}$); 32.53 (s, 4C, C$_{methyl}$).

ESI-MS (pos) (m/z in MeCN) calculated for $C_{82}H_{54}FeN_{10}^{2+}$: 617.1936; found: 617.2028 $[M]^{2+}$.

2,6-di(1H-imidazol-1-yl)pyridin-4-amine **11**:

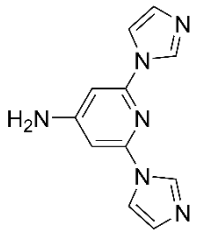

11

6Br (1 eq.), imidazole (2.4 eq.), potassium carbonate (2.4 eq.) and copper(I)oxide (0.2 eq.) were suspended in DMF (10 ml/mmol), degassed by bubbling through with argon and stirred at 150°C for 48 h. DMF was removed under reduced pressure. Flash chromatography with pure DCM gave not reacted and incompletely coupled 4-amino-2,6-dichloropyridine and imidazole. **11** was obtained by flash chromatography with DCM/MeOH (9/1 V/V) afterwards (67 %).[36]

^{1}H-NMR (700 MHz, $CDCl_3$): δ (ppm) = 8.39 (s, 2H, $H_{imidazole}$), 7.67 (t, 2H, $^3J_{HH}$ = 1.4 Hz, $H_{imidazole}$), 7.23 (s, 2H, $H_{imidazole}$), 7.10 (s, 2H, $H_{pyridine}$).

2,6-Di-(1H-imidazol-1-yl)-4-iodopyridine **12**:

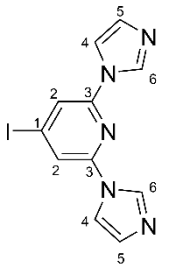

12

According to literature 2,6-di(1H-imidazol-1-yl)pyridin-4-amine **11** (1,61 g; 7,13 mmol; 1 eq.) was suspended in a mixture of conc. HCl and water (1/5 V/V). After addition of KI (12 eq.) at 0 °C the mixture was stirred for 1 h. After stepwise addition of $NaNO_2$ (3.5 eq.) the reaction was slowly brought to room temperature and neutralized with solid $NaHCO_3$ and subsequently deactivated with $NaSO_3$. The mixture was extracted with DCM, the organic layer was dried with $MgSO_4$ and the product was obtained after purification by column chromatography (stationary phase: SiO_2, solvent: acetone) as an orange solid (38 %).[89]

^{1}H-NMR (700 MHz, DMSO-d_6): δ (ppm) = 8.77 (dd, *J* = 1.1 Hz, 2H, H_6), 8.23 (s, 2H, H_2), 8.16 (dd, *J* = 1.4 Hz, 2H, H_4), 7.14 (dd, *J* = 1.2 Hz, 2H, H_5).

^{13}C-NMR (176 MHz, DMSO-d_6): δ (ppm) = 147.62 (C_3), 135.79 (C_6), 130.40 (C_5), 118.26 (C_2), 116.89 (C_4), 111.88 (C_1).

ESI-MS (pos) (m/z in MeOH) calculated for $C_{11}H_8N_5I$: 336.9897; found 337.9934 $[M+H]^+$.

9-Ethinylanthracene **13**:

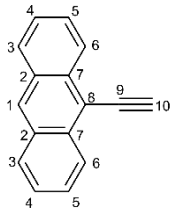

13

According to literature 9-bromoanthracene (1 eq.), CuI (0.11 eq.) and $[Pd(PPh_3)_2]Cl_2$ (0.1 eq.) were degassed and solved in a mixture of TEA and DIPA (1/7 V/V). After addition of trimethylsilyl acetylene (2.7 eq.) the reaction was stirred at 110 °C for 17 h. The reaction was cooled down to room temperature and stopped by adding a saturated solution of NH_4Cl. The aqueous solution was extracted with cyclohexane and dried over Na_2SO_4. The product was obtained after purification by column chromatography (stationary phase: SiO_2, solvent: cyclohexane) as red solid (72 %).[90]

^{1}H-NMR (700 MHz, $CDCl_3$): δ (ppm) = 8.59 (dd, *J* = 8.7, 1.1 Hz, 2H, H_6), 8.46 (s, 1H, H_1), 8.02 (d, *J* = 8.2 Hz, 2H, H_3), 7.60 (ddd, *J* = 8.6, 6.5, 1.3 Hz, 3H, H_5), 7.51 (ddd, *J* = 8.0, 6.4, 1.2 Hz, 3H, H_4), 4.00 (s, 1H, H_{10}).

^{13}C-NMR (176 MHz, $CDCl_3$): δ (ppm) = 133.30 (C_7), 131.16 (C_2), 128.81 (C_3), 128.37 (C_1), 126.97 (C_5), 126.69 (C_6), 125.82 (C_4), 116.15 (C_8), 88.34 (C_{10}), 80.48 (C_9).

EI-MS (pos) (m/z) calculated for $C_{16}H_{10}$: 202.0783; found: 202.0056.

4-(Anthracen-9-ylethinyl)-2,6-di(1*H*-imidazol-1-yl)pyridine **14**:

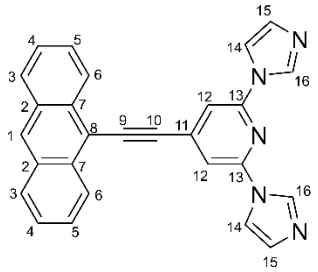

14

According to literature 9-ethinylanthracene **13** (1 eq.), 2,6-di-(1H-imidazol-1-yl)-4-iodopyridine **12** (1.2 eq.), $[Pd(PPh_3)_2]Cl_2$ (0.1 eq.) and CuI (0.11 eq.) were dissolved in a degassed mixture of toluene and TEA (1/1 V/V) and DIPA (7.6 eq.) was added. The reaction was heated to 110 °C for 17 h. The reaction was quenched by the addition of NH_4Cl (aq.) and the mixture was extracted with DCM. After purification by column chromatography (stationary phase: SiO_2; mobile phase: cyclohexane/acetone 1/1 V/V). **14** was obtained as yellow solid (58 %).[90]

^{1}H-NMR: (700 MHz, DMSO-d_6): δ (ppm) = 8.90 (t, *J* = 1.1 Hz, 2H, H_{16}), 8.85 (s, 1H, H_1), 8.75 (dd, *J* = 8.7, 1.1 Hz, 2H, H_6), 8.29 (dd, *J* = 1.4 Hz, 2H, H_{14}), 8.25 (s, 2H, H_{12}), 8.24 (d, *J* = 8.5 Hz, 2H, H_3), 7.80 (ddd, 2H, H_5), 7.68 (ddd, *J* = 8.0, 6.5, 1.1 Hz, 2H, H_4), 7.21 (dd, *J* = 1.2 Hz, 2H, H_{15}).

^{13}C-NMR (176 MHz, DMSO-d_6): δ (ppm) = 148.21 (C_{13}), 136.47 (C_{11}), 135.87 (C_{16}), 132.51 (C_7), 130.69 (C_2), 130.38 (C_{15}), 130.19 (C_1), 129.14 (C_3), 128.12 (C_5), 126.33 (C_4), 126.05 (C_6), 117.05 (C_{14}), 114.00 (C_8), 111.53 (C_{12}), 97.33 (C_{10}), 91.71 (C_9).

ESI-MS (pos) (m/z in MeCN) calculated for $C_{27}H_{17}N_5$: 412.1557; found: 412.1547 $[M+H]^+$.

[H_2-bim-ac-3](PF_6)$_2$:

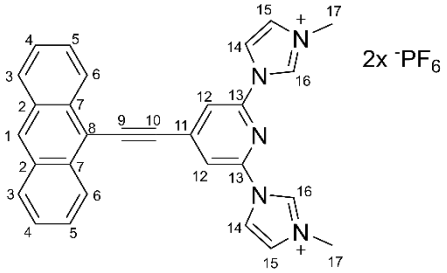

[H_2-bim-ac-3](PF_6)$_2$

According to literature 4-(Anthracen-9-ylethinyl)-2,6-di(1*H*-imidazol-q-yl)pyridine (0.071 g, 0.173 mmol, 1 eq.) was dissolved in DCM (30 ml) under inert conditions. The solution was cooled to -78 °C and MeOTf (0.05 ml, 0.36 mmol, 2.1 eq.) was added dropwise. The solution slowly returned to room temperature within 17 h and *n*-pentane was added. The resulting precipitate was filtered off. The crude product was dissolved in DMSO and precipitated in an aqueous KPF_6 solution (0.318 g; 1.73 mmol; 10 eq.) for anion exchange. Final purification was done by diffusion crystallization (solvent: acetone; antisolvent: diethyl ether; 83 %).[36]

^{1}H-NMR: (700 MHz, DMSO-d_6): δ (ppm) = 10.35 (s, 2H, H_{16}), 8.94 (s, 1H, H_1), 8.85 (t, *J* = 2.0 Hz, 2H, H_{14}), 8.70 (d, *J* = 9.3 Hz, 2H, H_6), 8.69 (s, 2H, H_{12}), 8.29 (d, *J* = 8.4 Hz, 2H, H_3), 8.11 (t, *J* = 1.8 Hz, 2H, H_{15}), 7.83 (ddd, *J* = 8.2, 6.5, 1.2 Hz, 2H, H_5), 7.72 (ddd, *J* = 7.9, 6.5, 1.1 Hz, 2H, H_4), 4.07 (s, 6H, H_{17}).

^{13}C-NMR: (176 MHz, DMSO-d_6): δ (ppm) = 145.84 (C_{13}), 137.66 (C_{11}), 136.47 (C_{16}), 132.71 (C_7), 131.19 (C_1), 130.70 (C_2), 129.45 (C_3), 128.48 (C_5), 126.46 (C_4), 125.50 (C_6), 125.06 (C_{15}), 119.31 (C_{14}), 115.67 (C_{12}), 113.10 (C_8), 96.39 (C_{10}), 94.30 (C_9), 36.72 (C_{17}).

ESI-MS (pos) (m/z in MeCN) calculated for $C_{29}H_{23}N_5^{2+}$: 220.5971; found 220.5966 $[M]^{2+}$.

[Fe(bim-ac-3)$_2$](PF_6)$_2$:

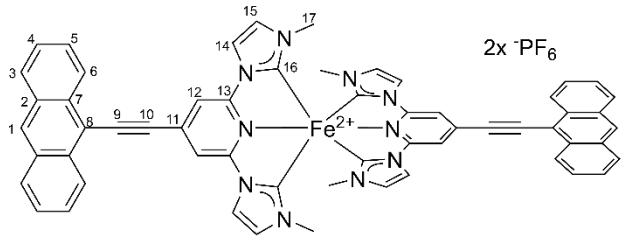

[Fe(bim-ac-3)$_2$](PF_6)$_2$

According to literature the **[H_2-bim-ac-3]**(PF_6)$_2$ pro-ligand (0.088 g, 0.12 mmol, 2 eq.) was suspended in THF (6 ml) under inert conditions and cooled down to -78 °C. LiHMDS (1 M in THF; 0.36 ml; 0.36 mmol, 6 eq.) was added dropwise. After complete deprotonation, evidenced by a clear solution, $FeBr_2$ (0.013 g, 0.06 mmol, 1 eq.), dissolved in THF (5 ml), was added dropwise to the carbene solution. The solution slowly returned to room temperature within 17 h. The solvent was removed under reduced pressure, dissolved in acetone and the residue was filtered. Acetone was reduced to a minimum amount and added dropwise to a solution of KPF_6 (aq., 0.11 g, 0.6 mmol, 10 eq.). The precipitate was filtered off and rinsed with water. The crude complex was purified by column chromatography (stationary phase: basic aluminum oxide; mobile phase: acetonitrile). The complex was finally purified by crystallization via solvent diffusion (acetone/diethyl ether) and the novel complex was obtained as violet needles (46 %).[36]

^{1}H-NMR (700 MHz, d_6-acetone): δ (ppm) = 8.84 (s, 1H, H_1), 8.78 (dd, *J* = 8.7, 1.0 Hz, 2H, H_6), 8.61 (s, 2H, H_{12}), 8.56 (d, *J* = 2.2 Hz, 2H, H_{14}), 8.26 (ddd, 2H, H_3), 7.80 (ddd, *J* = 8.7, 6.5, 1.2 Hz, 2H, H_5), 7.69 (ddd, *J* = 8.5, 6.5, 1.1 Hz, 2H, H_4), 7.40 (d, *J* = 2.1 Hz, 2H, H_{15}), 2.94 (s, 6H, H_{17}).

^{13}C-NMR (176 MHz, d_6-acetone): δ (ppm) = 200.61 (C_{16}), 155.18 (C_{13}), 134.04 (C_7), 133.10 (C_{11}), 132.23 (C_2), 131.35 (C_1), 130.22 (C_3), 128.90 (C_5), 127.99 (C_{15}), 127.18 (C_4), 126.85 (C_6), 117.83 (C_8), 115.40 (C_{14}), 108.14 (C_{12}), 99.19 (C_{10}), 94.53 (C_9), 35.64 (C_{17}).

ESI-MS (pos) (m/z in MeCN) calculated for $C_{58}H_{42}N_{10}Fe^{2+}$: 467,1466; found: 467,1475 $[M]^{2+}$.

Buta-1,3-diyn-1-yltrimethylsilane **15**:

15

1,4-bis(trimethylsilyl)-butadiyne (26.4 ml; 1 eq.) was dissolved in dry diethyl ether (30 ml) and cooled to 0 °C. MeLi (20 ml; 1.5 M in diethyl ether, 1.15 eq.) was added dropwise over 15 min. It was stirred at room temperature for 2 d. Completion of the reaction was tracked by GC-MS. The solution was cooled to -80 °C and saturated aqueous NH_4Cl-solution (30 ml) was added. The mixture was extracted with diethyl ether. Combined organic phase was dried with Na_2SO_4. The solvent was removed under reduced pressure and the crude product was purified by distillation (54 %).[91]

^{1}H-NMR (700 MHz, $CDCl_3$): δ (ppm) = 2.11 (s, 1H, $H_{acetylene}$); 0.20 (s, 9H, H_{TMS}).

^{13}C-NMR (176 MHz, $CDCl_3$): δ (ppm) = 87.6 (s, C_q, 1C, $C_{acetylene}$); 84.9 (s, C_q, 1C, $C_{acetylene}$); 68.5 (s, C_q, 1C, $C_{acetylene}$); 66.8 (s, 1C, $C_{acetylene}$); -0.35 (s, 3C, C_{TMS}).

9-(buta-1,3-diyn-1-yl)anthracene **16**:

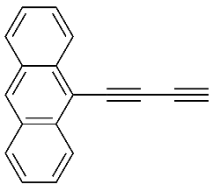

16

According to literature 9-bromoanthracene (1 eq.), CuI (0.11 eq.) and $[Pd(PPh_3)_2]Cl_2$ (0.1 eq.) were degassed and dissolved in a mixture of triethylamine and diisopropylamine (1/7 V/V). After addition of **15** (2.7 eq.) the reaction was stirred at 110 °C for 17 h. The reaction was cooled down to room temperature and stopped by adding a saturated solution of NH_4Cl. The aqueous solution was extracted with cyclohexane and dried over Na_2SO_4. The product was obtained after purification by column chromatography (stationary phase: SiO_2, solvent: cyclohexane) as red solid (26 %).[90]

^{1}H-NMR (700 MHz, $CDCl_3$): δ (ppm) = 8.53 (dd, $^3J_{HH}$ = 8.7 Hz, $^3J_{HH}$ = 0.8 Hz, 2H, $H_{anthracene}$); 8.47 (s, 1H, $H_{anthracene}$); 8.02 (d, $^3J_{HH}$ = 8.5 Hz, 2H, $H_{anthracene}$); 7.62-7.60 (m, 2H, $H_{anthracene}$); 7.53-7.51 (m, 2H, $H_{anthracene}$); 2.82 (s, 1H, H_{TMS}).

^{13}C-NMR (176 MHz, $CDCl_3$): δ (ppm) = 134.6 (s, C_q, 2C, $C_{anthracene}$); 131.2 (s, C_q, 2C, $C_{anthracene}$); 129.5 (s, 1C, $C_{anthracene}$); 129.1 (s, 1C, $C_{anthracene}$); 127.6 (s, 1C, $C_{anthracene}$); 126.6 (s, 1C, $C_{anthracene}$); 126.1 (s, 1C, $C_{anthracene}$); 114.9 (s, C_q, 1C, $C_{anthracene}$); 84.4 (s, C_q, 1C, C_{TMS}); 74.2 (s, 1C, C_{TMS}); 72.9 (s, C_q, 1C, C_{TMS}); 68.7 (s, C_q, 1C, C_{TMS}).

4-(anthracene-9-ylbuta-1,3-diyn-1-yl)-2,6-di(imidazole-1-yl)pyridine **17**:

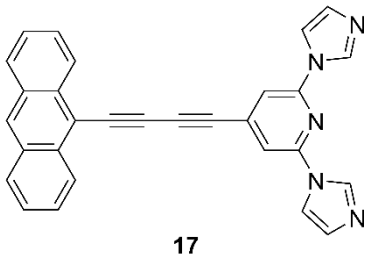

17

According to literature **16** (1 eq.), 2,6-di-(1H-imidazol-1-yl)-4-iodopyridine **12** (1.2 eq.), the palladium catalyst (0.1 eq.) and CuI (0.11 eq.) were dissolved in a mixture of degassed toluene/NEt_3 and DIPA (7.6 eq.) was added. The reaction was heated to 110°C for 17 h. The reaction was quenched by the addition of NH_4Cl (aq.) and the mixture was extracted with DCM.[90] The product has not been purified yet.

2,6-diethynylpyridine **18**:

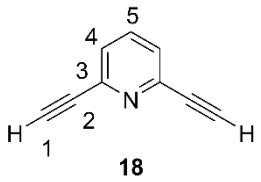

18

2,6-Dibromopyridine (1eq.) and palladium(bis(triphenylphosphan)dichloride) (0.05 eq.) were suspended in TEA and degassed by three cycles of freeze, pump, and thaw. Trimethylsilyl acetylene (2.3 eq.) and copper(I)iodide (0.05 eq.) were added, and the suspension was stirred for 1 d at room temperature and 2 d at 65 °C. The suspension was neutralized by HCl and extracted with DCM.[95] The organic layers were washed with water again. The solvents were removed, and *n*-hexane was added. The suspension was filtered through a silica plug and TMS-protected product was obtained as withe solid. Deprotection was performed with KF (10 eq.) in MeOH/THF (1/1 V/V) at room temperature within 16 h. The solution was extracted with DCM and water. The combined organic layers were dried over $NaSO_4$ and the product obtained as white solid (85 %).[94]

^{1}H-NMR (700 MHz, $CDCl_3$): δ (ppm) = 7.63 (t, 1H, $^3J_{HH}$ = 7.8 Hz, H_5); 7.43 (d, 2H, $^3J_{HH}$ = 7.8 Hz, H_4); 3.14 (s, 2H, H_1).

^{13}C-NMR (176 MHz, $CDCl_3$): δ (ppm) = 142.2 (s, C_q, 2C, C_3); 136.0 (s, 1C, C_5); 126.6 (s, 2C, C_4); 81.5 (s, C_q, 2C, C_2); 77.2 (s, 2C, C_1).

ESI-MS (pos) (m/z in MeCN) calculated for C_9H_5N: 127.0422; found: 128.0518 $[M+H]^+$.

2,6-bis(1-ethyl-1H-1,2,3-triazol-4-yl)pyridine **btp**:

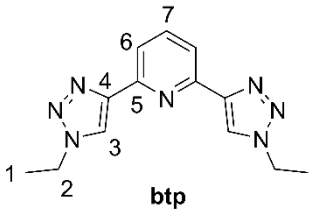

btp

Iodoethane (3.3 eq.) and sodium azide (9 eq.) were stirred in a mixture of THF and water for 2 h at room temperature. 2,6-diethynylpyridine **18** (1 eq.), ascorbic acid (0.8 eq.), copper sulfate (0.4 eq.), potassium carbonate (2 eq.) and pyridine (10 eq.) were added to the *in situ* formed ethyl azide.[96] The mixture was stirred for 3 d at room temperature, while arising precipitate was observed. DCM was added to the suspension and was extracted 3x with a saturated TEA/EDTA solution. The combined organic layers were dried over $NaSO_4$, filtered and the solvent was removed under reduced pressure. The crude product was purified by column chromatography (mobile phase: DCM/acetone; 5/1 V/V, 69 %).[94]

^{1}H-NMR (700 MHz, $CDCl_3$): δ (ppm) = 8.17 (s, 2H, H_3); 8.08 (d, 2H, $^3J_{HH}$ = 7.8 Hz, H_6); 7.84 (t, 1H, $^3J_{HH}$ = 7.8 Hz, H_7); 4.47 (q, 4H, $^3J_{HH}$ = 7.3 Hz, H_2); 1.60 (t, 6H, $^3J_{HH}$ = 7.4 Hz, H_1).

^{13}C-NMR (176 MHz, $CDCl_3$): δ (ppm) = 150.2 (s, C_q, 2C, C_4); 148.6 (s, C_q, 2C, C_5); 137.8 (s, 1C, C_7); 121.5 (s, 2C, C_3); 119.4 (s, 2C, C_6); 45.6 (s, 2C, C_2); 15.6 (s, 2C, C_1).

ESI-MS (pos) (m/z in MeCN) calculated for $C_{13}H_{15}N_7Na^+$: 292.1282; found: 292.1309 $[M+Na]^+$.

[Fe(btp)$_2$](PF$_6$)$_2$:

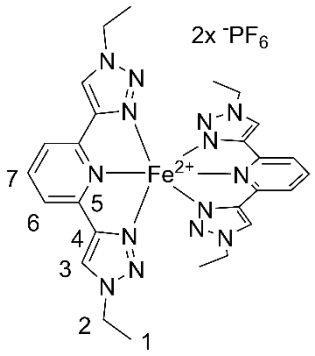

[Fe(btp)$_2$](PF$_6$)$_2$

2,6-bis(1-ethyl-1H-1,2,3-triazol-4-yl)pyridine **btp** (2 eq.) and $FeBr_2$ (1 eq.) were stirred in MeOH for 16 h. Insolouble solid was filterd, the filtrate was concentrated and dropped in a aqueous KPF_6 solution. Arising precipitate was filtered and washed with water. The crude product was dissolved in acetone and precipitated in diethylether. After filtering, the product was purified by crystallization (74 %).[94]

^{1}H-NMR (700 MHz, d_6-acetone): δ (ppm) = 9.28 (s, 4H, H_3); 8.94 (d, $^3J_{HH}$ = 6.0 Hz, H_6); 8.53 (t, $^3J_{HH}$ = 7.9 Hz, H_7); 4.46 (q, $^3J_{HH}$ = 7.3 Hz, H_2); 1.36 (t, $^3J_{HH}$ = 7.9 Hz, H_1).

^{13}C-NMR (176 MHz, $CDCl_3$): δ (ppm) = 153.3 (s, C_q, 4C, C_4); 149.0 (s, C_q, 4C, C_5) 140.7 (s, 2C, C_7); 125.6 (s, 4C, C_3); 123.4 (s, 4C, C_6); 49.0 (s, 4C, C_2); 15.2 (s, 4C, C_1).

ESI-MS (pos) (m/z in MeCN) calculated for $C_{26}H_{30}FeN_{14}^{2+}$: 297.1058; found: 297.1108 $[M]^{2+}$.

Elemental analysis calculated for $C_{26}H_{30}F_{12}FeN_{14}P_2$: C = 35.31 %, H = 3.42 %, N = 22.17 %.

Found: C = 35.34 %, H = 3.74 %, N = 22.14 %.

4,4'-(pyridine-2,6-diyl)bis(1-ethyl-3-methyl-1H-1,2,3-triazol-3-ium)triflate **[H_2-tri](PF_6)$_2$**:

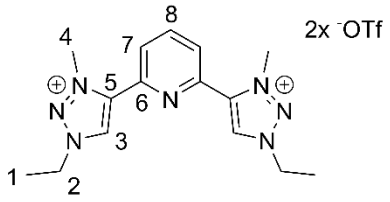

[H_2-tri](OTf)$_2$

2,6-bis(1-ethyl-1H-1,2,3-triazol-4-yl)pyridine **btp** (1 eq.) was dissolved in DCM and cooled to -80 °C. MeOTf (2.2 eq.) was added dropwise. Reaction was stirred for 16 h while slowly warming to room temperature. The arising precipitate was filtered and washed with *n*-pentane. The product was purified by crystallization (92 %).[94]

^{1}H-NMR (700 MHz, d_6-acetone): δ (ppm) = 9.52 (s, 2H, H_3); 8.42 (t, 1H, $^3J_{HH}$ = 7.9 Hz, H_8); 8.35 (d, 2H, $^3J_{HH}$ = 8.2 Hz, H_7); 4.88 (q, 4H, $^3J_{HH}$ = 7.4 Hz, H_2); 4.75 (s, 6H, H_4); 1.74 (t, 6H, $^3J_{HH}$ = 7.4 Hz, H_1).

^{13}C-NMR (176 MHz, d_6-acetone): δ (ppm) = 144.9 (s, C_q, 2C, C_6); 141.4 (s, 1C, C_8); 131.1 (s, C_q, 2C, C_5); 131.0 (s, 2C, C_3); 127.6 (s, 2C, C_7); 122.2 (quartet, 2C, $C_{triflate}$); 50.6 (s, 2C, C_2); 41.5 (s, 2C, C_4); 14.6 (s, 2C, C_1).

ESI-MS (pos) (m/z in MeCN) calculated for $C_{15}H_{21}N_7^{2+}$: 149.5924; found: 149.5960 $[M]^{2+}$.

[Fe(tri)$_2$](PF_6)$_2$:

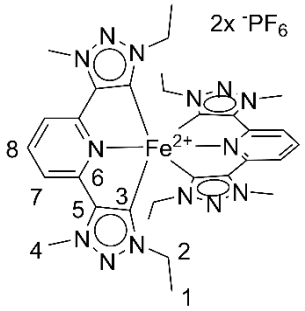

[Fe(tri)$_2$](PF_6)$_2$

4,4'-(pyridine-2,6-diyl)bis(1-ethyl-3-methyl-1H-1,2,3-triazol-3-ium)triflate **[H_2-tri]**(OTf)$_2$ (2 eq.) was suspended in THF and cooled to -80 °C. LiHMDS (6 eq.) was added dropwise. Complete deprotonation of the ligand precursor was observed after about 1 h resulting in a clear solution. $FeBr_2$ (1 eq.) was suspended in THF and added dropwise to the solution prepared before. Solution turns dark instandly and was stirred for 16 h while slowly warming to room temperature. Insoluble solid was filtered and washed with acetone, the filtrate was concentrated and dropped in a aqueous KPF_6 solution. Arising precipitate was filterd and washed with water. The crude product was dissolved in acetone and precipitated in diethylether. After filtering, the product was purified by crystallization (46 %).[94]

^{1}H-NMR (700 MHz, d_6-DMSO): δ (ppm) = 8.04 (m, 6H, H_7 & H_8); 4.52 (s, 12H, H_4); 3.15 (q, 8H, $^{3}J_{HH}$ = 7.3 Hz; H_2); 0.67 (t, 12H, $^{3}J_{HH}$ =7.3 Hz, H_1).

^{13}C-NMR (176 MHz, d_6-DMSO): δ (ppm) = 191.1 (s, C_q, 4C, C_3); 152.5 (s, 4C, C_6); 143.1 (s, 4C, C_5); 133.0 (s, 2C, C_8); 116.3 (s, 4C, C_7); 46.7 (s, 4C, C_2); 15.4 (s, 4C, C_1).

ESI-MS (pos) (m/z in MeCN) calculated for $C_{30}H_{38}FeN_{14}^{2+}$: 325.1371; found: 325.1389 $[M]^{2+}$.

Elemental analysis calculated for $C_{30}H_{38}F_{12}FeN_{14}P_2$: C = 38.31 %, H = 4.07 %, N = 20.85 %.

Found: C = 39.60 %, H = 4.70 %, N = 19.60 %.

4-(anthracenyl-9-yl)-2,6-diethynylpyridine **19-3**:

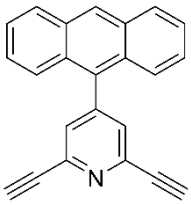

19-3

8-3 (1eq.) and (3-chlorpyridyl)-(1,3-diisopropylimidazol-2-yliden)-palladium(II)-dichlorid (PEPPSI, 0.05 eq.) were suspended in toluene/TEA (1/1 V/V) and degassed by three cycles of freeze, pump, and thaw. Trimethylsilyl acetylene (2.3 eq.) and copper(I)iodide (0.05 eq.) were added, and the suspension was stirred for 1 d at room temperature and 2 d at 90 °C. The suspension was neutralized by HCl and extracted with only DCM. The organic layers were washed with water again. The solvent was removed, and DCM was added. The suspension was filtered through a silica plug and TMS-protected product was obtained as yellow solid after removing the solvent. Deprotection was performed with K_2CO_3 (10 eq.) in MeOH/THF (1/1 V/V) at room temperature within 16 h. The solution was extracted with DCM and water. The combined organic layers were dried over Na_2SO_4 and the product obtained as white solid (70 %).

^{1}H-NMR (700 MHz, $CDCl_3$): δ (ppm) = 8.55 (s, 1H, $H_{anthracene}$); 8.06 (d, 2H, $^{3}J_{HH}$ = 8.4 Hz, $H_{anthracene}$); 7.57 (s, 2H, $H_{pyridine}$); 7.52 (d, 2H, $^{3}J_{HH}$ = 8.8 Hz, $H_{anthracene}$); 7.50-7.58 (m, 2H, $H_{anthracene}$); 7.43-7.41 (m, 2H, $H_{anthracene}$); 3.21 (s, 2H, $H_{acetylene}$).

^{13}C-NMR (176 MHz, $CDCl_3$): δ (ppm) = 148.8 (s, C_q, 1C, $C_{anthracene}$); 143.3 (s, C_q, 2C, $C_{pyridine}$); 131.7 (s, C_q, 1C, $C_{pyridine}$); 131.3 (s, C_q, 2C, $C_{anthracene}$); 130.1 (s, 2C, $C_{pyridine}$); 129.5 (s, C_q, 2C, $C_{anthracene}$); 128.9 (s, 2C, $C_{anthracene}$); 128.4 (s, 1C, $C_{anthracene}$); 126.7 (s, 2C, $C_{anthracene}$); 125.6 (s, 4C, $C_{anthracene}$) 82.3 (s, C_q, 2C, $C_{acetylene}$); 78.4 (s, 2C, $C_{acetylene}$).

ESI-MS (pos) (m/z in MeOH) calculated for $C_{23}H_{13}N+Na^{+}$: 326.0940; found: 326.0913 $[M+Na]^{+}$.

4-(anthracen-9-yl)-2,6-bis(1-ethyl-1*H*-1,2,3-triazol-4-yl)pyridine **btp-3**:

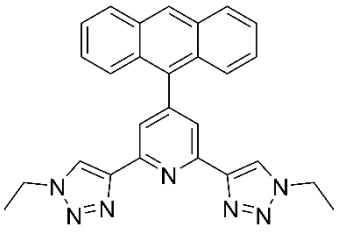

btp-3

Ethyl azide was prepared *in situ* by stirring ethyl iodide (6.6 eq.) and NaN_3 (18 eq.) for two hours in a THF/water/HO^{t}Bu (2/2/1 V/V/V) mixture. To the resulting solution **19-3** (1 eq.), Tris[(1-benzyl-1*H*-1,2,3-triazol-4-yl)methyl]amin) (0.02 eq.), copper(I) iodide (0.1 eq.) and L-ascorbic acid (1 eq.) were added and heated to 100°C for 2d. After cooling to room temperature DCM was added and it was extracted with a saturated TEA/EDTA solution. The organic layer was dried over Na_2SO_4 and the product was purified by column chromatography (stationary phase: SiO_2; mobile phase: acetone/chloroform 1/5 V/V) (67 %).[96]

^{1}H-NMR (700 MHz, $CDCl_3$): δ (ppm) = 8.52 (s, 1H, $H_{anthracene}$); 8.33 (s, 2H, $H_{triazole}$); 8.23 (s, 2H, $H_{pyridine}$); 8.03 (d, 2H, $^3J_{HH}$ = 8.5 Hz, $H_{anthracene}$); 7.72 (d, 2H, $^3J_{HH}$ = 8.9 Hz, $H_{anthracene}$); 7.46-7.44 (m, 2H, $H_{anthracene}$); 7.37-7.35 (m, 2H, $H_{anthracene}$); 4.44 (q, 4H, $^3J_{HH}$ = 7.4 Hz, H_{ethyl}); 1.57 (t, 6H, $^3J_{HH}$ = 7.4 Hz, H_{ethyl}).

^{13}C-NMR (176 MHz, $CDCl_3$): δ (ppm) = 150.5 (s, C_q, 2C, $C_{anthracene}$); 149.5 (s, C_q, 1C, $C_{pyridine}$); 148.3 (s, C_q, 2C, $C_{pyridine}$); 133.6 (s, C_q, 1C, $C_{anthracene}$); 131.3 (s, C_q, 2C, $C_{anthracene}$); 129.5 (s, C_q, 2C, $C_{anthracene}$); 128.6 (s, 2C, $C_{anthracene}$); 127.7 (s, 1C, $C_{anthracene}$); 126.1 (s, 2C, $C_{anthracene}$); 126.1 (s, 2C, $C_{anthracene}$); 125.4 (s, 2C, $C_{anthracene}$); 122.2 (s, 2C, $C_{pyridine}$); 122.0 (s, 2C, $C_{triazole}$); 45.6 (s, 2C, C_{CH2}); 15.6 (s, 2C, C_{CH3}).

ESI-MS (pos) (m/z in MeCN) calculated for $C_{27}H_{23}N_7$: 445.2015; found: 446.2110 $[M+H]^+$.

[Fe(btp-3)$_2$](PF$_6$)$_2$:

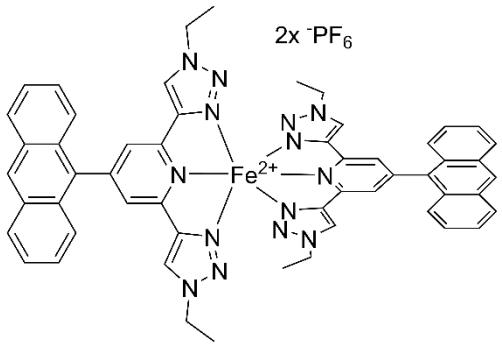

[Fe(btp-3)$_2$](PF$_6$)$_2$

4-(anthracen-9-yl)-2,6-bis(1-ethyl-1*H*-1,2,3-triazol-4-yl)pyridine **btp-3** (2 eq.) and $FeBr_2$ (1 eq.) were stirred in MeOH for 16 h. Insolouble solid was filterd, the filtrate was concentrated and dropped in an aqueous KPF_6 solution. Arising precipitate was filterd and washed with water. The crude product was dissolved in acetone and pricipitated in diethylether. After filtering, the product was purified by crystallization using diffusion techniques (solvent: acetone; anitsolvent: diethyl ether; 94 %).[94]

^{1}H-NMR (700 MHz, d_6-acetone): δ (ppm) = 9.58 (two overlapping singlets, evidenced by temperature variation NMR, 8H, $H_{triazole}$ + $H_{pyridine}$); 8.93 (s, 2H, $H_{anthracene}$); 8.34 (d, 4H, $^3J_{HH}$ = 8.4 Hz, $H_{anthracene}$); 7.94 (d, 4H, $^3J_{HH}$ = 8.6 Hz, $H_{anthracene}$); 7.70-7.65 (m, 8H, $H_{anthracene}$); 4.72 (q, 8H, $^3J_{HH}$ = 6.8 Hz, H_{ethyl}); 1.53 (t, 12H, $^3J_{HH}$ = 7.2 Hz, H_{ethyl}).

^{13}C-NMR (176 MHz, d_6-acetone): δ (ppm) = 152.5; 149.9; 147.9; 145.5; 132.6; 132.4; 130.6; 130.1; 129.9; 128.1; 126.8; 126.3; 126.1; 50.2; 15.3.

Due to short relaxation times of the carbon atom spins, the exact assignment of the ^{13}C-NMR is not possible.

ESI-MS (pos) (m/z in MeCN) calculated for $C_{54}H_{46}FeN_{14}^{2+}$: 473.1684; found: 473.1703 $[M]^{2+}$.

[H_2-tri-3](PF_6)$_2$:

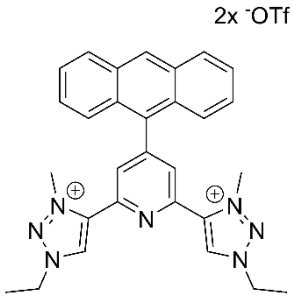

[H_2-tri-3](OTf)$_2$

Btp-3 (1 eq.) was suspended in DCM under inert conditions and cooled down to -78°C. MeOTf (2.05 eq.) was added dropwise. The suspension was stirred for 16 h while slowly getting up to room temperature. It was cooled in an ice bath again and *n*-pentane was added. The product was obtained as unsolved particles, filtered and if necessary, washed again by cold *n*-pentane (90 %).[94]

^{1}H-NMR (700 MHz, DMSO-d_6): δ (ppm) = 9.60 (s, 2H, $H_{triazolylidene}$); 8.90 (s, 1H, $H_{anthracene}$); 8.47 (s, 2H, $H_{pyridine}$); 8.28 (d, 2H, $^3J_{HH}$ = 8.3 Hz, $H_{anthracene}$); 7.46-7.62 (m, 4H, $H_{anthracene}$); 7.55-7.54 (m, 2H, $H_{anthracene}$); 4.72 (q, 4H, $^3J_{HH}$ = 7.3 Hz, H_{ethyl}); 4.71 (s, 6H, H_{methyl}); 1.58 (t, 6H, $^3J_{HH}$ = H_{ethyl}).

^{13}C-NMR (176 MHz, DMSO-d_6): δ (ppm) = 150.4 (s, C_q, 1C, $C_{pyridine}$); 144.2 (s, C_q, 2C, $C_{pyridine}$); 139.5 (s, C_q, 2C, $C_{triazolylidene}$); 130.8 (s, C_q, 1C, $C_{anthracene}$); 130.7 (s, C_q, 2C, $C_{anthracene}$); 130.3 (s, 2C, $C_{triazolylidine}$); 128.8 (s, C_q, 2C, $C_{anthracene}$); 128.7 (s, 2C, $C_{anthracene}$); 128.6 (s, 1C, $C_{anthracene}$); 128.4 (s, 2C, $C_{pyridine}$); 127.0 (s, 2C, $C_{anthracene}$); 125.8 (s, 2C, $C_{anthracene}$); 125.2 (s, 2C, $C_{anthracene}$); 49.1 (s, 2C, $C_{CH2,ethyl}$); 40.9 (s, 2C, C_{methyl}); 13.8 (s, 2C, $C_{CH3,ethyl}$).

ESI-MS (pos) (m/z in MeCN) calculated for $C_{29}H_{29}N_7^{2+}$: 273.6237; found: 273.6249 $[M]^{2+}$.

[Fe(tri-3)$_2$](PF_6)$_2$:

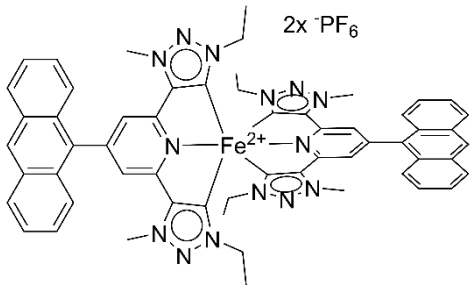

[Fe(tri-3)$_2$](PF_6)$_2$

[H_2-tri-3]($OTf)_2$ (2 eq.) was suspended in THF under inert conditions and cooled down to -78°C. LiHMDS (6 eq., 1M in THF) was added dropwise. Successful deprotonation can be seen by getting from a suspension of the triazolium salt to a clear solution of the free carbene. After complete deprotonation $FeBr_2$ (1 eq.) is dissolved in THF under inert conditions and added dropwise to the carbene solution. The mixture instantly turned into a dark suspension, which was stirred for 16 h while slowly getting to room temperature. The solvent was removed, and the residue was solved in acetone. Not soluble residue was filtered off.[94] Acetone was removed to a minimum amount and added dropwise to an aqueous solution of KPF_6 (10 eq.) in water cooled by an ice bath and stirred for 15 min. Precipitate was filtered off and rinsed with cold water. The crude complex was purified by column chromatography (stationary phase: SiO_2/ mobile phase: acetone/H_2O/$KNO_{3(aq.,sat.)}$ 10/3/1 V/V/V).[46] The eluent added dropwise to a solution of KPF_6 (10 eq.) in water cooled by an ice bath and stirred for 15 min. Precipitate was filtered off and rinsed with cold water and finally purified by crystallization (solvent: acetone/ antisolvent: diethyl ether). The complex was obtained as blue crystals (37 %).

^{1}H-NMR (700 MHz, d_6-acetone): δ (ppm) = 8.87 (s, 2H, $H_{anthracene}$); 8.31-8.29 (m, 4H, $H_{anthracene}$); 8.30 (s, 4H, $H_{pyridine}$); 7.83 (d, 4H, $^3J_{HH}$ = 8.8 Hz, $H_{anthracene}$); 7.67-7.64 (m, 4H, $H_{anthracene}$); 7.61-7.57 (m, 4H, $H_{anthracene}$); 4.62 (s, 12H, H_{methyl}); 3.73 (q, 8H, $^3J_{HH}$ = 7.3 Hz, H_{ethyl}); 1.12 (t, 12H, $^3J_{HH}$ = 7.3 Hz, H_{ethyl}).

^{13}C-NMR (176 MHz, d_6-acetone): δ (ppm) = 193.4 (s, 4C, C_q, $C_{carbene}$); 154.7 (s, 4C, C_q, $C_{pyridine}$); 145.5 (s, 2C, C_q, $C_{pyridine}$); 144.6 (s, 4C, C_q, $C_{triazolylidene}$); 133.9 (s, 2C, C_q, $C_{anthracene}$); 132.5 (s, 4C, C_q, $C_{anthracene}$); 130.7 (s, 4C, C_q, $C_{anthracene}$); 129.9 (s, 4C, $C_{pyridine}$); 129.2 (s, 2C, $C_{anthracene}$); 127.7 (s, 4C, $C_{anthracene}$); 126.6 (s, 4C, $C_{anthracene}$); 126.6 (s, 4C, $C_{anthracene}$); 119.7 (s, 4C, $C_{anthracene}$); 48.5 (s, 4C, $C_{CH2,ethyl}$); 39.1 (s, 4C, C_{methyl}); 16.3 (s, 4C, $C_{CH3,ethyl}$).

ESI-MS (pos) (m/z in MeCN) calculated for $C_{58}H_{54}FeN_{14}^{2+}$: 501.1997; found: 501.2018 $[M]^{2+}$.

General procedure for the synthesis of the ruthenium complexes:

Corresponding pro-ligands (2 eq.) and $RuCl_3x6{\cdot}H_2O$ (1 eq.) were suspended in a small amount of ethylene glycol and heated to 185 °C for 4 h. The resulting brown solution was slowly cooled to room temperature and the crude product precipitated by adding an aqueous solution of KPF_6. The resulting precipitate was filtered off and rinsed with cold water. The crude complex was first purified by column chromatography (stationary phase: basic aluminum oxide/ mobile phase: acetonitrile) and finally purified by crystallization via solvent diffusion (acetone/diethyl ether).[100,101]

[Ru(bbp)$_2$]$(PF_6)_2$:

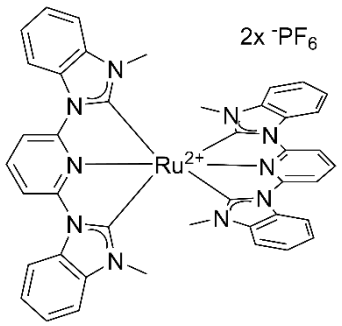

[Ru(bbp)$_2$]$(PF_6)_2$

The product was obtained as yellow crystals (64 %).

^{1}H-NMR (700 MHz, d_6-acetone): δ (ppm) = 8.82 (d, 4H, $^3J_{HH}$ = 8.3 Hz, $H_{pyridine}$); 8.74 (dd, 4H, $^3J_{HH}$ = 8.9 Hz, $^3J_{HH}$ = 7.8 Hz, $H_{pyridine}$); 8.56 (d, 4H, $^3J_{HH}$ = 8.4 Hz, $H_{benzimidazole}$);7.85-7.55 (m, 4H, $H_{benzimidazole}$); 7.48-7.45 (m, 8H, $H_{benzimidazole}$); 3.04 (s, 12H, H_{methyl}).

^{13}C-NMR (176 MHz, d_6-acetone): δ (ppm) = 201.1 (s, C_q, 4C, $C_{carbene}$); 153.3 (s, C_q, 4C, $C_{pyridine}$); 140.5 (s, 2C, $C_{pyridine}$); 137.4 (s, C_q, 4C, $C_{benzimidazole}$); 132.4 (s, C_q, 4C, $C_{benzimidazole}$); 125.9 (s, 4C, $C_{benzimidazole}$);125.2 (s, 4C, $C_{benzimidazole}$); 113.2 (s, 4C, $C_{benzimidazole}$); 111.9 (s, 4C, $C_{benzimidazole}$); 108.7 (s, 4C, $C_{pyridine}$); 33.2 (s, 4C, C_{methyl}).

ESI-MS (pos) (m/z in MeCN) calculated for $[C_{42}H_{34}N_{10}Ru]^{2+}$: 390.1000; found: 390.0984 $[M]^{2+}$.

Elemental analysis calculated for $C_{42}H_{34}F_{12}N_{10}P_2Ru$: C = 47.15 %, H = 3.20 %, N = 13.09 %.

Found: C = 46.86 %, H = 3.40 %, N = 12.79 %.

[Ru(bbp-1)$_2$](PF_6)$_2$:

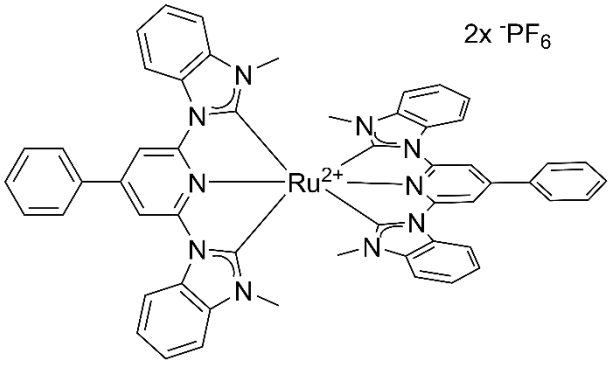

[Ru(bbp-1)$_2$](PF_6)$_2$

The product was obtained as yellow crystals (52 %).

^{1}H-NMR (700 MHz, d_6-acetone): δ (ppm) = 8.91 (s, 4H, $H_{pyridine}$); 8.77 (d, 4H, $^3J_{HH}$ = 8.5 Hz, $H_{benzimidazole}$); 8.39-8.38 (m, 4H, H_{phenyl}); 7.79-7.77 (m, 4H, H_{phenyl}); 7.74-7.73 (m, 2H, H_{phenyl}); 7.59-7.57 (m, 4H, $H_{benzimidazole}$); 7.50-7.47 (m, 8H, $H_{benzimidazole}$); 3.14 (s, 12H, H_{methyl}).

^{13}C-NMR (176 MHz, d_6-acetone): δ (ppm) = 201.4 (s, 4C, C_q, $C_{carbene}$); 153.6 (s, 4C, C_q, $C_{pyridine}$); 153.1 (s, 2C, C_q, C_{phenyl}); 138.1 (s, 2C, C_q, $C_{pyridine}$); 137.4 (s, 4C, C_q, $C_{benzimidazole}$); 132.4 (s, 4C, C_q, $C_{benzimidazole}$); 131.6 (s, 2C, C_{phenyl}); 130.5 (s, 4C, C_{phenyl}); 129.4 (s, 4C, C_{phenyl}); 126.0 (s, 4C, $C_{benzimidazole}$); 125.3 (s, 4C, $C_{benzimidazole}$); 113.8 (s, 4C, $C_{benzimidazole}$); 111.9 (s, 4C, $C_{benzimidazole}$); 106.5 (s, 4C, $C_{pyridine}$); 33.4 (s, 4C, C_{methyl}).

ESI-MS (pos) (m/z in MeCN) calculated for $[C_{54}H_{42}RuN_{14}]^{2+}$: 466.1313; found: 466.1359 $[M]^{2+}$.

Elemental analysis calculated for $C_{54}H_{42}F_{12}N_{10}P_2Ru$: C = 53.08 %, H = 3.46 %, N = 11.46 %.

Found: C = 52.79 %, H = 3.94 %, N = 11.21 %.

[Ru(bbp-3)$_2$](PF_6)$_2$:

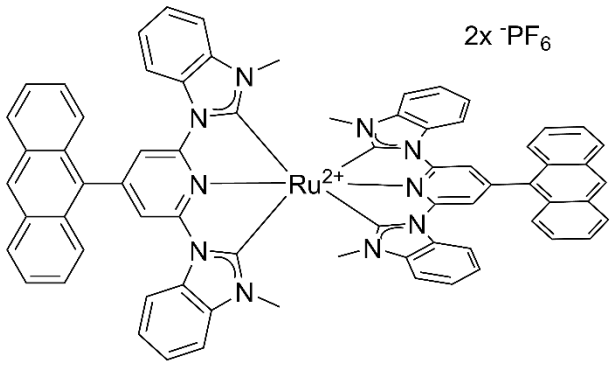

[Ru(bbp-3)$_2$](PF_6)$_2$

The product was obtained as yellow crystals (85 %).

^{1}H-NMR (700 MHz, d_6-acetone): δ (ppm) = 8.97 (s, 4H, $H_{pyridine}$); 8.97 (s, 2H, $H_{anthracene}$); 8.60 (d, 4H, $^3J_{HH}$ = 8.5 Hz, $H_{benzimidazole}$); 8.37 (d, 4H, $^3J_{HH}$ = 8.6 Hz, $H_{anthracene}$); 8.03 (d, 4H, $^3J_{HH}$ = 8.9 Hz, $H_{anthracene}$); 7.71-7.68 (m, 4H, $H_{anthracene}$); 7.62-7.60 (m, 4H, $H_{anthracene}$); 7.57 (d, 4H, $^3J_{HH}$ = 7.9 Hz, $H_{benzimidazole}$); 7.46 (t, 4H, $^3J_{HH}$ = 7.5 Hz, $H_{benzimidazole}$); 7.39 (t, 4H, $^3J_{HH}$ = 7.5 Hz, $H_{benzimidazole}$); 3.48 (s, 12H, H_{methyl}).

^{13}C-NMR (176 MHz, d_6-acetone): δ (ppm) = 201.4 (s, C_q, 4C, $C_{carbene}$); 135.7 (s, C_q, 4C, $C_{pyridine}$); 152.2 (s, C_q, 2C, $C_{anthracene}$); 137.4 (s, C_q, 4C, $C_{benzimidazole}$); 133.5 (s, C_q, 2C, $C_{pyridine}$); 132.6 (s, C_q, 4C, $C_{benzimidazole}$); 132.5 (s, C_q, 4C, $C_{benzimidazole}$); 130.8 (s, C_q, 4C, $C_{anthracene}$); 129.9 (s, 4C, $C_{anthracene}$); 129.7 (s, 2C, $C_{anthracene}$); 127.9 (s, 4C, $C_{anthracene}$); 126.8 (s, 4C, $C_{anthracene}$); 126.7 (s, 4C, $C_{anthracene}$); 126.0 (s, 4C, $C_{benzimidazole}$); 125.2 (s, 4C, $C_{benzimidazole}$); 113.9 (s, 4C, $C_{benzimidazole}$); 111.9 (s, 4C, $C_{benzimidazole}$); 111.4 (s, 4C, $C_{pyridine}$); 33.7 (s, 4C, C_{methyl}).

ESI-MS (pos) (m/z in MeCN) calculated for $[C_{70}H_{50}RuN_{10}]^{2+}$: 566.1626; found: 566.1641 $[M]^{2+}$.

Elemental analysis calculated for ($C_{54}H_{42}F_{12}N_{10}P_2Ru)_2(H_2O)$: C = 58.74 %, H = 3.59 %, N = 9.78 %.

Found: C = 58.53 %, H = 3.89 %, N = 9.43 %.

References

[1] Deutscher Wetterdienst (DWD), "Temperature Anomaly Germany Year", zu finden unter https://www.dwd.de/EN/ourservices/zeitreihen/zeitreihen.html.

[2] Scripps Institute for Oceanography, "Monthly Average Carbon Dioxide Concentration", zu finden unter https://scrippsco2.ucsd.edu/graphics_gallery/mauna_loa_record/mauna_loa_record.html .

[3] Umweltbundesamt, "Erneuerbare Energien in Zahlen", zu finden unter https://www.umweltbundesamt.de/themen/klima-energie/erneuerbare-energien/erneuerbare-energien-in-zahlen#strom.

[4] K. Fath, *Technical and economic potential for photovoltaic systems on buildings*, KIT Scientific Publishing.

[5] I. e. A. IEA, *Key World Energy Statistics 2021*.

[6] V. Quaschning, *Systemtechnik einer klimaverträglichen Elektrizitätsversorgung in Deutschland für das 21. Jahrhundert*. Zugl.: Berlin, Techn. Univ., Habil.-Schr., 2000, VDI-Verl., Düsseldorf, **2000**.

[7] P. Dierks, Y. Vukadinovic, M. Bauer, *Inorg. Chem. Front.* **2022**, *9*, 206.

[8] F. K. Crundwell, *Extractive metallurgy of nickel, cobalt and platinum-group materials*, Elsevier, Amsterdam, **2011**.

[9] A. Lutz and D. Heubach, C. L.-K., *Umweltwirkungen der Fabstoffsolarzelle - Analyse des Ruthenium-Vorkommens und Bewertung des Ruthenium-Farbstoffs*. *Bericht des BMBF-Forschungsprojekt ColorSol*, **2007**.

[10] T. E. Graedel, E. M. Harper, N. T. Nassar, P. Nuss, B. K. Reck, *Proceedings of the National Academy of Sciences of the United States of America* **2015**, *112*, 4257.

[11] A. Cowley, *Johnson Matthey - PGM market report May 2021*, **2021**.

[12] The World Bank, "World Bank Commodities Price Data", **2021**.

[13] E. Riedel, *Anorganische Chemie,* 9. Aufl., De Gruyter, Berlin, Bosten, **2015**.

[14] Bundesministerium für Bildung und Forschung, "Eine kleine Wasserstoff Farbenlehre", zu finden unter https://www.bmbf.de/bmbf/shareddocs/kurzmeldungen/de/eine-kleine-wasserstoff-farbenlehre.html, **2020**.

[15] J. Töpler, J. Lehmann (Hrsg.) *Wasserstoff und Brennstoffzelle*. *Technologien und Marktperspektiven*, Springer Berlin Heidelberg, Berlin, Heidelberg, **2017**.

[16] N. Sánchez-Bastardo, R. Schlögl, H. Ruland, *Chemie Ingenieur Technik* **2020**, *92*, 1596.

[17] S. J. Paddison (Hrsg.) *Topics in applied physics*, *v. 113*, Springer, New York, **2009**.

[18] E. Amouyal, *Solar Energy Materials and Solar Cells* **1995**, *38*, 249.

[19] M. Graetzel, *Acc. Chem. Res.* **1981**, *14*, 376.

[20] K. Kalyanasundaram, J. Kiwi, M. Grätzel, *HCA* **1978**, *61*, 2720.

[21] G. M. Brown, B. S. Brunschwig, C. Creutz, J. F. Endicott, N. Sutin, *J. Am. Chem. Soc.* **1979**, *101*, 1298.

[22] F. H. Burstall, *J. Chem. Soc.* **1936**, 173.

[23] C. Elschenbroich, *Organometallchemie,* 6. Aufl., Vieweg+Teubner Verlag / GWV Fachverlage GmbH Wiesbaden, Wiesbaden, **2008**.

[24] S.-P. Luo, E. Mejía, A. Friedrich, A. Pazidis, H. Junge, A.-E. Surkus, R. Jackstell, S. Denurra, S. Gladiali, S. Lochbrunner et al., *Angewandte Chemie (International ed. in English)* **2013**, *52*, 419.

[25] M. Kirch, J.-M. Lehn, J.-P. Sauvage, *Helv. Chim. Acta* **1979**, *62*, 1345.

[26] H. Ozawa, K. Sakai, *Chemical communications (Cambridge, England)* **2011**, *47*, 2227.

[27] F. Gärtner, B. Sundararaju, A.-E. Surkus, A. Boddien, B. Loges, H. Junge, P. H. Dixneuf, M. Beller, *Angewandte Chemie (International ed. in English)* **2009**, *48*, 9962.

[28] M. Wang, Y. Na, M. Gorlov, L. Sun, *Dalton transactions (Cambridge, England : 2003)* **2009**, 6458.

[29] O. S. Wenger, *Journal of the American Chemical Society* **2018**, *140*, 13522.

[30] C. Förster, K. Heinze, *Chemical Society reviews* **2020**, *49*, 1057.

[31] V. Balzani, S. Campagna (Hrsg.) *Topics in Current Chemistry*, Springer Berlin Heidelberg, Berlin, Heidelberg, **2007**.

[32] J. K. McCusker, *Science (New York, N.Y.)* **2019**, *363*, 484.

[33] N. H. Damrauer, G. Cerullo, A. Yeh, T. R. Boussie, C. V. Shank, J. K. McCusker, *Science (New York, N.Y.)* **1997**, *275*, 54.

[34] C. K. Prier, D. A. Rankic, D. W. C. MacMillan, *Chemical reviews* **2013**, *113*, 5322.

[35] Y. Liu, P. Persson, V. Sundström, K. Wärnmark, *Accounts of chemical research* **2016**, *49*, 1477.

[36] P. Dierks, A. Päpcke, O. S. Bokareva, B. Altenburger, T. Reuter, K. Heinze, O. Kühn, S. Lochbrunner, M. Bauer, *Inorganic chemistry* **2020**, *59*, 14746.

[37] T. J. Penfold, E. Gindensperger, C. Daniel, C. M. Marian, *Chemical reviews* **2018**, *118*, 6975.

[38] L. L. Jamula, A. M. Brown, D. Guo, J. K. McCusker, *Inorganic chemistry* **2014**, *53*, 15.

[39] Y. Liu, T. Harlang, S. E. Canton, P. Chábera, K. Suárez-Alcántara, A. Fleckhaus, D. A. Vithanage, E. Göransson, A. Corani, R. Lomoth et al., *Chemical communications (Cambridge, England)* **2013**, *49*, 6412.

[40] a) L. Lindh, P. Chábera, N. W. Rosemann, J. Uhlig, K. Wärnmark, A. Yartsev, V. Sundström, P. Persson, *Catalysts* **2020**, *10*, 315; b) O. S. Wenger, *Nature chemistry* **2020**, *12*, 323; c) O. S. Wenger, *Chemistry (Weinheim an der Bergstrasse, Germany)* **2019**, *25*, 6043; d) S. Kaufhold, K. Wärnmark, *Catalysts* **2020**, *10*, 132.

[41] A. Britz, W. Gawelda, T. A. Assefa, L. L. Jamula, J. T. Yarranton, A. Galler, D. Khakhulin, M. Diez, M. Harder, G. Doumy et al., *Inorganic chemistry* **2019**, *58*, 9341.

[42] A. K. C. Mengel, C. Förster, A. Breivogel, K. Mack, J. R. Ochsmann, F. Laquai, V. Ksenofontov, K. Heinze, *Chemistry (Weinheim an der Bergstrasse, Germany)* **2015**, *21*, 704.

[43] C. Förster, M. Dorn, T. Reuter, S. Otto, G. Davarci, T. Reich, L. Carrella, E. Rentschler, K. Heinze, *Inorganics* **2018**, *6*, 86.

[44] M. Darari, A. Francés-Monerris, B. Marekha, A. Doudouh, E. Wenger, A. Monari, S. Haacke, P. C. Gros, *Molecules (Basel, Switzerland)* **2020**, *25*.

[45] L. A. Fredin, M. Pápai, E. Rozsályi, G. Vankó, K. Wärnmark, V. Sundström, P. Persson, *The journal of physical chemistry letters* **2014**, *5*, 2066.

[46] L. Liu, T. Duchanois, T. Etienne, A. Monari, M. Beley, X. Assfeld, S. Haacke, P. C. Gros, *Physical chemistry chemical physics : PCCP* **2016**, *18*, 12550.

[47] a) G. Guisado-Barrios, M. Soleilhavoup, G. Bertrand, *Accounts of chemical research* **2018**; b) K. F. Donnelly, A. Petronilho, M. Albrecht, *Chemical communications (Cambridge, England)* **2013**, *49*, 1145; c) R. Maity, B. Sarkar, *JACS Au* **2021**, *280*, 1.

[48] Y. Liu, K. S. Kjaer, L. A. Fredin, P. Chábera, T. Harlang, S. E. Canton, S. Lidin, J. Zhang, R. Lomoth, K.-E. Bergquist et al., *Chemistry (Weinheim an der Bergstrasse, Germany)* **2015**, *21*, 3628.

[49] H. Tatsuno, K. S. Kjaer, K. Kunnus, T. C. B. Harlang, C. Timm, M. Guo, P. Chàbera, L. A. Fredin, R. W. Hartsock, M. E. Reinhard et al., *Angewandte Chemie (International ed. in English)* **2020**, *59*, 364.

[50] P. Chábera, L. Lindh, N. W. Rosemann, O. Prakash, J. Uhlig, A. Yartsev, K. Wärnmark, V. Sundström, P. Persson, *Coordination Chemistry Reviews* **2021**, *426*, 213517.

[51] P. Chábera, Y. Liu, O. Prakash, E. Thyrhaug, A. E. Nahhas, A. Honarfar, S. Essén, L. A. Fredin, T. C. B. Harlang, K. S. Kjær et al., *Nature* **2017**, *543*, 695.

[52] K. S. Kjær, N. Kaul, O. Prakash, P. Chábera, N. W. Rosemann, A. Honarfar, O. Gordivska, L. A. Fredin, K.-E. Bergquist, L. Häggström et al., *Science (New York, N.Y.)* **2019**, *363*, 249.

[53] M. Bauer, J. Steube, A. Päpcke, O. Bokareva, T. Reuter, S. Demeshko, R. Schoch, S. Hohloch, F. Meyer, K. Heinze et al., *Janus-type dual emission of a Cyclometalated Iron(III) complex*, **2020**.

[54] E. A. Medlycott, G. S. Hanan, *Chemical Society reviews* **2005**, *34*, 133.

[55] a) C. Berg-Brennan, P. Subramanian, M. Absi, C. Stern, J. T. Hupp, *Inorg. Chem.* **1996**, *35*, 3719; b) D. S. Tyson, C. R. Luman, X. Zhou, F. N. Castellano, *Inorganic chemistry* **2001**, *40*, 4063.

[56] D. S. Tyson, J. Bialecki, F. N. Castellano, *Chem. Commun.* **2000**, 2355.

[57] D. S. Tyson, F. N. Castellano, *J. Phys. Chem. A* **1999**, *103*, 10955.

[58] W. E. Ford, M. A. J. Rodgers, *J. Phys. Chem.* **1992**, *96*, 2917.

[59] N. D. McClenaghan, F. Barigelletti, B. Maubert, S. Campagna, *Chem. Commun.* **2002**, 602.

[60] A. F. Morales, G. Accorsi, N. Armaroli, F. Barigelletti, S. J. A. Pope, M. D. Ward, *Inorg. Chem.* **2002**, *41*, 6711.

[61] G. J. Wilson, A. Launikonis, W. H. F. Sasse, A. W.-H. Mau, *J. Phys. Chem. A* **1997**, *101*, 4860.

[62] R. Passalacqua, F. Loiseau, S. Campagna, Y.-Q. Fang, G. S. Hanan, *Angewandte Chemie (International ed. in English)* **2003**, *42*, 1608.

[63] J. E. Yarnell, J. C. Deaton, C. E. McCusker, F. N. Castellano, *Inorganic chemistry* **2011**, *50*, 7820.

[64] J. E. Yarnell, K. A. Wells, J. R. Palmer, J. M. Breaux, F. N. Castellano, *The journal of physical chemistry. B* **2019**, *123*, 7611.

[65] K. A. Wells, J. E. Yarnell, J. R. Palmer, T. S. Lee, C. M. Papa, F. N. Castellano, *Inorganic chemistry* **2020**, *59*, 8259.

[66] a) S. Chakraborty, T. J. Wadas, H. Hester, C. Flaschenreim, R. Schmehl, R. Eisenberg, *Inorganic chemistry* **2005**, *44*, 6284; b) E. O. Danilov, I. E. Pomestchenko, S. Kinayyigit, P. L. Gentili, M. Hissler, R. Ziessel, F. N. Castellano, *J. Phys. Chem. A* **2005**, *109*, 2465; c) E. O. Danilov, A. A. Rachford, S. Goeb, F. N. Castellano, *The journal of physical chemistry. A* **2009**, *113*, 5763; d) C. E. McCusker, A. Chakraborty, F. N. Castellano, *The journal of physical chemistry. A* **2014**, *118*, 10391; e) R. Narayana-Prabhu, R. H. Schmehl, *Inorganic chemistry* **2006**, *45*, 4319; f) V. Prusakova, C. E. McCusker, F. N. Castellano, *Inorganic chemistry* **2012**, *51*, 8589; g) A. A. Rachford, S. Goeb, F. N. Castellano, *Journal of the American Chemical Society* **2008**, *130*, 2766; h) A. A. Rachford, S. Goeb, R. Ziessel, F. N. Castellano, *Inorganic chemistry* **2008**, *47*, 4348; i) A. Y.-Y. Tam, K. M.-C. Wong, G. Wang, V. W.-W. Yam, *Chemical communications (Cambridge, England)* **2007**, 2028; j) E. Shikhova, E. O. Danilov, S. Kinayyigit, I. E. Pomestchenko, A. D. Tregubov, F. Camerel, P. Retailleau, R. Ziessel, F. N. Castellano, *Inorganic chemistry* **2007**, *46*, 3038; k) X. Wang, S. Goeb, Z. Ji, F. N. Castellano, *The journal of physical chemistry. B* **2010**, *114*, 14440; l) V. W.-W. Yam, R. P.-L. Tang, K. M.-C. Wong, K.-K. Cheung, *Organometallics* **2001**, *20*, 4476; m) Q.-Z. Yang, L.-Z. Wu, Z.-X. Wu, L.-P. Zhang, C.-H. Tung, *Inorganic chemistry* **2002**, *41*, 5653; n) C. Yu, K. M.-C. Wong, K. H.-Y. Chan, V. W.-W. Yam, *Angew. Chem.* **2005**, *117*, 801; o) D. Zhang, L.-Z. Wu, Q.-Z. Yang, X.-H. Li, L.-P. Zhang, C.-H. Tung, *Organic letters* **2003**, *5*, 3221.

[67] I. E. Pomestchenko, C. R. Luman, M. Hissler, R. Ziessel, F. N. Castellano, *Inorganic chemistry* **2003**, *42*, 1394.

[68] C. Wegeberg, D. Häussinger, O. S. Wenger, *Journal of the American Chemical Society* **2021**, *143*, 15800.

[69] A. Francés-Monerris, P. C. Gros, M. Pastore, X. Assfeld, A. Monari, *Theor Chem Acc* **2019**, *138*, 13522.

[70] A. M.W. Cargill Thompson, *Coordination Chemistry Reviews* **1997**, *160*, 1.

[71] E. C. Constable, D. R. Smith, *Supramolecular Chemistry* **1994**, *4*, 5.

[72] W. Leslie, R. A. Poole, P. R. Murray, L. J. Yellowlees, A. Beeby, J. G. Williams, *Polyhedron* **2004**, *23*, 2769.

[73] A. Maroń, A. Szlapa, T. Klemens, S. Kula, B. Machura, S. Krompiec, J. G. Małecki, A. Switlicka-Olszewska, K. Erfurt, A. Chrobok, *Organic & biomolecular chemistry* **2016**, *14*, 3793.

[74] M. Nettekoven, C. Jenny, *Org. Process Res. Dev.* **2003**, *7*, 38.

[75] A. Breivogel, M. Meister, C. Förster, F. Laquai, K. Heinze, *Chemistry (Weinheim an der Bergstrasse, Germany)* **2013**, *19*, 13745.

[76] J. V. Mello, N. S. Finney, *Org. Lett.* **2001**, *3*, 4263.

[77] J. Hübscher, W. Seichter, T. Gruber, J. Kortus, E. Weber, *J. Heterocyclic Chem.* **2015**, *52*, 1062.

[78] A. Krasovskiy, V. Krasovskaya, P. Knochel, *Angewandte Chemie (International ed. in English)* **2006**, *45*, 2958.

[79] C. Amatore, A. Jutand, *Acc. Chem. Res.* **2000**, *33*, 314.

[80] S. Lou, G. C. Fu, *Advanced synthesis & catalysis* **2010**, *352*, 2081.

[81] G. Jander, K. F. Jahr, G. Schulze, J. Simon, R. Martens-Menzel, *Maßanalyse*. *Theorie und Praxis der Titrationen mit chemischen und physikalischen Indikationen,* 18. Aufl., De Gruyter, Berlin, **2012**.

[82] P. A. Cox, M. Reid, A. G. Leach, A. D. Campbell, E. J. King, G. C. Lloyd-Jones, *Journal of the American Chemical Society* **2017**, *139*, 13156.

[83] a) A. Cravcenco, M. Hertzog, C. Ye, M. N. Iqbal, U. Mueller, L. Eriksson, K. Börjesson, *Science advances* **2019**, *5*, eaaw5978; b) A. Cravcenco, C. Ye, J. Gräfenstein, K. Börjesson, *The journal of physical chemistry. A* **2020**, *124*, 7219.

[84] H.-J. Park, Y. K. Chung, *Dalton transactions (Cambridge, England : 2003)* **2012**, *41*, 5678.

[85] D. H. Brown, G. L. Nealon, P. V. Simpson, B. W. Skelton, Z. Wang, *Organometallics* **2009**, *28*, 1965.

[86] F. Monnier, M. Taillefer, *Angewandte Chemie (International ed. in English)* **2009**, *48*, 6954.

[87] H.-M. Kim, D. Jeong, H. C. Noh, Y. K. Kang, Y. K. Chung, *Bulletin of the Korean Chemical Society* **2014**, *35*, 448.

[88] P. Zimmer, L. Burkhardt, A. Friedrich, J. Steube, A. Neuba, R. Schepper, P. Müller, U. Flörke, M. Huber, S. Lochbrunner et al., *Inorganic chemistry* **2018**, *57*, 360.

[89] C. Rajadurai, F. Schramm, S. Brink, O. Fuhr, M. Ghafari, R. Kruk, M. Ruben, *Inorganic chemistry* **2006**, *45*, 10019.

[90] T. K. Claus, S. Telitel, A. Welle, M. Bastmeyer, A. P. Vogt, G. Delaittre, C. Barner-Kowollik, *Chemical communications (Cambridge, England)* **2017**, *53*, 1599.

[91] F. Ungeheuer, A. Fürstner, *Chemistry (Weinheim an der Bergstrasse, Germany)*, *21*, 11387.

[92] S. D. Walker, T. E. Barder, J. R. Martinelli, S. L. Buchwald, *Angewandte Chemie (International ed. in English)* **2004**, *43*, 1871.

[93] a) J. Sugiyama, I. Tomita, *Eur. J. Org. Chem.*, *2007*, 4651; b) J.-C. Deng, C.-W. Kuo, S.-C. Chuang, *Chemical communications (Cambridge, England)* **2014**, *50*, 10580.

[94] P. Dierks, A. Kruse, O. S. Bokareva, M. J. Al-Marri, J. Kalmbach, M. Baltrun, A. Neuba, R. Schoch, S. Hohloch, K. Heinze et al., *Chemical communications (Cambridge, England)* **2021**, *49*, 1057.

[95] A. Orita, T. Nakano, D. L. An, K. Tanikawa, K. Wakamatsu, J. Otera, *Journal of the American Chemical Society* **2004**, *126*, 10389.

[96] S. Hohloch, S. Kaiser, F. L. Duecker, A. Bolje, R. Maity, J. Košmrlj, B. Sarkar, *Dalton transactions (Cambridge, England : 2003)* **2015**, *44*, 686.

[97] H. Oshio, H. Spiering, V. Ksenofontov, F. Renz, P. Gütlich, *Inorganic chemistry* **2001**, *40*, 1143.

[98] H. Iwasaki, Y. Koga, *Organic Chem Curr Res* **2016**, *5*.

[99] T. R. Chan, R. Hilgraf, K. B. Sharpless, V. V. Fokin, *Organic letters* **2004**, *6*, 2853.

[100] H.-J. Park, S. Yoo, I.-S. Shin, Y. K. Chung, J. Kim, *Electroanalysis* **2013**, *25*, 1111.

[101] S. U. Son, K. H. Park, Y.-S. Lee, B. Y. Kim, C. H. Choi, M. S. Lah, Y. H. Jang, D.-J. Jang, Y. K. Chung, *Inorganic chemistry* **2004**, *43*, 6896.

[102] T. Duchanois, T. Etienne, M. Beley, X. Assfeld, E. A. Perpète, A. Monari, P. C. Gros, *Eur. J. Inorg. Chem.* **2014**, *2014*, 3747.

[103] P. Zimmer, P. Müller, L. Burkhardt, R. Schepper, A. Neuba, J. Steube, F. Dietrich, U. Flörke, S. Mangold, M. Gerhards et al., *Eur. J. Inorg. Chem.* **2017**, *2017*, 1504.

[104] M. U. Kumke, H. G. Löhmannsröben, T. Roch, *Journal of fluorescence* **1995**, *5*, 139.

[105] J. R. Lakowicz, *Principles of fluorescence spectroscopy,* 3. Aufl., Springer, New York, **2006**.

[106] T. Duchanois, T. Etienne, C. Cebrián, L. Liu, A. Monari, M. Beley, X. Assfeld, S. Haacke, P. C. Gros, *Eur. J. Inorg. Chem.* **2015**, *2015*, 2469.

[107] J. Heinze, *Angew. Chem.* **1984**, *96*, 823.

[108] P. S. Braterman, J. I. Song, R. D. Peacock, *Inorg. Chem.* **1992**, *31*, 555.

[109] T. Förster, *Journal of biomedical optics* **2012**, *17*, 11002.

[110] C. Lochenie, K. Schötz, F. Panzer, H. Kurz, B. Maier, F. Puchtler, S. Agarwal, A. Köhler, B. Weber, *Journal of the American Chemical Society* **2018**, *140*, 700.

[111] S. A. Kovalenko, R. Schanz, H. Hennig, N. P. Ernsting, *The Journal of Chemical Physics* **2001**, *115*, 3256.

[112] T. Duchanois, L. Liu, M. Pastore, A. Monari, C. Cebrián, Y. Trolez, M. Darari, K. Magra, A. Francés-Monerris, E. Domenichini et al., *Inorganics* **2018**, *6*, 63.

[113] C. Schweitzer, R. Schmidt, *Chemical reviews* **2003**, *103*, 1685.

[114] J. A. Howard, G. D. Mendenhall, *Can. J. Chem.* **1975**, *53*, 2199.

[115] S. L. Murov, *Handbook of photochemistry*, Dekker, New York, **1973**.

[116] M. Pápai, G. Vankó, T. Rozgonyi, T. J. Penfold, *The journal of physical chemistry letters* **2016**, *7*, 2009.

[117] P. W. Atkins, J. de Paula, J. J. Keeler, *Physikalische Chemie,* 6. Aufl.

[118] S. Mukherjee, D. E. Torres, E. Jakubikova, *Chemical science* **2017**, *8*, 8115.

[119] Y. Vukadinovic, L. Burkhardt, A. Päpcke, A. Miletic, L. Fritsch, B. Altenburger, R. Schoch, A. Neuba, S. Lochbrunner, M. Bauer, *Inorganic chemistry* **2020**, *59*, 8762.

[120] a) A. Cannizzo, C. J. Milne, C. Consani, W. Gawelda, C. Bressler, F. van Mourik, M. Chergui, *Coordination Chemistry Reviews* **2010**, *254*, 2677; b) C. Consani, M. Prémont-Schwarz, A. Elnahhas, C. Bressler, F. van Mourik, A. Cannizzo, M. Chergui, *Angewandte Chemie (International ed. in English)* **2009**, *48*, 7184.

[121] A. M. Brown, C. E. McCusker, J. K. McCusker, *Dalton transactions (Cambridge, England : 2003)* **2014**, *43*, 17635.

[122] D. G. Brown, N. Sanguantrakun, B. Schulze, U. S. Schubert, C. P. Berlinguette, *Journal of the American Chemical Society* **2012**, *134*, 12354.

[123] H.-Y. Ding, X.-S. Wang, L.-Q. Song, J.-R. Chen, J.-H. Yu, Chao-Li, B.-W. Zhang, *Journal of Photochemistry and Photobiology A: Chemistry* **2006**, *177*, 286.

[124] I. Reim, B. Wriedt, Ü. Tastan, D. Ziegenbalg, M. Karnahl, *ChemistrySelect* **2018**, *3*, 2905.

[125] M. Huber-Gedert, M. Nowakowski, A. Kertmen, L. Burkhardt, N. Lindner, R. Schoch, R. Herbst-Irmer, A. Neuba, L. Schmitz, T.-K. Choi et al., *Chemistry (Weinheim an der Bergstrasse, Germany)* **2021**, *27*, 9905.

[126] a) F. Strieth-Kalthoff, F. Glorius, *Chem* **2020**, *6*, 1888; b) J. Großkopf, T. Kratz, T. Rigotti, T. Bach, *Chemical reviews* **2022**, *122*, 1626.

[127] M. Bregnhøj, M. Westberg, B. F. Minaev, P. R. Ogilby, *Accounts of chemical research* **2017**, *50*, 1920.

[128] A. A. Ghogare, A. Greer, *Chemical reviews* **2016**, *116*, 9994.

[129] P. Irmler, R. F. Winter, *Organometallics* **2018**, *37*, 235.

[130] P. Zimmer, L. Burkhardt, R. Schepper, K. Zheng, D. Gosztola, A. Neuba, U. Flörke, C. Wölper, R. Schoch, W. Gawelda et al., *Eur. J. Inorg. Chem.* **2018**, *2018*, 5203.

[131] J. Leonard, *Advanced Practical Organic Chemistry, Third Edition,* 3. Aufl., CRC Press, Hoboken, **2013**.

[132] G. R. Fulmer, A. J. M. Miller, N. H. Sherden, H. E. Gottlieb, A. Nudelman, B. M. Stoltz, J. E. Bercaw, K. I. Goldberg, *Organometallics* **2010**, *29*, 2176.

[133] S. Hünig, *Arbeitsmethoden in der organischen Chemie*. *(mit Einführungspraktikum)*, Lehmanns Media LOB.de, Berlin, **2006**.

[134] "Messprinzip der Elementaranalyse", zu finden unter https://chemie.uni-paderborn.de/?id=31151.

[135] L. Krause, R. Herbst-Irmer, G. M. Sheldrick, D. Stalke, *Journal of applied crystallography* **2015**, *48*, 3.

[136] a) G. M. Sheldrick, *Acta Crystallographica Section A* **2015**, *71*, 3; b) G. M. Sheldrick, *Acta Crystallographica Section C* **2015**, *71*, 3.

[137] a) A. L. Spek, *Acta crystallographica. Section D, Biological crystallography* **2009**, *65*, 148; b) A. L. Spek, *Acta crystallographica. Section C, Structural chemistry* **2015**, *71*, 9.

[138] A. Päpcke, A. Friedrich, S. Lochbrunner, *Journal of physics. Condensed matter : an Institute of Physics journal* **2019**, *32*, 153001.

[139] R. S. Nicholson, I. Shain, *Anal. Chem.* **1964**, *36*, 706.

[140] J. E. B. Randles, *Trans. Faraday Soc.* **1948**, *44*, 327.

[141] a) E. Livshits, R. Baer, *The journal of physical chemistry. A* **2008**, *112*, 12789; b) T. Stein, L. Kronik, R. Baer, *Journal of the American Chemical Society* **2009**, *131*, 2818; c) T. Stein, L. Kronik, R. Baer, *The Journal of Chemical Physics* **2009**, *131*, 244119.

[142] T. Möhle, O. S. Bokareva, G. Grell, O. Kühn, S. I. Bokarev, *Journal of chemical theory and computation* **2018**, *14*, 5870.

[143] M. J. Frisch, G. W. Trucks, H. B. Schlegel, G. E. Scuseria, M. A. Robb, J. R. Cheeseman, G. Scalmani, V. Barone, G. A. Petersson, H. Nakatsuji et al., *Gaussian 16 Rev. C.01*, Wallingford, CT, **2016**.

[144] F. Plasser, *The Journal of Chemical Physics* **2020**, *152*, 84108.

List of figures

Figure 1.1.1: Annual temperature anomaly in Germany in the time period 1881-2021 with positive (red) and negative (blue) anomalies with respect to the multi-annual mean (1961-1990) of 8.2 °C. Dashed line shows the linear trend of the mean annual temperature from 1881 to 2021 of +1.6 K.[1] 1

Figure 1.1.2: Atmospheric CO_2 in ppm at Mauna Loa Observatory (Keeling-Curve 1958-2021).[2]. 2

Figure 1.2.1: Diagram of selected categories included in the criticality score according to Graedl et al. and the corresponding CS for ruthenium, iridium and iron.[10,7] 4

Figure 2.1.1: Schematic illustration of different colors of hydrogen including grey, blue, turquoise, and green hydrogen..... 9

Figure 2.1.2: Schematic representation (top) and examples (bottom) of a molecular dyad (left panel)[26] and multicomponent systems (right panel) [24]. 11

Figure 2.2.1: Schematic ground- and excited-state landscapes of ruthenium(II) (left) and iron(II) (right) polypyridine complexes. Middle: Simplified molecular orbital diagrams for the corresponding ruthenium(II) and iron(II) complexes.[35,36] 12

Figure 2.2.2: Molecular structures and excited state lifetimes of **$[Fe(dcpp)_2]^{2+}$**,[38] **$[Fe(dcpp)(ddpd)]^{2+}$**,[42,43] **$[Fe(dqp)_2]^{2+}$**[44] and **$[Fe(pdmmi)_2]^{2+}$**[44] with optimized octahedral geometry..... 14

Figure 2.2.3: Molecular structures and excited state lifetimes of **$[Fe(bim)_2]^{2+}$**,[39] **$[Fe(bbp)_2]^{2+}$**[46] and **$[Fe(btz)_2(bpy)]^{2+}$**[48] with strongly σ-donating ligands..... 15

Figure 2.2.4: Schematic ground- and excited-state landscapes of iron(III) complexes (top). Molecular structures and excited state lifetimes of **$[Fe(btz)_3]^{3+}$**,[51] **$[Fe(phtmeimb)_2]^{+}$**[52] and **$[Fe(ImP)_2]^{+}$**[53] with iron(III) as central atom (bottom). 17

Figure 2.2.5: Effective prolongation of ^{3}MLCT lifetimes by chromophore-states populated by MLCT states and repopulation (reservoir effect) in Ru^{II} complexes according to Castellano et al.[56,57] 18

Figure 2.2.6: Molecular structures and excited state lifetimes of **$[Ru(tpy)_2]^{2+}$**, **$[Ru(tpy\text{-}pym\text{-}ant)_2]^{2+}$**,[62] **$[Ru(phen)_3]^{2+}$** and **$[Ru(phen\text{-}pyr)_3]^{2+}$**[56] as examples of the multichromophoric approach. 19

Figure 2.2.7: Molecular structures, triplet-energy differences of the MLCT and NI character states and excited state lifetimes of **Re0**-**Re5** as examples of Re(I)-based multichromophoric complexes.[64] 20

Figure 2.2.8: Molecular structures, triplet-energy of the MLCT states and excited state lifetimes of **Re6**-**Re10** as examples of Re(I)-based multichromophoric complexes. Triplett energy of **PNI** (right side).[65] 21

Figure 2.2.9: Molecular structures of **Pt1** and **Cr1** as examples of platinum[67] and chromium[68] based multichromophoric complexes. 21

Figure 2.2.10: Molecular structures of **Fe1** and **Fe2** predicted to have ^{3}MLCT states localized at the anthracenyl-chromophore.[69] 22

Figure 3.1.1: Schematic representation of the two main strategies to improve photophysical properties of iron(II) complexes followed in this work: The variation of σ-donor and π-acceptor properties (left side, red) and the variation of organic chromophores in 4-position of the central pyridine ring (right side, blue) of the ligands. Abbreviations used in the following in bold letters. 23

Figure 4.2.1: Single crystal X-Ray structure of **$[Fe(bbp\text{-}R)_2]$**$(PF_6)_2$. 31

Figure 4.2.2: Provisional single crystal X-Ray structure of **$[Fe(bim\text{-}ac\text{-}3)_2]$**$(PF_6)_2$. 33

Figure 4.2.3: NMR-spectrum and ESI-MS data proving the synthesis of **17** not separated from educt **12**. 34

Figure 4.3.1: Single crystal X-Ray structures of **[Fe(btp)$_2$]**$(PF_6)_2$ (left) and **[Fe(tri)$_2$]**$(PF_6)_2$ (right). . 36
Figure 5.1.1: Optical absorption and emission spectroscopy data (left panel) and cyclic voltammograms (right panel) of **tpy-R** ligands and **[Fe(tpy-R)$_2$]**$(PF_6)_2$ complexes. 42
Figure 5.1.2: Decay associated spectrum (DAS; left panel) and TCSPC data (right panel) of **[Fe(tpy-3)$_2$]**$(PF_6)_2$ 43
Figure 5.2.1: Optical absorption and emission spectroscopy data (left panel) and cyclic voltammograms (right panel) of **[Fe(bim-R)$_2$]**$(PF_6)_2$ complexes in MeCN. 44
Figure 5.2.2: Steady state absorption and emission spectroscopy (top left panel), experimental data and analysis of time resolved emission spectroscopy performed by streak camera measurements (top right panel) and transient absorption and decay associated spectra including results of spectroelectrochemical experiments ΔA_{ex}^{sim} (bottom panel). These experimental data are shown for **[H$_2$-bim-3]**$(PF_6)_2$ and **[Fe(bim-3)$_2$]**$(PF_6)_2$ as examples. ... 47
Figure 5.2.3: Schematic representation of excited-state dynamics in **[Fe(bim-3)$_2$]**$(PF_6)_2$ as example. ^{3}MLCT lifetime as seen by transient absorption spectroscopy (black arrow). ^{1}Chrom lifetime and IC time as deduced from streak camera measurements (black dotted/green arrow). ^{3}Chrom is not effectively populated by ^{1}Chrom or ^{3}MLCT state according to $^1O_2$ experiments (gray dotted arrows). The nomenclature ^{3}Chrom indicates a chromophore-dominated electronic state within the bim-chromophore ligand assembly. 49
Figure 5.2.4: Steady state absorption and emission spectroscopy of **[H$_2$-bim-ac-3]**$(PF_6)_2$ pro-ligand and **[Fe(bim-ac-3)$_2$]**$(PF_6)_2$ complex..... 50
Figure 5.3.1: Optical absorption and emission spectroscopy data (left panel) and cyclic voltammograms (right panel) of **[Fe(bbp-R)$_2$]**$(PF_6)_2$ complexes. 52
Figure 5.3.2: absorption (top left panel) and decay associated spectra (top right panel) of **[Fe(bbp-3)$_2$]**$(PF_6)_2$ and emission of anthracene, **[H$_2$-bbp-3]**$(PF_6)_2$ and **[Fe(bbp-3)$_2$]**$(PF_6)_2$ at 77 K (bottom panel). 54
Figure 5.3.3: Schematic representation of excited-state dynamics in **[Fe(bbp-3)$_2$]**$(PF_6)_2$ as example. ^{3}MLCT lifetime as seen by transient absorption spectroscopy (black arrow). ^{1}Chrom lifetime and FRET time could not be deduced by streak camera measurements due to weak emission (black dotted/green arrow). ^{3}Chrom is not effectively populated by ^{1}Chrom or ^{3}MLCT state according to $^1O_2$ experiments (gray dotted arrows). The nomenclature ^{3}Chrom indicates a chromophore-dominated electronic state within the bbp-chromophore ligand assembly. 55
Figure 5.4.1: Optical absorption spectroscopy data of **[Fe(btp)$_2$]**$(PF_6)_2$, **btp-3** and **[Fe(btp-3)$_2$]**$(PF_6)_2$ (left panel) and cyclic voltammograms of **[Fe(btp)$_2$]**$(PF_6)_2$ and **[Fe(btp-3)$_2$]**$(PF_6)_2$ (right panel). 57
Figure 5.4.2: Transient absorption and decay associated spectra including results of spectroelectrochemical experiments **[Fe]$^+$-[Fe]** (left panel) and schematic representation of excited-state dynamics in **[Fe(btp)$_2$]**$(PF_6)_2$ (right panel). 58
Figure 5.4.3: Steady state emission spectroscopy (left panel) and time streak camera measurments (right panel) of **btp-3** and **[Fe(btp-3)$_2$]**$(PF_6)_2$ 59
Figure 5.5.1: Optical absorption spectroscopy data of **[Fe(tri)$_2$]**$(PF_6)_2$, **[H$_2$-tri-3]**$(PF_6)_2$ and **[Fe(tri-3)$_2$]**$(PF_6)_2$ (left panel) and cyclic voltammograms of **[Fe(tri)$_2$]**$(PF_6)_2$ and **[Fe(tri-3)$_2$]**$(PF_6)_2$ (right panel). 60
Figure 5.5.2: Schematic representation of excited-state dynamics in **[Fe(tri)$_2$]**$(PF_6)_2$ (left panel) and transient absorption and decay associated spectra including results of spectroelectrochemical experiments **[Fe]$^+$-[Fe]** (right panel)..... 61
Figure 5.6.1: Optical absorption spectroscopy data (left panel) and cyclic voltammograms (right panel) of **[Ru(bbp)$_2$]**$(PF_6)_2$, **[Ru(bbp-1)$_2$]**$(PF_6)_2$ and **[Ru(bbp-3)$_2$]**$(PF_6)_2$. 63
Figure 5.6.2: Steady state absorption (black), emission (blue/orange dotted) and excitation spectra (red/pink) of **[Ru(bbp)$_2$]**$(PF_6)_2$ (top panel), **[Ru(bbp-1)$_2$]**$(PF_6)_2$ (bottom left panel) and **[Ru(bbp-3)$_2$]**$(PF_6)_2$ (bottom right panel). 65

Figure 5.6.3: Provisional schematic representation of excited-state dynamics in **[Ru(bbp-3)$_2$]**$(PF_6)_2$. ^{3}MLCT lifetime as seen by streak camera measurements (black arrow). Relaxation cascade from ^{1}Ant into ^{1}MLCT by FRET and from ^{3}MLCT into ^{3}Ant is deduced by emission spectroscopy at room temperature and at 77 K. Back-IC ($k_{back\text{-}IC}$) seems not to be possible at 77 K. This representation bases on the current results and might be completed by further detailed spectroscopic investigations and quantum chemical calculations..... 66
Figure 6.1.1: Molecular structures of used photosensitizer **[Ru(bbp-R)$_2$]**$(PF_6)_2$ and **[Co(dmgH)pyCl]** as water reduction catalyst (top) and schematic representation of the catalytic mechanism (bottom)..... 67
Figure 6.1.2: Pressure differences in photocatalytic proton reduction in acetonitrile (left panel) and THF (right panel). 68
Figure 6.2.1: [4+2] cycloaddition of **DPBF** and $^1O_2$ (top) and resulting change in emission intensities for different conditions and with **[Ru(bpy)$_3$]**Cl_2 as reference plotted at different reaction times (bottom). 70
Figure 6.2.2: [4+2] cycloaddition of anthracene and $^1O_2$ (top) and resulting change in absorption (left bottom) and emission (right bottom) at different reaction times for a mixture of anthracene and **[Fe(btp)$_2$]**$(PF_6)_2$. 70
Figure 6.2.3: [4+2] cycloaddition of naphthalene-1,5-diole and $^1O_2$ (top) and resulting changes in absorption intensities of the mixture of naphthalene-1,5-diole and **[Fe(btp)$_2$]**$(PF_6)_2$ at different reaction times (bottom). 71
Figure 8.1.1: Molecular structure of **[Fe(tri-3)$_2$]**$(PF_6)_2$ which is a promising candidate as multichromophoric photosensitizer due to the small energy gap between ^{3}MLCT and ^{3}Chromophore states..... 77
Figure 8.1.2: Molecular structure of a **Dyad** carrying an aromatic chromophore at one ligand. The antenna effect might increase the population of the ^{3}MLCT state by the proposed Förster Resonance Energy Transfer. This could increase the photocatalytic properties of this type of molecular dyads..... 78
Figure 8.1.3: Molecular structure of **[Fe^{III}(ImP-3)$_2$]**PF_6. The multichromophoric approach could help to increase the photophysical properties of iron(III) complexes. 79
Figure 8.1.4: Schematic representation of photophysical processes in multichromophoric iron (II) complexes (left side) and multichromophoric iron (III) complexes (right side). Effects that have been found and discussed in terms of this work are highlighted in green boxes. Effects that are still under investigation and of huge interest for following projects are highlighted in red boxes. 79

List of schemes

Scheme 4.1.1: Syntheses of **tpy-R** ligands and **[Fe(tpy-R)$_2$]**$(PF_6)_2$ complexes. 25
Scheme 4.2.1: Optimization of the synthesis of **7** starting from a four-step synthesis (upper reaction)[74–76] over one-step synthesis using n-BuLi (middle reaction)[77] resulting in a more selective one-step synthesis using TMPMgCl as base (lower reaction).[78] 27
Scheme 4.2.2: Syntheses of pro-ligands **[H$_2$-bim-R]**$(PF_6)_2$ and **[Fe(bim-R)$_2$]**$(PF_6)_2$ complexes.[36] 28
Scheme 4.2.3: Syntheses of pro-ligands **[H$_2$-bbp-R]**$(PF_6)_2$ and **[Fe(bbp-R)$_2$]**$(PF_6)_2$ complexes. 30
Scheme 4.2.4: Syntheses of pro-ligand **[H$_2$-bim-ac-3]**$(PF_6)_2$ and **[Fe(bim-ac-3)$_2$]**$(PF_6)_2$ complex. 32
Scheme 4.2.5: Synthetic procedure attempting to yield in **17**. 34
Scheme 4.3.1: Syntheses of complexes **[Fe(btp)$_2$]**$(PF_6)_2$ and **[Fe(tri)$_2$]**$(PF_6)_2$.[94] 35
Scheme 4.3.2: Synthetic procedure attempting to yield in **19-3**. 37
Scheme 4.3.3: Syntheses of complexes **[Fe(btp-3)$_2$]**$(PF_6)_2$ and **[Fe(tri-3)$_2$]**$(PF_6)_2$. 39
Scheme 4.4.1: Synthetic procedure of **[Ru(bbp)$_2$]**$(PF_6)_2$. The same procedure results in the formation of **[Ru(bbp-1)$_2$]**$(PF_6)_2$ and **[Ru(bbp-3)$_2$]**$(PF_6)_2$.[100,101] 40

List of tables

Table 4.1.1: Yields of the syntheses of **(tpy-R)** ligands and **[Fe(tpy-R)$_2$]**$(PF_6)_2$ complexes. 26
Table 4.2.1: Yields of the syntheses described in this section. ***3** is commercially available [1)]Yield of the Sandmeyer reaction, [2)]Yield of deprotonation using TMPMgCl. 27
Table 4.2.2: Parameters in the optimization process of the Suzuki-Coupling resulting in **8-R** products. In this table the yields of **8-3** are shown. 28
Table 4.2.3: Yields of syntheses performed according to the procedures described in this section.[1)]**8-1** was not obtained without impurities. [2)] Synthesis of **9-1** was not performed as **8-1** was used in a neat coupling to result in **[H$_2$-bim-1](PF$_6$)$_2$**. 29
Table 4.2.4: Yields of syntheses of **10-R** derivatives, pro-ligands **[H$_2$-bbp-R]**$(PF_6)_2$ and **[Fe(bbp-R)$_2$]**$(PF_6)_2$ complexes performed according to the procedures described in this section. .. 30
Table 4.2.5: Parameters in the optimization process of the Sonogashira-Coupling of **12** and **13** resulting in **14**. 32
Table 4.2.6: Yields of syntheses of **11**-**14**, pro-ligand **[H$_2$-bim-ac-3]**$(PF_6)_2$ and **[Fe(bim-ac-3)$_2$]**$(PF_6)_2$ complex performed according to the procedures described in this section. [1)] **17** could not be purified. 34
Table 4.3.1: Yields of syntheses performed according to the procedures described in this section resulting in **[Fe(btp)$_2$]**$(PF_6)_2$ and **[Fe(tri)$_2$]**$(PF_6)_2$. 36
Table 4.3.2: Parameters in the optimization process of the Sonogashira-Coupling resulting in **19-3**. 38
Table 4.3.3: Parameters in the optimization process of the Huisgen-[2+3]-cyclization resulting in **btp-3**. 38
Table 4.3.4: Yields of syntheses performed according to the procedures described in this section resulting in **[Fe(btp-3)$_2$]**$(PF_6)_2$ and **[Fe(tri-3)$_2$]**$(PF_6)_2$. 40
Table 4.4.1: Yields of syntheses performed according to the procedures described in this section resulting in **[Ru(bbp)$_2$]**$(PF_6)_2$, **[Ru(bbp-1)$_2$]**$(PF_6)_2$ and **[Ru(bbp-3)$_2$]**$(PF_6)_2$. 40
Table 5.1.1: Photo- and electrochemical properties of **tpy-R** ligands and **[Fe(tpy-R)$_2$]**$(PF_6)_2$ complexes. 43
Table 5.2.1: Photo- and electrochemical properties of **[Fe(bim-R)$_2$]**$(PF_6)_2$ complexes. 45
Table 5.2.2: Excited state properties of **[H$_2$-bim-R]**$(PF_6)_2$ pro-ligands and **[Fe(bim-R)$_2$]**$(PF_6)_2$ complexes. [a)]Data not collected due to weak emission. [b)] Measurements still in progress.48
Table 5.3.1: Photo- and electrochemical properties of **[Fe(bbp-R)$_2$]**$(PF_6)_2$ complexes. 52
Table 5.3.2: Excited state properties of **[Fe(bbp-R)$_2$]**$(PF_6)_2$ complexes. 54
Table 5.4.1: Ground and excited state properties of **[Fe(btp)$_2$]**$(PF_6)_2$, **btp-3** and **[Fe(btp-3)$_2$]**$(PF_6)_2$.[a)]MC lifetime of **[Fe(btp-3)$_2$]**$(PF_6)_2$ has not been determined yet..... 58
Table 5.5.1: Ground and excited state properties of **[Fe(tri)$_2$]**$(PF_6)_2$ and **[Fe(tri-3)$_2$]**$(PF_6)_2$.[a)]Transient absorption of **[Fe(tri-3)$_2$]**$(PF_6)_2$ has not been determined yet. 62
Table 5.6.1: Ground and excited state properties of **[Ru(bbp)$_2$]**$(PF_6)_2$, **[Ru(bbp-1)$_2$]**$(PF_6)_2$ and **[Ru(bbp-3)$_2$]**$(PF_6)_2$. [a)]Streak camera experiments of **[Ru(bbp-1)$_2$]**$(PF_6)_2$ have not been performed yet..... 66
Table 6.1.1: Parameters used to calculate the TON in photocatalytic proton reduction in THF/H_2O/TEA (8/1/1 V/V/V). 68

Scientific publications and presentations

List of publications

Photoactive iron complexes: more sustainable, but still a challenge
Philipp Dierks, Yannik Vukadinovic, Matthias Bauer
Inorg. Chem. Front., **2022**, 9, 206-220.

Distinct photodynamics of κ-N and κ-C pseudoisomeric iron(II) complexes
Philipp Dierks, Ayla Kruse, Olga S. Bokareva, Mohammed J. Al-Marri, Jens Kalmbach, Marc Baltrun, Adam Neuba, Roland Schoch, Stephan Hohloch, Katja Heinze, Michael Seitz, Oliver Kühn, Stefan Lochbrunner, Matthias Bauer
Chem. Commun., **2021**, 57, 6640-6643.

Ground- and Excited-State Properties of Iron(II) Complexes Linked to Organic Chromophores
Philipp Dierks, Ayla Päpcke, Olga S. Bokareva, Björn Altenburger, Thomas Reuter, Katja Heinze, Oliver Kühn, Stefan Lochbrunner, Matthias Bauer
Inorg. Chem., **2020**, 59, 20, 14746-14761.

Electroluminescent and Optoelectronic Properties of OLEDs with Bay-Extended, Distorted Perylene Esters as Emitter Materials
Joachim Vollbrecht, Simon Blazy, Philipp Dierks, Samuel Peurifoy, Harald Bock, Heinz Kitzerow
ChemPhysChem, **2017**, *18, 2024 - 2032.*

List of oral presentations

15.02.2022	**Ground- and Excited-State Properties of Iron(II) Complexes Linked to Organic Chromophores** Central European Conference on Photochemistry 2022, Bad Hofgastein, Österreich
06.12.2021	**Multichromophoric Iron-Complexes – A New Design Concept in Photoactive Fe(II)-Complexes** Seminar der Jungen Wöhler Vereinigung (online)
30.08.2021 (invited)	**Ground- and Excited-State Properties of Iron(II) Complexes Linked to Organic Chromophores** Flashvortrag beim Wissenschaftsforum Chemie 2021 in der Kategorie „Highlights der anorganischen Chemie“ (online)
26.07.2021	**Multichromophoric Iron-Complexes – New Liganddesign in Photoactive Fe(II)-Complexes** 4. Ligandendesign Workshop 2021 an der Universität zu Köln (online)
27.05.2020	**Mit Photokatalyse zu nachhaltigen Kraftstoffen** Kolloquium des Studienfonds OWL (online)
14.02.2020	**Multichromophore Fe-Komplexe** Regionales Stipendiatentreffen des Fonds der Chemischen Industrie

List of poster presentations

29.08.-01.09.2021	**Iron Complexes Linked to Organic Chromophores** Wissenschaftsforum Chemie 2021 (online)
29.03.-01.04.2021	**New Concept of Multichromophoric Iron Complexes** JCF Frühjahrssymposium 2021 (online)
26.02.2020	**New Concept of Multichromophoric Iron Complexes** JCF Paderborn Bring-Your-Own-Poster Session 2020
20.-22.03.2019	**New Concept of Multichromophoric Iron Complexes** SPP 2102 2nd Regular Meeting (Bonn)
03.-05.03.2019	**New Concept of Multichromophoric Iron Complexes** Koordinationschemiker Treffen 2019 (München)
05.12.2018	**New Concept of Multichromophoric Iron Complexes** JCF Paderborn Bring-Your-Own-Poster Session 2018

Appendix

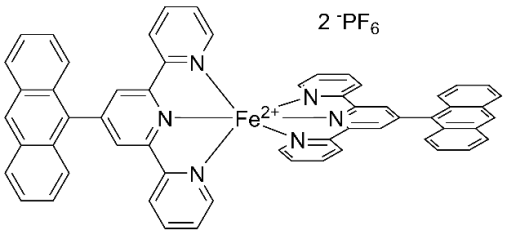

[Fe(typ-3)$_2$](PF$_6$)$_2$

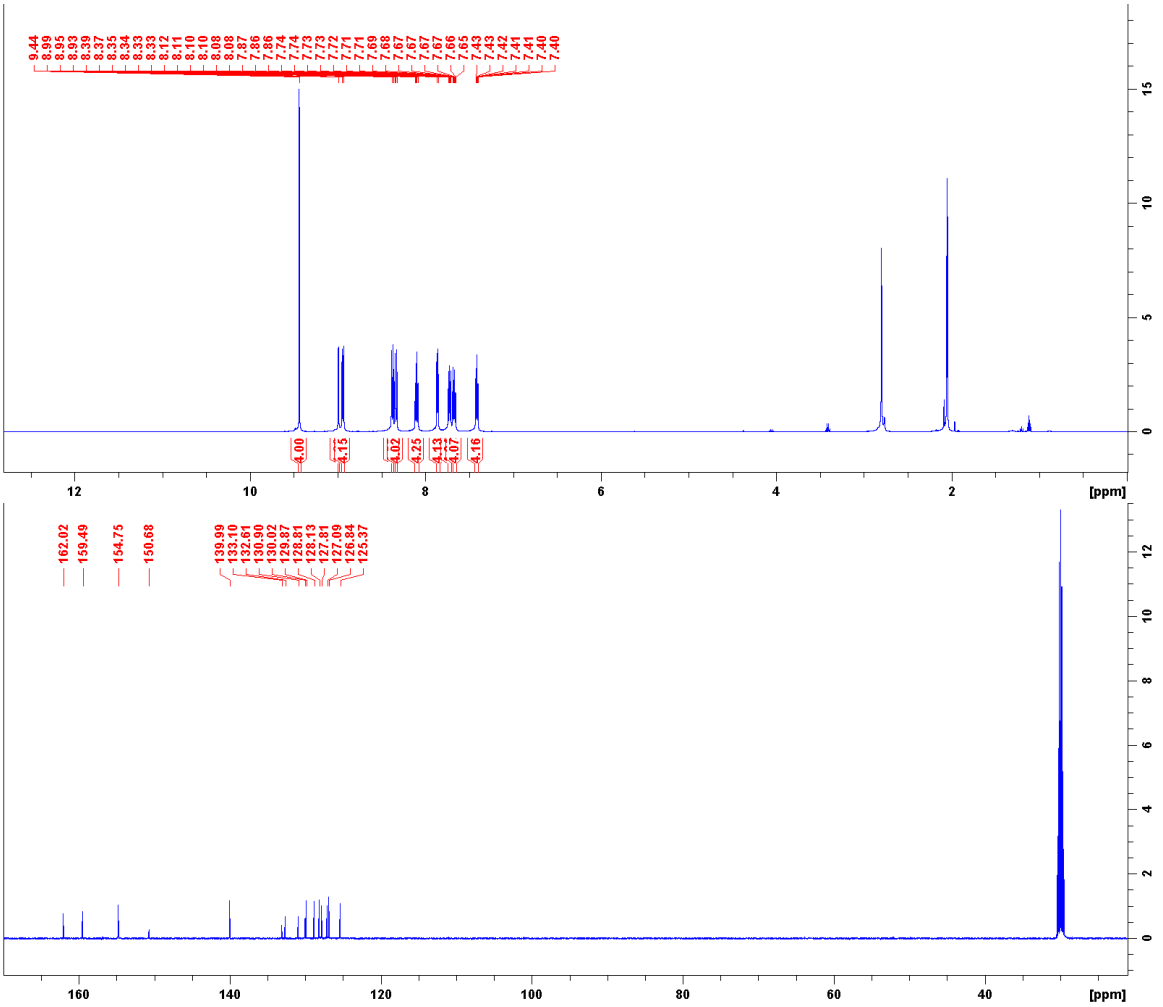

*Figure A 1: ^{1}H (top) and ^{13}C (bottom) NMR spectra of **[Fe(tpy-3)$_2$]**(PF$_6$)$_2$ in d_6-acetone at 303 K.*

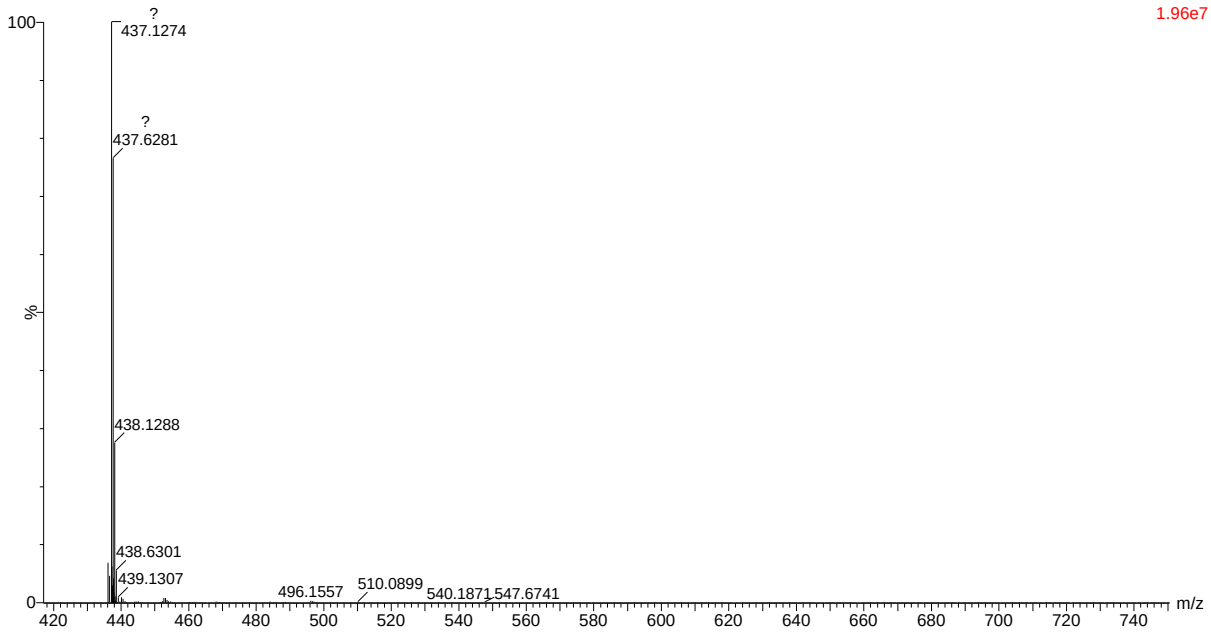

Figure A 2: ESI MS data of ***[Fe(tpy-3)$_2$]***$(PF_6)_2$ *in MeCN.*

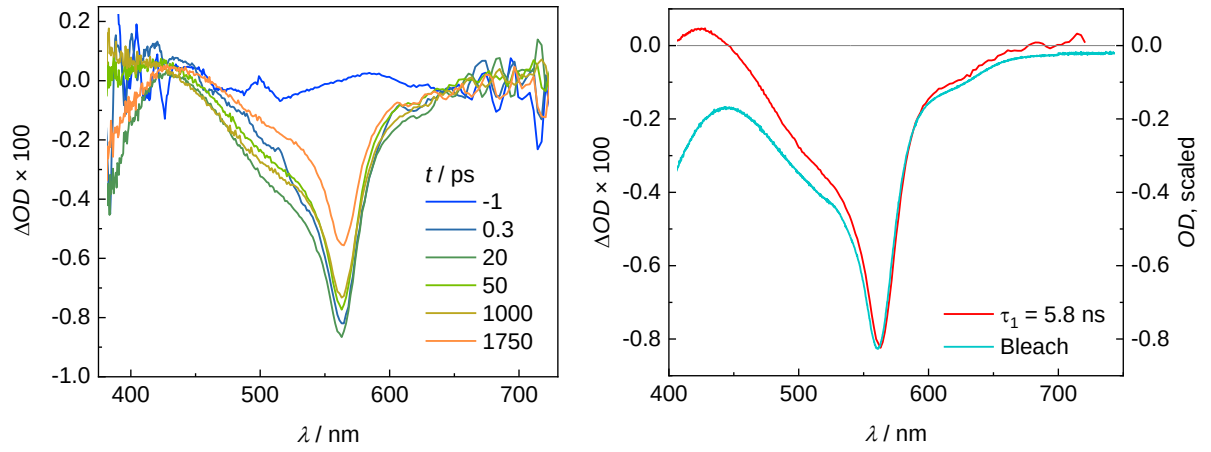

Figure A 3: Transient absorption (left) and decay associated spectra (right) of ***[Fe(tpy-3)$_2$]***$(PF_6)_2$ *in MeCN as recordedy by the group of Prof. Stefan Lochbrunner.*

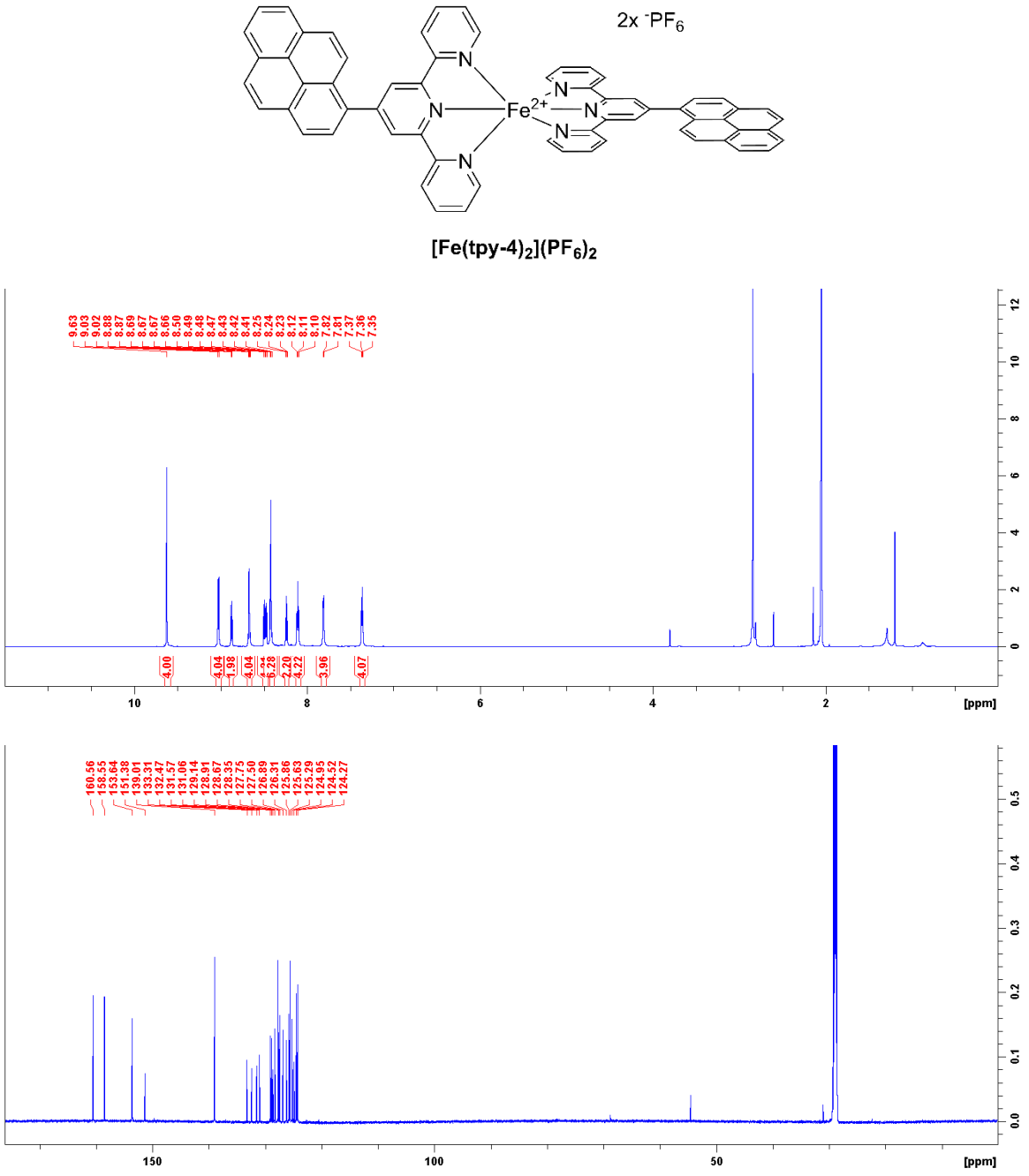

*Figure A 4: ^{1}H (top) and ^{13}C (bottom) NMR spectra of **[Fe(tpy-4)$_2$]**$(PF_6)_2$ in d_6-acetone at 303 K.*

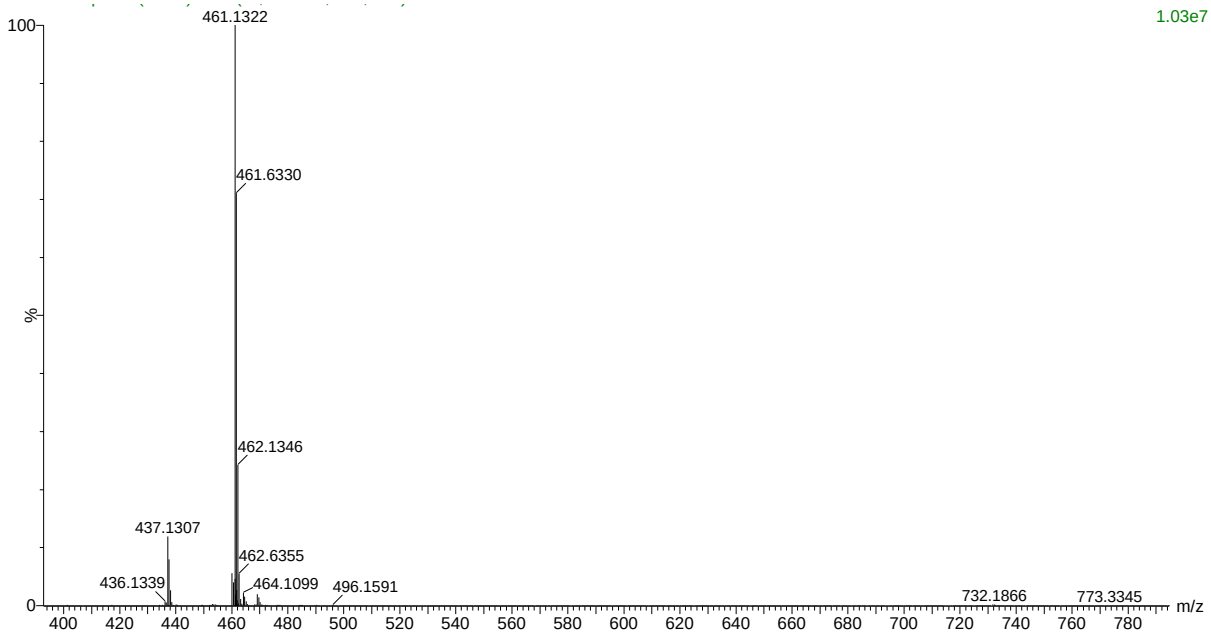

Figure A 5: ESI MS data of ***[Fe(tpy-4)$_2$]***$(PF_6)_2$ *in MeCN.*

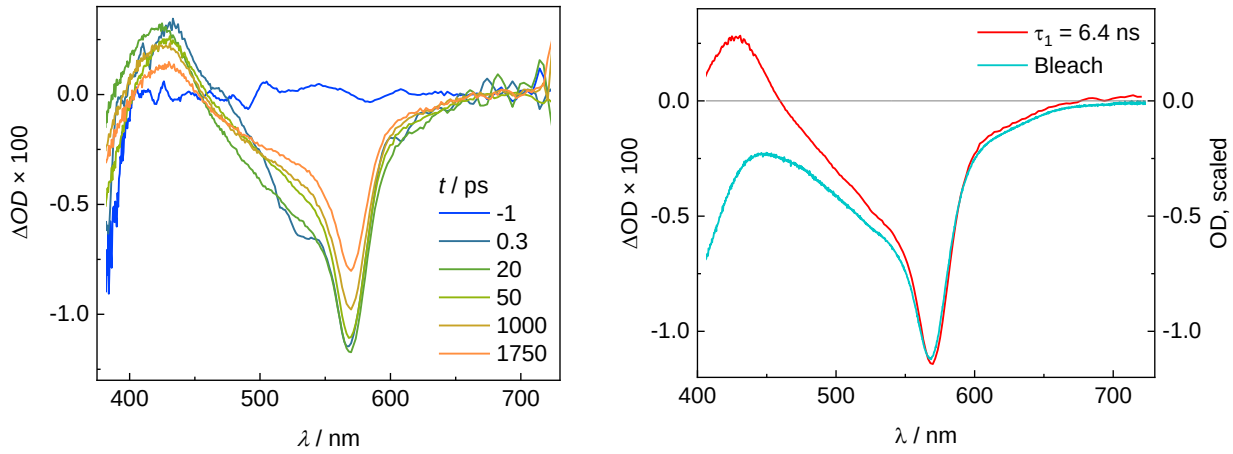

Figure A 6: Transient absorption (left) and decay associated spectra (right) of ***[Fe(tpy-4)$_2$]***$(PF_6)_2$ *in MeCN as recordedy by the group of Prof. Stefan Lochbrunner.*

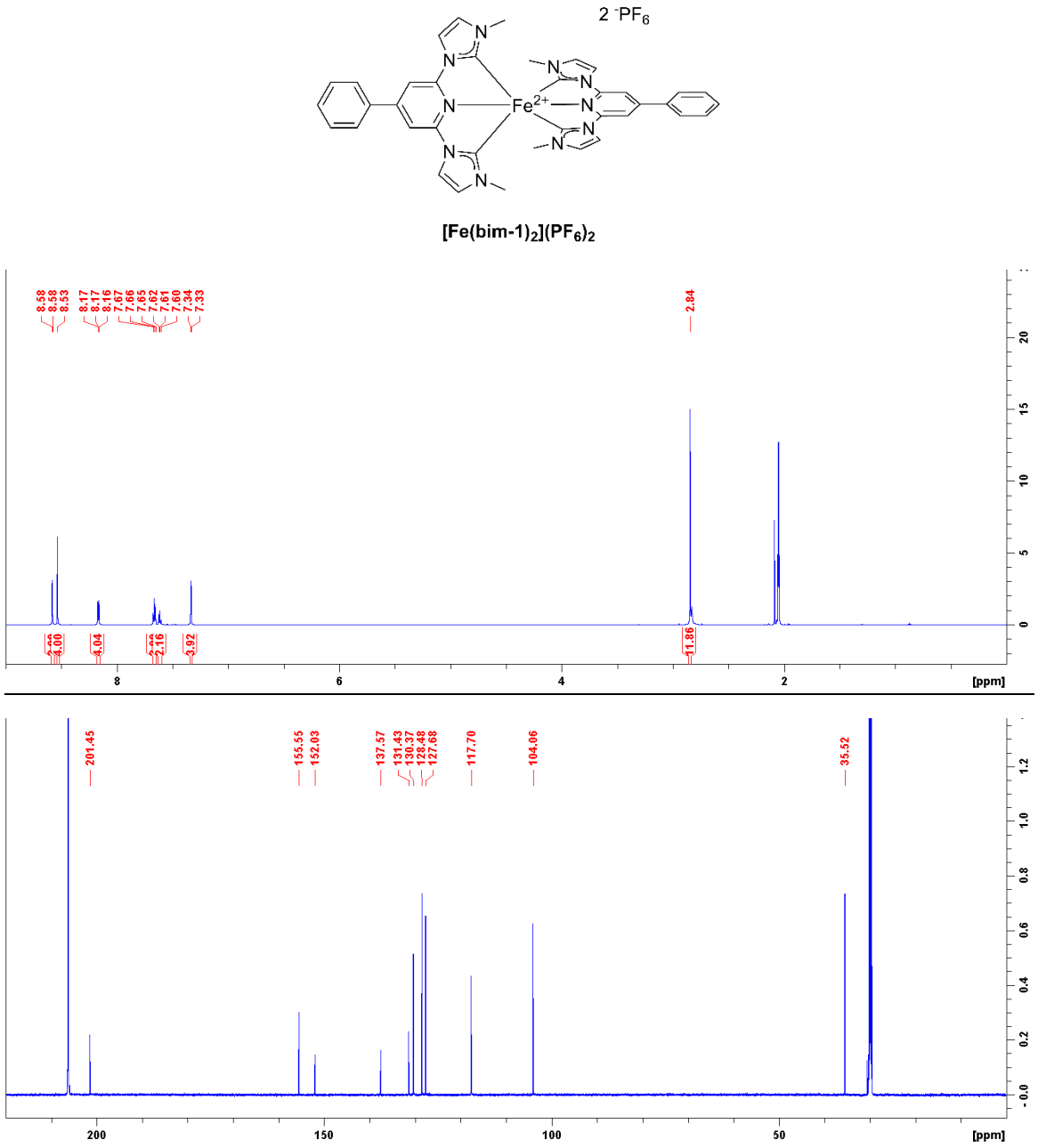

*Figure A 7: ^{1}H (top) and ^{13}C (bottom) NMR spectra of **[Fe(bim-1)$_2$]**$(PF_6)_2$ in d_6-acetone at 303 K.*

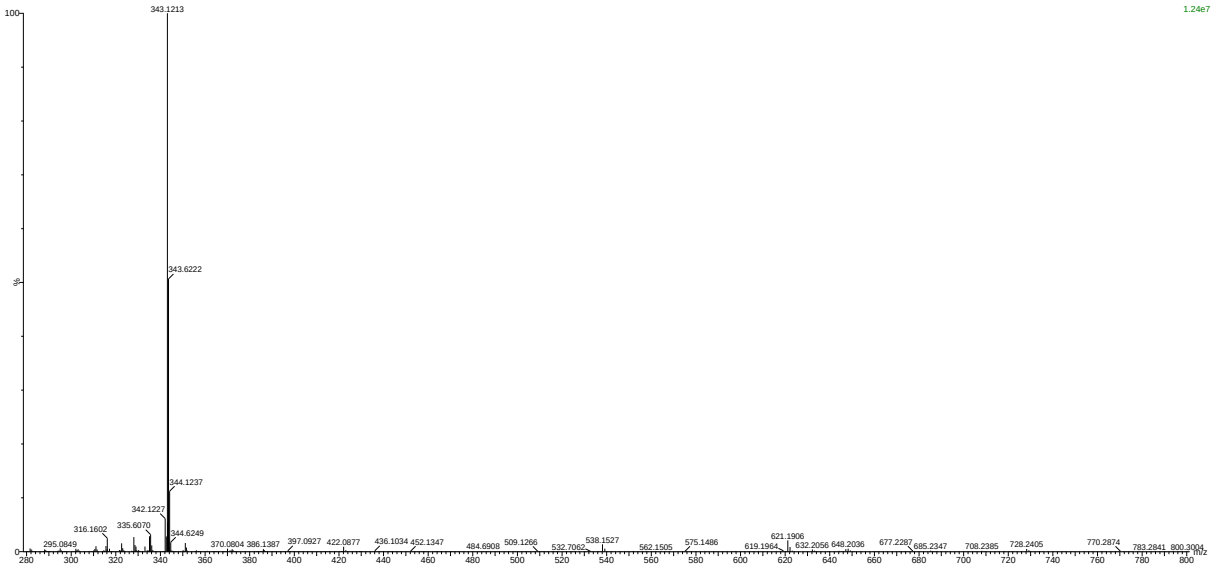

Figure A 8: ESI MS data of ***[Fe(bim-1)$_2$]***$(PF_6)_2$ *in MeCN.*

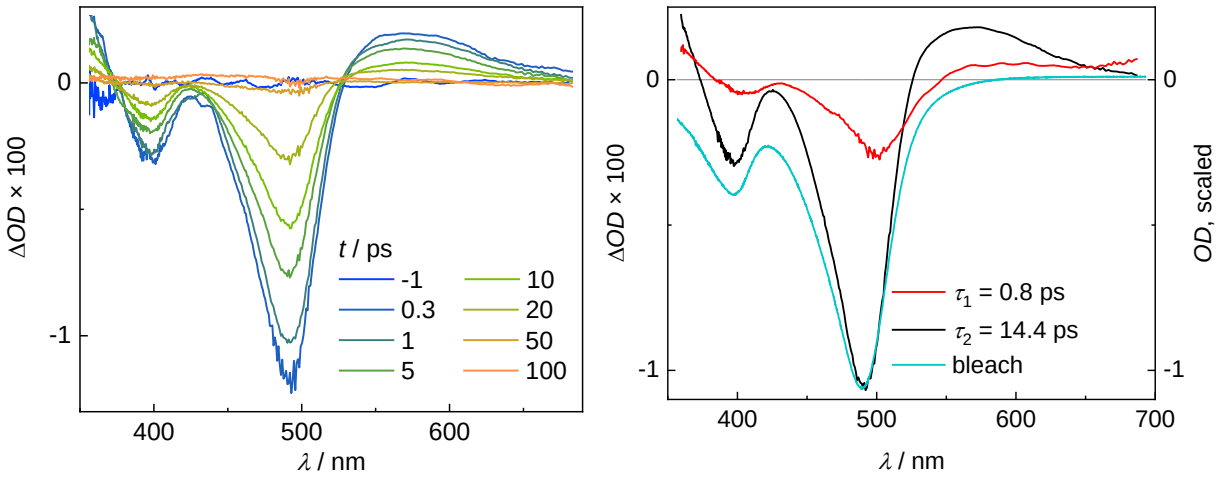

Figure A 9: Transient absorption (left) and decay associated spectra (right) of ***[Fe(bim-1)$_2$]***$(PF_6)_2$ *in MeCN as recordedy by the group of Prof. Stefan Lochbrunner.*

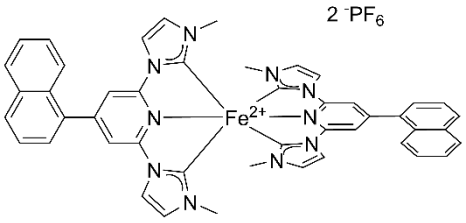

$[Fe(bim\text{-}2)_2](PF_6)_2$

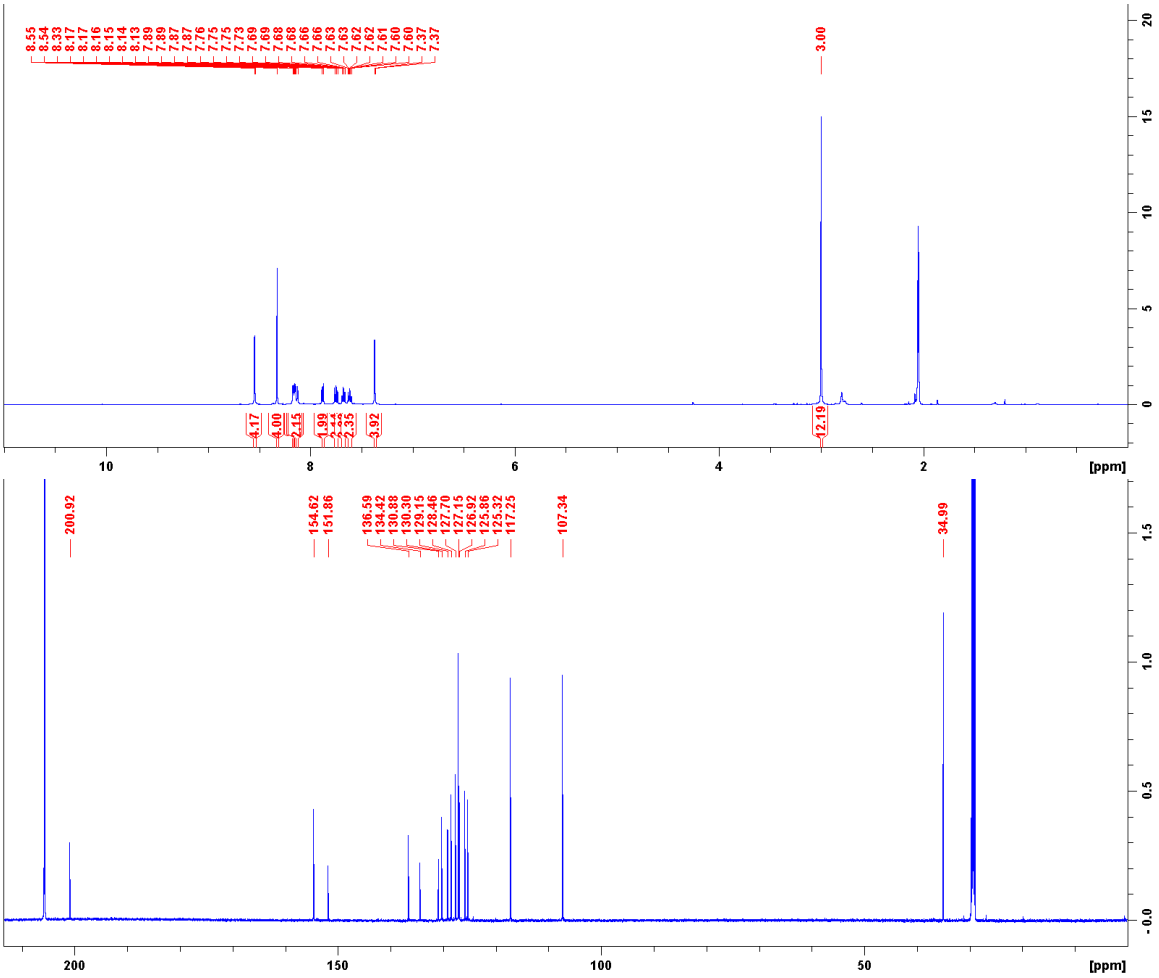

*Figure A 10: ^{1}H (top) and ^{13}C (bottom) NMR spectra of **$[Fe(bim\text{-}2)_2](PF_6)_2$** in d_6-acetone at 303 K.*

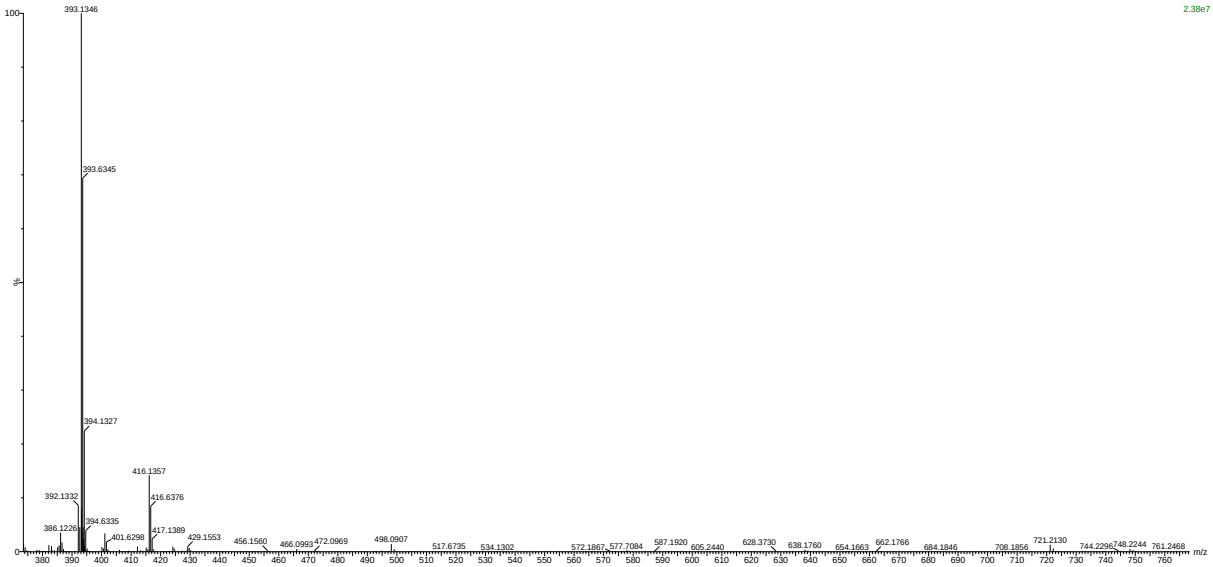

Figure A 11: ESI MS data of ***[Fe(bim-2)$_2$]***$(PF_6)_2$ *in MeCN.*

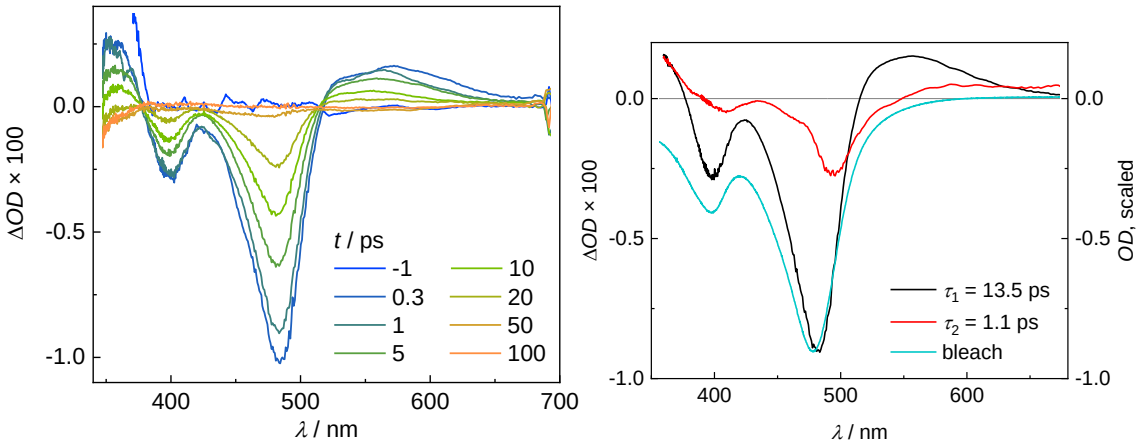

Figure A 12: Transient absorption (left) and decay associated spectra (right) of ***[Fe(bim-2)$_2$]***$(PF_6)_2$ *in MeCN as recordedy by the group of Prof. Stefan Lochbrunner.*

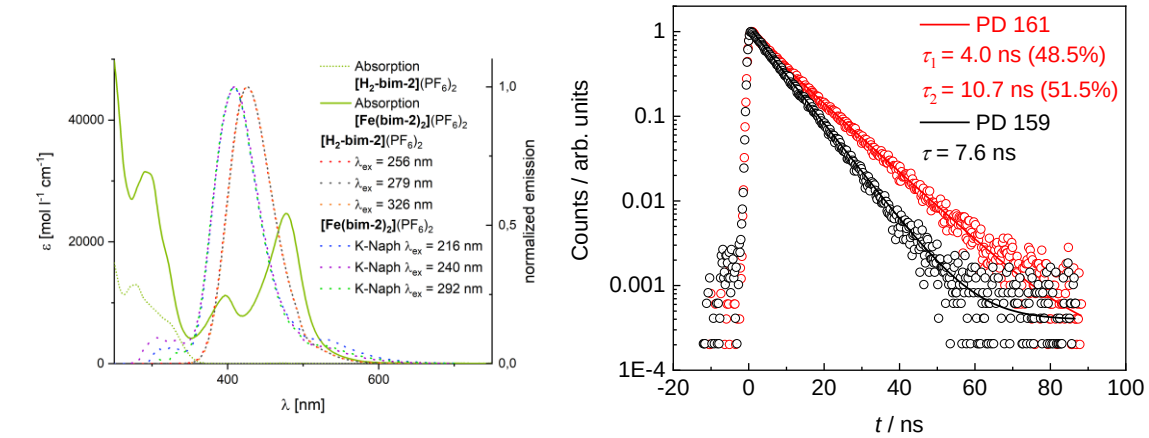

Figure A 13: Absorption and emission (left) of ***[H$_2$-bim-2]***$(PF_6)_2$ *and* ***[Fe(bim-2)$_2$]***$(PF_6)_2$ *and streak camara data and analysis (right) of* ***[H$_2$-bim-2]***$(PF_6)_2$ *(PD 159, black) and* ***[Fe(bim-2)$_2$]***$(PF_6)_2$ *(PD 161, red) as recorded by the group of Prof. Stefan Lochbrunner.*

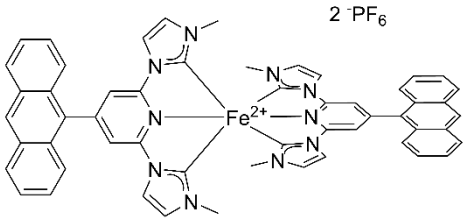

$[Fe(bim\text{-}3)_2](PF_6)_2$

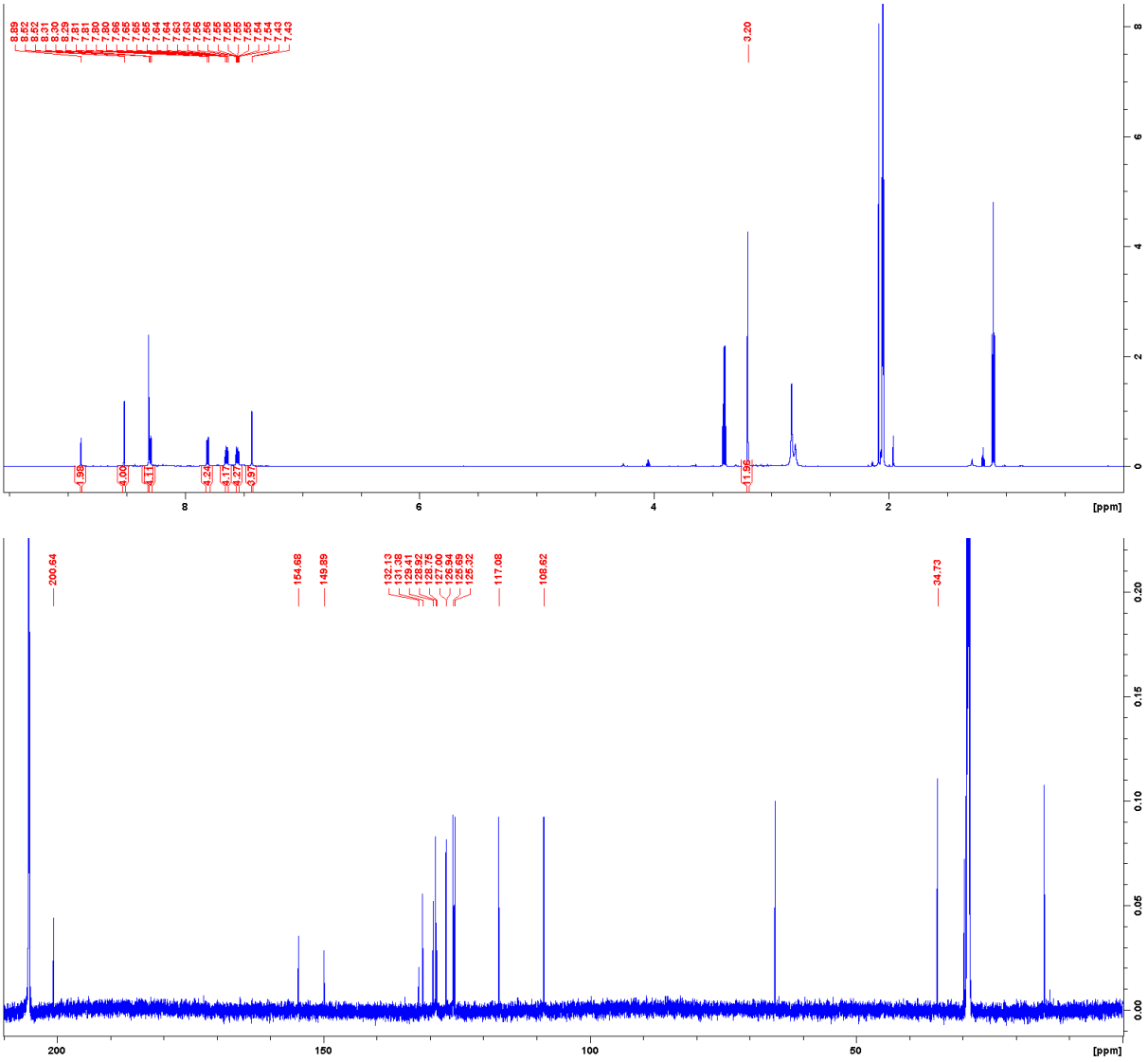

*Figure A 14: ^{1}H (top) and ^{13}C (bottom) NMR spectra of **$[Fe(bim\text{-}3)_2]$**$(PF_6)_2$ in d_6-acetone at 303 K.*

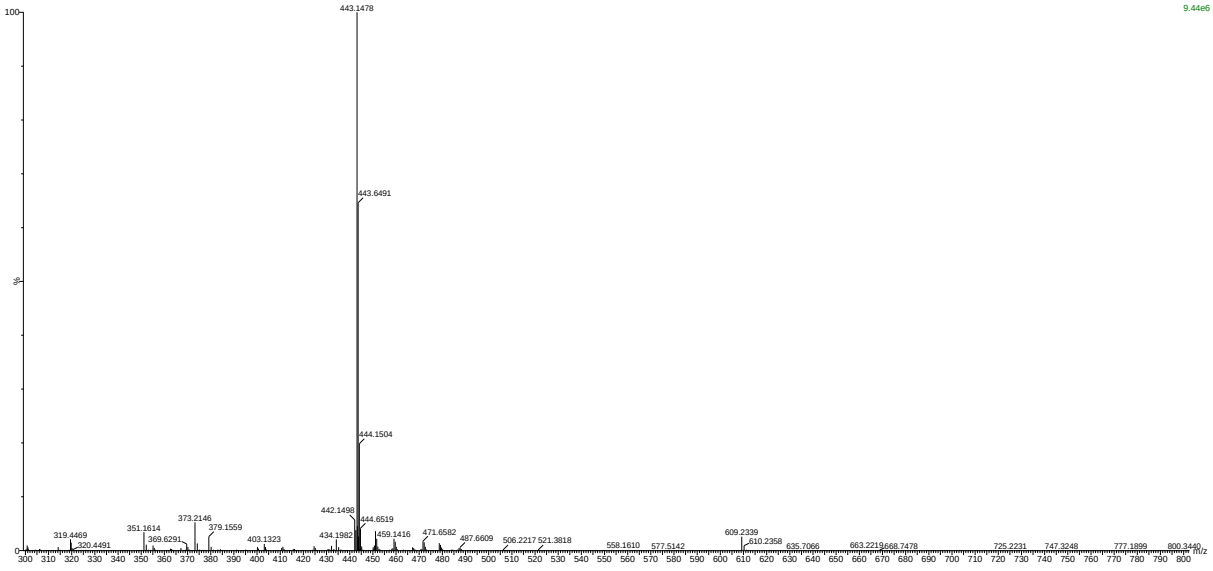

Figure A 15: ESI MS data of ***[Fe(bim-3)$_2$]***$(PF_6)_2$ *in MeCN.*

Data of steady state and time resolved absorption and emission spectroscopy are shown in the thesis. Details on the quantum chemical calculations of **[Fe(bim-3)$_2$]**$(PF_6)_2$ can be found in the published data.

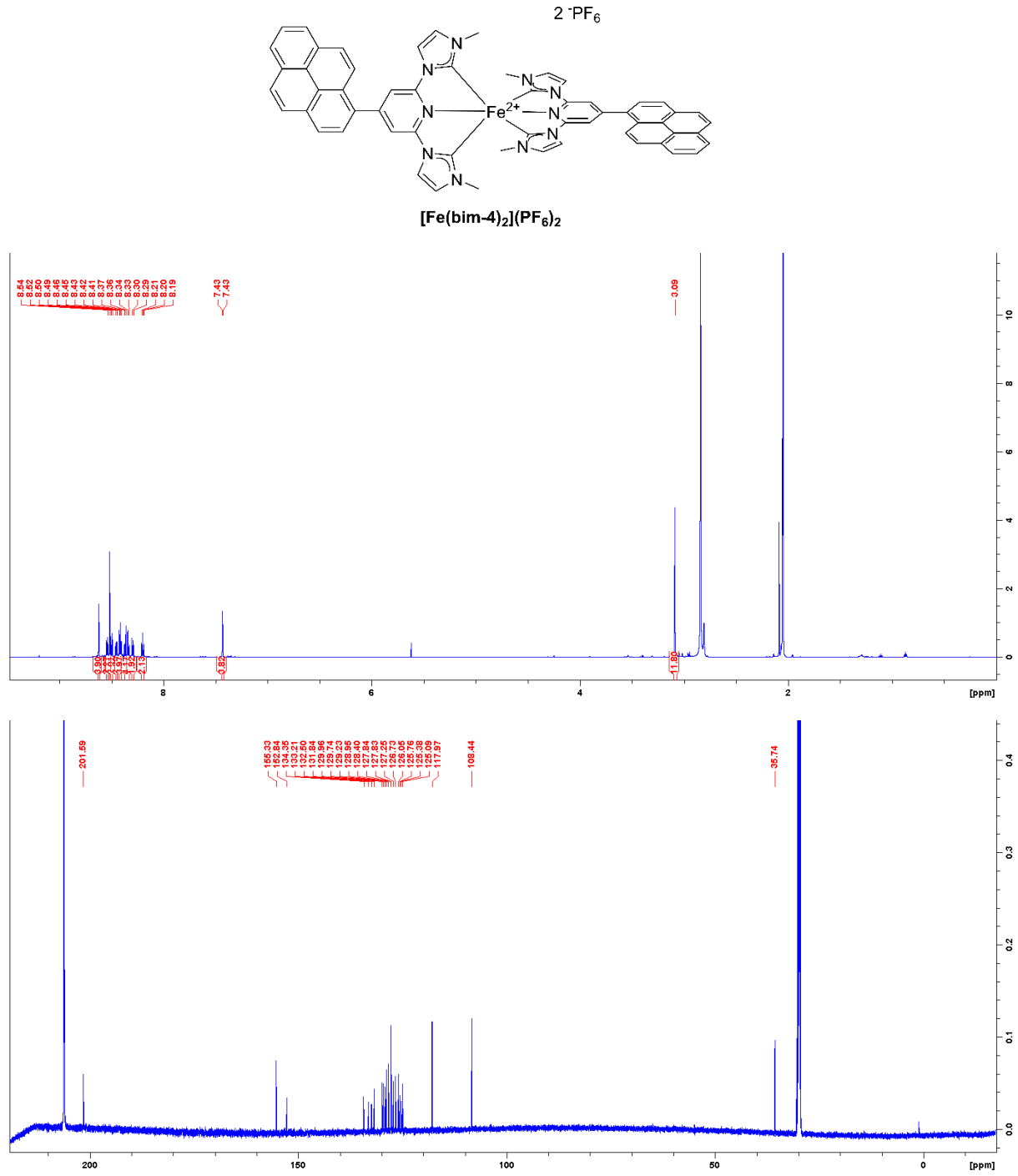

*Figure A 16: ^{1}H (top) and ^{13}C (bottom) NMR spectra of **[Fe(bim-4)$_2$]**$(PF_6)_2$ in d_6-acetone at 303 K.*

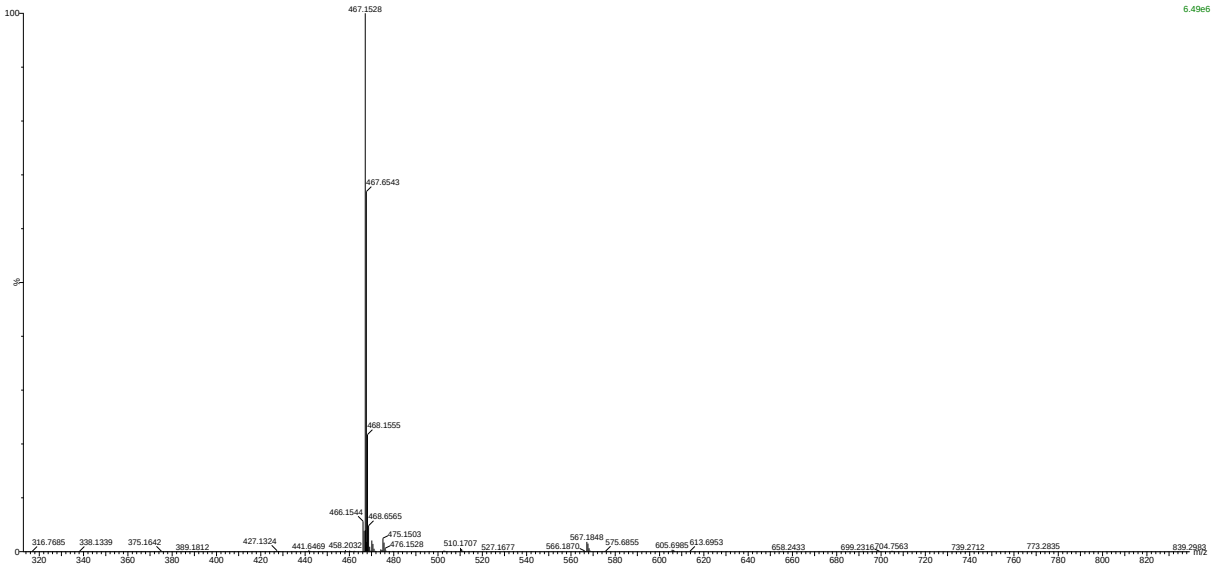

Figure A 17: ESI MS data of ***[Fe(bim-4)$_2$]***$(PF_6)_2$ *in MeCN.*

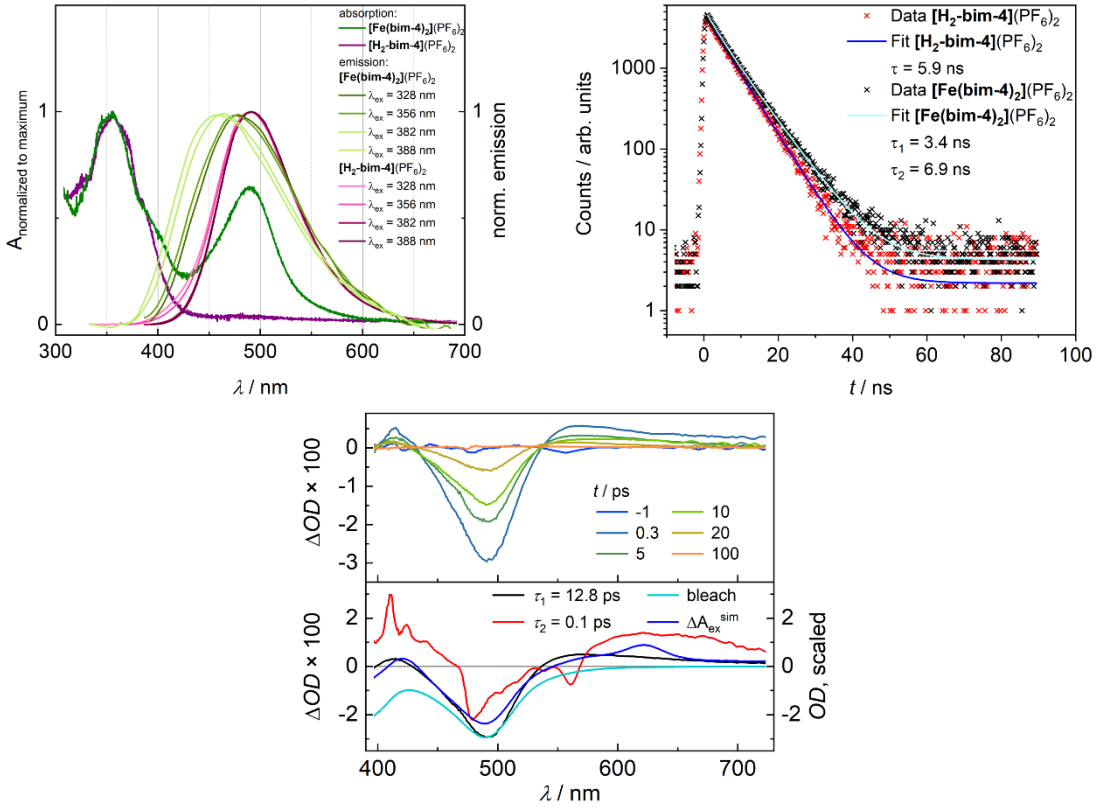

Figure A 18: Steady state absorption and emission spectroscopy (left panel), experimental data and analysis of time resolved emission spectroscopy performed by streak camera measurements (middle panel) and transient absorption and decay associated spectra including results of spectroelectrochemical experiments ΔA_{ex}^{sim} (right panel). These experimental data are shown for ***[H$_2$-bim-4]***$(PF_6)_2$ *and* ***[Fe(bim-4)$_2$]***$(PF_6)_2$.

Details on the quantum chemical calculations of **[Fe(bim-4)$_2$]**$(PF_6)_2$ can be found in the published data.

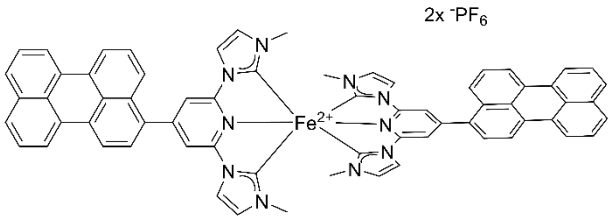

$[Fe(bim\text{-}5)_2](PF_6)_2$

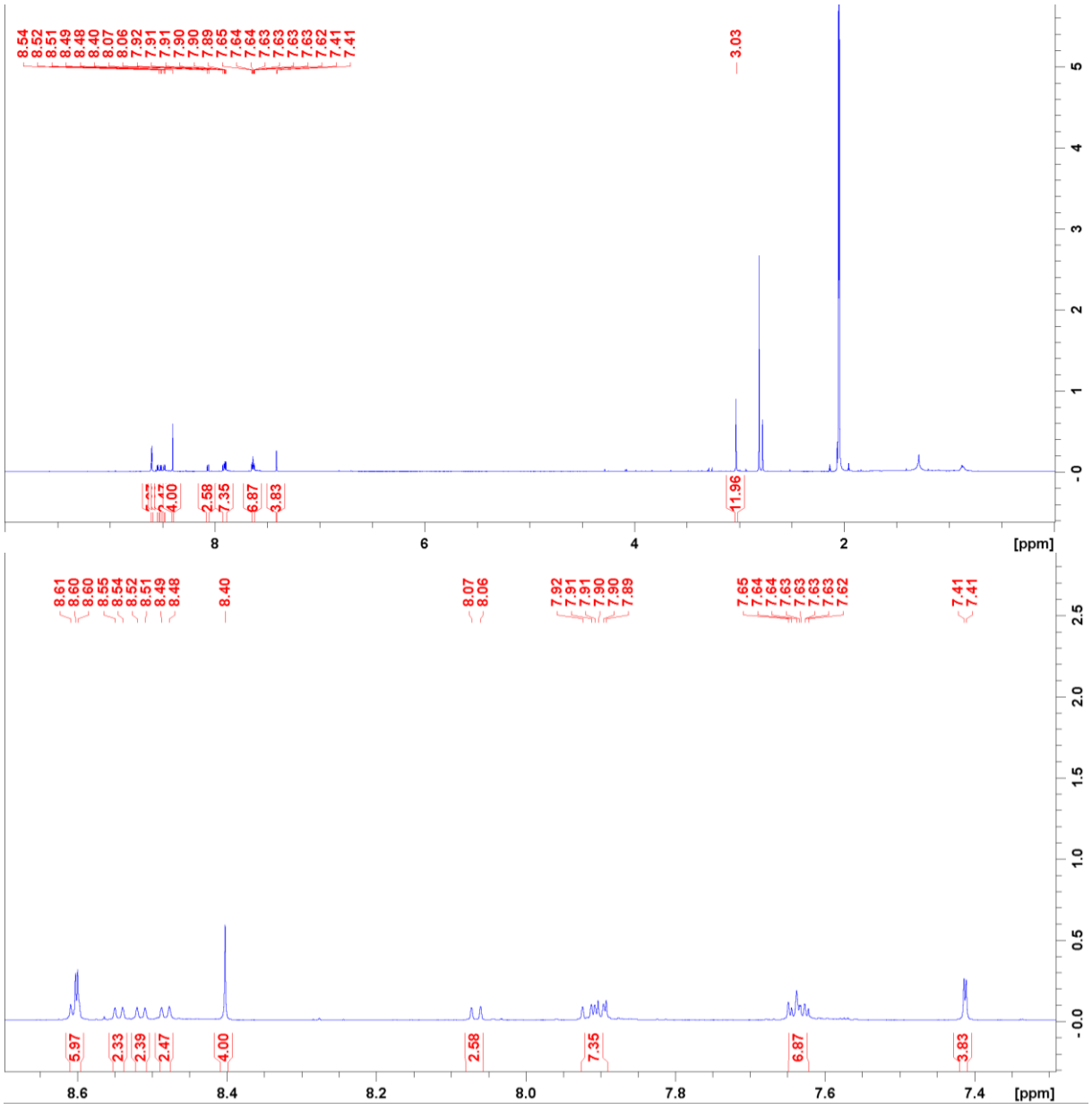

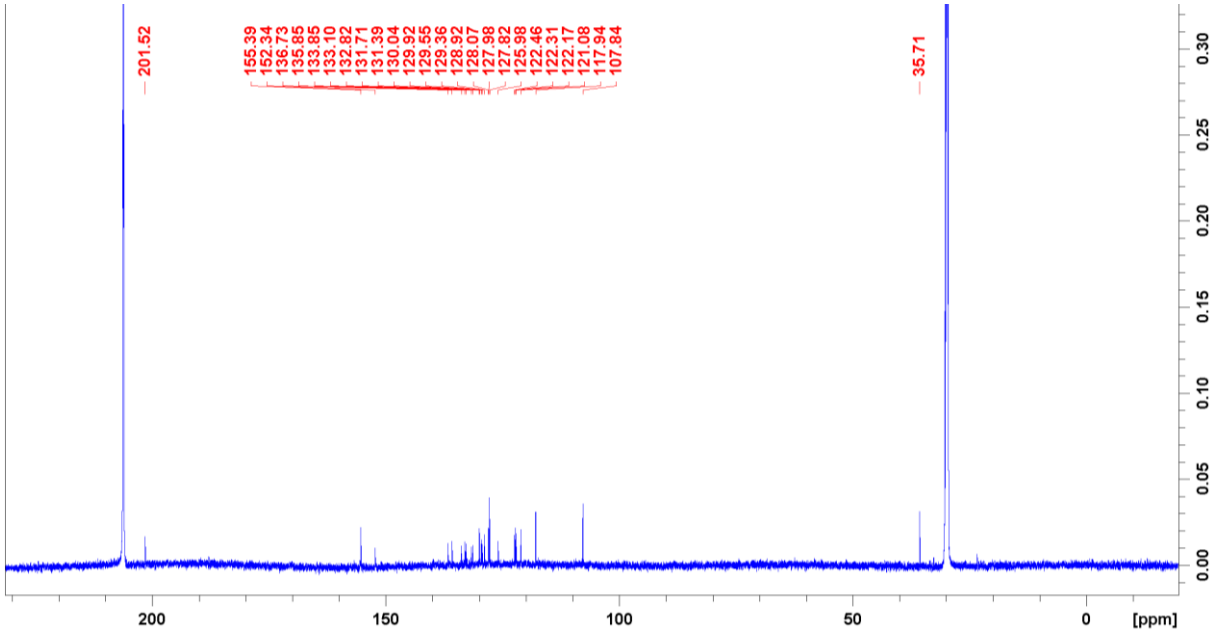

*Figure A 19: ^{1}H (top and middle) and ^{13}C (bottom) NMR spectra of **[Fe(bim-5)$_2$]**$(PF_6)_2$ in d_6-acetone at 303 K.*

*Figure A 20: ESI MS data of **[Fe(bim-5)$_2$]**$(PF_6)_2$ in MeCN.*

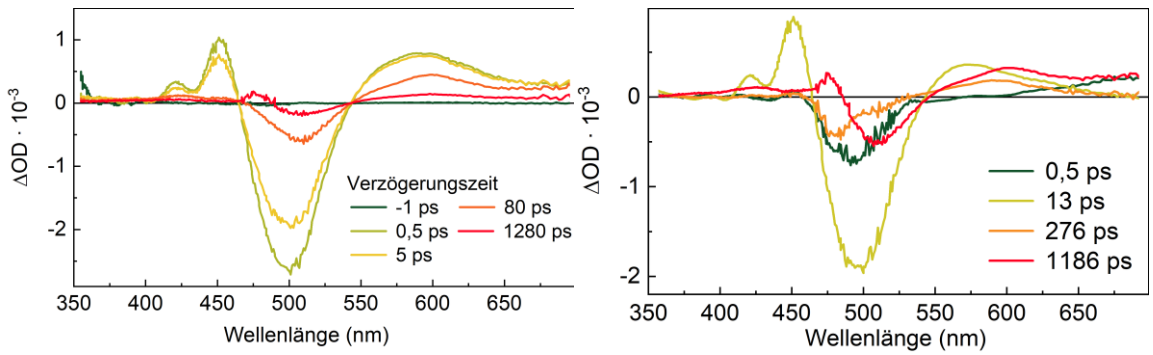

*Figure A 21: Transient absorption (left) and decay associated spectra (right) of **[Fe(bim-5)$_2$]**$(PF_6)_2$ in MeCN as recordedy by the group of Prof. Stefan Lochbrunner.*

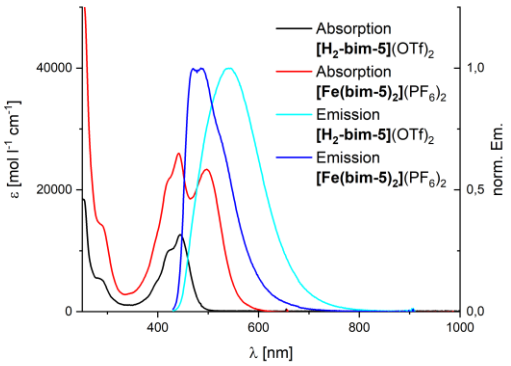

Figure A 22: Absorption and emission spectra of ***[Fe(bim-5)$_2$]***$(PF_6)_2$ *and* ***[H$_2$-bim-5]***$(OTf)_2$.

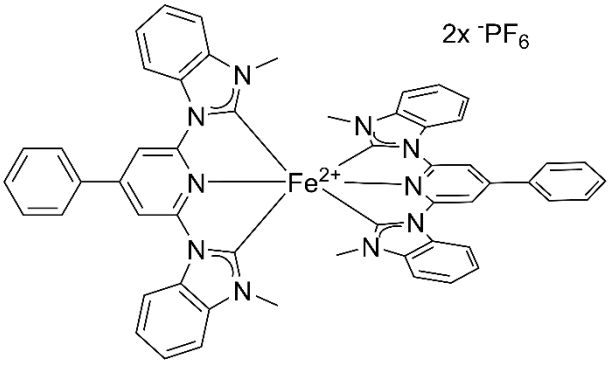

[Fe(bbp-1)$_2$](PF$_6$)$_2$

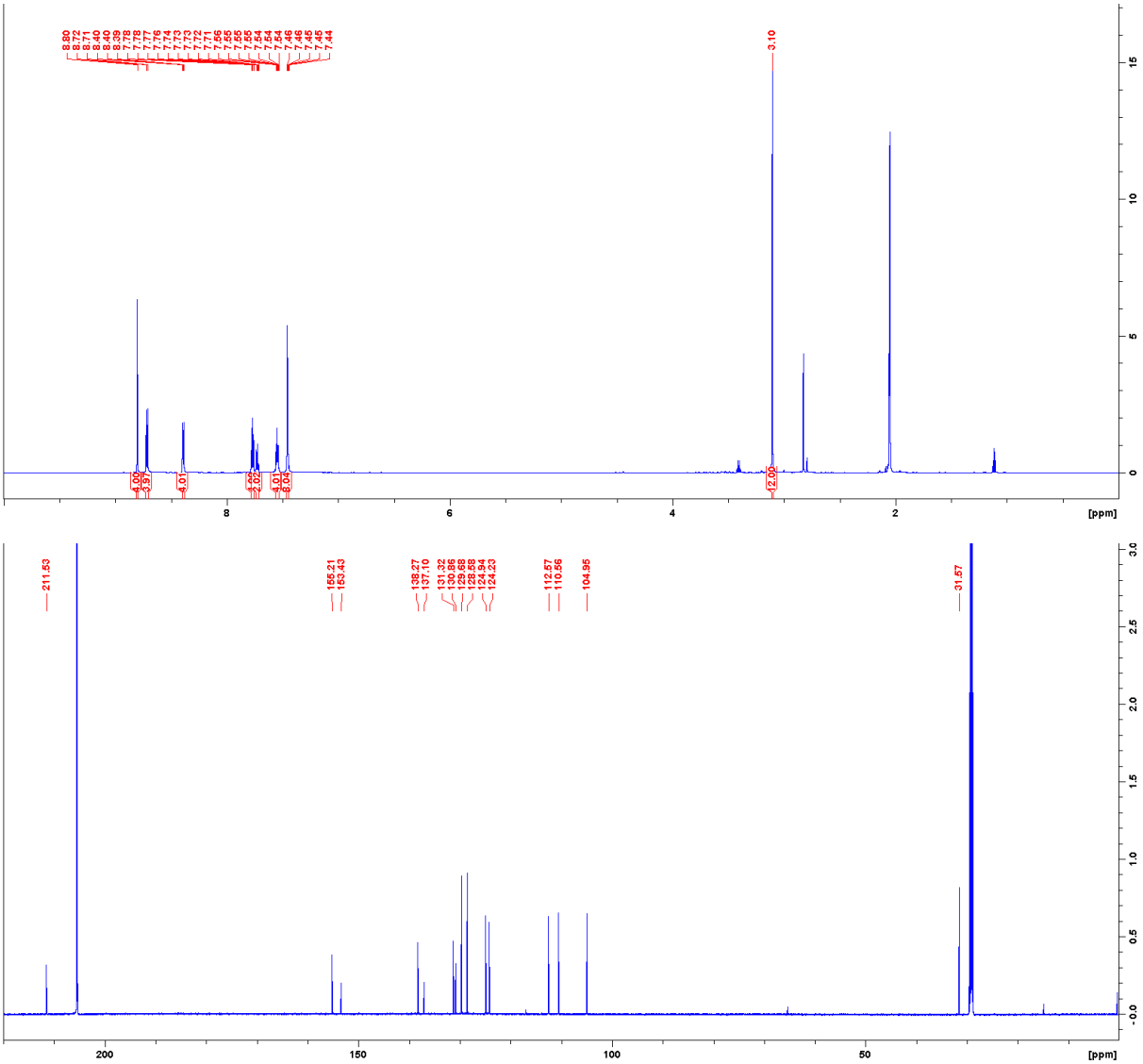

*Figure A 23: ^{1}H (top) and ^{13}C (bottom) NMR spectra of **[Fe(bbp-1)$_2$]**(PF$_6$)$_2$ in d$_6$-acetone at 303 K.*

Figure A 24: ESI MS data of ***[Fe(bbp-1)$_2$]***$(PF_6)_2$ *in MeCN.*

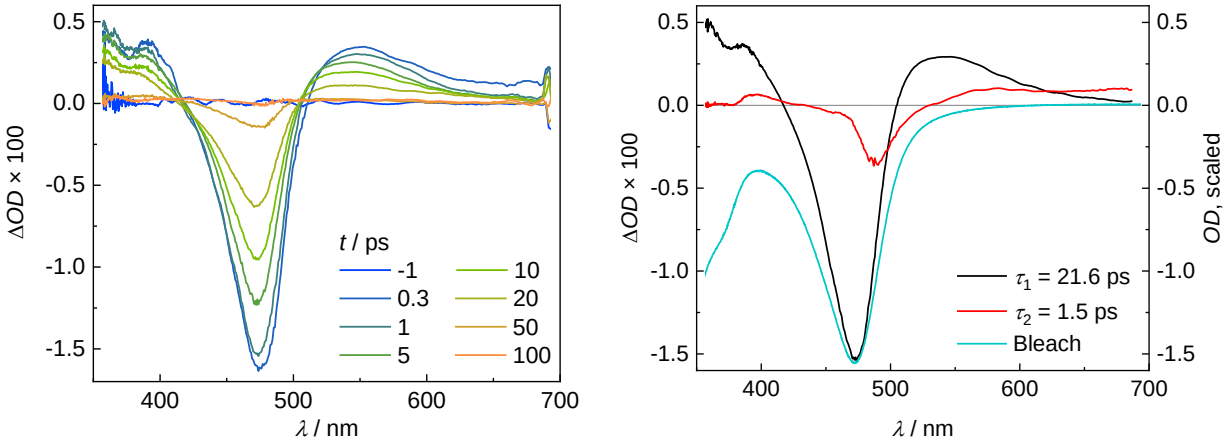

Figure A 25: Transient absorption (left) and decay associated spectra (right) of ***[Fe(bbp-1)$_2$]***$(PF_6)_2$ *in MeCN as recordedy by the group of Prof. Stefan Lochbrunner.*

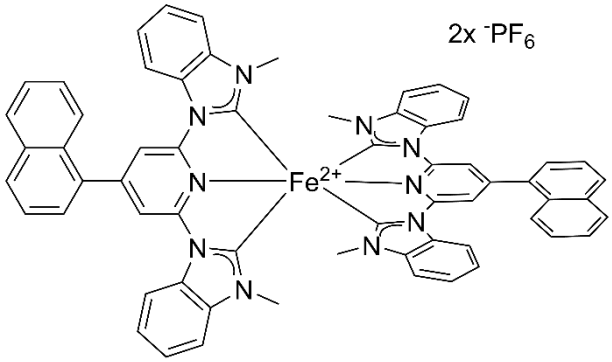

$[Fe(bbp\text{-}2)_2](PF_6)_2$

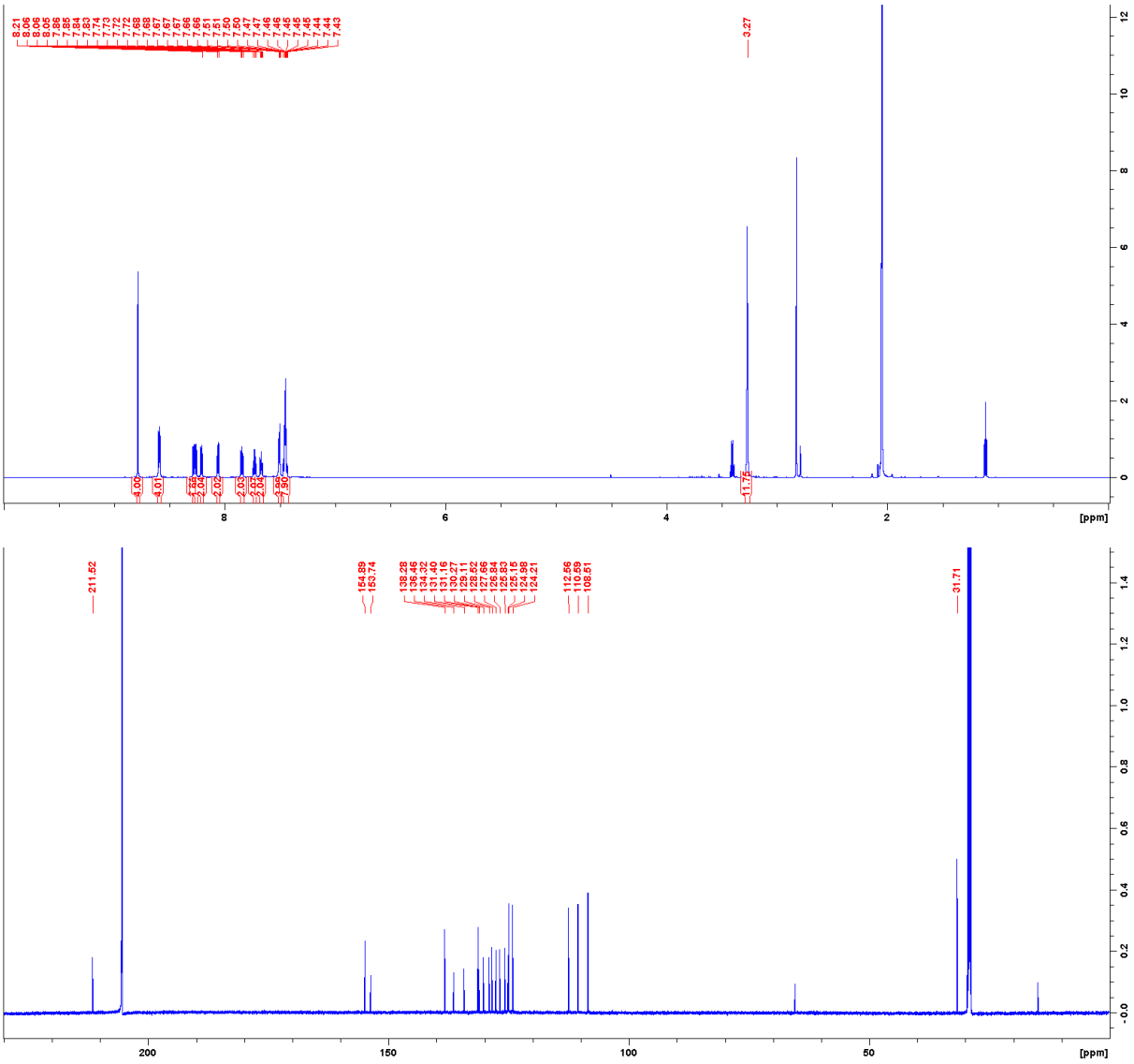

*Figure A 26: ^{1}H (top) and ^{13}C (bottom) NMR spectra of **$[Fe(bbp\text{-}2)_2]$**$(PF_6)_2$ in d_6-acetone at 303 K.*

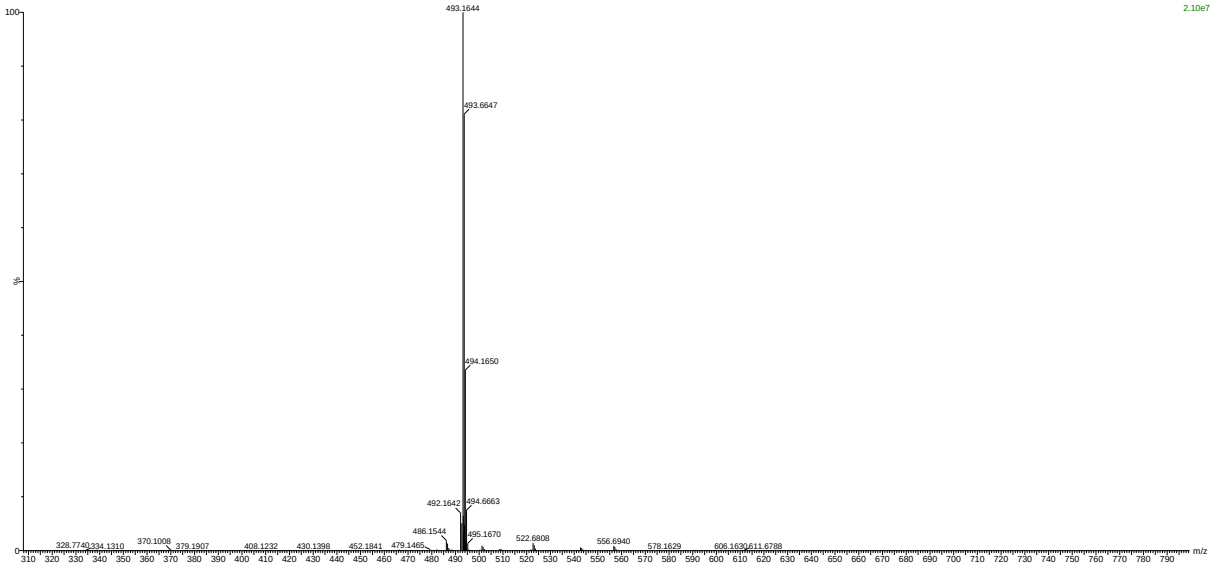

Figure A 27: ESI MS data of ***[Fe(bbp-2)$_2$]***$(PF_6)_2$ *in MeCN.*

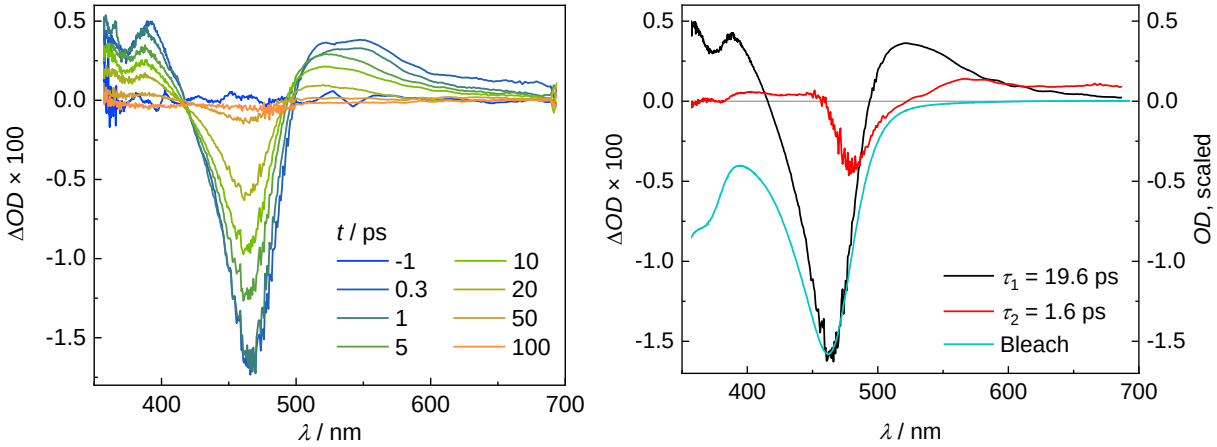

Figure A 28: Transient absorption (left) and decay associated spectra (right) of ***[Fe(bbp-2)$_2$]***$(PF_6)_2$ *in MeCN as recordedy by the group of Prof. Stefan Lochbrunner.*

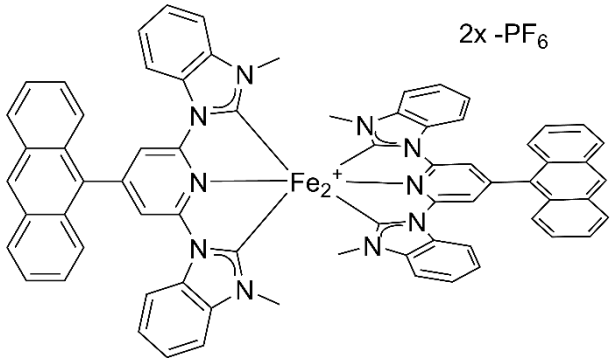

[Fe(bbp-3)$_2$](PF$_6$)$_2$

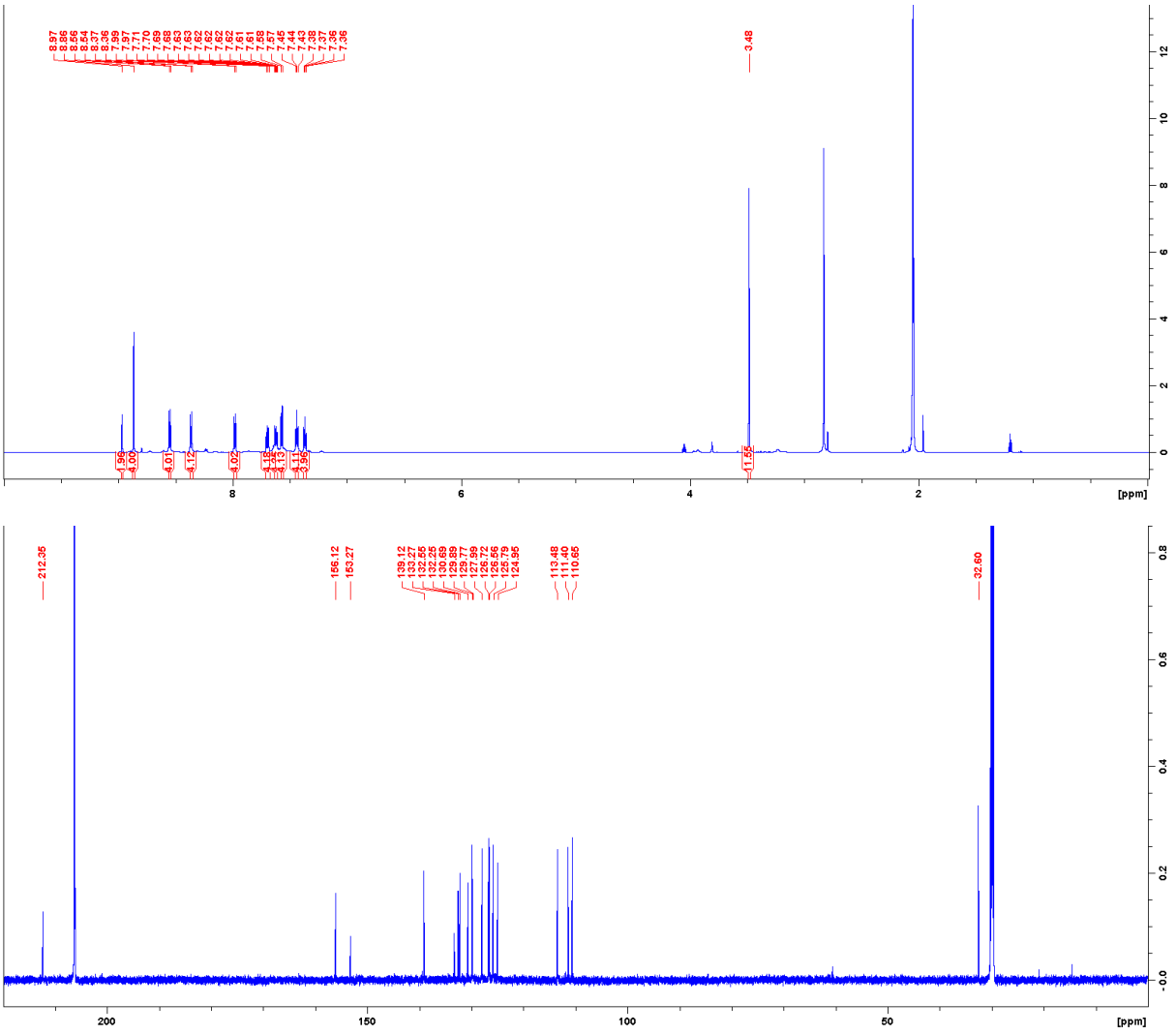

*Figure A 29: ^{1}H (top) and ^{13}C (bottom) NMR spectra of **[Fe(bbp-3)$_2$]**(PF$_6$)$_2$ in d$_6$-acetone at 303 K.*

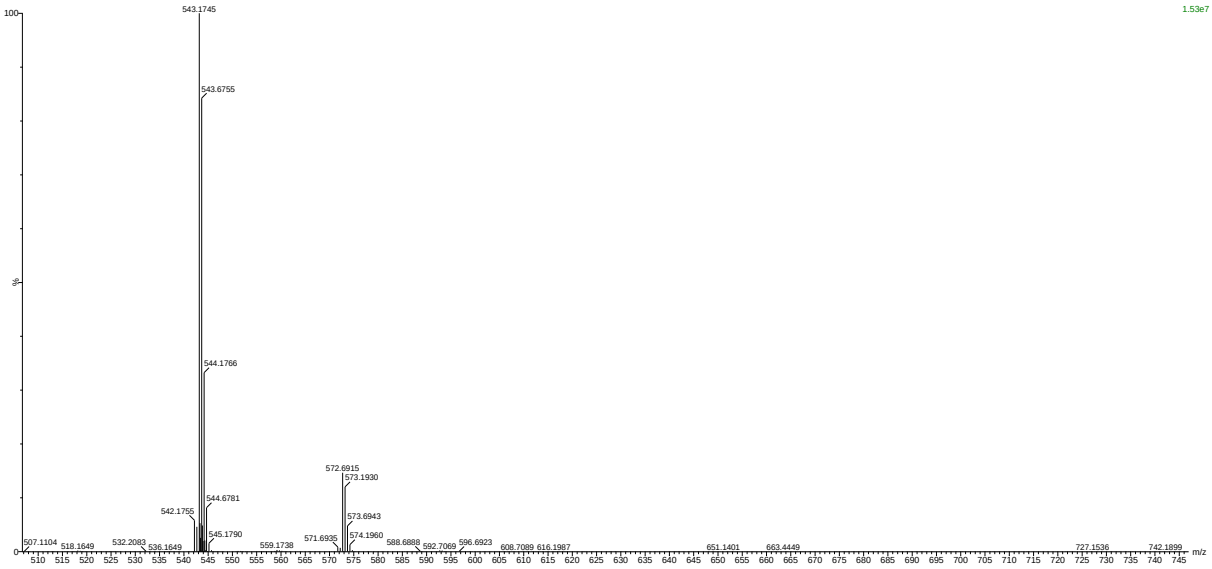

Figure A 30: ESI MS data of ***[Fe(bbp-3)$_2$]***$(PF_6)_2$ *in MeCN.*

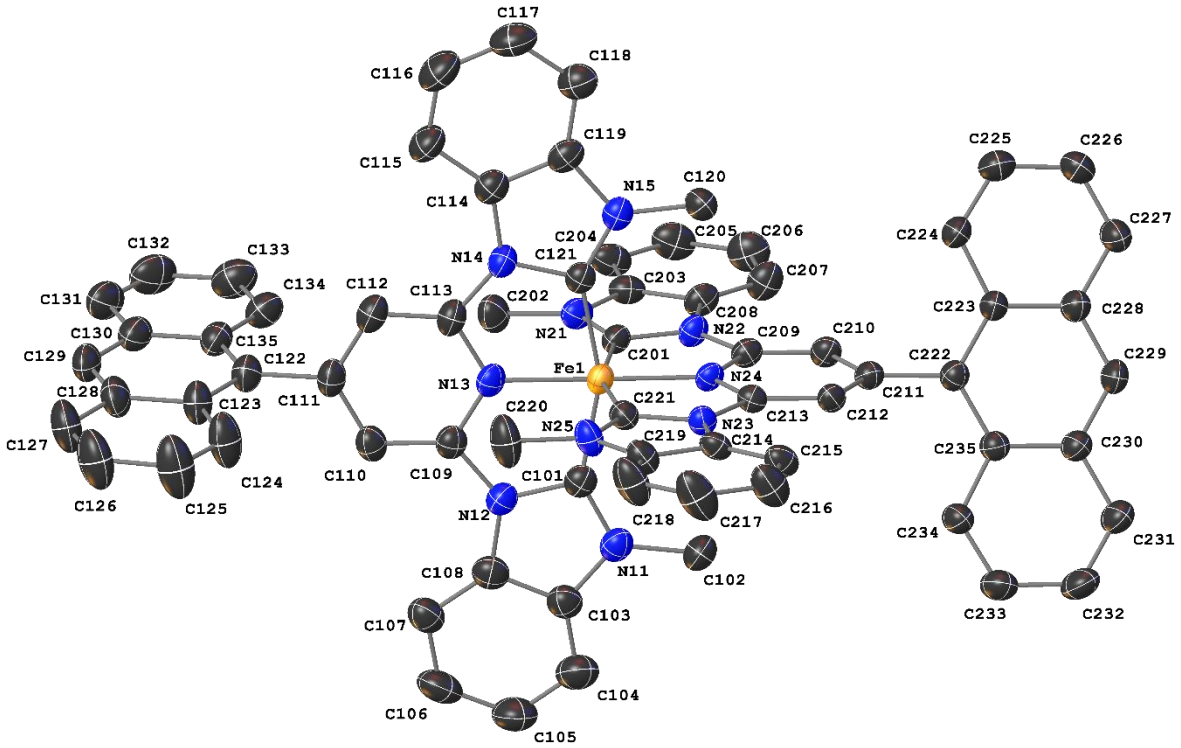

CCDC-No.	2160553
Empirical formula	C70 H50 N10 Fe, 2(P F6), 0.59(C4 H10 O), 0.67(C2 H3 N), 2[C4 H10 O]
Formula weight	1448.35
Temperature	120(2) K
Wavelength	0.71073 Å

Crystal system	Triclinic	
Space group	P-1	
Unit cell dimensions	a = 13.9083(16) Å	α= 111.175(3)°.
	b = 15.733(2) Å	β= 94.855(3)°.
	c = 19.420(2) Å	γ = 93.506(3)°.
Volume	3929.0(8) $Å^3$	
Z	2	
Density (calculated)	1.224 Mg/m^3	
Absorption coefficient	0.307 mm^{-1}	
F(000)	1487	
Crystal size	0.280 x 0.180 x 0.100 mm^3	
Theta range for data collection	1.929 to 26.583°.	
Index ranges	-17<=h<=17, -19<=k<=19, -24<=l<=24	
Reflections collected	280936	
Independent reflections	16204 [R(int) = 0.0946]	
Completeness to theta = 25.242°	99.5 %	
Absorption correction	Semi-empirical from equivalents	
Refinement method	Full-matrix least-squares on F^2	
Data / restraints / parameters	16204 / 0 / 982	
Goodness-of-fit on F^2	1.092	
Final R indices [I>2sigma(I)]	R1 = 0.1020, wR2 = 0.2530	
R indices (all data)	R1 = 0.1296, wR2 = 0.2740	
Extinction coefficient	n/a	
Largest diff. peak and hole	2.329 and -0.537 $e.Å^{-3}$	

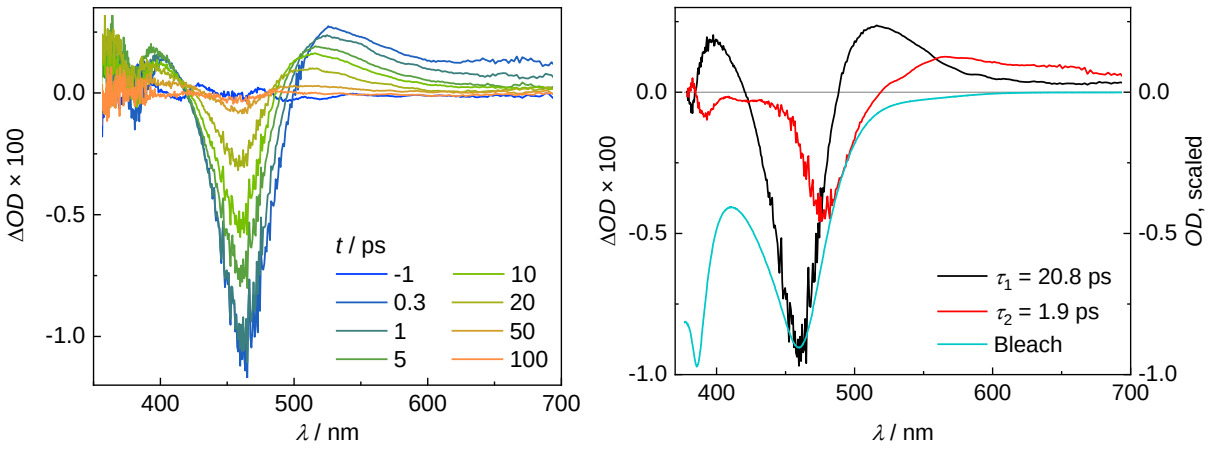

Figure A 31: Transient absorption (left) and decay associated spectra (right) of ***[Fe(bbp-3)$_2$]***$(PF_6)_2$ *in MeCN as recordedy by the group of Prof. Stefan Lochbrunner.*

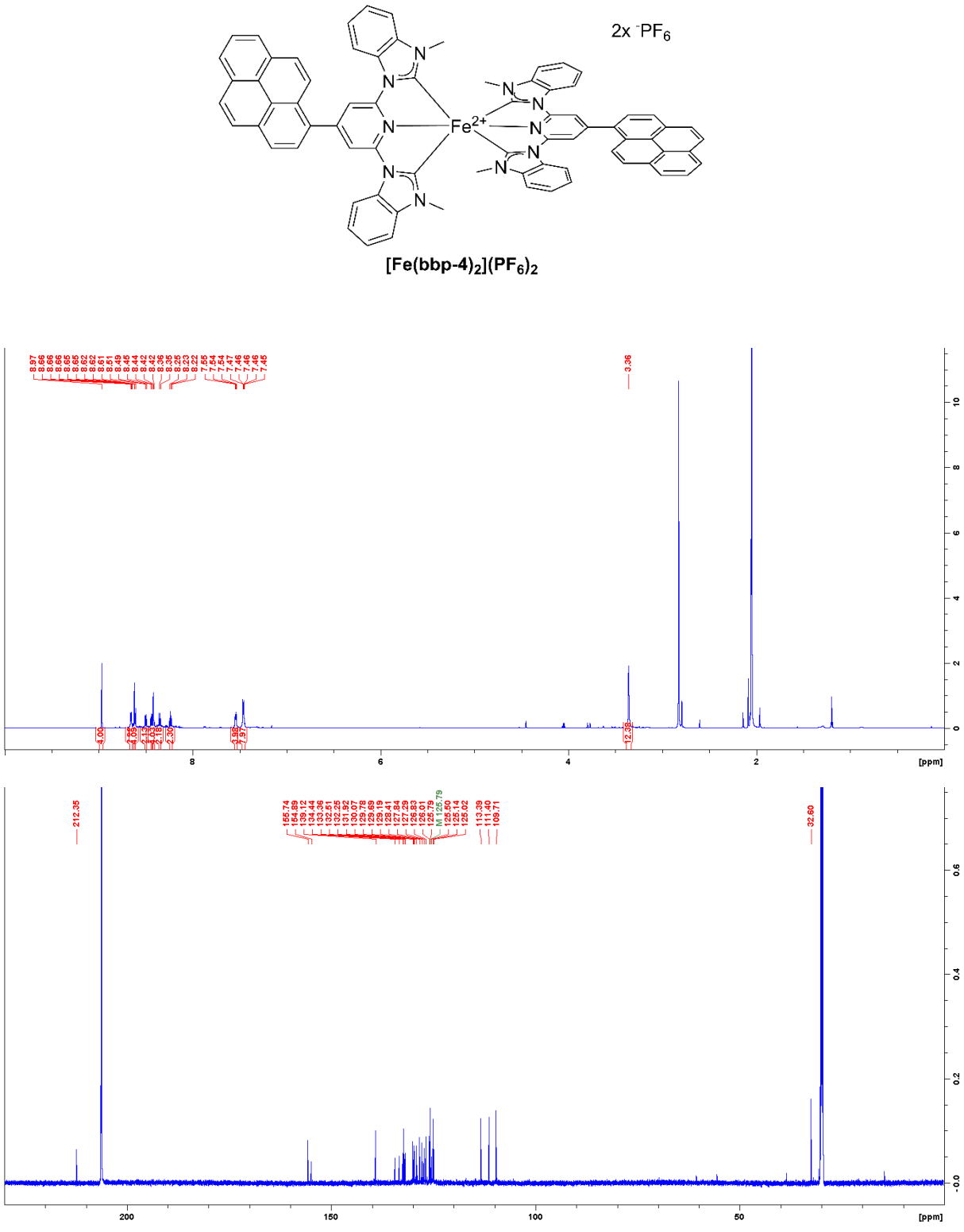

Figure A 32: ^{1}H (top) and ^{13}C (bottom) NMR spectra of ***[Fe(bbp-4)$_2$]***$(PF_6)_2$ *in* d_6*-acetone at 303 K.*

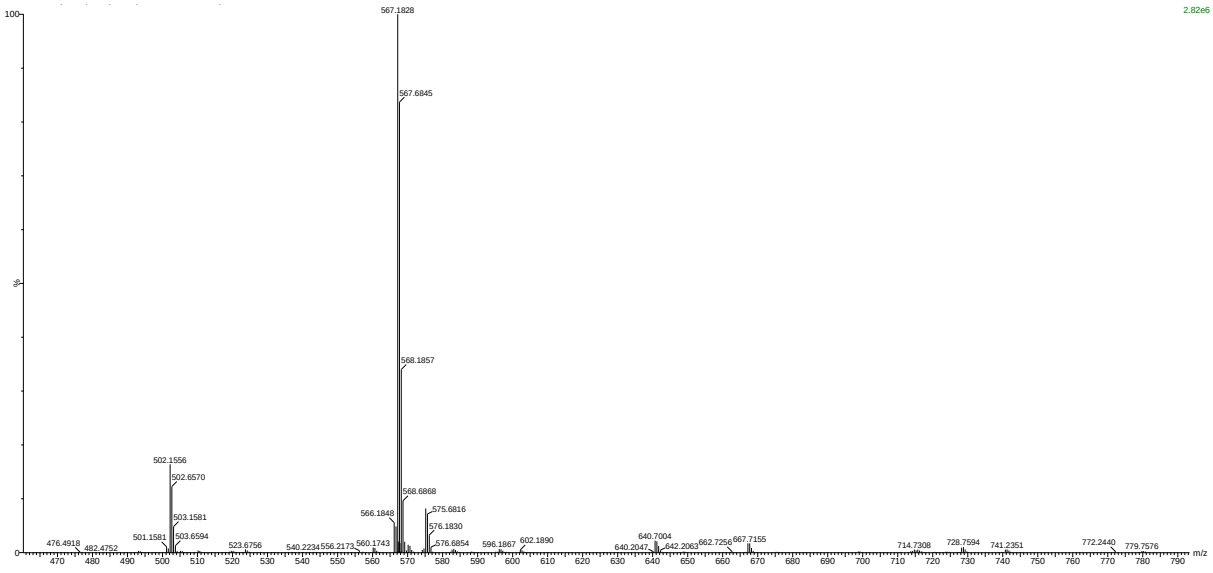

Figure A 33: ESI MS data of ***[Fe(bbp-4)$_2$]***$(PF_6)_2$ *in MeCN.*

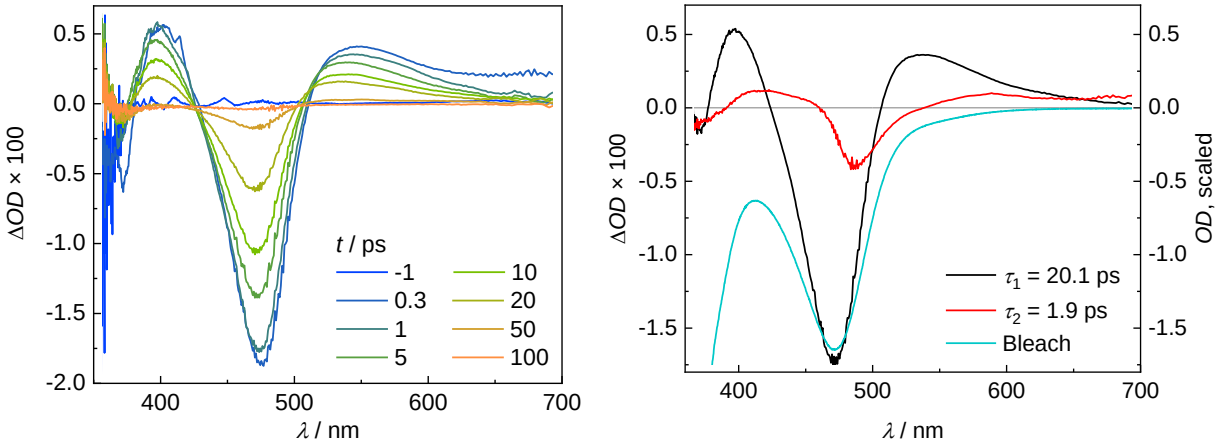

Figure A 34: Transient absorption (left) and decay associated spectra (right) of ***[Fe(bbp-4)$_2$]***$(PF_6)_2$ *in MeCN as recordedy by the group of Prof. Stefan Lochbrunner.*

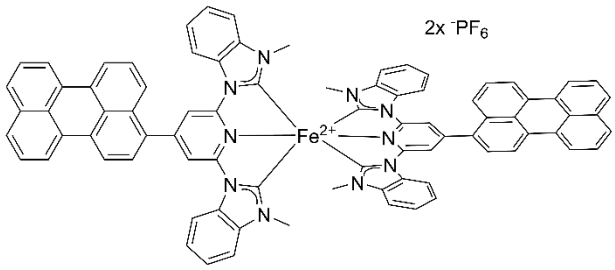

$[Fe(bbp\text{-}5)_2](PF_6)_2$

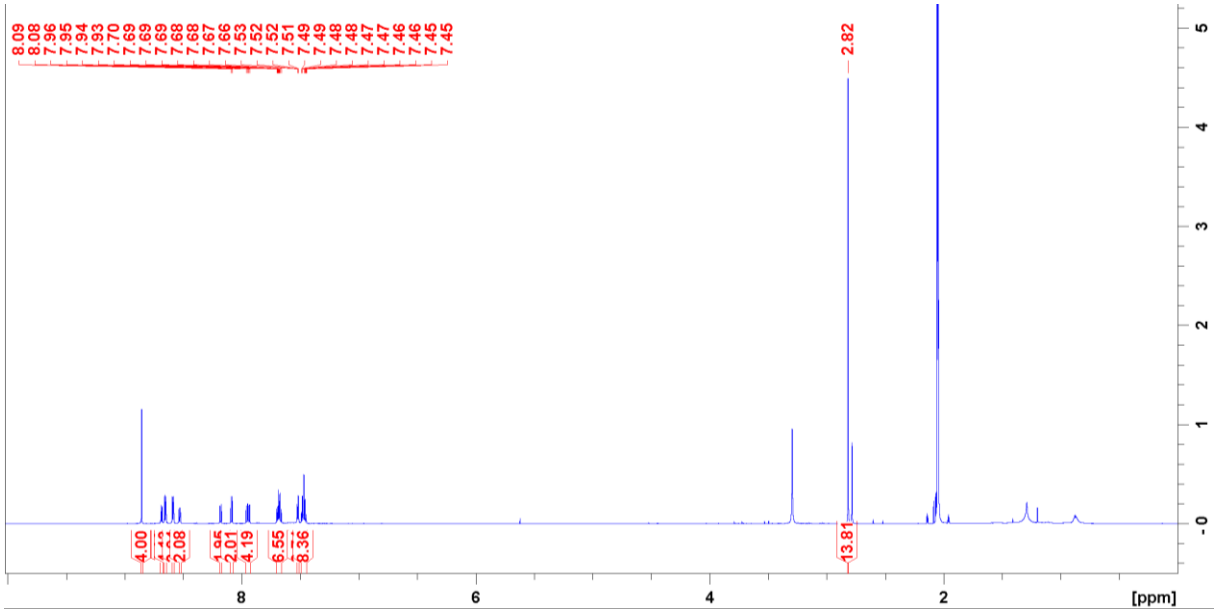

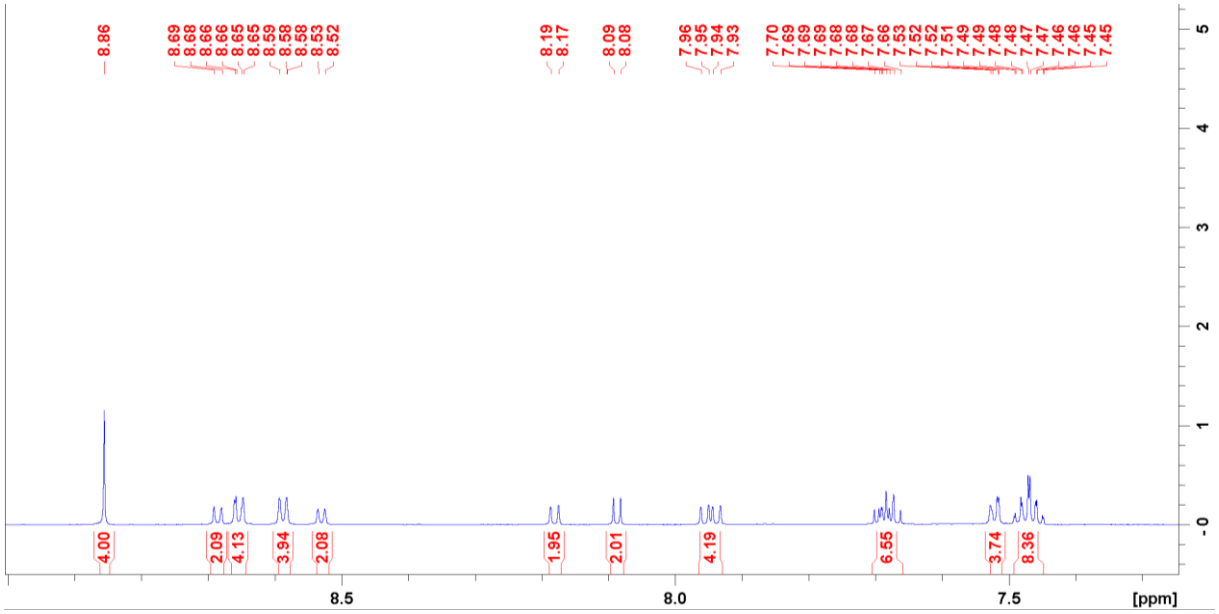

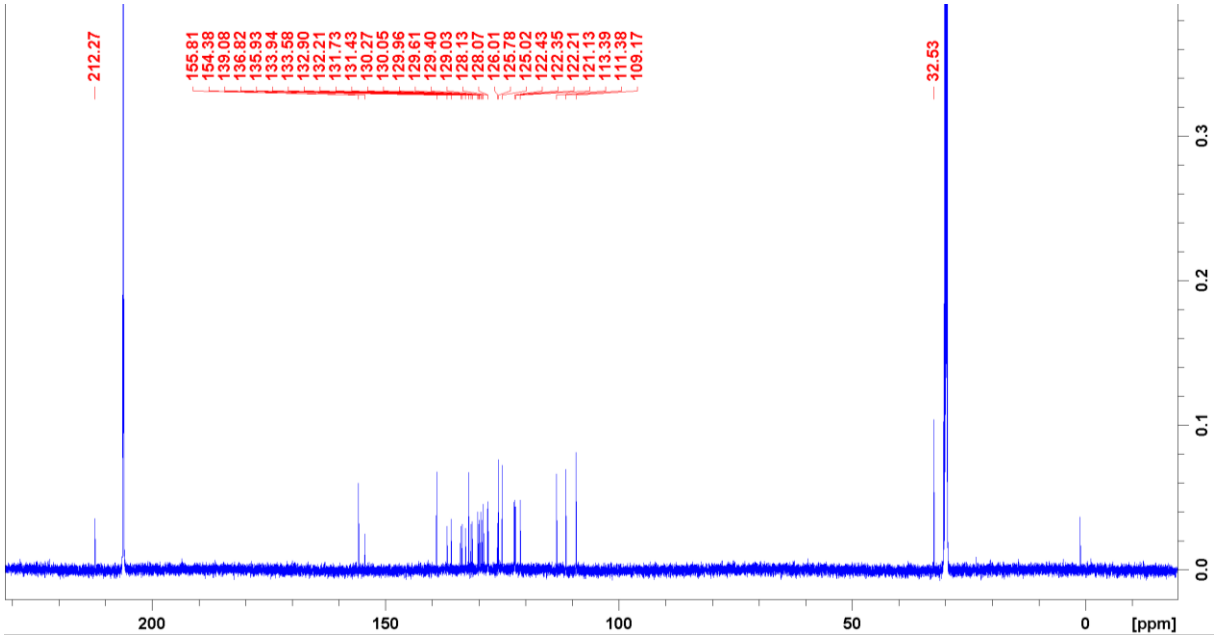

*Figure A 35: ^{1}H (top and middle) and ^{13}C (bottom) NMR spectra of **[Fe(bbp-5)$_2$]**$(PF_6)_2$ in d_6-acetone at 303 K.*

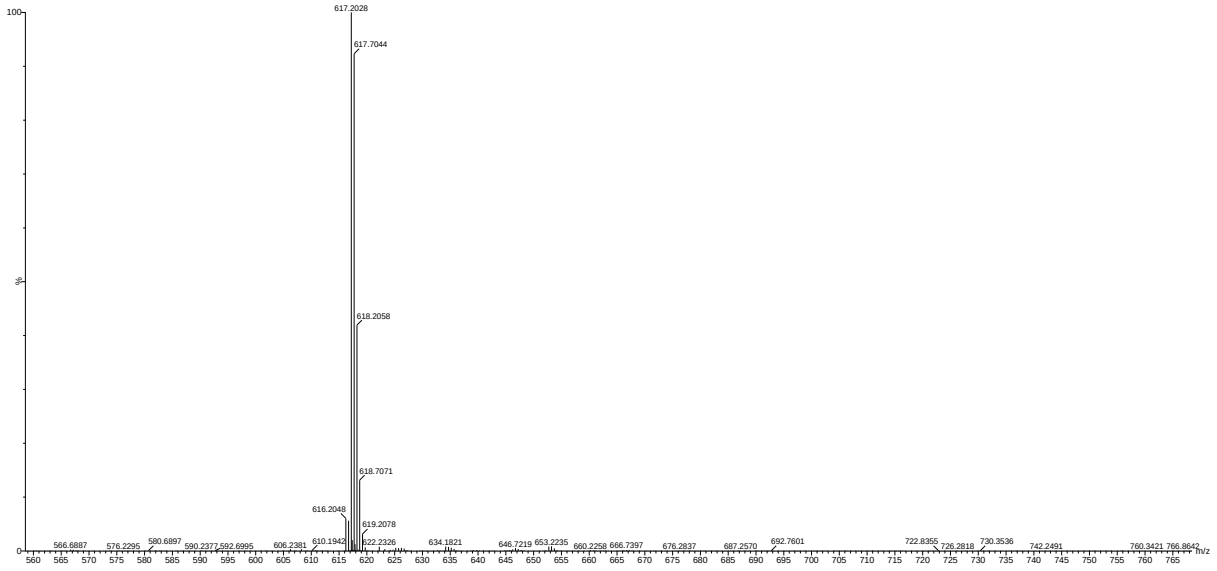

*Figure A 36: ESI MS data of **[Fe(bbp-5)$_2$]**$(PF_6)_2$ in MeCN.*

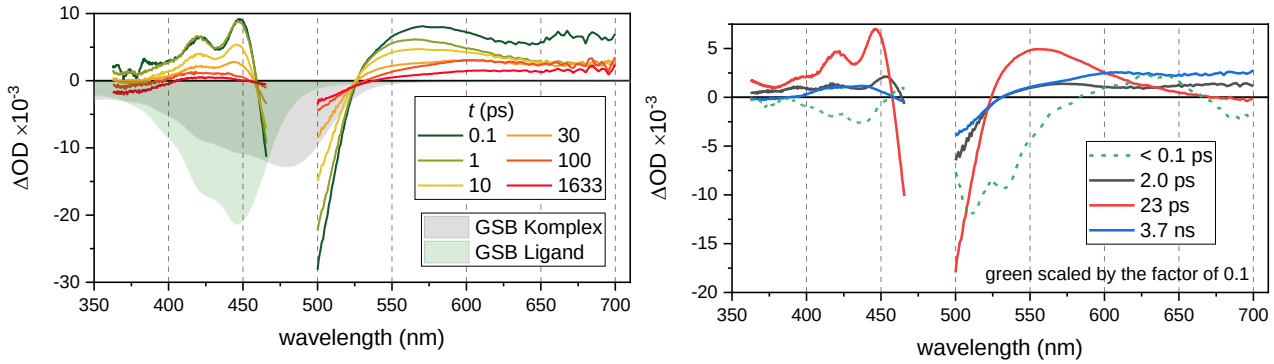

*Figure A 37: Transient absorption (left) and decay associated spectra (right) of **[Fe(bbp-5)$_2$]**$(PF_6)_2$ in MeCN as recordedy by the group of Prof. Stefan Lochbrunner.*

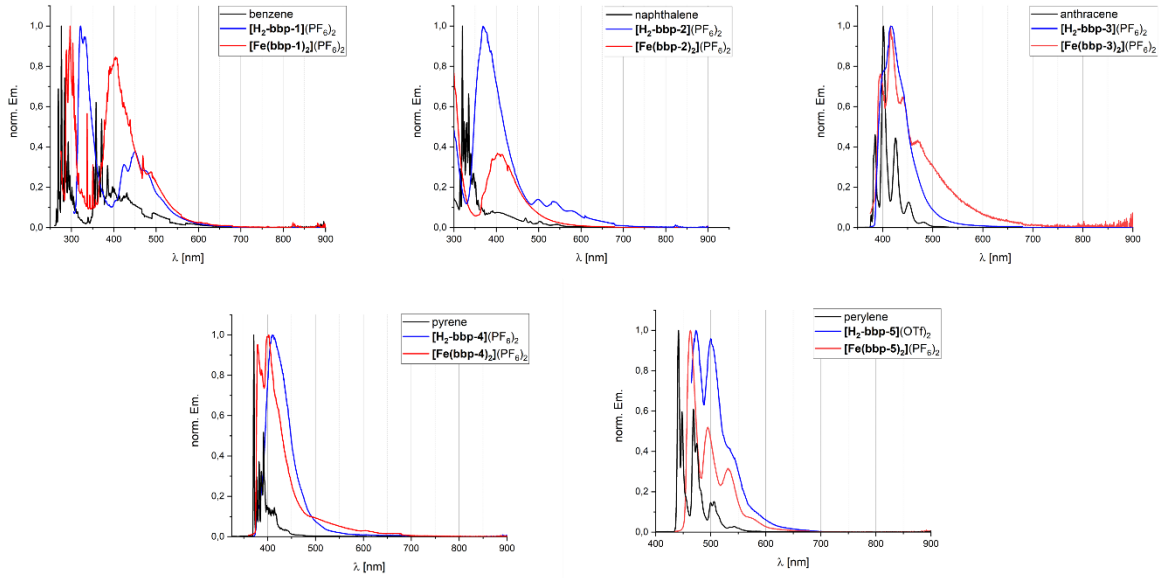

Figure A 38: Emission spectra of all ***[Fe(bbp-R)$_2$]$^{2+}$*** *type complexes and the backbone chromophor*

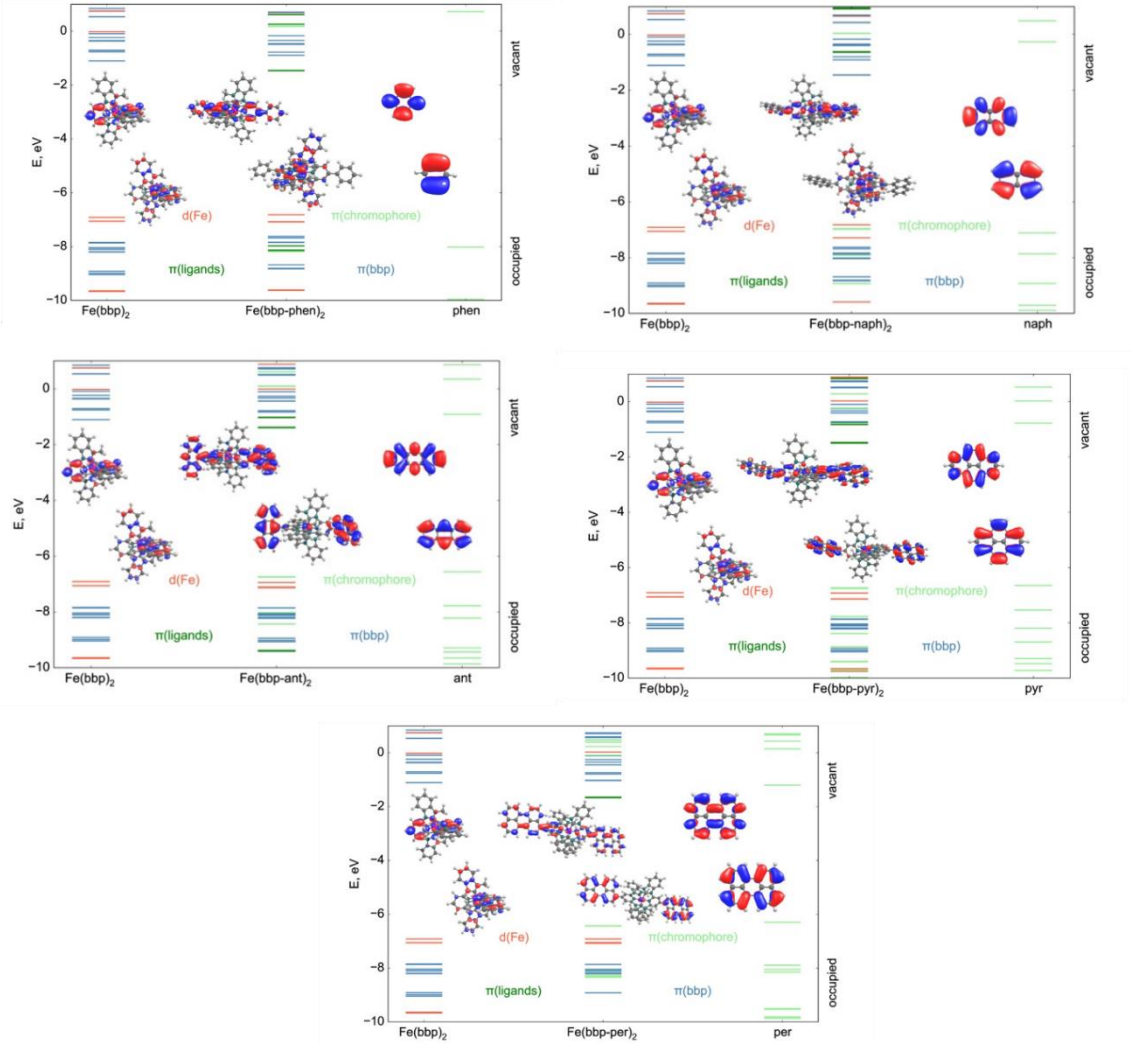

Figure A 39: Molecular orbital scheme of all ***[Fe(bbp-R)$_2$]$^{2+}$*** *type complexes (left) compared to the orbitals of fragments (right). The localization of orbitals is shown with different color code. The shapes of all HOMO and LUMO orbitals are shown as insets. Calculations of the fragments further lead to the triplet energies of the chromophores discussed in the main sections.*

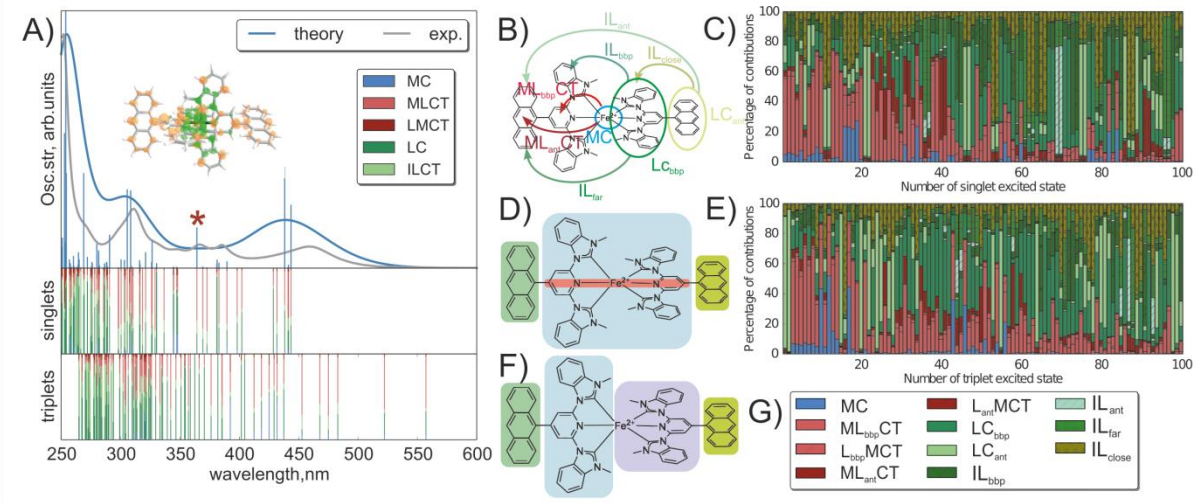

Figure A 40: Absorption spectra of ***[Fe(bbp-3)$_2$]$^{2+}$*** *compared to the experimental data (A). In the two lower panels of A), the transitional density-matrix analysis of TDDFT transitions of singlet and triplet excitation are shown versus the relative energetic position, the color code is given as inset. The part B presents the partitioning of a supermolecule into fragments for TDDFT analysis shown in panels C) and E), the color code is given in G). The inset of A) shows the transition density difference of the long-range MLCT (marked with an asterisk), the green color corresponds to the hole and orange to the particle (isovalue of the surface = 0.0002). Panels D) and F) present the results of clustering analysis performed for singlets and triplets, respectively.*

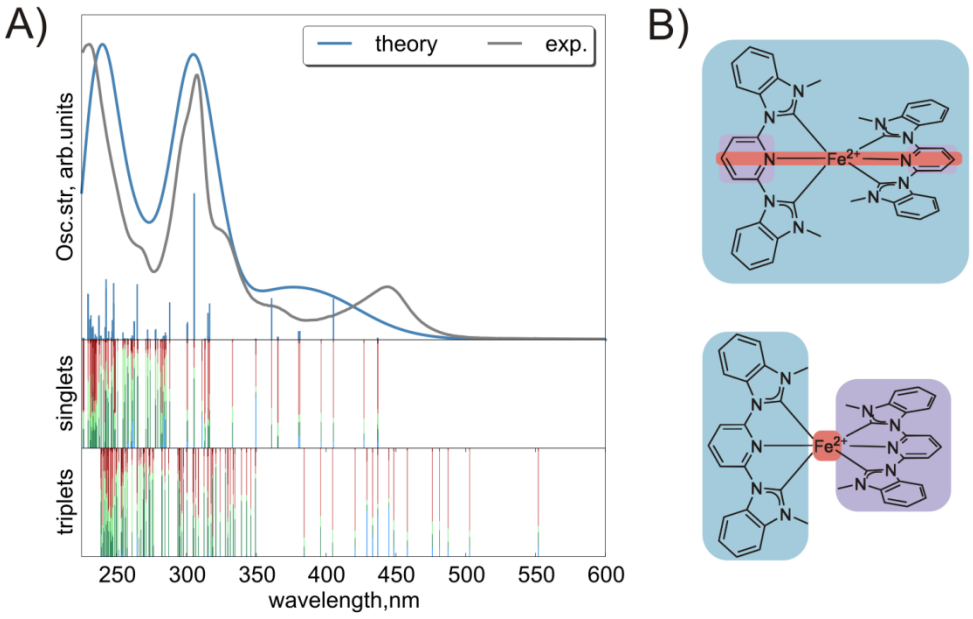

Figure A 41: Computed absorption spectrum of ***[Fe(bbp)$_2$]$^{2+}$*** *as well assignment and fragmentation according to the clustering analysis (the color code is the same as in the figure above).*

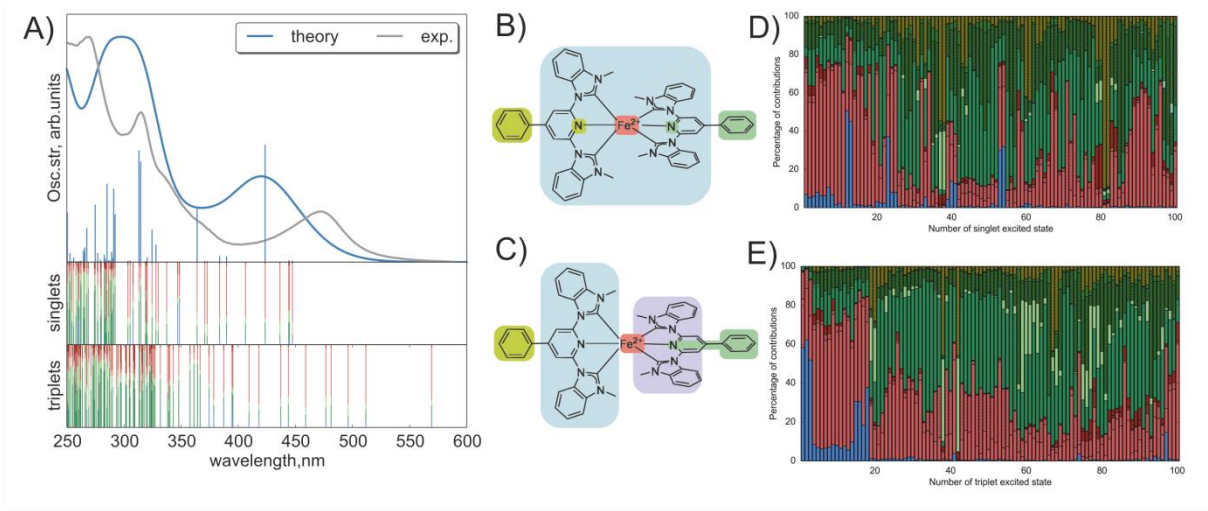

Figure A 42: Computed absorption spectrum of ***[Fe(bbp-1)$_2$]$^{2+}$*** *as well assignment and fragmentation according to the clustering analysis (the color code is the same as in the figure above).*

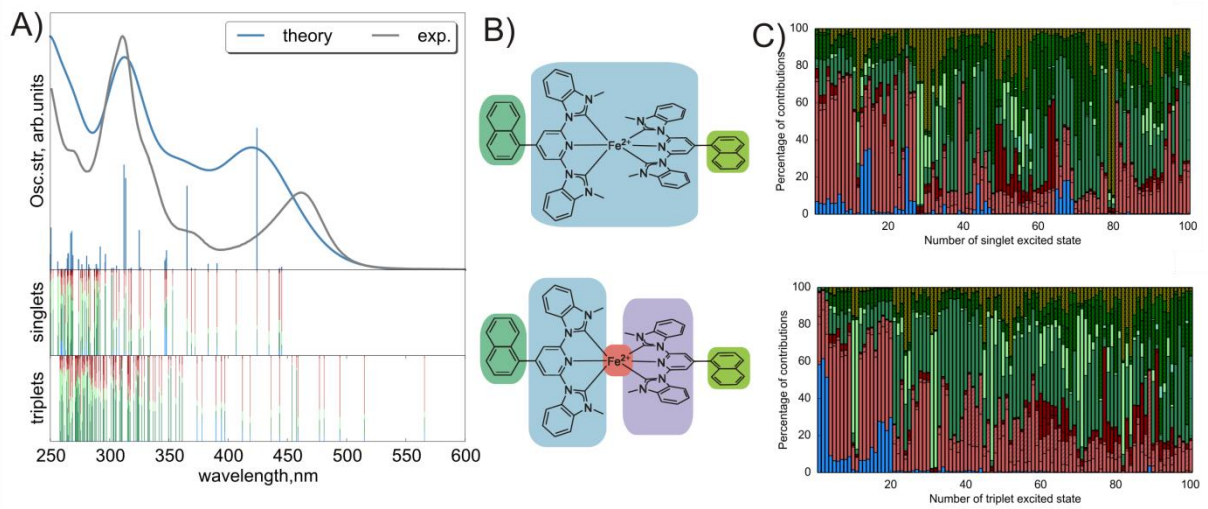

Figure A 43: Computed absorption spectrum of ***[Fe(bbp-2)$_2$]$^{2+}$*** *as well assignment and fragmentation according to the clustering analysis (the color code is the same as in the figure above).*

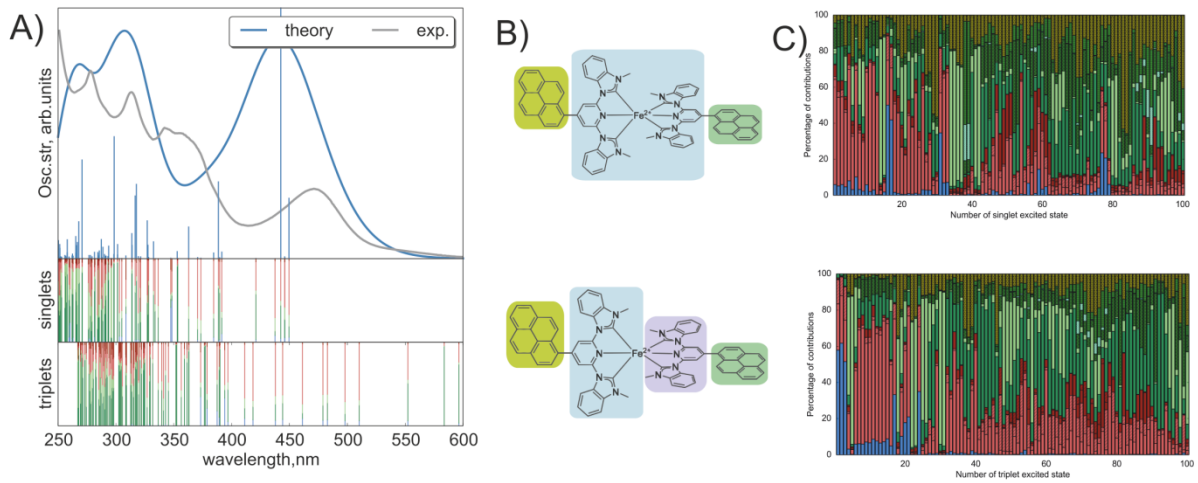

Figure A 44: Computed absorption spectrum of ***[Fe(bbp-4)$_2$]$^{2+}$*** *as well assignment and fragmentation according to the clustering analysis (the color code is the same as in the figure above).*

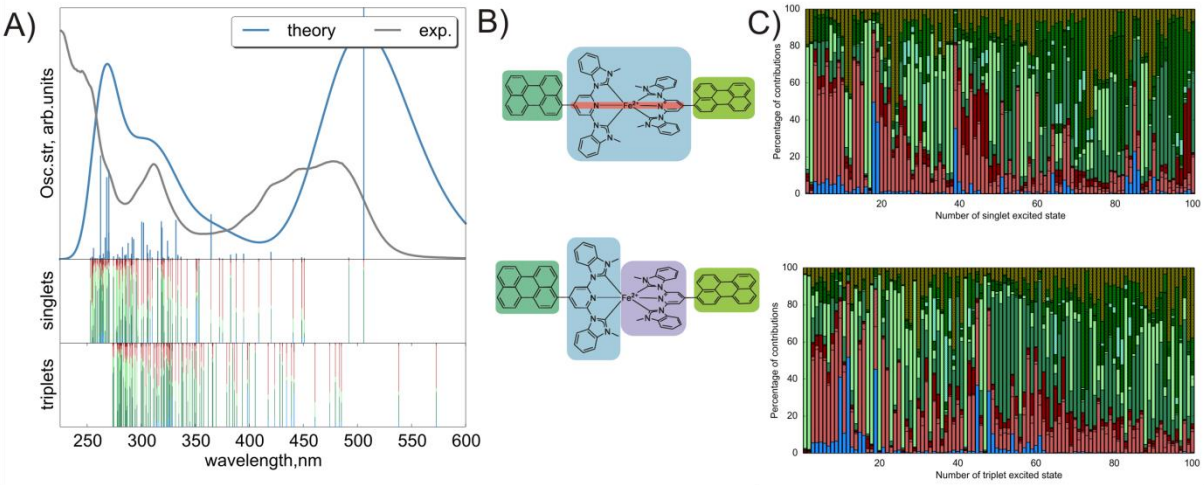

Figure A 45: Computed absorption spectrum of ***[Fe(bbp-5)$_2$]$^{2+}$*** *as well assignment and fragmentation according to the clustering analysis (the color code is the same as in the figure above).*

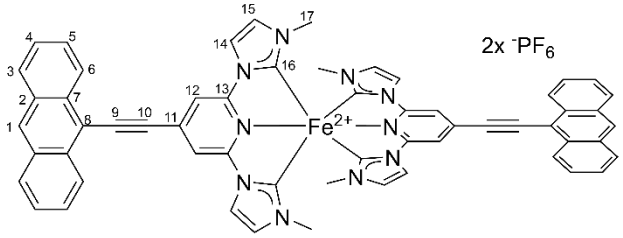

[Fe(bim-ac-3)$_2$](PF_6)$_2$

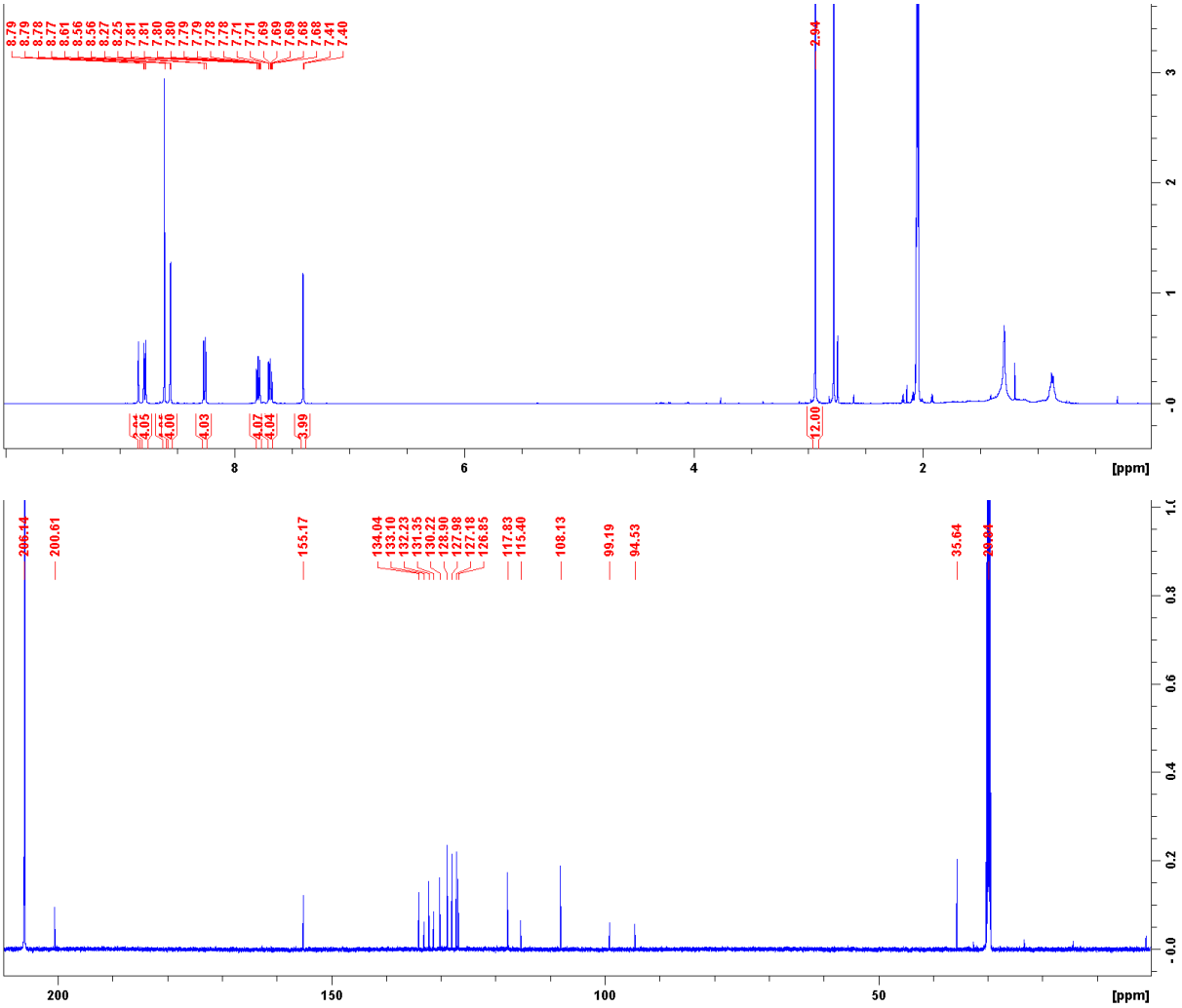

*Figure A 46: ^{1}H (top) and ^{13}C (bottom) NMR spectra of **[Fe(bim-ac-3)$_2$]**(PF_6)$_2$ in d_6-acetone at 303 K.*

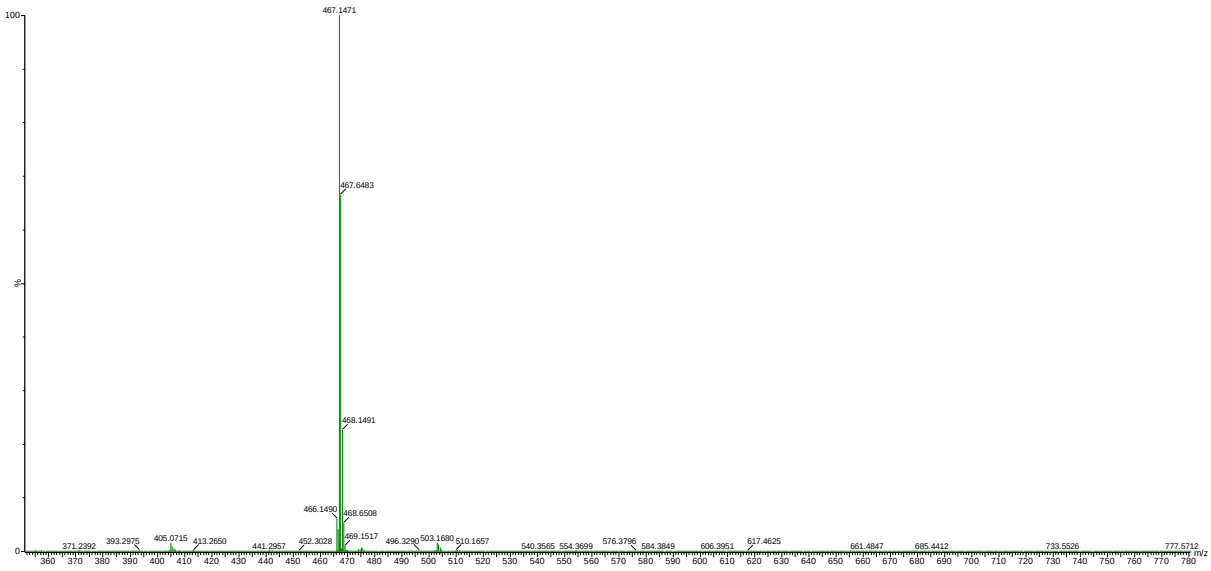

Figure A 47: ESI MS data of ***[Fe(bim-ac-3)$_2$]***$(PF_6)_2$ *in MeCN.*

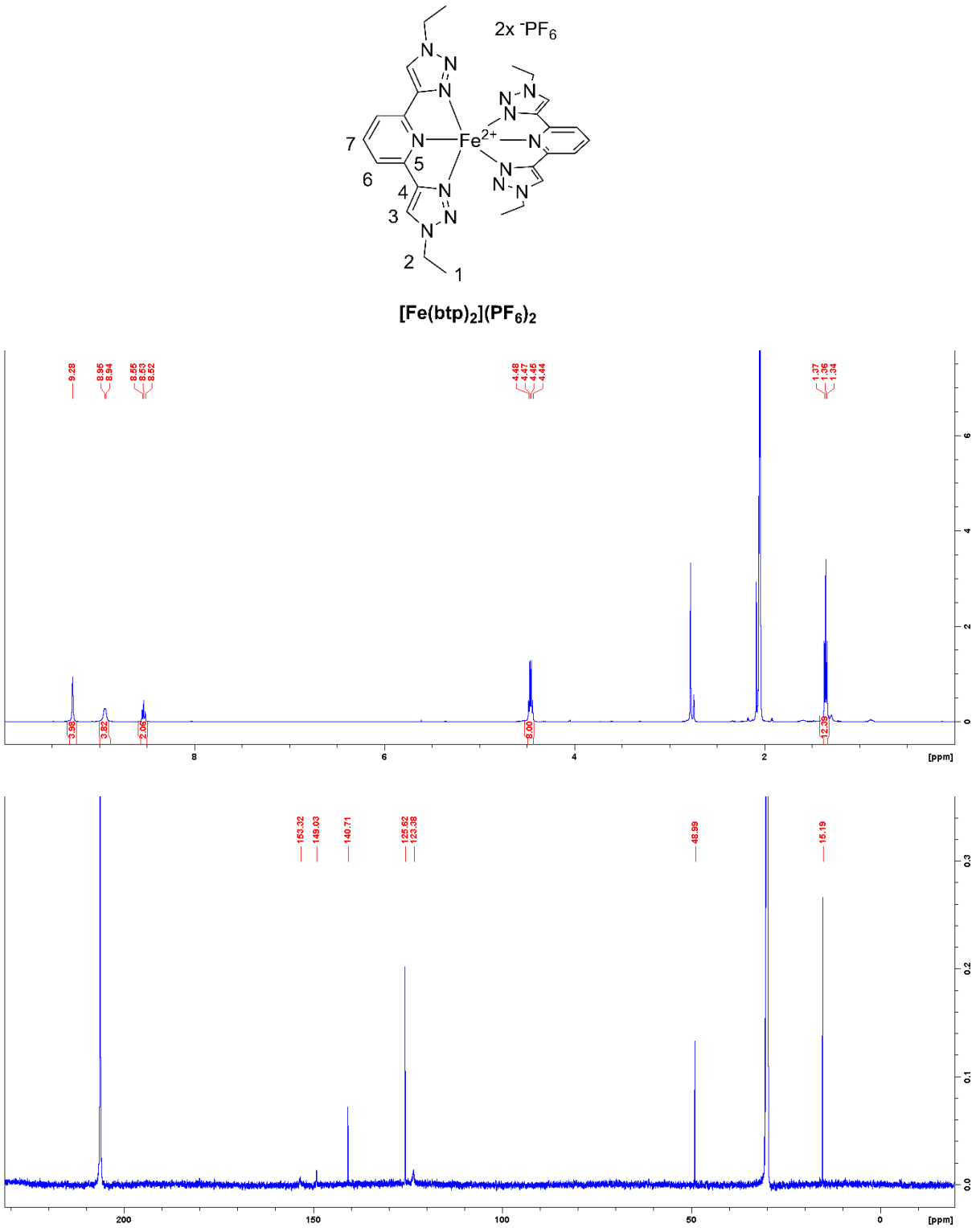

*Figure A 48: ^{1}H (top) and ^{13}C (bottom) NMR spectra of **[Fe(btp)$_2$]**(PF$_6$)$_2$ in d$_6$-acetone at 303 K.*

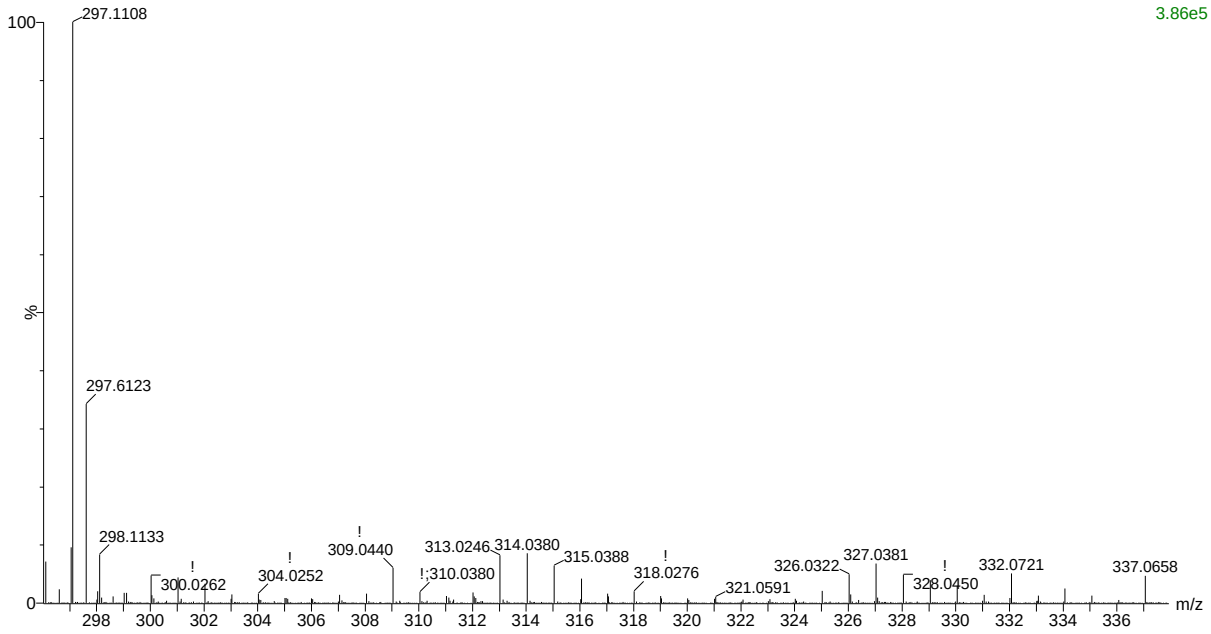

Figure A 49: ESI MS data of ***[Fe(btp)$_2$]***$(PF_6)_2$ *in MeCN.*

Details on the quantum chemical calculations of **[Fe(btp)$_2$]**$(PF_6)_2$ can be found in the published data.

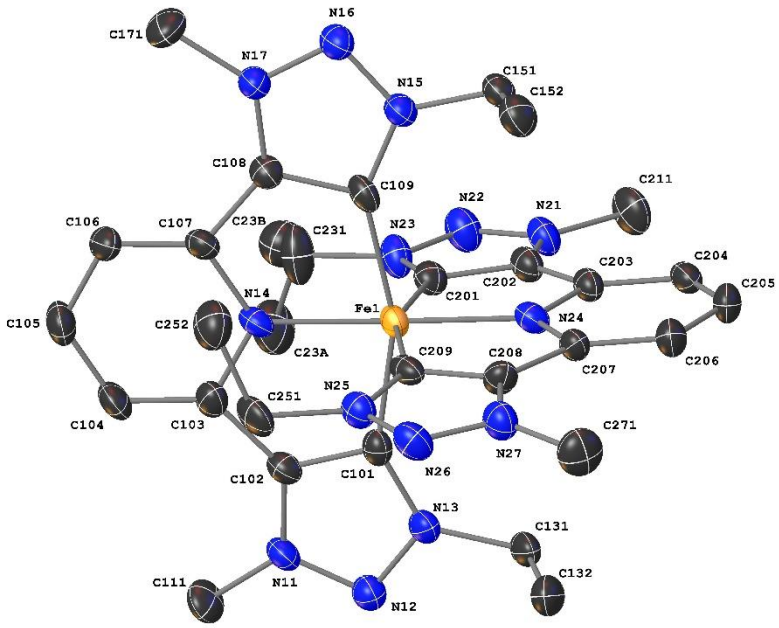

CCDC number	2050317	
Empirical formula	C26 H30 F12 Fe N14 P2	
Formula weight	884.43	
Temperature	120(2) K	
Wavelength	0.71073 Å	
Crystal system	Triclinic	
Space group	P-1	
Unit cell dimensions	a = 11.6525(6) Å	α= 92.055(2)°.
	b = 13.4838(7) Å	β= 103.119(2)°.
	c = 13.7533(7) Å	γ = 111.670(2)°.
Volume	1938.61(18) $Å^3$	
Z	2	
Density (calculated)	1.515 Mg/m^3	
Absorption coefficient	0.569 mm^{-1}	
F(000)	896	
Crystal size	0.30 x 0.12 x 0.10 mm^3	

Theta range for data collection	1.947 to 31.575°.
Index ranges	-17<=h<=17, -19<=k<=19, -20<=l<=20
Reflections collected	273411
Independent reflections	12923 [R(int) = 0.0359]
Completeness to theta = 25.242°	99.5 %
Absorption correction	Semi-empirical from equivalents
Refinement method	Full-matrix least-squares on F^2
Data / restraints / parameters	12923 / 0 / 500
Goodness-of-fit on F^2	1.038
Final R indices [I>2sigma(I)]	R1 = 0.0310, wR2 = 0.0797
R indices (all data)	R1 = 0.0352, wR2 = 0.0837
Extinction coefficient	n/a
Largest diff. peak and hole	0.720 and -0.612 e.$Å^{-3}$

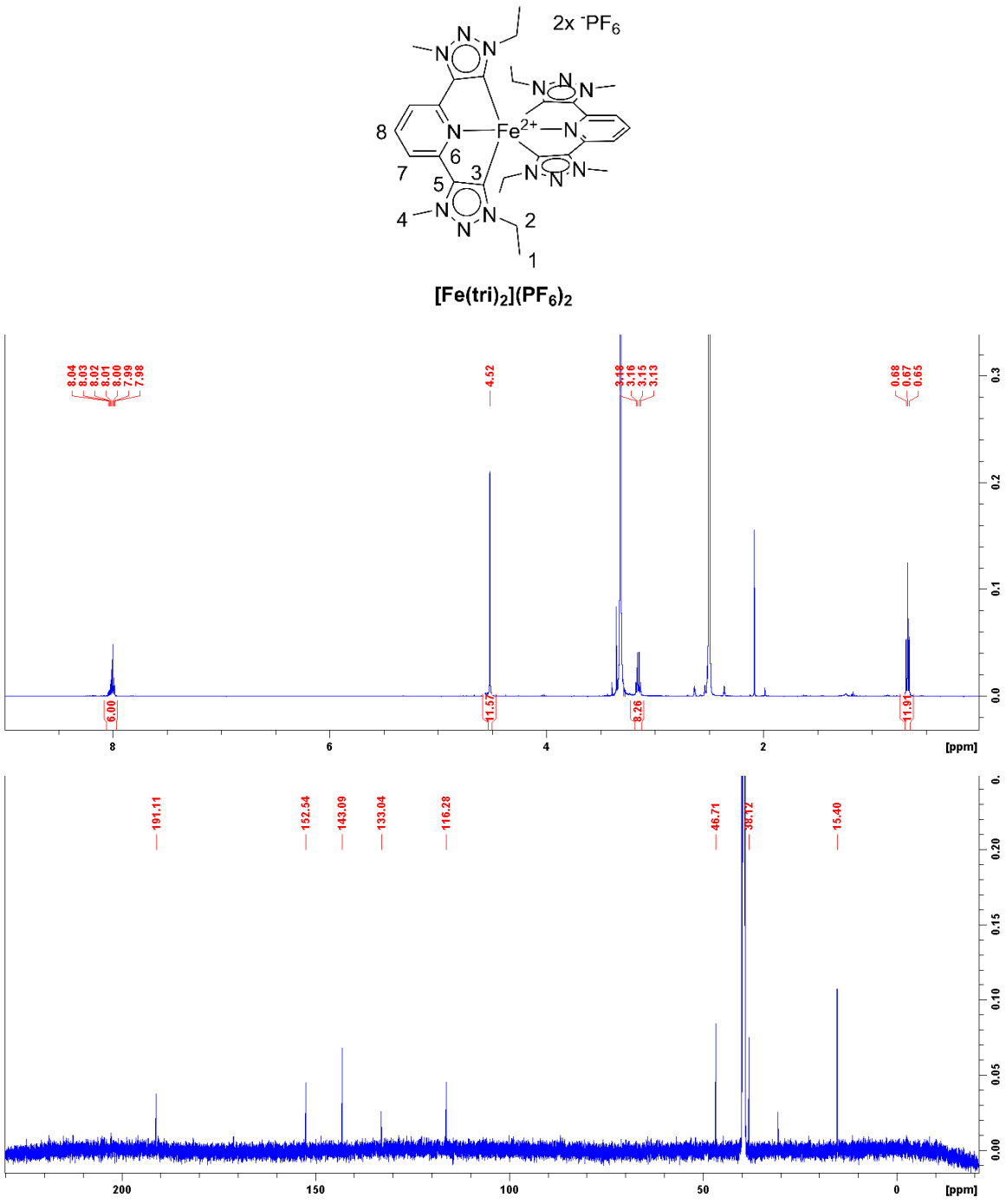

*Figure A 50: ^{1}H (top) and ^{13}C (bottom) NMR spectra of **[Fe(tri)$_2$]**$(PF_6)_2$ in d_6-DMSO at 303 K.*

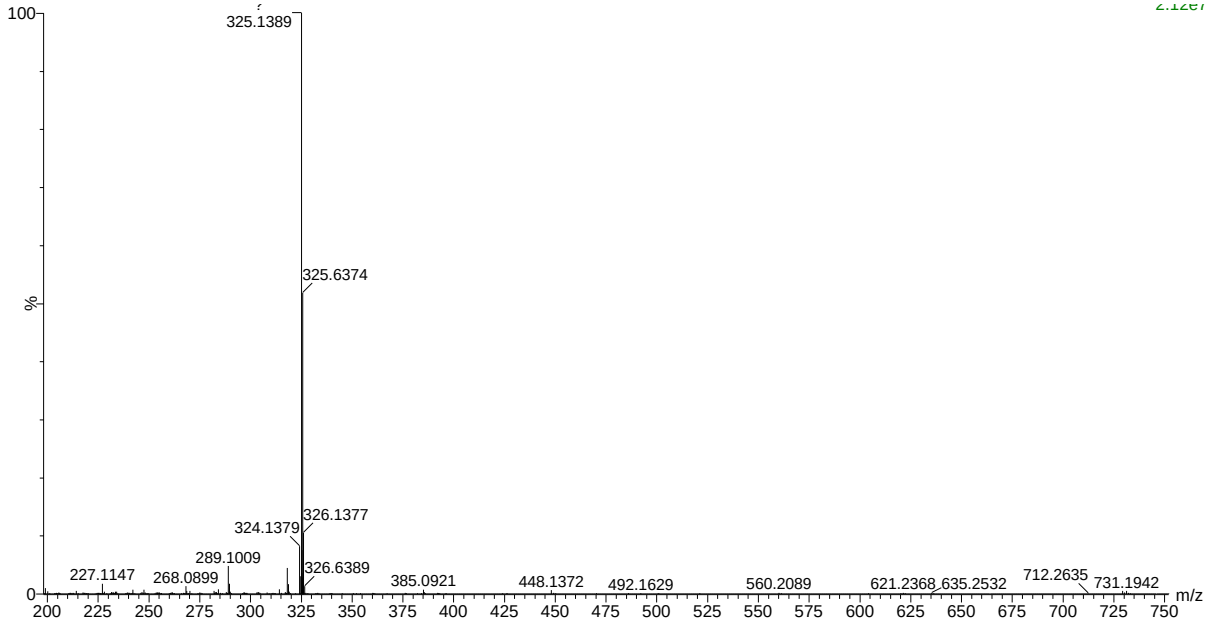

*Figure A 51: ESI MS data of **[Fe(tri)$_2$]**$(PF_6)_2$ in MeCN.*

Details on the quantum chemical calculations of **[Fe(tri)$_2$]**$(PF_6)_2$ can be found in the published data.

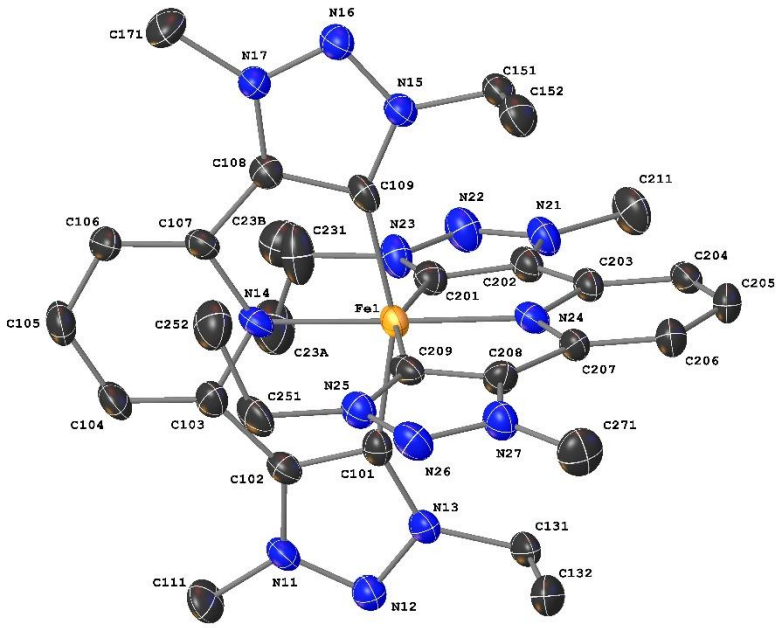

CCDC number	2049729	
Empirical formula	C_{30} H_{38} F_{12} Fe N_{14} P_2	
Formula weight	940.53	
Temperature	130(2) K	
Wavelength	0.71073 Å	
Crystal system	Monoclinic	
Space group	$P2_1/c$	
Unit cell dimensions	a = 8.5217(14) Å	α= 90°.
	b = 36.898(6) Å	β= 94.519(3)°.
	c = 13.416(2) Å	γ = 90°.
Volume	4205.4(12) $Å^3$	
Z	4	
Density (calculated)	1.486 Mg/m^3	
Absorption coefficient	0.530 mm^{-1}	
F(000)	1920	
Crystal size	0.25 x 0.24 x 0.21 mm^3	
Theta range for data collection	1.104 to 25.528°.	

Index ranges	-10<=h<=10, -44<=k<=44, -16<=l<=16
Reflections collected	46348
Independent reflections	7800 [R(int) = 0.1377]
Completeness to theta = 25.242°	100.0 %
Absorption correction	Semi-empirical from equivalents
Max. and min. transmission	0.7452 and 0.6344
Refinement method	Full-matrix least-squares on F^2
Data / restraints / parameters	7800 /0 / 548
Goodness-of-fit on F^2	0.986
Final R indices [I>2sigma(I)]	R1 = 0.0608, wR2 = 0.1500
R indices (all data)	R1 = 0.0998, wR2 = 0.1651
Largest diff. peak and hole	0.838 and -0.595 e.$Å^{-3}$

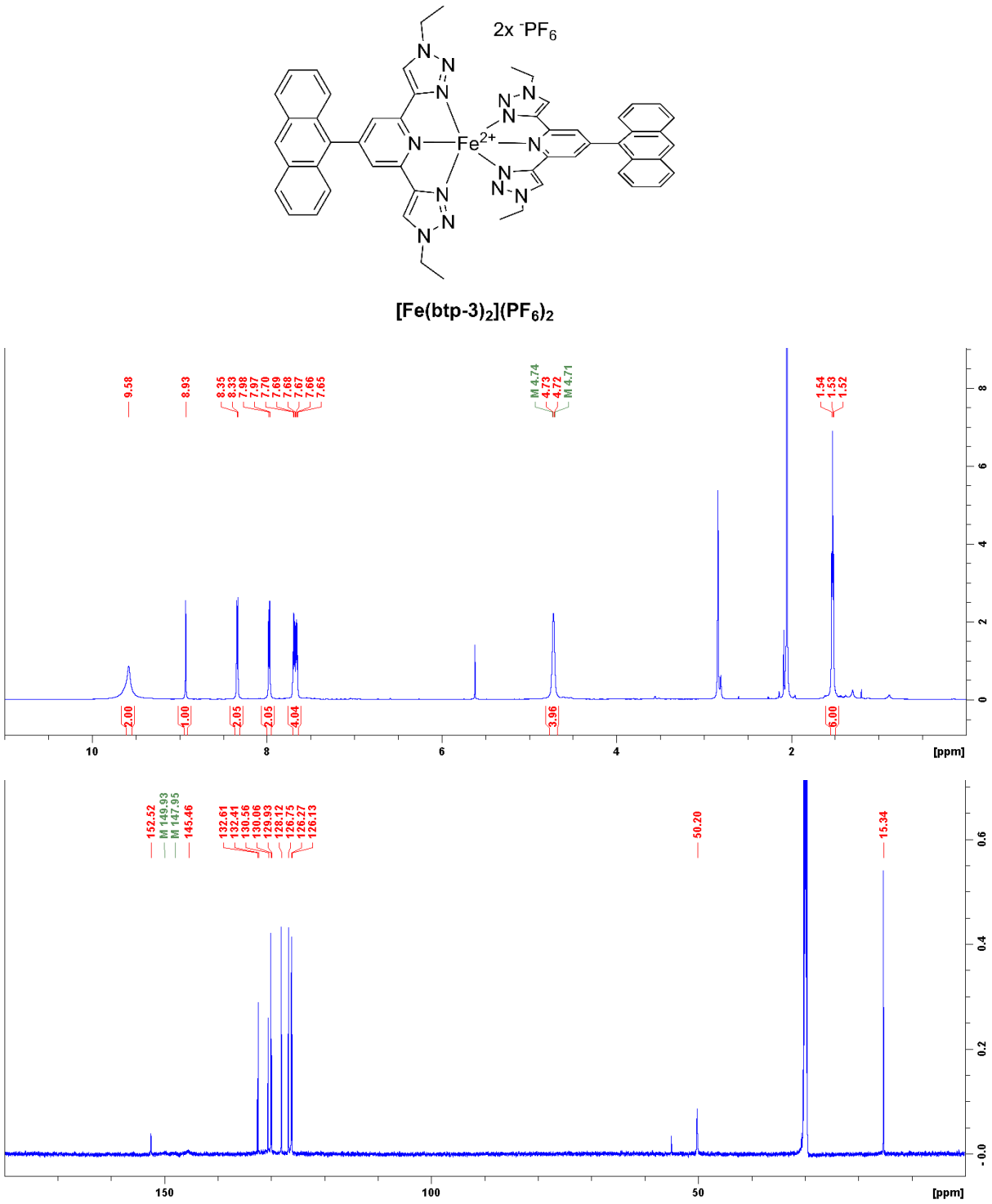

*Figure A 52: ^{1}H (top) and ^{13}C (bottom) NMR spectra of **[Fe(btp-3)$_2$]**$(PF_6)_2$ in d_6-acetone at 303 K.*

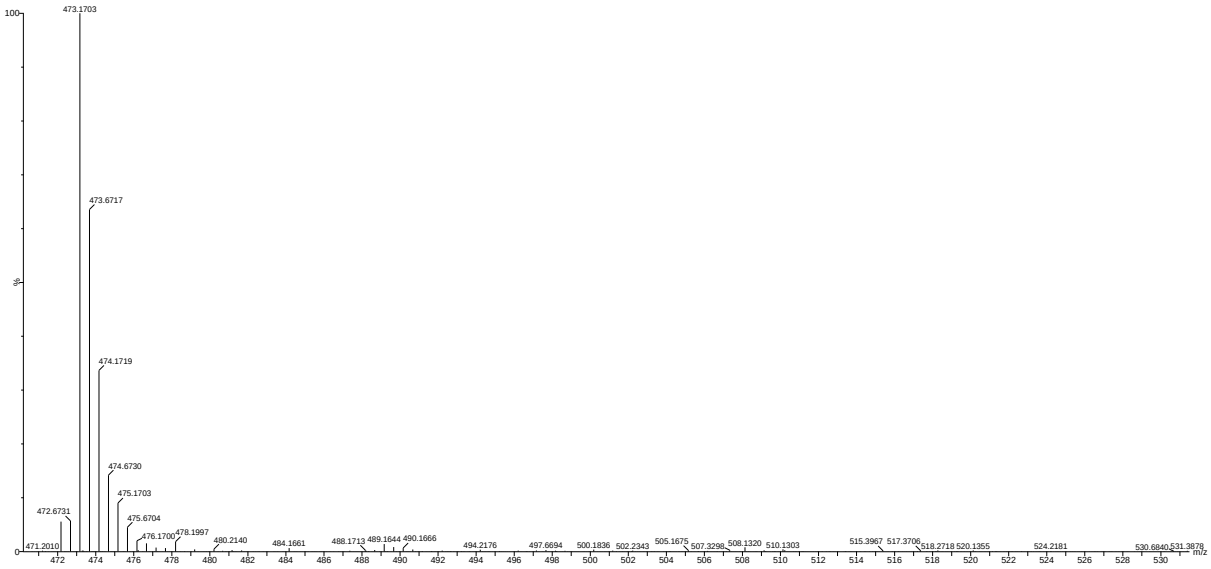

Figure A 53: ESI MS data of ***[Fe(btp-3)$_2$]***$(PF_6)_2$ *in MeCN.*

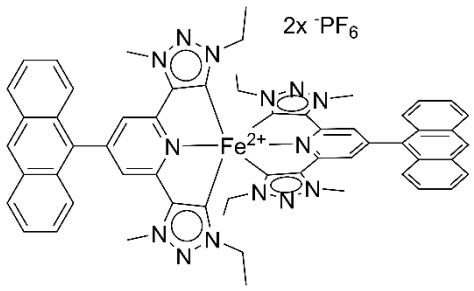

$[Fe(tri\text{-}3)_2](PF_6)_2$

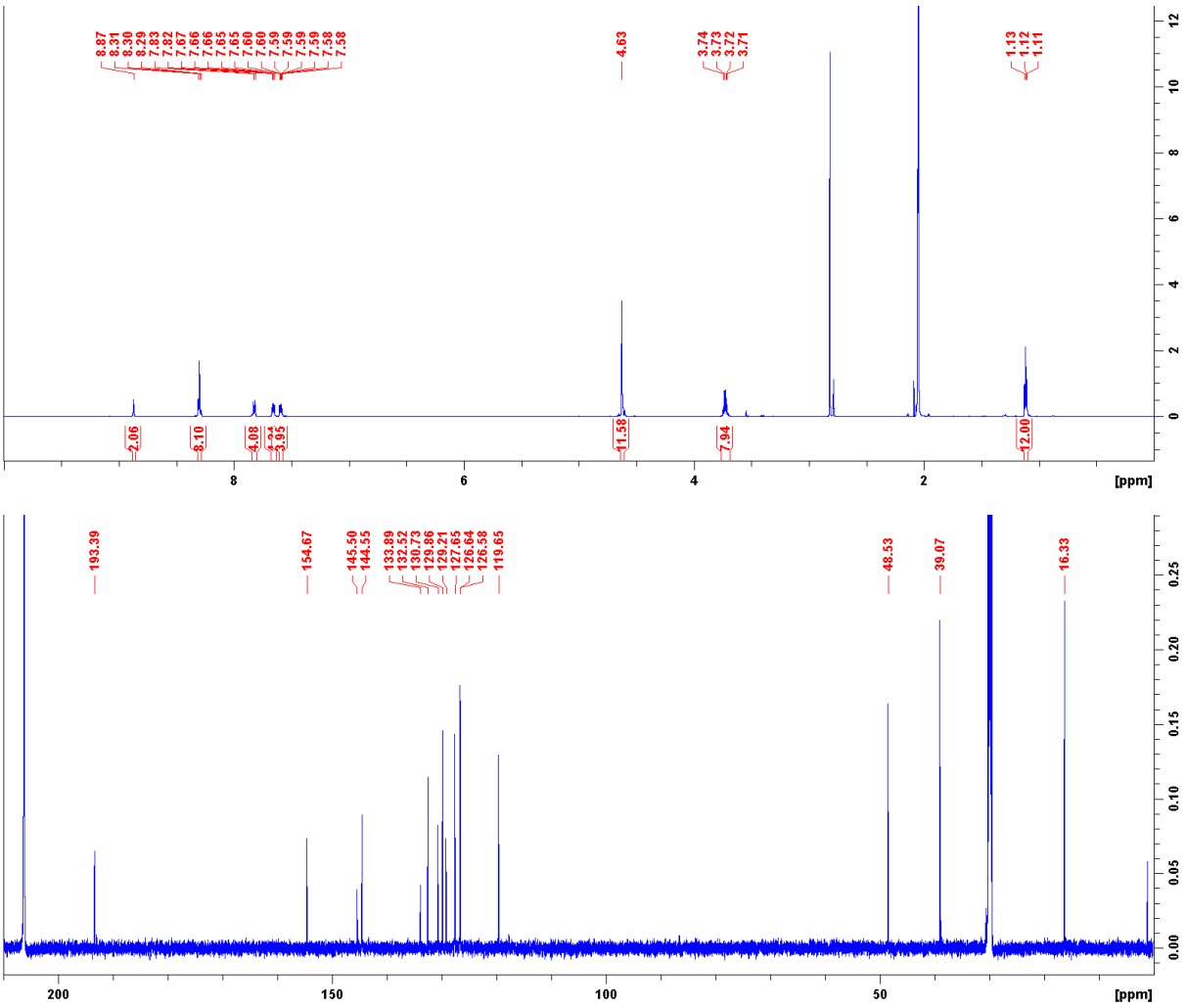

*Figure A 54: ^{1}H (top) and ^{13}C (bottom) NMR spectra of **$[Fe(tri\text{-}3)_2]$**$(PF_6)_2$ in d_6-acetone at 303 K.*

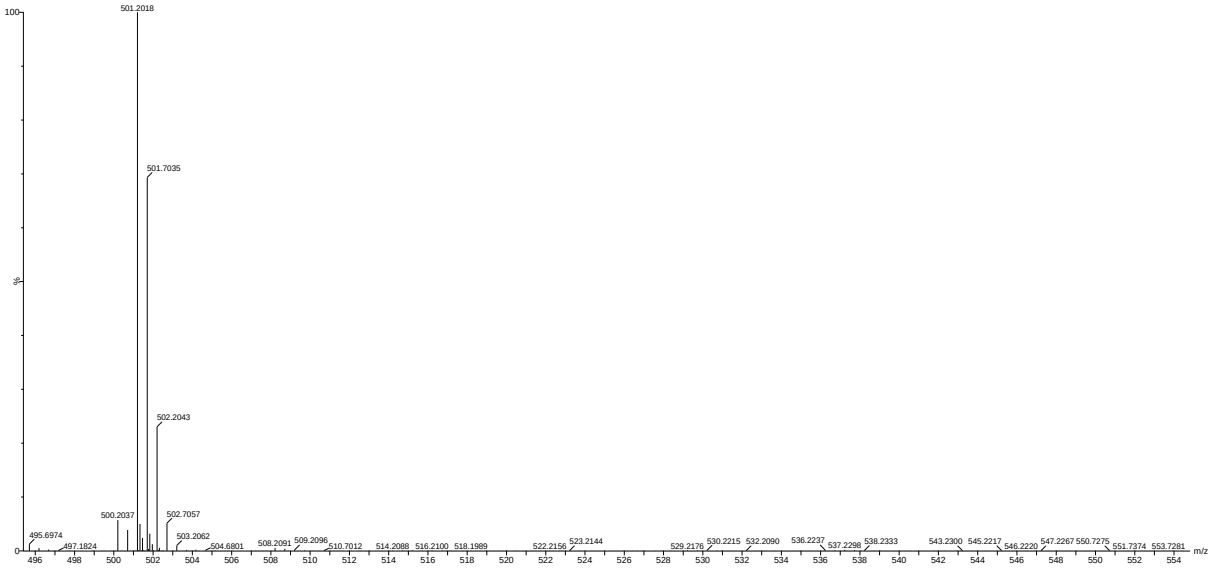

Figure A 55: ESI MS data of ***[Fe(tri-3)$_2$]***$(PF_6)_2$ *in MeCN.*

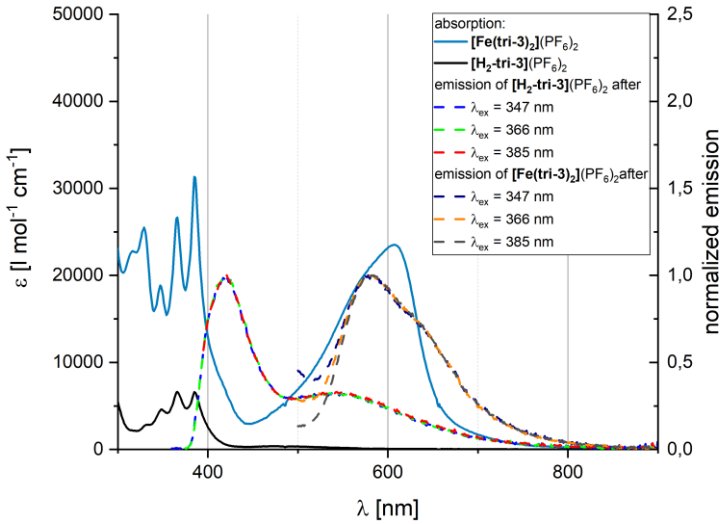

Figure A 56: Steady state absorption and emission spectra of ***[H$_2$-tri-3]***$(PF_6)_2$ *and* ***[Fe(tri-3)$_2$]***$(PF_6)_2$.

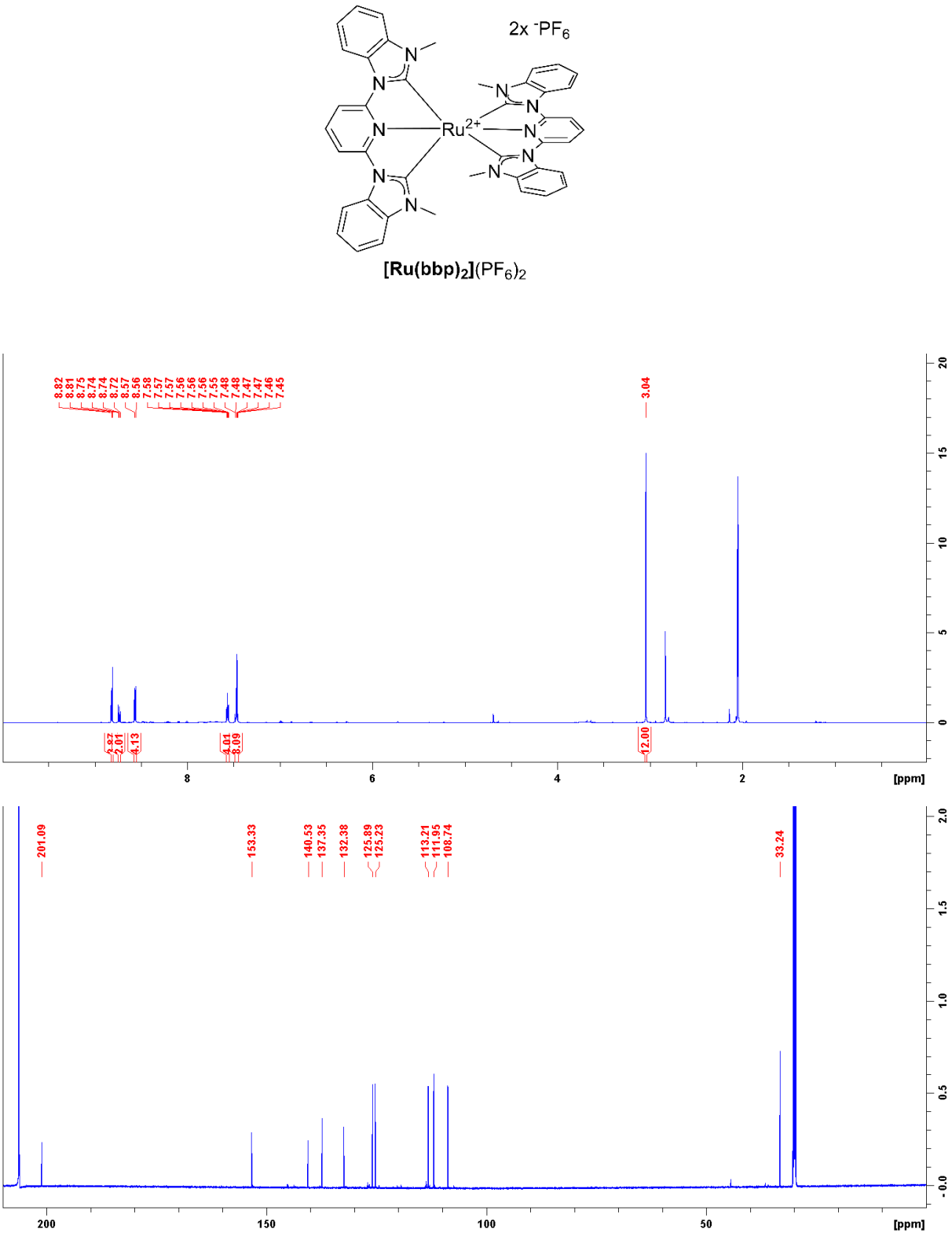

*Figure A 57: ^{1}H (top) and ^{13}C (bottom) NMR spectra of **[Ru(bbp)$_2$]**$(PF_6)_2$ in d_6-acetone at 303 K.*

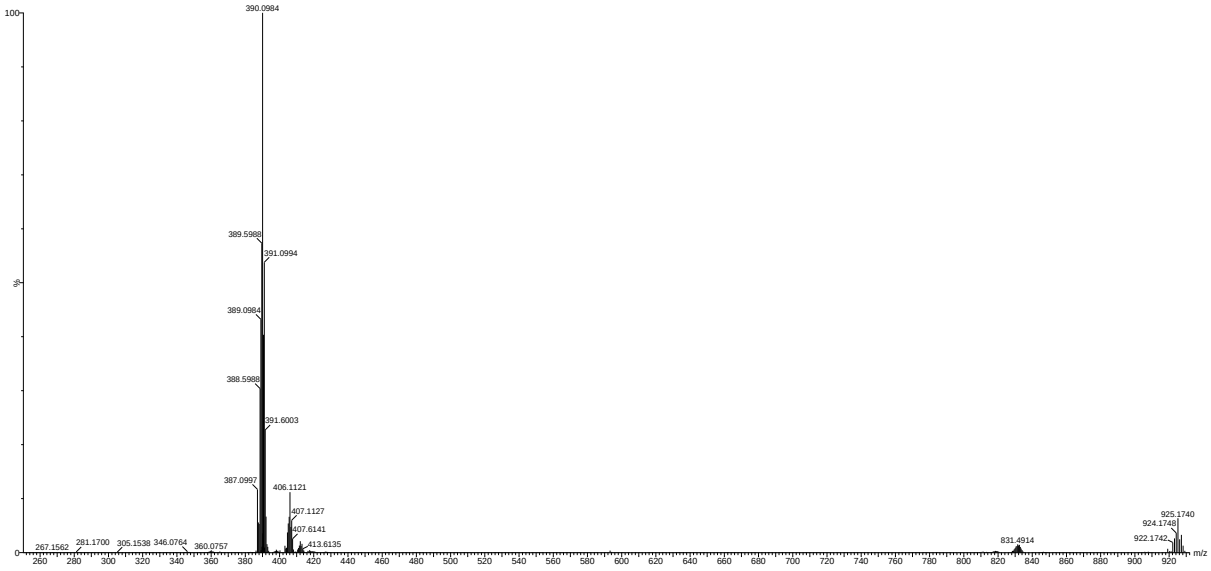

Figure A 58: ESI MS data of ***[Ru(bbp)$_2$]***$(PF_6)_2$ *in MeCN.*

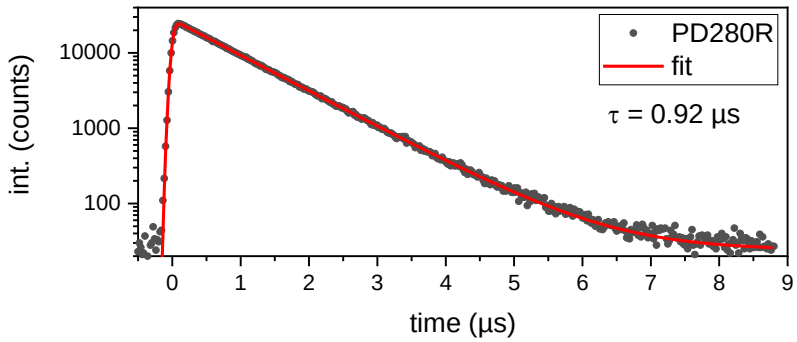

Figure A 59: Streak camara data and analysis of ***[Ru(bbp)$_2$]***$(PF_6)_2$ *(PD280R) recorded by the group of Prof. Stefan Lochbrunner.*

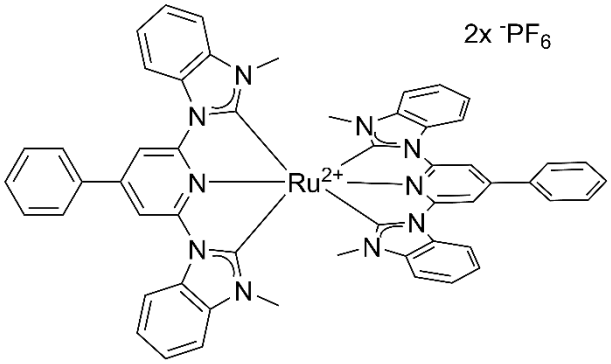

[Ru(bbp-1)$_2$]$(PF_6)_2$

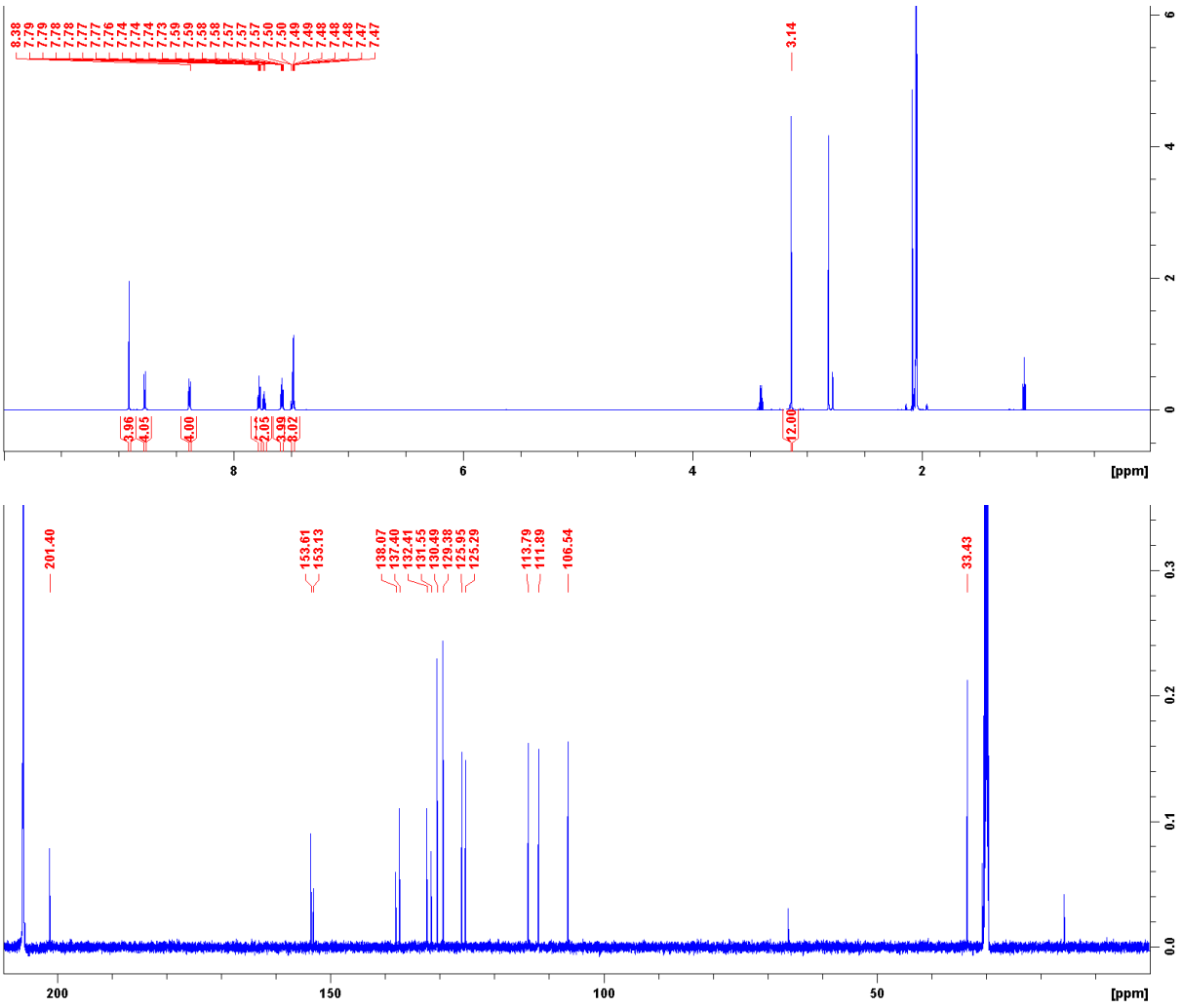

*Figure A 60: ^{1}H (top) and ^{13}C (bottom) NMR spectra of **[Ru(bbp-1)$_2$]**$(PF_6)_2$ in d_6-acetone at 303 K.*

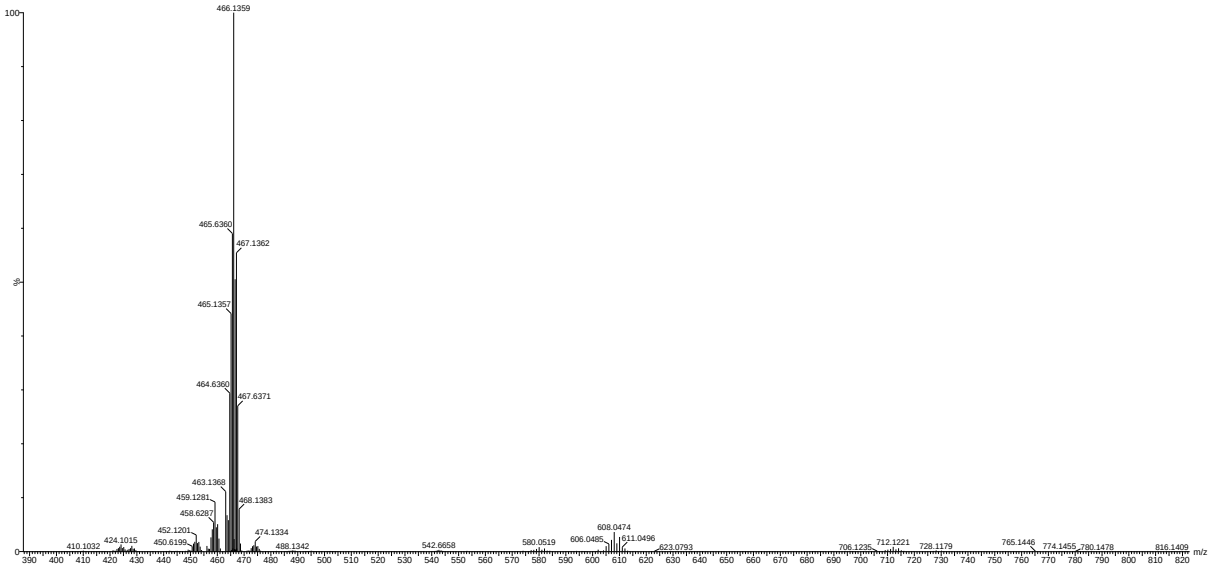

Figure A 61: ESI MS data of ***[Ru(bbp-1)$_2$]***$(PF_6)_2$ *in MeCN.*

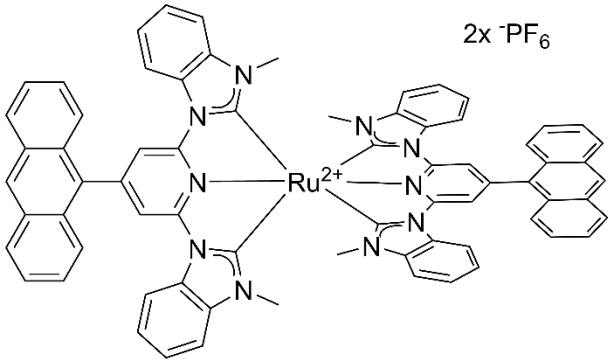

[Ru(bbp-3)$_2$]$(PF_6)_2$

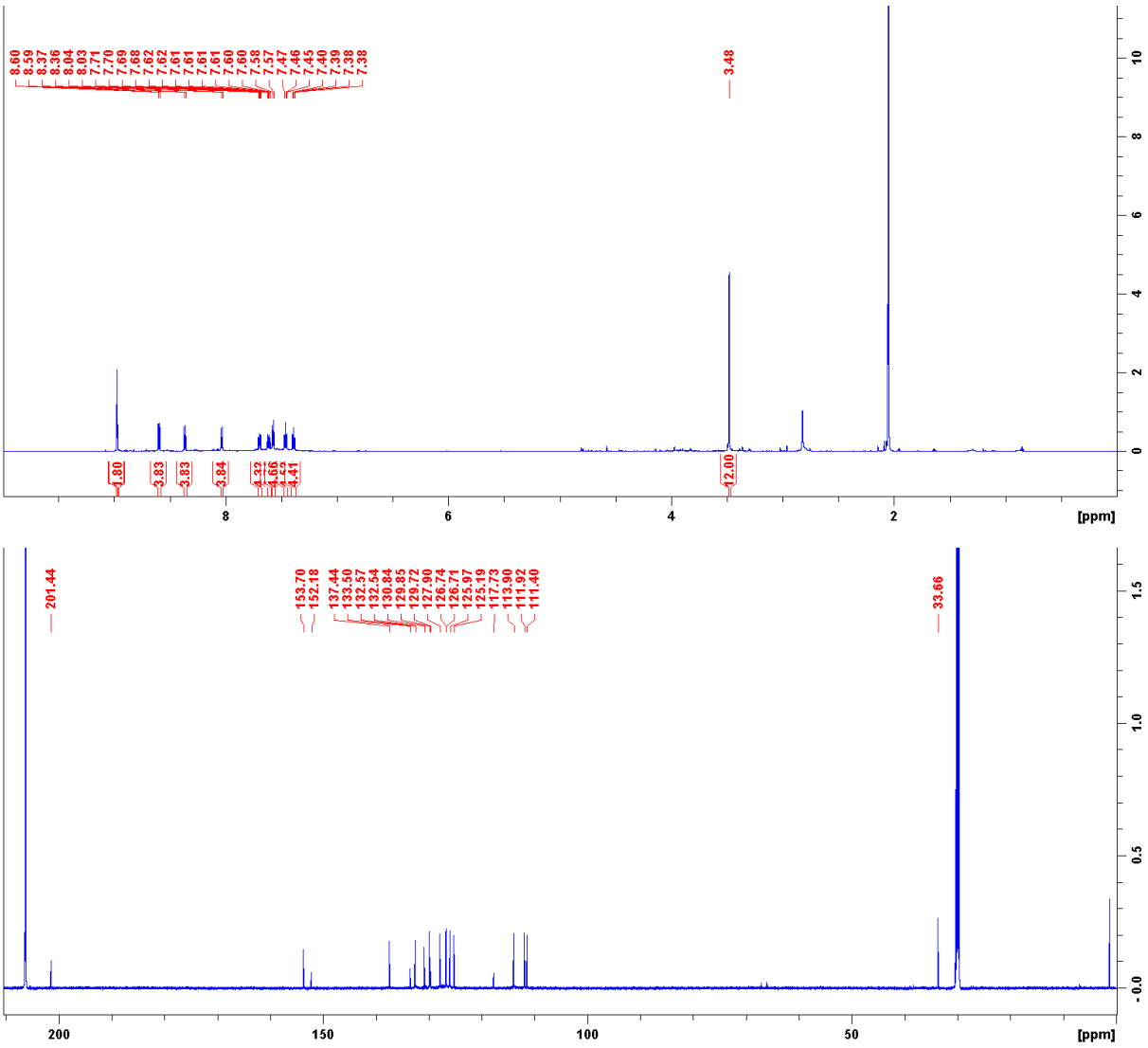

*Figure A 62: ^{1}H (top) and ^{13}C (bottom) NMR spectra of **[Ru(bbp-3)$_2$]**$(PF_6)_2$ in d_6-acetone at 303 K.*

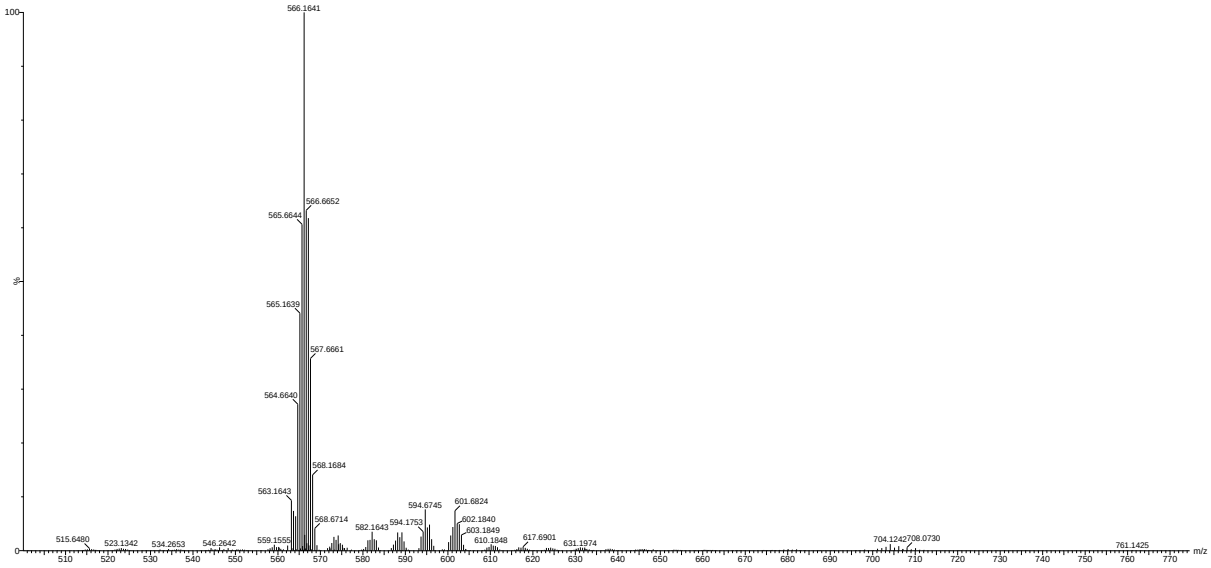

Figure A 63: ESI MS data of ***[Ru(bbp-3)$_2$]***$(PF_6)_2$ *in MeCN.*

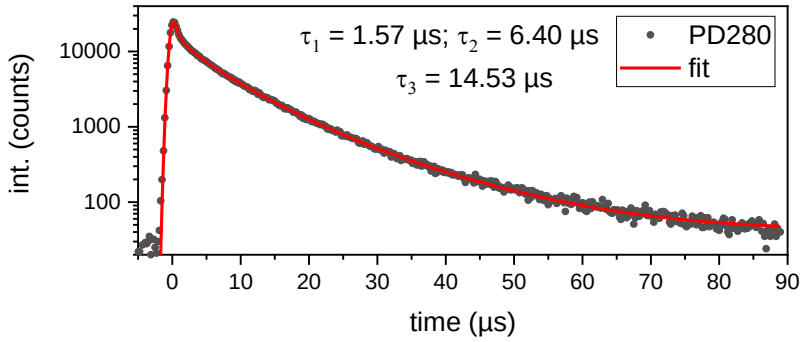

Figure A 64: Streak camara data and analysis of ***[Ru(bbp-3)$_2$]***$(PF_6)_2$ *(PD-280) recorded by the group of Prof. Stefan Lochbrunner.*